POLITECNICO DI TORINO

Master’s degree in Automotive Engineering
A.Y. 2024/2025
Degree session October 2025

Hydrogen use in Internal Combustion Engine:
Analysis and comparison of turbulent combustion models

Supervisor at Chalmers:
Andrei Lipatnikov
Supervisor at Politecnico di Torino:
Mirko Baratta

Candidate:
Francesco Riccardo

Summary

Abstract

The main challenge of the transport sector today is the reduction of emissions, and one of the most innovative solutions currently under investigation in this direction is the use of hydrogen as fuel, in particular the application of it in the internal combustion engines (ICEs). The present thesis attempts to firstly provide an overview of what are the main solutions for the application of hydrogen in the transport sector and compare them from the environmental and economical point of view. Secondly, three combustion models highly used in the study of ICEs run by hydrogen will be compared through simulations using the CONVERGE software, with the aim of identifying the key parameters that influence the results, and the conditions under which the models yield predictions that converge or diverge. The simulations will be done on a single-cylinder, spark-ignition (SI) engine operating exclusively on hydrogen. Moreover, the parameters that will change will be the air/fuel ratio and the Spark Time (ST). The combination of those factors will show how much both influence the results for this type of engine simulations for each model.

Introduction

Hydrogen: the new fuel

Today one of the most important challenges in the transport sector, and in general in the energy one, is the development of new way of propulsion. Electricity is the most used now, through the battery electric vehicles (BEVs), but this solution led to several difficulties that prevent some people to buy them. From an environmental point of view there is the problem related on how effectively the electricity is produced, if in a green way or not, also if the batteries could be recycled or not and how. Instead, from a more practical point of view some people avoid the choice of an eclectic vehicle for the high cost, the time spend recharging the batteries and sometimes also the absence of the iconic sound of a thermal engine.

For this reason, there is another element that is considered as a valid alternative for the follis fuels, the hydrogen.

The application of hydrogen in the transport sector is already present nowadays, through the fuel cell electric vehicles (FCEVs) and with the hydrogen internal combustion engine (H2ICE). A lot of car makers like VOLVO [1] already study both solution and make comparison of them.

Hydrogen FCEVs generate electricity through a chemical reaction between hydrogen gas and oxygen inside a fuel cell, which powers an electric motor. Unlike traditional BEVs that store energy in large batteries, FCEVs carry hydrogen in onboard tanks and use a smaller battery to assist with energy recovery and acceleration. This technology is both clean and efficient, producing only water vapor as a byproduct. FCEVs also benefit from quick refuelling times, comparable to gasoline cars, and generally provide a longer driving range than most BEVs.

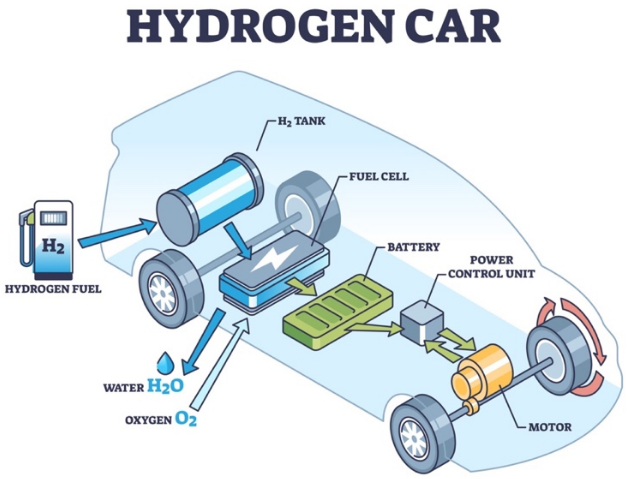

Figure 1. How FCEVs works

H2ICE is another solution from the use of hydrogen, that basically burns hydrogen in a modified internal combustion engine, adapted to handle the fast-burning nature of it. While they function similarly to diesel engines, they require specialized technologies, such as custom fuel injectors and ignition systems, to accommodate hydrogen's unique properties. There are already some solutions of this type, like the Hyundai Doosan Infracore [2], an 11 L engine that produces a power output of 300 kW and a torque of 1700 Nm at 2000 RPM. It satisfies Euro 7 regulations which require the emission to be 90% reduced to the current level to meet Zero CO_2 (below 1g/kwh) and Zero Impact Emission (Zero Emission in EU). This engine is powered by low-purity hydrogen, making it durable, economical and energy-dense. A single charge of 10 minutes enables up to 500km.

Figure 2. Hyundai H2ICE engine **[2]**

These solutions that have been explained are innovated from a general point of view in the transport sector, without considering the actual application of them in the reality with the related costs, emission and advantages with respect to the conventional fossil fuels engines. Baldinelli et. al [3] studied the application of hydrogen in the public transport, in particular busses, where, talking about hydrogen, the fuel cells seam more difficult to apply. The authors compare the H2ICE to the already present diesel engine in the Well-to-Whell (WTW) process. The results of the study shown that, compared to conventional diesel used for busses, hydrogen can compete from the point of view of CO_2 emission reduction, −29% in the actual case of electrolysis run with electricity from the EU grid, while it shows

an increment of 40% of primary energy consumption. Must be considered that this value should decrease with more "greener" way of hydrogen production and with higher power-to-hydrogen efficiency, that could reach up to 80-85% for high-temperature technology.
The previous results underline how important the production process is considering the use of hydrogen as fuel, due to the high complexity and way to do it.

Way to produce hydrogen

Hydrogen is one of the most present elements on the planet, 75% [4], but is always bounded with other elements, and this the main problem when it is needed alone, it must be separated. There are several processes that bring to the separation of hydrogen from other element, and they depend on the starting material that is used. Based on that, it's classified in three types by the environmental impact: grey, blue and green hydrogen.

- *Grey hydrogen* is primarily produced through the reforming of fossil fuels, especially natural gas. Although it is the most cost-effective form of hydrogen to produce, the process results in significant CO_2 emissions. Today, it remains the most widely used type of hydrogen.

- *Blue hydrogen* is likewise derived from fossil fuels, but its production involves carbon capture and storage technologies that reduce CO_2 emissions. While it is less polluting than grey hydrogen, it only mitigates emissions rather than eliminating them entirely.

- *Green hydrogen*, also known as renewable hydrogen, is produced through the electrolysis of water. What makes it particularly important is that the process is powered exclusively by renewable energy sources, resulting in zero atmospheric emissions. It is the cleanest and most sustainable form of hydrogen available.

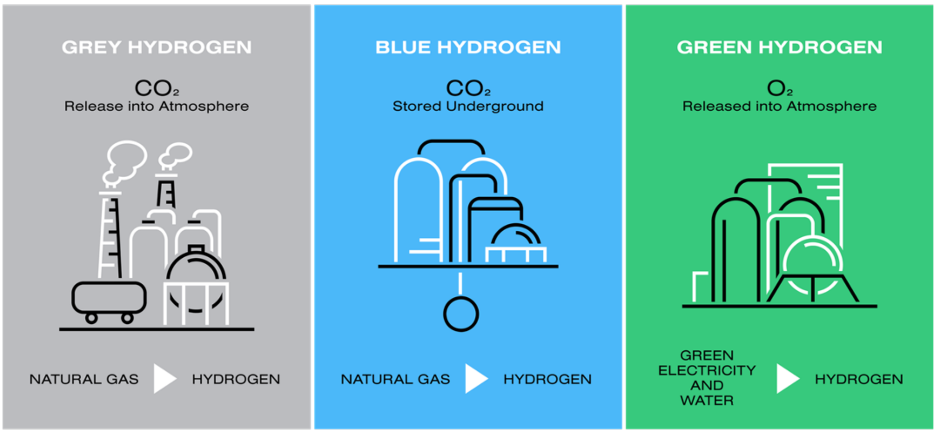

Figure 3. The three types of hydrogen

Abdalla et. al [5] explained in a complete way what are the processes used for the production of hydrogen that bring to the differentiation already explained. Generation of hydrogen from fossil fuels could be through *steam reforming*, *partial oxidation*, *autothermal oxidation*. Generation of hydrogen from renewable sources could be through *gasification of biomass/biofuels* and *water splitting by solar energy or wind energy*. In particular, for the production from fossil fuels:

- *Steam reforming* achieves a high hydrogen yield efficiency of around 74%. The process involves several key steps: impurity removal, catalytic reforming (or synthesis gas generation), water-gas shift reaction, and methanation or gas purification. To obtain purified hydrogen and avoid coke formation on the catalyst surface, the reaction is carried out at temperatures between 700–850 °C, pressures of 3–25 bar. The catalysts used can be either non-precious metals, such as nickel, or precious metals like platinum and rhodium. However, due to significant limitations in both mass and heat transfer, catalyst effectiveness is generally limited to about 5%. The hydrogen generated is subsequently purified.

- In *partial oxidation*, hydrogen is produced by reacting steam, oxygen, and hydrocarbons. This process can be carried out either catalytically or non-catalytically. In the non-catalytic version, temperatures typically range from 1150 to 1315 °C, and in some cases up to 1500 °C to ensure complete conversion and minimize carbon or soot formations. The feedstock can include methane, heavy oils, or coal. In the catalytic version, the process operates at lower temperatures, around 950 °C, and typically uses lighter feedstocks such as methane or naphtha.

- *Autothermal reforming* combines steam reforming and partial oxidation, using the exothermic heat from partial oxidation to drive the endothermic steam reforming reaction, resulting in a thermally balanced process. Effective operation requires precise control of the oxygen-to-fuel ratio within a limited time frame to prevent coke formation and to regulate both the reaction temperature and gas composition. In this process, reactor outlet temperatures typically range from 950 °C to 1100 °C, with gas pressures reaching up to 100 bar.

Moving instead to the production from biomass/biofuels, *gasification* occurs at higher temperatures (above 1000K) hence biomass can be converted into a gas. The particles undergo partial oxidation producing gas and charcoal. Hydrogen (H_2), carbon monoxide (CO), carbon dioxide (CO_2) and methane (CH_4) are produced from the reduction of charcoal. The main target of gasification is to obtain gaseous products. The limitations of gasification process are the low thermal efficiency, the moisture contained must be totally vaporized as much as possible. some essential parameters such as biomass type, particle size, temperature ranges/rates, steam-to-biomass ratio and catalyst types affect the hydrogen yield percentage. The main challenge for biomass gasification is the low thermal efficiency due to the moisture content. The gasification process can only be used for biomass with moisture content less than 35%.

Lastly, the greener way to produce hydrogen the *water splitting* (electrolysis), this process requires electricity that should be produced through solar panels or wind. For what concern the use of the solar light through photovoltaic cells, the photo-converter efficiency is about 20% with the electrolyser's efficiency of about 80%. In addition, the efficiency for solar energy conversion is about 16%. This technology faces several challenges, including the high cost of photovoltaic (PV) cells. For large-scale hydrogen production, it is essential to reduce energy consumption, operational costs, and system maintenance. Additionally, aspects such as energy efficiency, safety, durability, and overall reliability require further research and improvement. In hydrogen production using PV cells, a related approach is solar thermal hydrogen production. This method also harnesses solar energy, but instead of using PV cells, it concentrates solar power to generate extremely high temperatures (above 2500 K), enabling the endothermic decomposition of water. In this process, water dissociates into hydrogen and oxygen in a single step.

Below, in Table 1, there are the main advantages and disadvantages for all the production process already explained.

PROCESS	ADVANTAGES	DISADVANTAGES
STEAM FORMING	- Most used in industrial processes - Existing infrastructures - Oxygen not required - Low operating temperatures	- CO_2 emission
PARTIAL OXIDATION	- No catalyst - Low methane slip - Existing infrastructures and technologies	- High operating temperatures - Complex process
AUTOTHERMAL REFORMING	- Low process temperature compared to partial oxidation - Low methane slip - Existing infrastructure and technologies	- Require air and O_2 - New technology
GASIFICATION OF BIOFUEL	- Abundant and cheap feedstock - CO_2 neutral	- H_2 content depend on feedstock availabilities and impurities
ELECTROLYSIS	- Abundant feedstock - Emission free - Byproduct is O_2	- Low conversion efficiency - Need sunlight or wind - No-effective photocatalytic materials - High costs

Table 1. Comparison of H_2 production processes **[5]**

Use of hydrogen in the transport sector

As already described before, the use of hydrogen as fuel has been already studied and there are a lot of application in the transport sector. The most used solution today are the hydrogen fuel cells, how they works have been explained before, but there are authors that describe in a very complete way this technology. Maniharan et. al [6] created an overview of all the technologies used for the fuel cells application. Something interesting, that is related both to the fuel cells, but also to the application of H2ICE, is the way to store the hydrogen, that the authors explained largely. The main issue to the storing of the hydrogen is related to his low energy density, storing enough fuel on a vehicle to achieve a sufficient driving range is challenging without making the storage container excessively large or heavy. The main technologies are:

- *Pressurized Tank Storage*: tanks designed for high strength and impact resistance in the event of collisions are typically made from carbon-fibre-wrapped cylinders. In such tanks, compressed hydrogen can be stored at a pressure of 34 MPa, with a mass of 32.5 kg and a volume of 186 L, sufficient for a driving range of around 500 km. However, due to hydrogen's low density, it is difficult to store adequate amounts compared to other gases. While some manufacturers continue limited research on the feasibility of storing hydrogen in liquid form at low temperatures, this method is not currently practical for everyday vehicle use. Additionally, liquid hydrogen storage systems can lose up to 1% of their volume per day due to boil-off and require intense refrigeration to maintain the hydrogen at 20 K.

- *Hydrogen Uptake in Metal-Based Compounds*: they can be used to store hydrogen at relatively low pressures, below 3 or 4 MPa, and at temperatures above room temperature. However, these metals significantly increase the overall weight, making them impractical for most vehicles, and they also tend to be expensive. Research has shown that lithium nitride is capable of reversibly storing large amounts of hydrogen. Under high vacuum conditions (10^{-9} MPa or 10^{-5} mbar), about two-thirds of the stored hydrogen can be released at temperatures below 200 °C, while the remaining third requires temperatures above 320 °C to be released.

- *Cryogenic Liquid Hydrogen Storage*: hydrogen is stored in liquid form by cooling it to the cryogenic temperature of −259.2 °C. Liquid hydrogen has a very low density, 1 L weighs only 71.37×10^{-3} kg. Maintaining hydrogen at such a low temperature significantly increases costs due to the need for high-performance insulation. Moreover, liquid hydrogen can become explosive when mixed with certain other gases. For this reason, before refuelling, nitrogen gas must be used to purge any residual gases from the tank.

Going back on the application of the fuel cells in the transport sector, there are other solutions that do not involve road vehicles. Jung et. al [7] examine a liquid hydrogen fuelled hybrid ship propulsion system consisting of an LH_2 fuel gas supply system, a polymer electrolyte membrane fuel cell (PEMFC), and battery systems. The work has been done considering three case studies: low (Case 1), medium (Case 2) and high (Case 3) power output. The maximum output of the battery system was 1300 kW in Cases 1 and 2, while in Case 3 it reached 1410 kW. However, the output was limited to a maximum duration of 5 seconds, depending on the hydrogen supply temperature of the PEMFC system. The average power consumption of the balance of plant (BOP) in the PEMFC system was 43.64 kW, 27.51 kW, and 44.06 kW for Cases 1, 2, and 3, respectively.

Considering instead the application of fuel cells in the aviation, Wu et. al [8] examine the HY4, a hydrogen-powered aircraft developed by the German Aerospace Center (DLR), through efficiency and energy density advantages. Based on the research, battery-electric aircraft of comparable size has a range of around 1200 km, whereas the HY4 hydrogen-powered aircraft has a range of up to 1500 km. At the same time, traditional aviation fuels release 3.16 kg of CO_2 per kilogram of fuel used, burning hydrogen results in negligible CO_2 emissions and, at very high temperatures, relatively low levels of NO_x. Also, it is possible to decrease aviation-related carbon dioxide emissions by 50% by 2040 using hydrogen-fuelled aircraft, but only if the challenges associated with infrastructure and hydrogen production will be overcome. The authors conclude declaring that innovations such as the HY4 demonstrate the growing feasibility of hydrogen-powered aircraft, highlighting the technology's potential to transform both commercial and regional aviation. However, to fully realize this potential, several technical and infrastructure-related challenges still need to be addressed.

Focusing on the application of hydrogen in the automotive sector for the H2ICE, the studies regarding this topic are a lot and is possible to find also starting from the '90. L. M. Das et. al [9] present an overview of the past H2ICE technologies through the analysis of several scientific articles, comparing it to the conventional fuel and discuss the possible way to avoid the undesirable combustion phenomena that characterize the hydrogen engines. The most studied problems, that creates more issues are the pre-ignition and the backfire. The first refers to the ignition of the air/fuel mixture before the timed spark occur. It could happen away from the inlet valve, in that case it could lead to combustion knock, which reduces engine power output and efficiency. In some cases, pre-ignition causes excessively high temperatures within the combustion chamber, increasing the risk of detonation. During detonation, thermal ignition occurs in one part of the chamber while spark ignition is already underway in another, resulting in the formation of two simultaneous combustion waves. This interaction causes an abnormally high rate of pressure rise.
The phenomenon of backfire, instead, occurs when the incoming air/fuel mixture contacts a high-temperature source with enough energy to trigger combustion while the intake valve is still open. In

hydrogen engines, the impact of backfire is more significant than in gasoline engines, ranging from a minor misfire to severe damage, including potential fires in the fuel system.

All the studies reveal that the mayor parameter that influence both pre-ignition and backfire is the equivalence ratio (φ), but there are other works that shows that, in addition to the equivalence ratio, the likelihood of backfire also strongly depends on the temperature of the residual gases, which is influenced by engine speed and load conditions.

Another feature that comes from the article is the higher diffusivity of the hydrogen, that is a major advantage in engine applications. Thanks to hydrogen's wide flammability range, it enables effective 'quality governing,' allowing engine power to be controlled by adjusting the hydrogen-to-air ratio in the mixture.

The authors report also tables with the most important differences in thermodynamic (Table 2) and combustion (Table 3) properties between hydrogen and other conventional fuels.

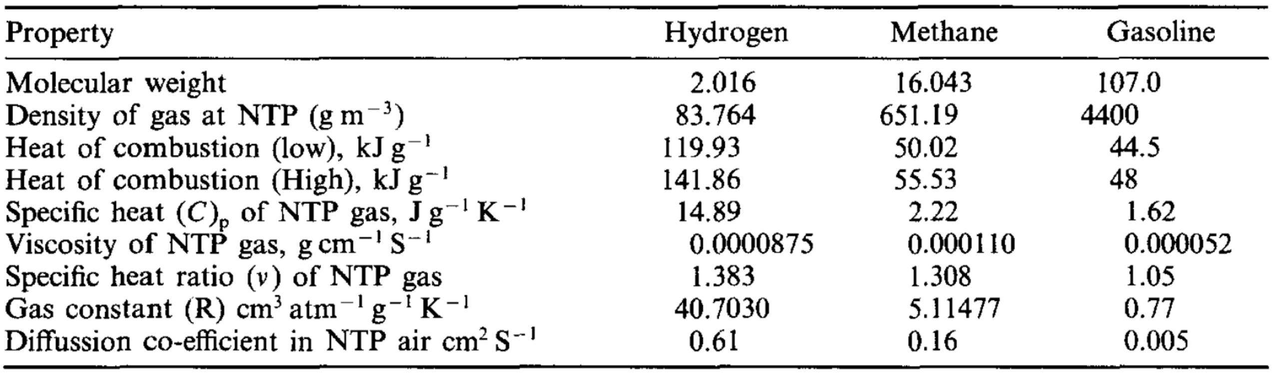

Property	Hydrogen	Methane	Gasoline
Molecular weight	2.016	16.043	107.0
Density of gas at NTP ($g\,m^{-3}$)	83.764	651.19	4400
Heat of combustion (low), $kJ\,g^{-1}$	119.93	50.02	44.5
Heat of combustion (High), $kJ\,g^{-1}$	141.86	55.53	48
Specific heat $(C)_p$ of NTP gas, $J\,g^{-1}\,K^{-1}$	14.89	2.22	1.62
Viscosity of NTP gas, $g\,cm^{-1}\,S^{-1}$	0.0000875	0.000110	0.000052
Specific heat ratio (v) of NTP gas	1.383	1.308	1.05
Gas constant (R) $cm^3\,atm^{-1}\,g^{-1}\,K^{-1}$	40.7030	5.11477	0.77
Diffussion co-efficient in NTP air $cm^2\,S^{-1}$	0.61	0.16	0.005

Table 2. Thermodynamic properties of hydrogen, methane and gasoline **[9]**

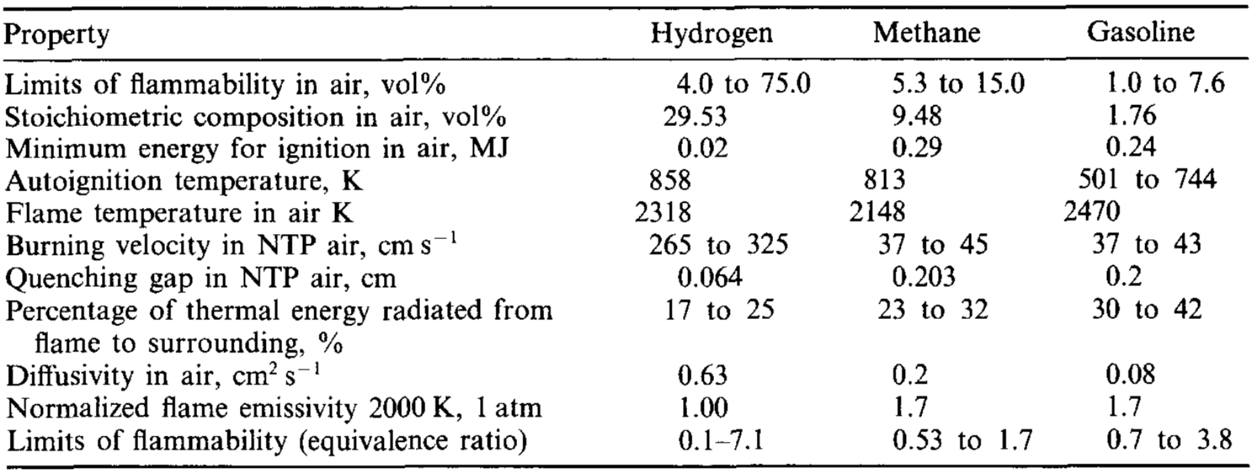

Property	Hydrogen	Methane	Gasoline
Limits of flammability in air, vol%	4.0 to 75.0	5.3 to 15.0	1.0 to 7.6
Stoichiometric composition in air, vol%	29.53	9.48	1.76
Minimum energy for ignition in air, MJ	0.02	0.29	0.24
Autoignition temperature, K	858	813	501 to 744
Flame temperature in air K	2318	2148	2470
Burning velocity in NTP air, $cm\,s^{-1}$	265 to 325	37 to 45	37 to 43
Quenching gap in NTP air, cm	0.064	0.203	0.2
Percentage of thermal energy radiated from flame to surrounding, %	17 to 25	23 to 32	30 to 42
Diffusivity in air, $cm^2\,s^{-1}$	0.63	0.2	0.08
Normalized flame emissivity 2000 K, 1 atm	1.00	1.7	1.7
Limits of flammability (equivalence ratio)	0.1–7.1	0.53 to 1.7	0.7 to 3.8

Table 3. Combustion properties of hydrogen, methane and gasoline **[9]**

Considering the emissions related to the hydrogen engine, the authors [9] compared NO_x emissions from hydrogen engines to those from hydrocarbon-fuelled engines, claiming that hydrogen engines produce lower NO_x levels than gasoline engines, even near stoichiometric equivalence ratios. However, hydrogen engines are generally expected to emit higher NO_x levels due to their higher combustion temperatures, particularly in the rich mixture range. Subsequent studies by other authors supported this, showing that at an equivalence ratio of around 0.64 to 0.7, H2ICE produced more NO_x than their gasoline counterparts.

Moving to a more recent work, but still a little old (2006), White et. al [10] provide a review on light to medium-duty port fuel injection (PFI) engines. It has been shown that premixed or port-fuel-injected hydrogen engines tend to have lower power densities compared to gasoline engines, mainly due to reduced volumetric efficiency and frequent pre-ignition events. However, significant advancements have been made in developing advanced hydrogen engines with enhanced power density. This work studied also the relationship of hydrogen with preignition compared to other fuels, and the interesting result is that, despite the high autoignition temperature, the hydrogen-air mixture has very low ignition energy. This mean that H2ICEs are predisposed towards the limiting effects of preignition.

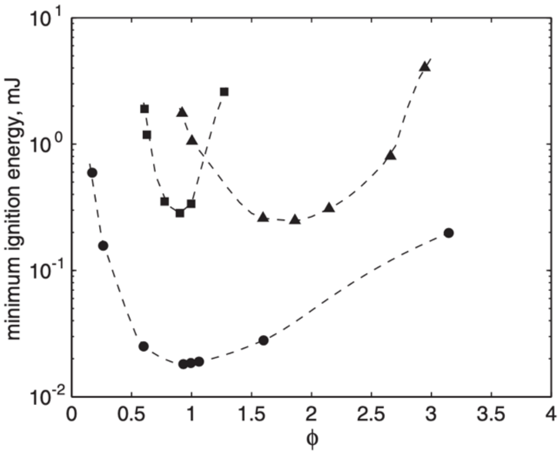

Figure 4. Minimum ignition energies of (•) hydrogen–air, (□) methane–air and (Δ) heptane-air mixtures in relation to the equivalence ratio at atmospheric pressure **[10]**

Figure 4 show the comparison of the ignition energy of hydrogen-air to other fuel-air mixture plotted as function of the air fuel ratio.

The authors define what are the possible ways to avoid preignition in a hydrogen ICEs, considering previous works. This must be considered because the lower power output, set by the preignition-limit, will decrease the performance of a H2ICE-powered vehicle in comparison to its gasoline equivalent. Despite extensive efforts, no preventive measures can fully guarantee the elimination of pre-ignition. However, identifying its primary sources, such as in-cylinder hot spots, oil contamination, combustion in crevice volumes, and residual energy in the ignition system, has enabled the implementation of effective mitigation strategies. These include the use of colder-rated spark plugs, maintaining lower coolant temperatures, and optimizing fuel injection timing. Among the advanced control strategies are intake charge cooling, variable valve timing for improved exhaust residual scavenging, enhanced ignition systems, and direct hydrogen injection.

Another important parameter that is shown in the article is related to the flammability. The flammability range (range of equivalence ratios) for the hydrogen, considered in a volume fraction in air, at 298 K and 1atm, is 0.1-7.1, instead gasoline is 0.7-4. This mean that H_2 is more compliant to stable operation under highly dilute conditions, which allows more control over engine operation for both emissions' reduction. For emissions reduction, as previously described with other studies [9], the main challenge is related to NO_x, which are directly related to the combustion temperature, leading to the necessity to reduce it through leaner mixtures. The results show an important increase in the emission also for values of equivalence ratio above 0.5, without the use of after treatment system. If, instead, the use of a three way catalyst (TWC) is considered, the data show that the emissions at an equivalence ratio higher that 0.95 are near zero. Moreover, if an exhaust gas recirculation (EGR) system is combined with an TWC, the NO_x concentration is highly reduced also for values of equivalence ratio equal or above 1.

In the description of the possible solution for H2ICE, the authors described what are the engines developed with the addition of other components to improve the efficiency, this because in a conventional one the loss in power density could reach 50%.

The first effective way to improve the energy density is through air pressure boosting, that some studies have done with turbocharged operation or supercharged. This last technique leads to the achievement of 30-35% increase in specific power output compared to a naturally aspirated gasoline engine. The main drawback of this operation of the increase of NO_x emissions due to the higher intake pressure, is reported that the preignition limited equivalence ratio decreased from 1 down to 0.5 when they increased intake pressure from 1 bar to 2.6 bar. One possible solution to reduce this effect is the water injection to mitigate the high charge temperature.

The authors, then, report some important work done on the possible use of liquid hydrogen as fuel. This means that the hydrogen is stored in the tank as liquid but not necessarily injected in that form. The first benefit of this solution is the higher stored energy density available with liquefaction. Also, the low temperature of the charge brings to a temperature deduction in the chamber that leads to several advantages, compared to conventional injection. Intake charge cooling enhances volumetric efficiency, reduces the risk of preignition, and lowers NO_x emissions. The resulting increase in volumetric efficiency, and consequently in power density, is a direct outcome of the inverse relationship between intake mixture density and temperature. A reported studies show that using hydrogen a 120 K, the peak power output reached by the H2ICE could be equal to a gasoline engine, and with injection of hydrogen at 210 K the power density could be 15% higher than gasoline. Moreover, the reduced charge temperature helps suppress preignition events, allowing for a higher preignition-limited maximum equivalence ratio.

Another important solution that has been reported in the article is the direct injection (DI) H2ICE, this solution has been seen as one of the most advanced solutions for the high volumetric efficiency, since the fuel is injected after the intake valve closing (IVC), and the potential to avoid preignition. The improved volumetric efficiency could reach values equal or higher to a PFI gasoline engine, and the higher flammability of hydrogen compared to the gasoline one lead to a potential power density to reach approximately 115% higher than gasoline. In particular, the study [10] show that have been measured a 15% increase in indicated mean effective pressure (IMEP) for engine operation with DI hydrogen compared to engine operation with PFI gasoline. On the other side, the main challenge with DI H2ICE is that, due to the high reactivity of the fuel, the mixing phase should be done in a very short time. For early injection, the maximum available mixing time decreases from approximately 20 ms at 1000 rpm to about 4 ms at 5000 rpm. In practice, to reduce the risk of preignition, the start of injection (SOI) is delayed relative to the IVC, which further shortens the effective mixing time.

Regarding the issues of the DI H2ICE, in particular related to the high auto-ignition temperature, there are authors that found solutions to fix those. Lung Yip et. Al [11] described a novel ignition strategy that utilize a small amount of pilot diesel jet to auto-ignite the hydrogen. This solution is called Dual-fuel hydrogen-diesel direct injection (H2DDI). The goal of this process is to create, through the injection of the diesel fuel, a high temperature environment to assist the gaseous fuel ignition to achieve a gas diffusion similar to the one of a compression ignition (CI) engine. The results of this technology are the alleviation of charge knocking and allowing the engine to operate at higher compression ratio in order to improve the thermal efficiency up to levels that are comparable to contemporary CI engines. Unfortunately, according to the authors, there are just few studies related to the combination of diesel and hydrogen but could be considered as valid alternative the solutions regarding the combination in the same way of diesel and carbon neutral gas (CNG). The paragon could be made due to comparable auto-ignition temperature to hydrogen. However, the main advantage is the high reduction of diesel, compared to other solutions like diesel-ignited hydrogen PFI, where pre-ignition and knocking limit hydrogen to 6–25% of total energy share at high load. Considering the use of hydrogen instead of CNG, the main advantage is the significant reduction of carbon-based emissions. Although pilot fuel potentially forms soot, the close-coupled high velocity hydrogen jet could enhance mixing within the chamber, which can subsequently lead to enhanced soot oxidation and suppress soot formation processes. The higher speed of sound and greater calorific value of hydrogen largely offset its roughly ten times lower density compared to CNG, resulting in only about a 20% longer injection duration at an injection pressure ratio of 249 K and a fuel temperature of 353 K.

Lastly, there are few studies that investigate the combination of hydrogen-CNG in dual-fuel DI combustion using heavy-duty engines and integrated dual-fuel injectors. Gas injection duration was regulated to achieve the same engine load as when operating with CNG. The results show a clear trend: carbon-based emissions, such as unburned hydrocarbons (UH), CO, and CO_2, decrease with increasing hydrogen content, though this comes at the cost of higher NO_x emissions. At low engine load, the use of a hydrogen-CNG results in a higher peak heat release rate, whereas the opposite is observed at high load. This difference is due to combustion dynamics: at low load, the reaction rate is chemically limited, and the presence of hydrogen introduces more reactive species, expanding the flammability range and enhancing combustion. In contrast, at high load, the early combustion phase is constrained by fuel availability, as hydrogen's lower density limits the amount of fuel that can be injected. Across all load conditions, increasing the hydrogen share leads to shorter ignition delays, indicating better fuel ignitability. Additionally, combustion stability improves significantly at low load with higher hydrogen content, thanks to more complete fuel consumption.

Considering a recent work related to the performance and emissions on an H2ICE, Fischer et. al [12] modified for hydrogen direct injection a 1L, 3-cylinder gasoline engine provided by Ford Werke GmbH. The engine was equipped with a high-pressure external exhaust gas recirculation system to investigate charge dilution at stoichiometric operation. The authors limited the operation to part load with brake mean effective pressure (BMEP) lower than 8 bar due to the limitation of turbocharging. The direct injection led to higher mixture heating values, that bring to higher power outputs per volume compared to gasoline operations. But the BMEP has limitations that comes from the low external mixture formation, also for the possible phenomenon of pre-ignition and backfiring.
Important results from the article is the comparison of hydrogen and gasoline at stoichiometric condition. The results, shown in Figure 5, came from a BMEP = 19 bar.

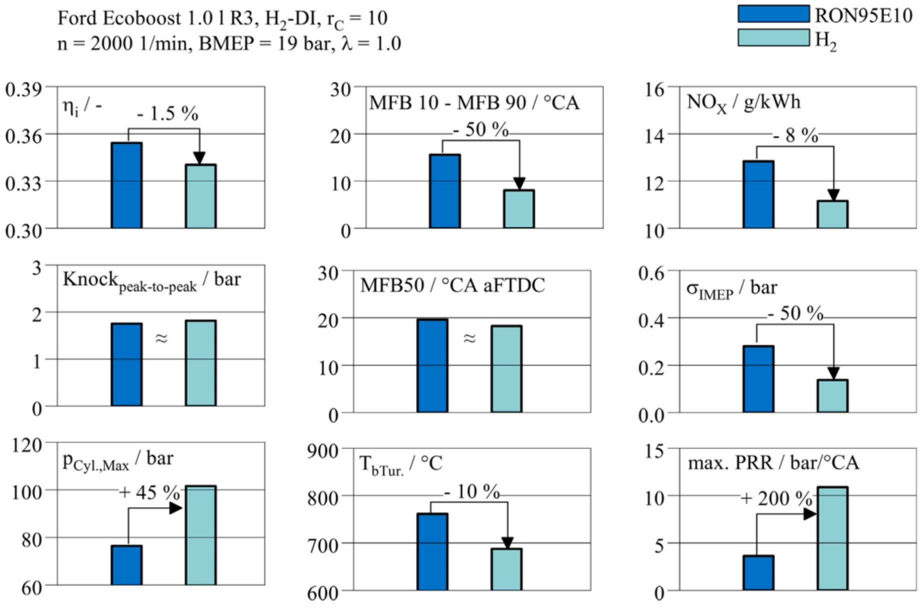

Figure 5. Comparison of Gasoline and hydrogen at stoichiometric condition in a gasoline-tailored engine **[12]**

The first comparison done regards the efficiency, where a difference of 1.5 % is observable, even though H_2 features a significant faster combustion MFB10-MFB90, that is the time in crank angle needed to pass from 10% of fuel mass burned to 90% of fuel mass burned. The factors that influence the efficiency and that bring it to be lower are several: the later injection timing of H_2 operations lead to a more stratified charge compared to the homogeneous injection timing of gasoline (200 °CA before top dead center (bTDC) for H_2 compared to 300°CA bTDC for gasoline); the significant higher heat overcompensate the effect of faster combustion resulting in a reduced indicated efficiency; the engine used for these investigations was not tailored for H_2 and therefore charge motion and stroke/bore ratio are not optimized to compensate the high heat losses of H_2 combustion.

Another parameter of comparison is the maximum in-cylinder pressure, where the rapid combustion of hydrogen results in significantly higher in-cylinder pressures compared to gasoline operation, even though the center of combustion occurs later, due to hydrogen's extremely fast burn rate.

Considering the emissions, the results in the article show that H_2 operations have slightly lower NO_x emissions compared to gasoline operations, although the adiabatic flame temperature is higher for H_2. This reduction comes from the unburned emissions of H_2 from quenching zones and crevices, which is a reducing agent for NO_x.

Lastly, Figure 5 shows that, with the operating condition of the case study, the combustion stability (σ_{IMEP}) is significantly better for H_2, this means that at that working condition, the H2ICE could avoid backfire and pre-ignition.

Next, the authors describe some way to reduce abnormal combustion phenomena and increase the indicated efficiency. The most significant for this case study is the operations at leaner working conditions, where the results of this is the reduction of NO_x emissions and could be achieved near-zero raw emissions engine operation. The numerical results of this solution are shown in Figure 6.

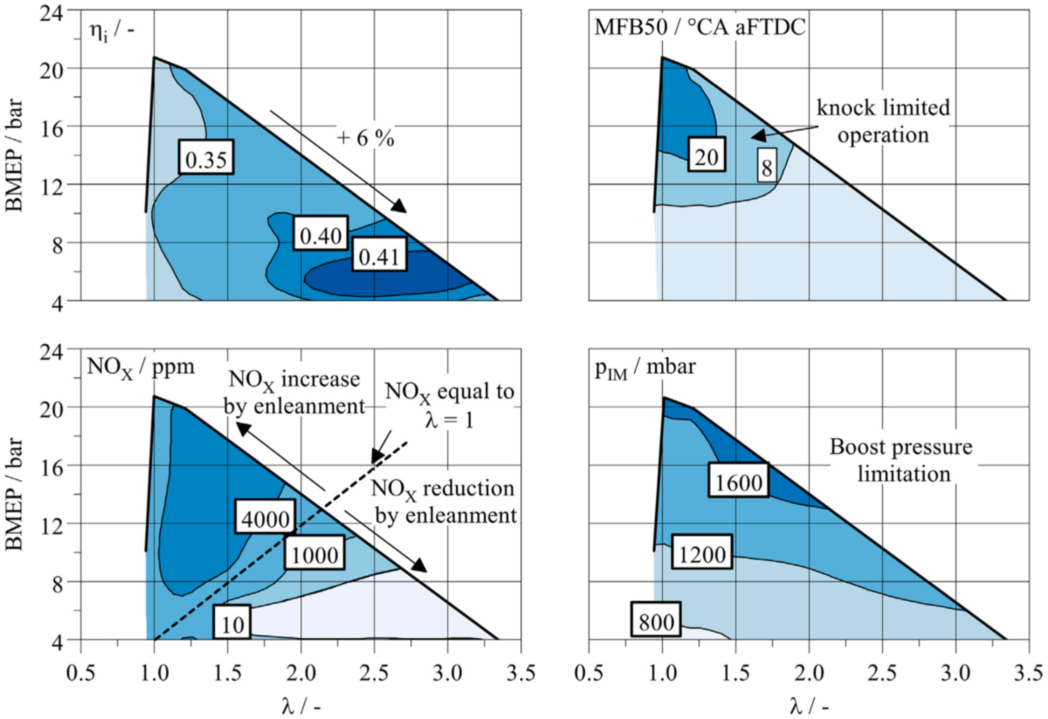

Figure 6. Results for leaner operation **[12]**

The use of hydrogen applied to ICE extend also to a more unconventional type of engine, like the rotary engine, that has been considered as an interesting solution due to lightweight construction, small size, high power density and adaptability of different fuels. Cabezas et. al [13] analyses the possibility to use a rotary engine fuelled with hydrogen, investigating the performance of air/fuel mixture using the PFI and DI configurations. The investigation has been done with 3D CFD (computational fluid dynamic) simulations that have been validated with experimental data. The results of the work show that DI strategy offers the potential to enhance engine performance by improving volumetric efficiency and providing better control over the amount of fuel retained in the combustion chamber. Injecting fuel directly into the chamber ensures a locally richer mixture for combustion and creates charge stratification, which moderates the heat release rate and boosts power output. This slower heat release also reduces heat transfer losses caused by flame-to-wall interaction, an important factor in improving the efficiency of Wankel engines. Additionally, operating with lean mixtures can help lower NO_x emissions during combustion.

In the article the simulations with PFI have been done with different injection timing: 0, 50, 90, 180, 270 Crank Angle Degrees (CAD). The results on the pressure are visible in Figure 7, it can be observed that for 180 and 270 CAD injection, the combustions are the weakest, this due to the extreme lean mixture. Looking instead on the other cases, which are the richest, there are a very high pressure rise and knock conditions.

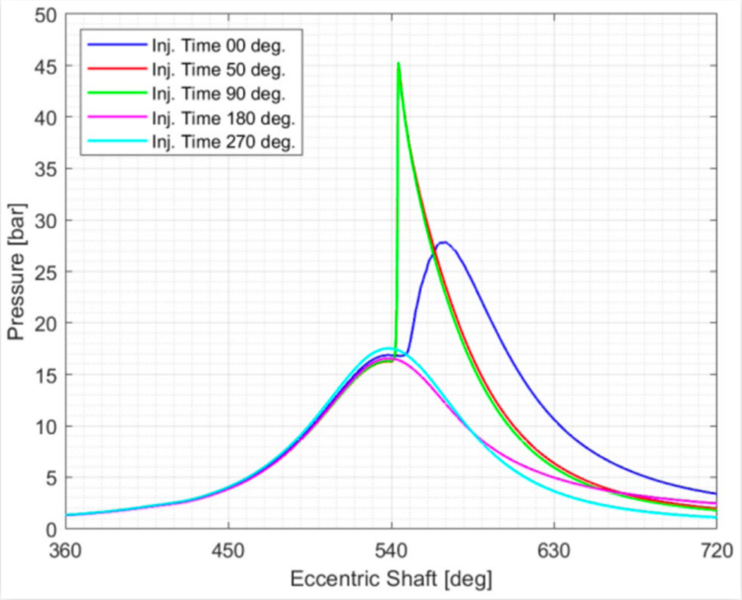

Figure 7. In-cylinder pressure during PFI injection for different timing **[13]**

Moreover, for the different simulation the author compared the efficiency and the NO_x emissions, listed in Table 4.

INJECTION TIME [CAD]	**0**	**50**	**90**	**180**	**270**
OVERALL EFFICIENCY [-]	0.263	0.123	0.108	0.048	-0.020
NO_X [g/kWh]	0.128	3.170	3.206	0.041	-0.104

Table 4. Overall efficiency and NO_x emission for PFI configuration **[13]**

The table above shows that in the cases of 50 and 90 CAD, the efficiencies are the highest, this due to the more available energy to release and to the faster combustion. The effect of slower combustion for the 0 CAD case is reflected in the almost doubled generated work, visible in terms of almost double efficiency. Concerning the emissions, the faster and stronger combustion resulting from the rich mixture of the 50 and 90 CAD cases also leads to a higher temperature, which lead to higher NO_x emissions compared to the other cases. In the simulation considered in the article only the 0 CAD case would meet the EURO VI standard's requirement of 0.4 g/kW-h for heavy-duty engines.

Moving to the DI simulations, the cases considered by the authors were based on the direction of injection in the combustion chamber, they are shown in Figure 8 in different conditions: *Coflow*, *Major axis*, *Normal to flank*, *Counterflow*. The figure also shows how the working conditions are defined.

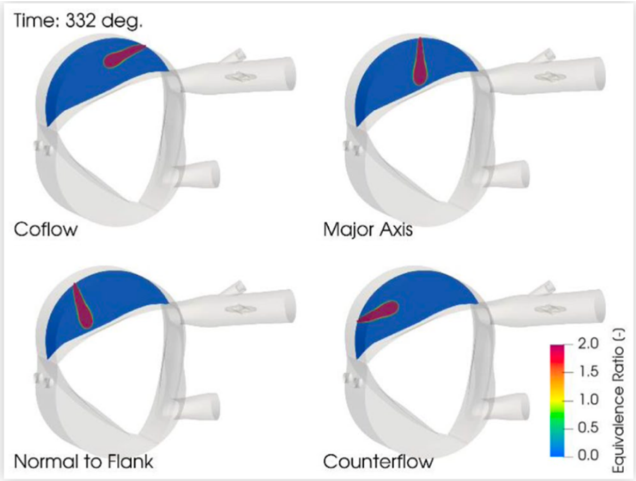

Figure 8. Study cases for the DI **[13]**

In Figure 9 are represented the pressure values for the different DI cases. In contrast to the PFI configuration, can be seen that the mixture is reach enough to burn, there is knock for the *coflow* and *counterflow* configuration, that are the richest ones. Comparing those two cases, the *counterflow* shows a slower combustion resulting in a peak pressure that occurs later compared to the *coflow* case, despite the latter being leaner due to the fuel accumulation on the trailing part of the chamber, arriving late to the spark plug region.

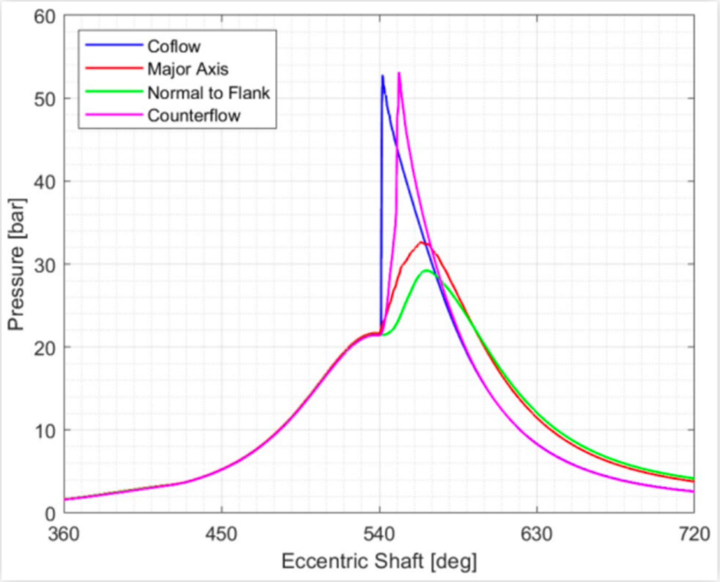

Figure 9. In-cylinder pressure during DI injection for different timing **[13]**

As already done for the PFI case, Table 5 shows the comparison for overall efficiency and NO_x emissions for the different case studies. As in the PFI cases, it can be observed that the richer cases, *coflow* and *counterflow*, produce less work due to the high pressure rise or knock. Instead, the slower and more controlled combustion of the *major axis* and *normal to flank* cases results in a more efficient energy transformation into work during the expansion stroke, represented as efficiency. The other parameter presented in the table is the NO_x emissions, that are low and reasonable for the *major axis* and *normal to flank* configurations due to the low temperature generated during the slow combustion. On the other hand, higher emissions were generated earlier for the *coflow* and *counterflow* configurations as a result of the rapid combustion of the richer mixture in these cases.

INJECTION TIME [CAD]	COFLOW	MAJOR AXIS	NORMAL TO FLANK	COUNTERFLOW
OVERALL EFFICIENCY [-]	0.154	0.251	0.262	0.157
NO_x [g/kWh]	1.094	0.037	0.015	1.556

Table 5. Overall efficiency and NO_x emission for DI configuration **[13]**

In conclusion, the author states that achieving an adequate level of mixture dilution is essential for controlling combustion and preventing knock during hydrogen injection in a Wankel rotary engine. When comparing the two configurations analysed, the DI strategy shows clear advantages over PFI, as it allows for local mixture enrichment and enables some mechanical energy recovery from the injected fuel, regardless of injector placement. The results indicate that the DI strategy is more favourable, as it delivers greater work output and reduces inefficiencies related to heat transfer and mass leakage compared to the PFI approach in the scenarios studied.

Environmental and economic impact of hydrogen

This section is related to an analysis on the effect of an implementation of hydrogen in different type of industries today, like production and transport.

Shen et. al [14] provides an overview of the possible impact of the large-scale hydrogen implementation using the life cycle assessment (LCA) methodology, that evaluate the environmental impacts of a product or service across its entire life cycle, from raw material extraction to end-of-life disposal.

The paper compares different models, where each represent a different decarbonization path scenario, compared to a baseline one that assumes no change in the current energy mix, particularly in terms of life cycle climate impact. The electricity transmission system is excluded from the LCA to maintain the focus of the work on hydrogen.

The different scenarios considered are the following:

- The *baseline scenario*, where the energy usage in the hard-to-abate sectors of industry and transport still relies on fossil fuels.
- *Scenario 1*: Decarbonization with green hydrogen. This scenario considers green hydrogen as a replace for the fossil fuels in the sectors of industry and transport. For this case study, regarding the production of hydrogen, only the proton exchange membrane (PEM) electrolysis process is considered as primary green hydrogen production process, this due to its superior performance compared to other methods, and thanks to its flexibility, PEM is more adaptable to wind-powered electrolysis.
- *Scenario 2:* Decarbonization with blue hydrogen. This scenario assumes blue hydrogen as an alternative to fossil fuels in the same sectors of the previous one. The concept is the same of the scenario 1 but in this case, there is a large-scale deployment of blue hydrogen.
- *Scenario 3:* Decarbonization without green hydrogen. The idea behind this scenario is to consider a combination of other clean energy sources such as biofuel, synfuel, blue hydrogen, and renewable electricity replace the fossil fuels in the industry and transport sectors. This scenario aims to draw a picture of a clean energy mix (excluding green hydrogen) applied in the sectors of industry and transport, as the other typical sample comparable to scenario.

Moving to the results of the work, the first relevant one, necessary to determine the differences of the scenarios, is related to the climate impact in terms of CO_2 emissions of the different hydrogen typers (Figure 10). The data are based on the Europe demand in the industry and transport sector until 2050.

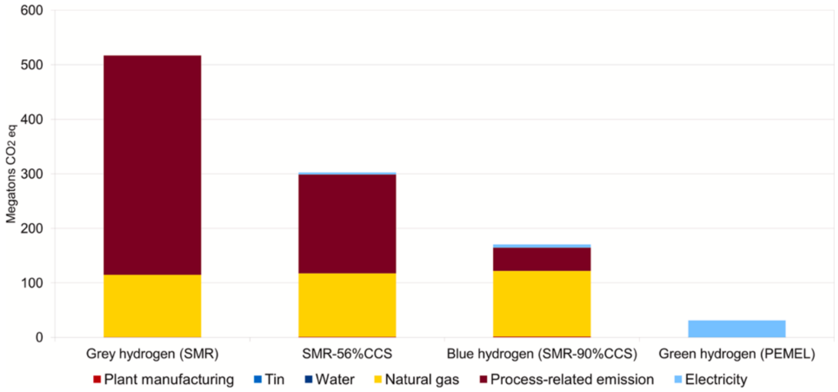

Figure 10. Life cycle climate change impact of green and blue hydrogen production based on demand in industry and transport in Europe until 2050 **[14]**

The life cycle climate change impact of green hydrogen production is significantly lower, 94% less than grey hydrogen and 82% less than blue hydrogen. 99.9% of green hydrogen's climate impact is attributed to the renewable electricity used in its production. In comparison, renewable electricity contributes only 26% to the climate impact associated with the natural gas supply for blue hydrogen. For grey hydrogen, the primary source of emissions is process-related, accounting for 78% of its total climate impact, while natural gas supply contributes the remaining 22%.

Next, another important statistical data reported by the authors is the monetary impact of life cycle cost for both blue and green hydrogen. The results are reported in Figure 11 and show that the total monetized life cycle impact of blue hydrogen is estimated at €40 billion (2019 values) to meet projected hydrogen demand in European industry and transport by 2050. The largest contributors to this cost are climate change and fossil resource depletion, accounting for 46% and 39% respectively. In comparison, green hydrogen is assessed to cost €16 billion, less than half that of blue hydrogen. For green hydrogen, the main contributors to the total impact are particulate matter (31%), human toxicity from cancer effects (24%), human toxicity from non-cancer effects (21%), and climate change (15%). Notably, the monetized impacts related to human toxicity (both cancer and non-cancer effects) and particulate matter are significantly higher in green hydrogen production than in blue hydrogen.

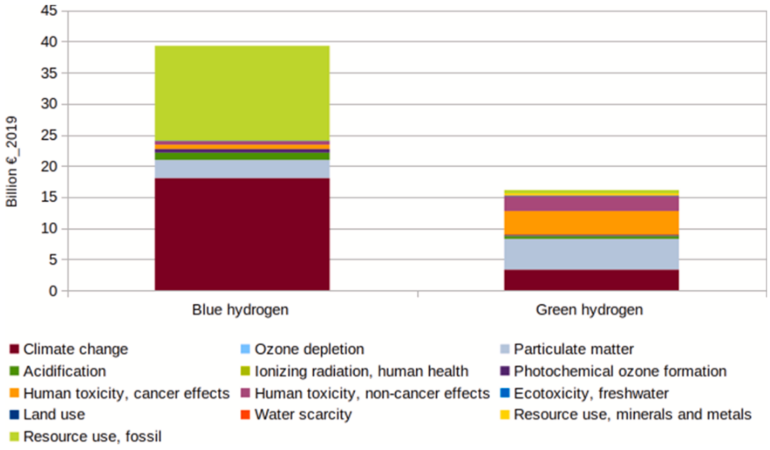

Figure 11. Monetized life cycle environmental impact cost of blue and green hydrogen based on demand in industry and transport in Europe until 2050 **[14]**

Comparing instead the different scenarios defined at the beginning of the article, Figure 12 analyses them from the climate impact point of view, specifically in the transport sector, that is more relevant for this thesis work.

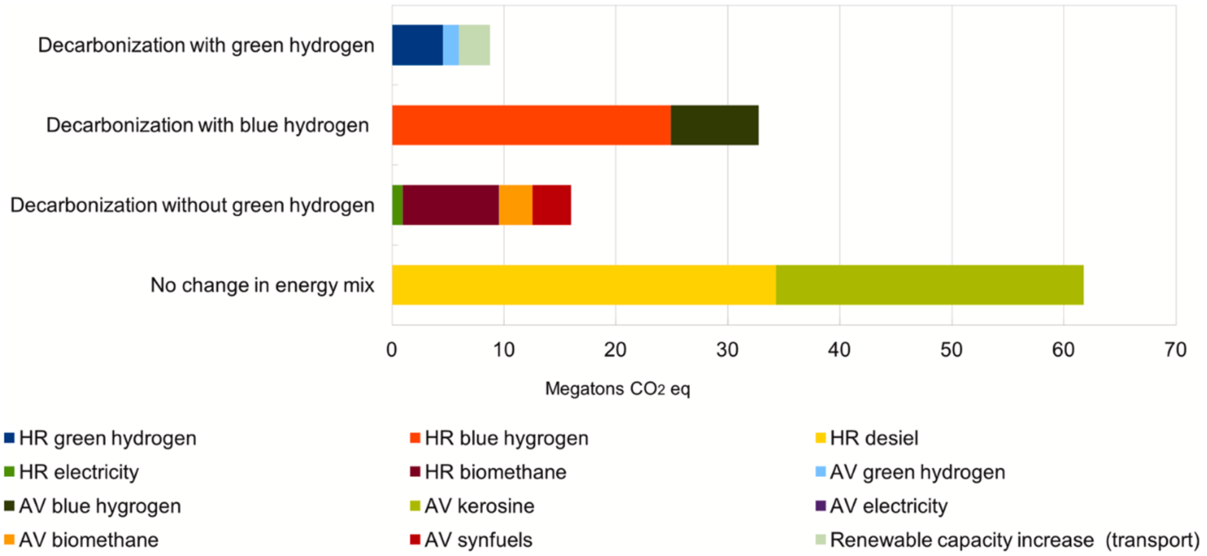

Figure 12. Comparisons of life cycle climate change impact in transport for different scenarios in Europe in 2050. (HR: Heavy Road, AV: Aviation) **[14]**

The *decarbonization with green hydrogen* scenario results in the lowest emissions, estimated at 8.7 megatons of CO_2-eq (including 2.7 megatons from the additional renewable energy capacity), while the *no change in energy mix* (baseline) scenario shows the highest impact with 62 megatons CO_2-eq. In contrast to the industrial sector, where blue hydrogen performs better, in the transport sector the *decarbonization with blue hydrogen* scenario leads to higher emissions (33 megatons CO_2-eq) compared to the *decarbonization without green hydrogen* scenario (16 megatons CO_2-eq). When compared to the baseline, the scenario with green hydrogen achieves a reduction of 85.9%. Compared to the blue hydrogen and no-green-hydrogen scenarios, the reductions are 73.3% and 45.4%, respectively. The results also show that, in heavy road transport, the use of green hydrogen results in lower emissions than electricity and biomethane in the no-green-hydrogen scenario, whereas both electricity and biomethane perform significantly better than blue hydrogen.

However, to the data shown, the authors highlight that some parameters are not taken into account in this report, like the environmental impact of the addiction of renewable infrastructure that inevitably would contribute and lead green hydrogen to be in a worst position than blue hydrogen from the life cycle perspective. Same concept for the transmission infrastructure of this element that would increase the impact. Also, what is not considered in the article are the possible leakage of hydrogen, due to the small size of the molecule, the hydrogen is defined as a short-lived greenhouse gas (GHG) that would impact in climate change if released in the atmosphere. Lastly, on the monetary part, there are uncertainties on the coefficients that define the results, this is due to different models and case studies, for example the cost of installation of infrastructure change with the location where it's installed.

The conclusions of the authors underline that to achieve defined sustainable standards there are pros and cons, like the necessity to build more infrastructure, that impact of the climate, in order to achieve the goal of green hydrogen demand for the industry and transport sector. Also, green hydrogen has the drawback of other environmental impacts including human toxicity, ecotoxicity, particulate matter, mineral resource use, land use, and water depletion, which are 2-29 times higher than blue hydrogen production. However, green hydrogen would reduce hugely the carbon emissions compared to the other scenarios considered, and the impacts of renewable electricity supply for green hydrogen are far lower than those of the natural gas supply for blue hydrogen.

Similarly to the previous article, Kuyumku et. al [15] analysed the wheel to tank (WTT), tank to well (TTW) and WTW in terms of carbon footprint, cost, equivalent electric vehicle efficiency and range analysis for an 18 m city bus equipped with different powertrains. The reason behind the choice of that vehicle, as the authors explained, was for the ability to operate at slow speed, make frequent stops for passenger's pickups (so a frequent use of the regenerative braking) and a manageable refuelling process.

The powertrains that have been analysed were diesel ICE, gasoline ICE, H2ICE, BEV configuration, gasoline ICE hybrid and H2ICE hybrid.

Considering that this article focussed both on production and use of hydrogen, the method for the production was the electrolysis one obtained from wind and solar panels and nuclear energy.

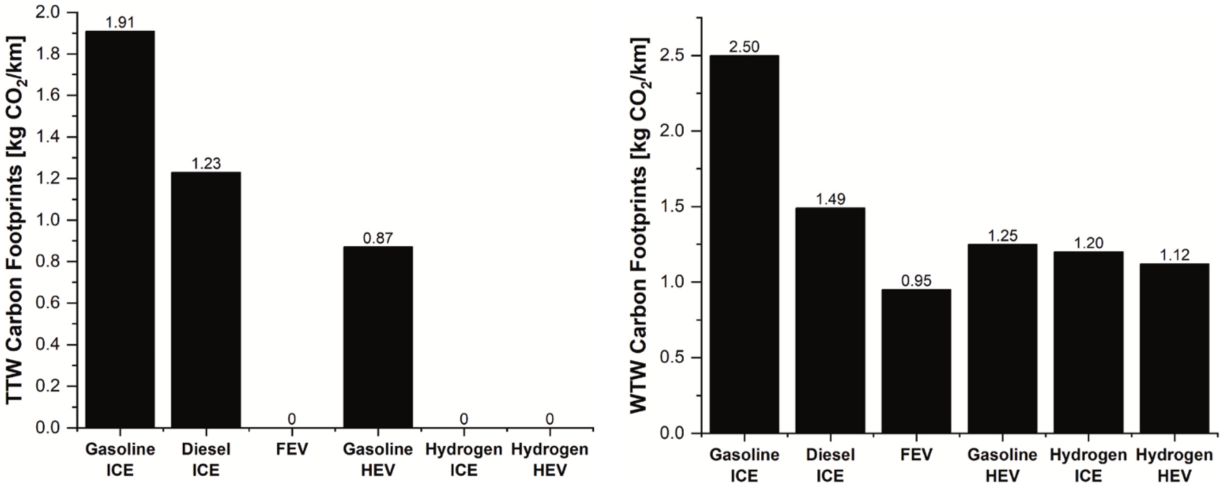

Figure 13. TTW and WTW CO_2 emission per kilometres for each powertrain type **[15]**

The results of the study are shown in Figure 13, where can be stated that, for the TTW emission, FEV and the powertrains fuelled by hydrogen do not cause carbon emissions and hybrid version of gasoline powertrain reduces its carbon footprint more than 2 times. The emissions of the diesel engine are 35% lower than the gasoline one due to the higher efficiency of the diesel engine.

Considering the WTW emissions, the analysis revealed a significant increase of fossil fuel for all the powertrains, leading eclectic vehicles to have the lowest emission values among the others. The emissions for the hydrogen increase due to the usage of renewable energy source in the production of electricity (must be considered that these emissions are highly influenced by the energy source acquisition method). The authors also define some projection to 2030 that leads to a significant reduction in carbon emission for the hydrogen supply chain.

Moving on the cost analysis made by the authors, Figure 14 expresses the cost per kilometre for both the WTT and the WTW analyses made. The gap between diesel and gasoline engines is higher in the WTW that TTW due to the lower fuel consumption of diesel engine, in particular for heavy-duty applications. FEV shows the lower cost among the different types for both WWT and WTW, the reason is the high efficiency and the less usage of hydrogen, that in the other cases of powertrain fuelled by it, the low production and the low efficiency increase the cost. Lastly, as expected, the hybrid electric vehicles (HEVs) models have a lower cost than the conventional version for the work as generator that the ICE at the highest efficiency points.

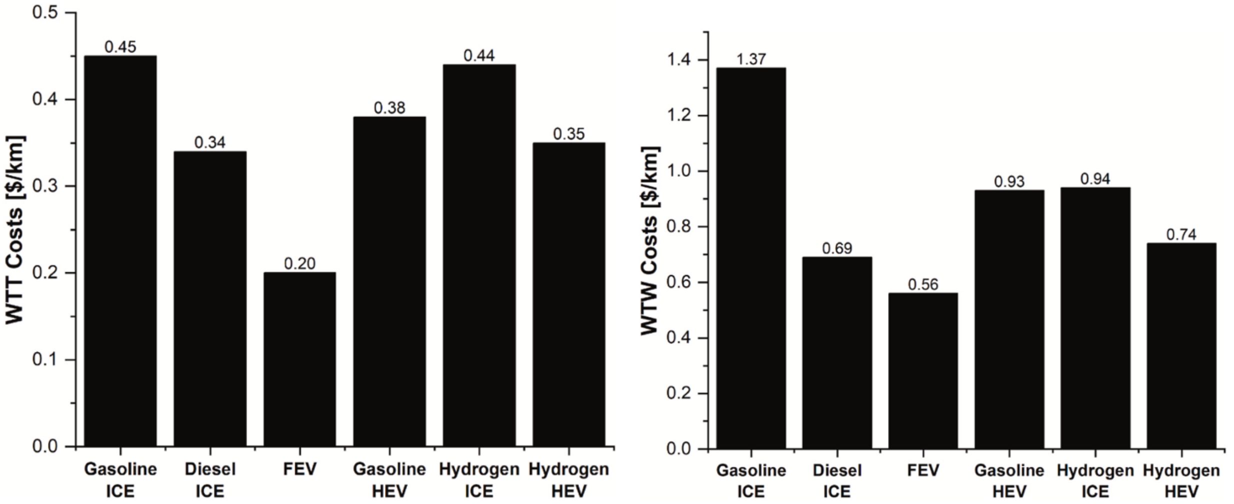

Figure 14. WTT and WTW cost per kilometre for each powertrain type **[15]**

Lastly, the authors also defined a possible estimation of what could be the same costs and the carbon footprint for the hydrogen fuelled powertrain in 2030. The results are shown in Figure 15.
Starting from the CO_2 emissions, where according to the data described above, FEV are the best options. However, following the estimation made by the authors for the 2030, H2ICE reaches a comparable value with the FEV powertrain, especially with the use of renewable sources for the hydrogen production, that is the way with less environmental impact, but also the more expensive one. The estimation, according to the authors, has taken into account the future increase of investment in this direction due to the zero-carbon legislation.

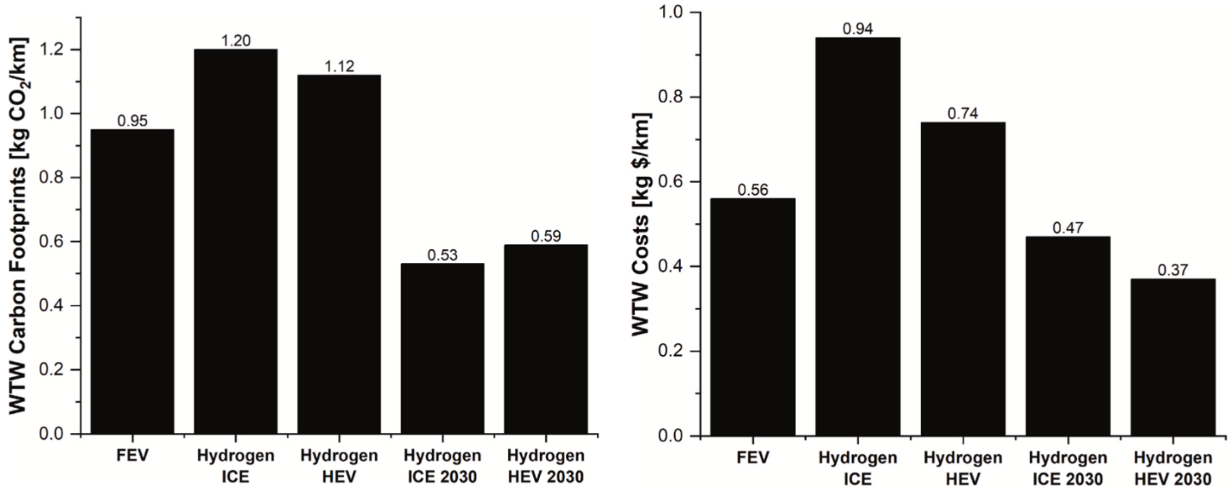

Figure 15. Current and estimation to 2030 of WTW carbon footprint and costs per kilometre for each powertrain type **[15]**

In the scenario outlined in the study, electricity prices and emission levels are not expected to decline by 2030 because, as explained by the authors, prices are unlikely to drop in the near future, and renewable energy sources are already being used extensively at current production levels.

Remaining in the economical field related to this subject, article [16] shows how the use of hydrogen applied on ICE should be good solution in the short term, considering that the ICE technology is well known and have been studied for many years, leading to the possibility to create cars with lower production costs, compared to the fuel cell ones, or to convert already existing engines running with gasoline or diesel in hydrogen ones. Moreover the cost of H_2 is expected to decrease: in the U.S., the Department of Energy's Hydrogen Shot seeks to reduce the cost of clean hydrogen by 80% to $1 per 1 kilogram in 1 decade. In Norway, for example, recent green hydrogen production projects report costs as low as $3.5 to $4.5 per kilogram of hydrogen. This is equivalent to about $30 to $40 per million British Thermal Units (BTU), less than the prices recently reached by natural gas on European markets.

Also, various hydrogen incentive and subsidy programs are currently moving through legislative and regulatory processes worldwide. For instance, the European Union is planning to revise its minimum energy taxation rules, aiming to introduce a reduced minimum tax rate for low-carbon hydrogen used as motor fuel. The proposed rate is €0.15 per gigajoule, equivalent to about €0.02 per gallon of gasoline equivalent, which is roughly 100 times lower than the minimum tax applied to gasoline, set at €10.75 per gigajoule (approximately €1.30 per gallon). Such measures could significantly narrow the cost gap between hydrogen and conventional fossil fuels.

Sari et. al [17] analyse the comparison of conventional diesel ICE, H2ICE and fuel cells EV. The comparison has been done on the VOLVO VNL 760 truck, a long-haul sleeper classified as a class-8 traction cabin with a maximum weight capacity of 36 tons. The work underlines the differences for the already defined powertrain in performance and total cost of ownership (TCO). Focusing on the second one in this section, for the core of the study, the authors explain that different benefits like tax and government incentives were not considered.

The factors used to define the total cost were:

- *MSRP* (Manufacturer Suggested Retail Price), the retail price that is suggested by the carmaker itself.
- *FC* (Fuel Consumption), total fuel consumption over 650’000 miles.
- *Driver*, cost associated with the driver.
- *M&R* (maintenance & repair), maintenance and reparation costs.

The sum of all of these factors defines the TCO. All the parameters are different depending on the type of motorization chosen, but the one that needs more attention is the *MSRP* one, where there were several factors that changed, indeed that parameter was defined considering the different parts of the truck for each powertrain.

Stating with the diesel engine, the costs are related to the glider, that is the same for all the other configurations, and the cost of the ICE engine. For the H2ICE, the costs are the same as the diesel one, the engine is considered as very similar due to just some little change, with the main difference of the hydrogen storing system. Finally, for the fuel cells, the costs are related to the fuel cells itself, the glider, the battery system, the electric motor and the hydrogen storage system as the H2ICE.

Starting from these settings, the first results obtained are shown in Figure 16.

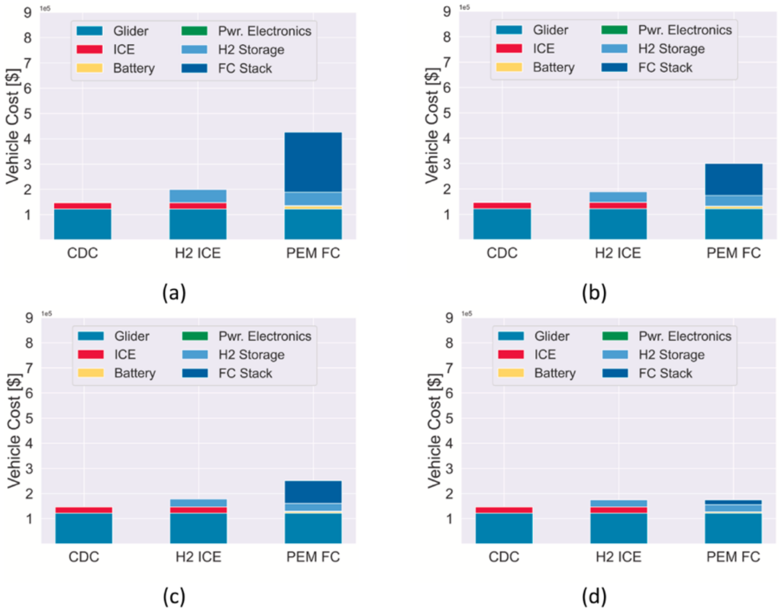

Figure 16. Estimation of all the costs for the different configuration in different years.

2023 (a), 2025 (b), 2030 (c), 2050 (d) **[17]**

The results above come from an estimation of prices based on a paper review, and have been used average, minimum and maximum value of this research to achieve those results.

As can be seen, both H2ICE and fuel cells are more expensive than the conventional diesel engine. The first is 30% more expensive and the second is almost 3 times more. The differences in costs would theoretically become lower in future years due to fuel cell stack, storage and battery prices reduction. By 2050, FC and H2ICE would become competitive in terms of *MSRP*, as their costs approach the targets set by the Department of Energy (DOE): \$80/kWh for battery packs and \$60/kW for fuel cells.

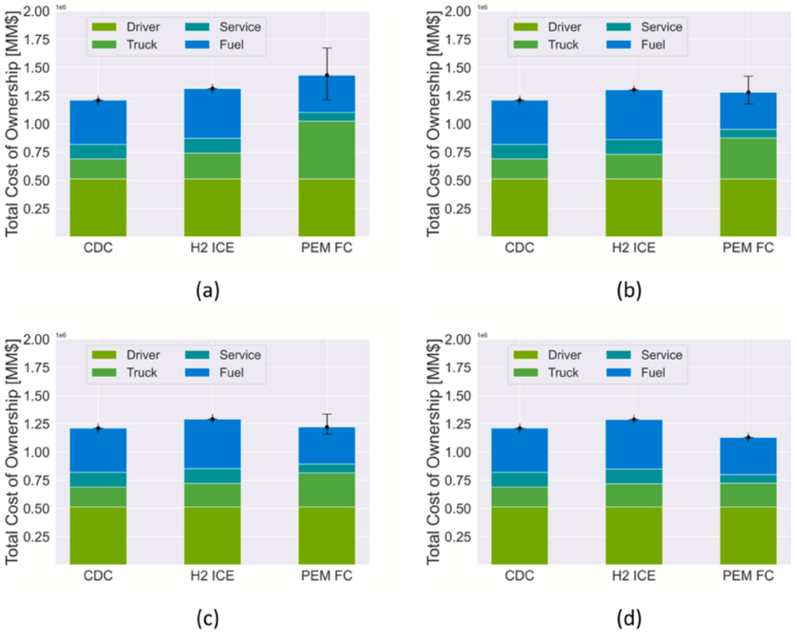

(a) (b) (c) (d)

Figure 17. Comparison of TCO for different powertrain configurations in different years.

2023 (a), 2025 (b), 2030 (c), 2050 (d) **[17]**

Lastly, after all the previous estimations, the TCO has been defined and compared in Figure 17. To obtain these results, as driving cycle has been used a World Harmonized Vehicle Cycle (WHVC) at 50% payload, that represent the condition for regulation for heavy-duty trucks. The data reported shows that, generally, the diesel engine is the cheepiest technology above the possibles. Focusing on the "low carbon" solution, H2ICE offers the most cost-effective one considering both the short and long term, using hydrogen as fuel. 2030 is estimated to be the breakeven point for fuel cells and H2ICEs, reaching in 2050 the situation when the fuel cells solution is considered the preferred among the others for the heavy-duty sector.

It's important to underline, like the authors explain, that the TCO is deeply dependent on the fuel consumption for each cycle. Leading cycles with lower difference between fuel cell and H2ICE consumption increase the benefits of ICEs. Instead, in the opposite case, the benefits will move more to the fuel cells vehicles. In detail, to achieve cost parity with H2ICE-based platforms under the considered cycle, fuel cell stack prices need to fall below \$300/kW.

Moreover, in the article the efficiency degradation was not considered. However, as the authors describe, there are articles showing that the useful life of the fuel cells is shorter than the lifetime of a truck, leading to reduction in efficiency and possible substitution of the fuel cells themselves. All these factors would increase the benefits of the H2ICEs with respect to the fuel cells from both efficiency and TCO point of view.

The conclusions of the article are that H2ICE offers lower upfront powertrain costs compared to fuel cells. Even when factoring in fuel expenses and calculating the TCO, H2ICE remains the more cost-effective option for introducing hydrogen into the long-haul sector. However, by 2030, anticipated reductions in component costs are expected to bring TCO parity between H2ICE and fuel cell technologies.

There are other authors that studied the TCO related to alternative and sustainable powertrain solutions in the transport sector, like Magnino et. al [18] who evaluated three potential solutions for the decarbonization of heavy-duty transport: Battery Electric Trucks (BETs), Fuel Cell Electric Trucks (FCETs) and Hydrogen-fuelled Internal Combustion Engine Trucks (H2ICETs). The study focused on the market of Finland, considered by the authors as an ideal environment for the development of this technology considering the affordable and low carbon electricity.

The study specifically analysed the costs directly incurred by the truck owner and electricity and hydrogen price.

For the analysis of the article three case studies have been considered: *Urban route* (U), *Extra-Urban route* (EU) and *Long-Haul route* (LH). The U and EU cases are applicable to most European countries, as they involve 18-tons and 42-tons trucks respectively. In contrast, the LH cases are specific to the Finnish context, where the use of 76-tons trucks is assumed.

In the U and EU scenarios, energy storage systems are sized to meet daily energy demands, with recharging or refuelling taking place exclusively overnight. In contrast, the LH scenarios assume an intraday recharge or refuelling to keep battery sizes within reasonable limits. For FCETs, the fuel cell operates as a load-follower, supported by a small battery designed to handle power demand peaks. Hydrogen is assumed to be stored in pressurised tanks at 700 bars.

For what concern the costs of the vehicle, the main elements are:

- Vehicle purchase cost.
- Fuel cost.
- Insurance cost.
- Maintenance and repair cost.
- Taxes and fees.
- Road tolls.
- Other costs related to HDVs.

A more specific description of them is reported in Table 6.

Vehicle purchase cost	Purchase cost	Price of the vehicle, evaluated basing on the component's teardown
	Financing	Evaluation of interest rates and type of financing
	Depreciation	Evaluation of the depreciation rate
Fuel cost	Energy consumption evaluation	Average energy consumption of the vehicle evaluated from literature
	Fuel price assumption	Assumption on "fuel" price, with possible scenarios
Insurance cost	-	Insurance costs evaluated on weight classes
Maintenance and repair costs	Maintenance and repair	Maintenance costs based on annual mileage
	Midlife	Midlife overhaul costs (battery replacement, FC substitution)
Taxes and fees	Vehicle registration taxes	Registration taxes according to Finnish legislation
	Annual fees	Evaluation of due annual according to weight classes and use
Road tolls	-	Road tolls evaluated on the different cases studies
Other costs related to HDVs	Payload reduction	Payload reduction due to additional weight of the alternative powertrain
	Driver cost	Driver cost based on annual driving hours
	Additional time for recharging	Additional time recharging of BEV

Table 6. List of the elements that defines the TCO **[18]**

Moving to the results, the first interesting consideration has been done on the purchase cost for the different powertrains in the LH case, shown in Figure 18.

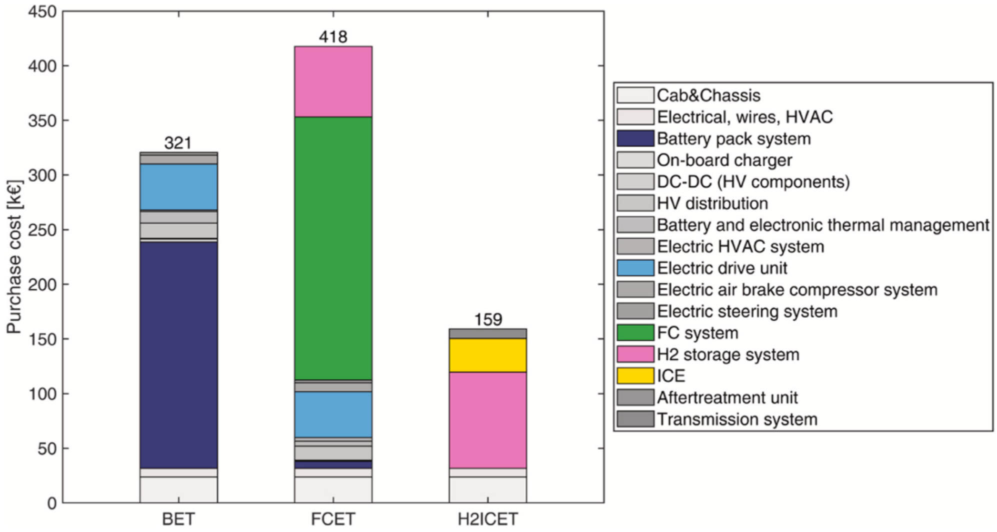

Figure 18. Purchase costs for the different powertrain in the LH case **[18]**

From the image above it is possible to state that the cost of the FCET is the highest, instead the lowest is the H2ICET. This in relation to the main components that increase the price of the BET and the fuel cells trucks, that are the battery pack system in the first case and the fuel cells system in the second, while for the H2ICET the component that increases highly the price is the H2 storage system, present also in the fuel cells powertrain.
Passing to the analysis of the different case studies considered in the article, the authors presented results both in terms of TCO, and LCOT, that is an indicator representing the total cost per unit of mass transported and distance travelled. The first parameter, for the different cases is shown in Figure 19, where it could be seen that the TCO increases with both vehicle size and travel distance. H2ICETs generally prove the most cost-effective across scenarios. Although ICE vehicles have a lower purchase price, their higher fuel consumption raises the TCO. H2ICETs have higher maintenance costs, but on urban routes, battery powertrains remain more efficient and economical due to lower energy use. FCETs are the most expensive in U1, EU1, and LH1, driven by high purchase costs and lower efficiency compared to BETs. In high-mileage cases (U2, EU2, LH2), FCETs become more competitive, as increased storage needs raise BET costs more significantly than hydrogen tank costs impact FCETs.

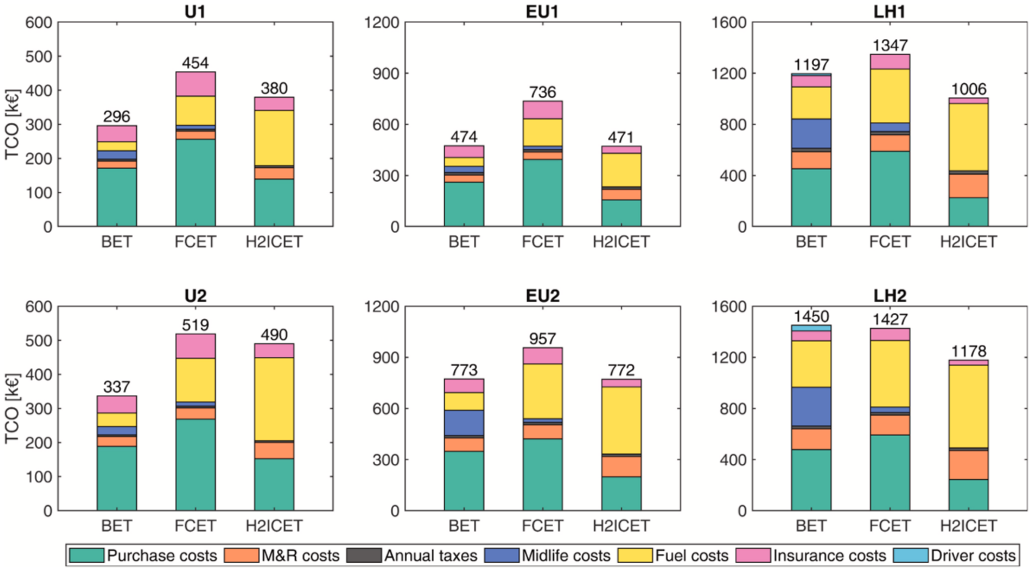

Figure 19. TCO for the different case studies and powertrains **[18]**

Passing to the second parameter defined, the LCOT, which is needed in order to consider also the effect of the payload, in Figure 20 the different cases with all the powertrains are compared. Due to the heavier battery system, LCOT tends to favour hydrogen-based powertrains over BETs for the same TCO. Among all options, H2ICETs are the most cost-effective in terms of LCOT. Results are generally consistent with the TCO analysis: BETs perform best in urban scenarios, where battery weight and cost are lower, while H2ICETs are the most economical in other cases thanks to their low purchase cost. FCETs are the least convenient at low mileage, as high fuel cell costs outweigh efficiency and maintenance advantages. At higher mileage, FCETs improve in competitiveness but never surpass alternatives in cost-effectiveness.

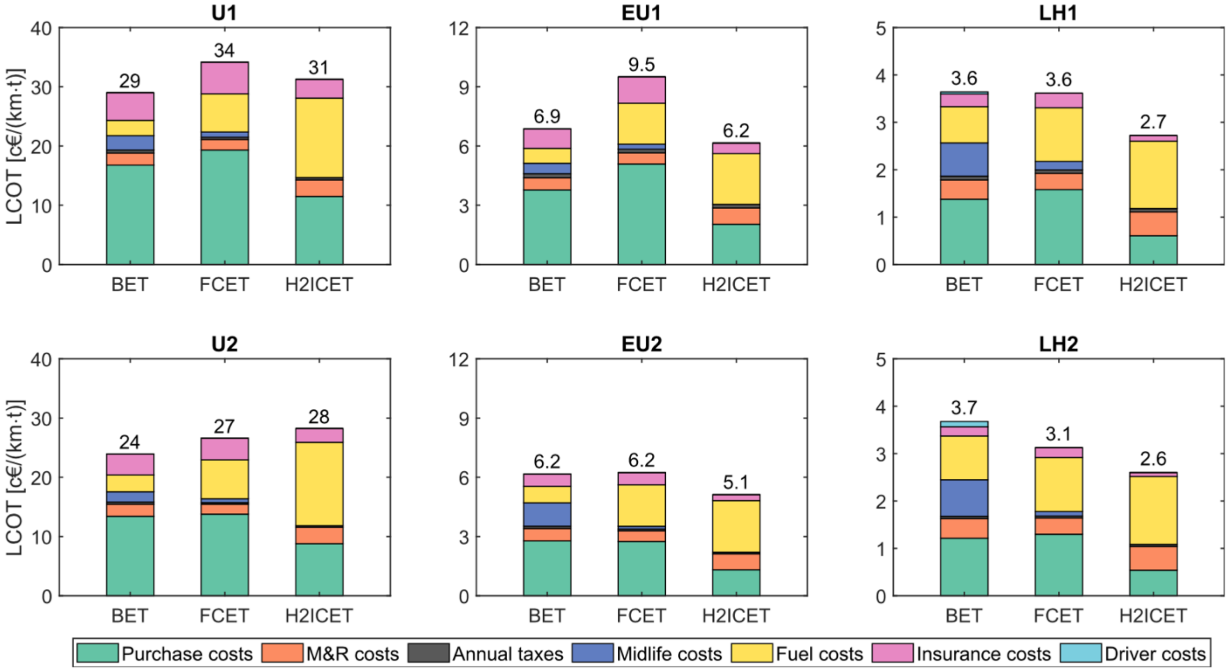

Figure 20. LCOT for the different case studies and powertrains **[18]**

Then, the authors also analysed what is the influence on the daily milage for the different solutions, considering a variable value from 100 to 700 km/day. The results are that BETs are the most cost-effective option for daily mileages around 100–200 km/day. However, as distance increases, battery costs and weight reduce their competitiveness. For trucks of 18-tons, covering daily distances of 200 km/day or more, FCETs offer the best solutions. In contrast, for bigger trucks, H2ICETs are the most economical choices in today's HDV market, mainly due to their lower engine costs compared to fuel cell and battery systems.
Lastly, the article concludes with an analysis related to the influence of the current and future costs of electricity and hydrogen. It can be summarized that if the prices of both electricity and hydrogen are high, BETs show a favourable application due to the high efficiency of the battery. Instead, if in the future the cost of hydrogen will decrease, the hydrogen-based solution will become more cost-effective solutions. Specifically, for the H2ICEs, the threshold necessary to reach these conditions, for the urban trucks should be 4 €/kg, instead for the extra urban and long haul, respectively 8 and 10 €/kg.

Pro and cons of H2ICEs

This section is related to the analysis of the advantages and disadvantages on the implementation of the H2ICEs in the transport sector, something has already been reported but in this part this theme will be the focus.

There are a lot of articles that express the main features and benefits of this technology, like [19], where a comparison with the fuel cells is done. But, focusing only on the ICE fuelled by hydrogen, the main pros of this solution are related to the emissions reduction, as already widely explained in the previous sections, mainly for the CO_2 reduction, but also from the NO_x point on view, with the appropriate exhaust treatment system, the emissions reduction led to better performance than the conventional gasoline engine. However, also with this setting, the emission will be higher than BEVs or FCEVs, where they are null.
The fact that it is still an ICE also is an advantage itself, due to the possibility to maintain an already existing technology that has been studied for a lot of years, well known for construction, repair and maintenance. However, for this reason, it maintains the disadvantages related to the ICEs, like the low efficiency that led to the necessity of a higher quantity of fuel with respect to other technologies,

like fuel cells for example. The type of hydrogen to run the engine could be also of low-quality, with the consequence of cost reduction.

An important company already mentioned that moves a lot in this direction is VOLVO, in particular for HDV application, already developed solution of this type. The main benefits that they found on this technology are the emissions, that with their injection system developed in 2024 [1], a high-pressure gas injection fuel systems (HPDI) for long haul and off-road applications. This solution is made by a patented injector with a dual concentric needle design, where a small amount of pilot fuel (which can be HVO, or diesel fuel) is injected into the cylinder prior to the gas, to initiate the ignition resulting in a reduction of almost 97% of CO_2 emissions, and only a small amount of NO_x and particles, in-line with the existing Euro 6 and proposed Euro 7 emissions regulations. This patented solution comes from the already mentioned, well known ICE technology, that gives the possibility to improve what already studied for several years.

The use of ICE fuelled by hydrogen gives also another element, that is not part of the engineering field but play a relevant role in the perception that a lot of people has of the car, in particular for who as a passion for cars. It’s the emotional impact that comes from the architecture of the engine, how it looks, but most importantly from the sound perspective, where the possibility to have a high-performance engine and actually fell it, gives to the owner a good emotional impact. For this reason, there are already present some companies that create H2ICE of high performance to maintain this element, like Yamaha and Toyota [20] that in 2022 collaborated to build a high-performance H2ICE. They developed a 5 L V8 engine totally fuelled by hydrogen, shown in Figure 21. It’s based on the 5 L engine in the Lexus RC F luxury sport coupe, with modifications made to the injectors, cylinder heads, intake manifold, and more, and delivers up to 450 hp at 6,800 rpm and a maximum 540 Nm of torque at 3,600 rpm.

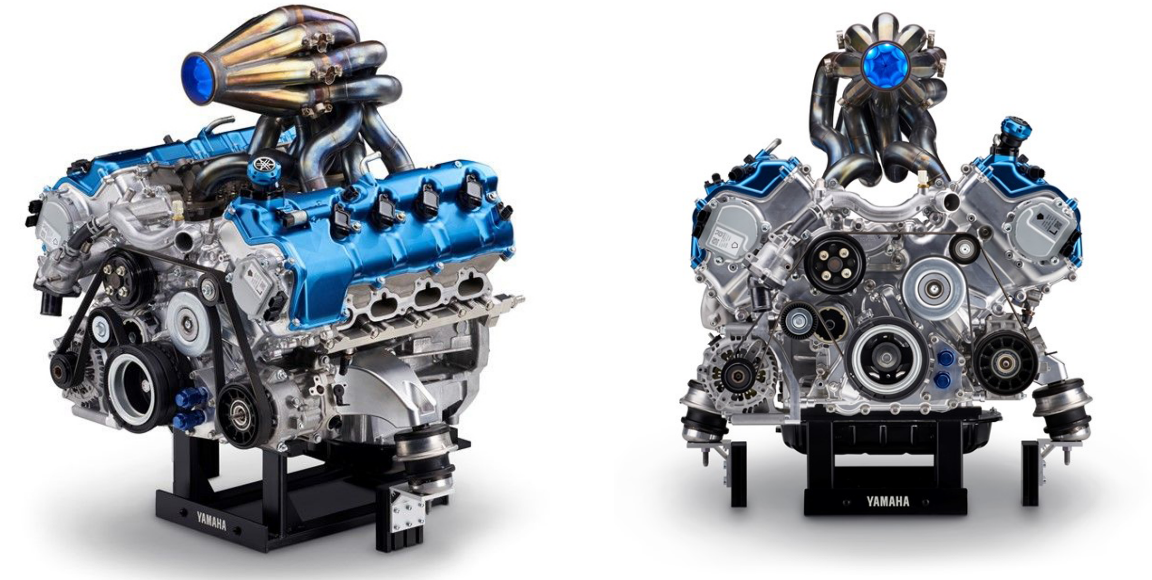

Figure 21. Lateral and frontal view of the 5L V8 Yamaha H2ICE **[20]**

On the other hand, there are disadvantages related to this type of engine, that should be fixed to increase the market of it. The main challenge [21] is the secondary costs that an H2ICE would bring, hydrogen fuel today is more expensive than the other fuels available, due to the high costs of production, especially for green hydrogen.

There is also a negative public perception of hydrogen to a very high number of people, this because they link it to negative events like the Hindenburg disaster, the H-Bomb. These examples lead to another main challenge, the storage and transport (both from the station to the car tank, but also from the tank to the engine onside the car), where the high reactivity and toxicity of the element need very precise component to accomplish this task. The necessity of this complex transport element would reflect also in the monetary impact of a car equipped with H2ICEs.

Ther are also articles that show why hydrogen should not be used in ICEs [22]. The main problem that is associated to it, is the low efficiency related to all types of ICE, that specifically of the hydrogen fuelled one at the peak cases reach around 40%. This is a high loss of fuel that, compared to other hydrogen-based technologies, lead the choice of powertrain to solutions like fuel based or BEV vehicles. Another problem related to H2ICEs are the NO_x emissions, generally higher that conventional diesel or gasoline ICEs due to the high temperatures that the hydrogen reaches during the combustion phase. The emissions could be mitigated through the use of an after-treatment system but still present, when in fuel cells or BEV vehicles these elements are null. Lastly, another problem is related to the waste of fuel not only in the engine, but also during the production process, indeed if considered the electrolysis as way to produce hydrogen, that is the greener way and also the more efficient, the efficiency of the process is around 70-80%, leading to other losses added to the one inside the engine.

Application of hydrogen for dual-fuel engines

The H2ICEs present a series of disadvantages and drawback presented in the previous sections that limit the large-scale application of them in the transport sector, especially for passenger cars. A consequence of this is the research from engineers of an intermediate solution, that is similar to the already establish situation of the BEV. Indeed, also for hydrogen fuelled engines, the solution of these problems are the hybrid engines, defined for this application as dual-fuel engines. The combination is done with different fuels depending on the application: gasoline, diesel and also ammonia for naval application.

Different studies show results in terms of both performance and emissions of this solution. Kumar et. al [23] studied the influence of the introduction of a fraction of hydrogen in a 3-cylinder gasoline DI engine (FORD-ECOBOOST), with 110 bars pressure of injection, the injection timing of 320° BTDC and engine speed of 2500 rpm. The operating parameters, including fuel injection time and pressure, were managed by an open electronic control unit (ECU). The experiments were done with three different conditions: pure gasoline, 5% and 10% hydrogen by volume along with gasoline. The hydrogen fraction was limited to 10% to avoid knocking and engine big modifications.

The first result coming from this study is the comparison for the different cases of the brake thermal efficiency (BTE), shown in Figure 22.

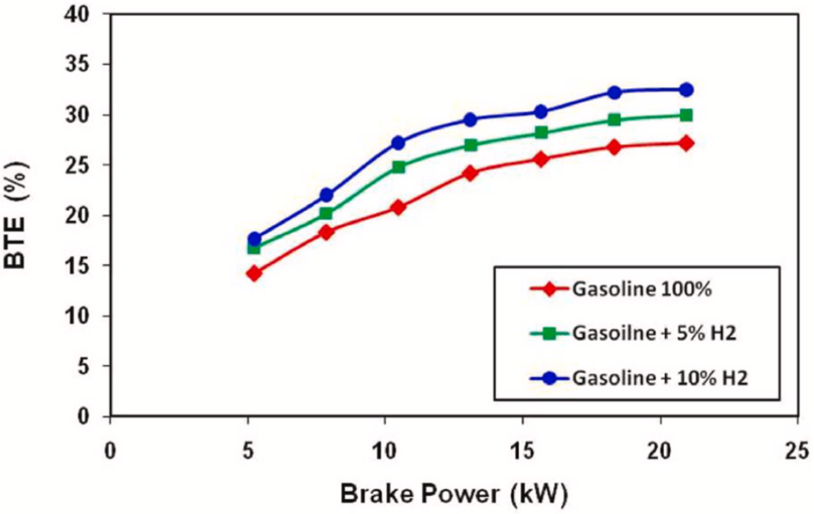

Figure 22. BTE for the different cases over the brake power **[23]**

In the results above it is possible to see that the efficiency increases with increasing brake power for all the cases. The trends of the diagrams for all the cases tends to increase until the last part where it seems to saturate. For the authors, the improvement in BTE with hydrogen introduction can be attributed to a more efficient combustion process, driven by the enhanced ignitability of the air/fuel mixture. The higher flame speed of hydrogen likely accelerated the combustion rate, promoting more complete fuel burn. Additionally, hydrogen's wider flammability range and lower ignition energy may have facilitated the combustion of lean mixtures, further contributing to the overall efficiency gains.

Moving to the analysis related to the emissions coming from the different cases, Figure 23 represent the hydrocarbon (HC) on the brake power and the unburned HC mass with respect to the crank angle for the entire cycle.

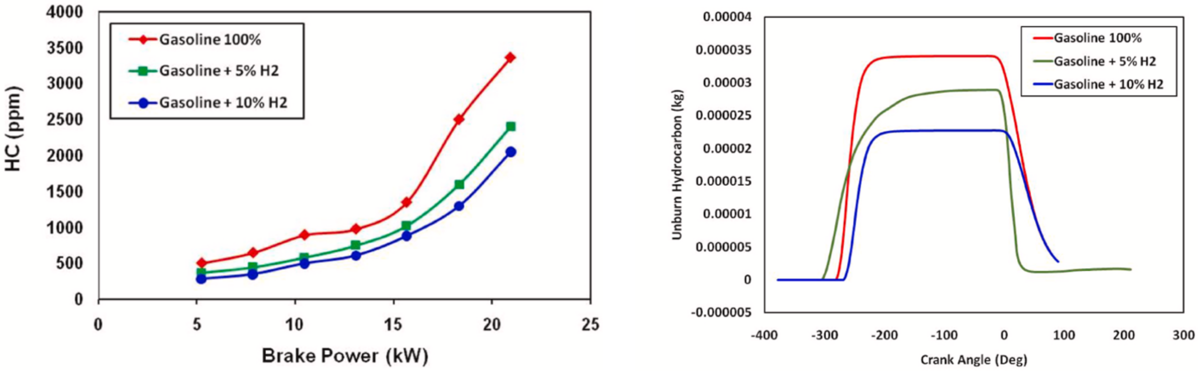

Figure 23. Analysis of HC emissions for the different cases **[23]**

For what concern the relation between HC and brake power, for all the cases the increase in the second leads to an increase in the first, this is particularly visible in the 100% gasoline one. The reasons that the authors give to the reduction in HC with the increase of hydrogen fraction, is the fast combustion rate, due to the high flame speed, and the wide flammability of this element. Also, the addition of H_2 could lead to slit effect and wall quenching effect coming from the small molecular weight, large diffusion coefficient and short wall quenching distance. Similar considerations can be done also for the HC emission over the cycle, where the increase of H_2 leads to a reduction in emissions. The general reduction of gasoline alone brings to an important reduction of emissions, but also the fast combustion rate of H_2 helps in the reduction of flame quenching and crevice effect.

Next, the article continues with the analysis of CO emissions, reported in Figure 24.

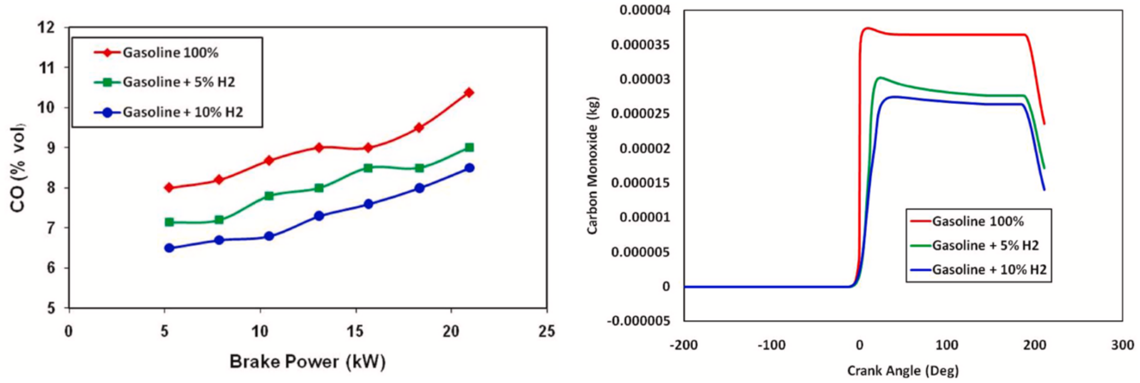

Figure 24. Analysis of CO emissions for the different cases **[23]**

In SI engines, CO emissions are typically generated due to insufficient oxygen availability, poor mixture homogeneity, and the presence of locally fuel-rich zones within the combustion chamber. The reasons behind those results are almost the same as the previous ones, mainly due to an improvement in the combustion. The same figure shows also the mass of CO for the entire cycle.

Other emissions results that are relevant are the NO_x emissions, Figure 25, when the addition of hydrogen leads to an increase of them.

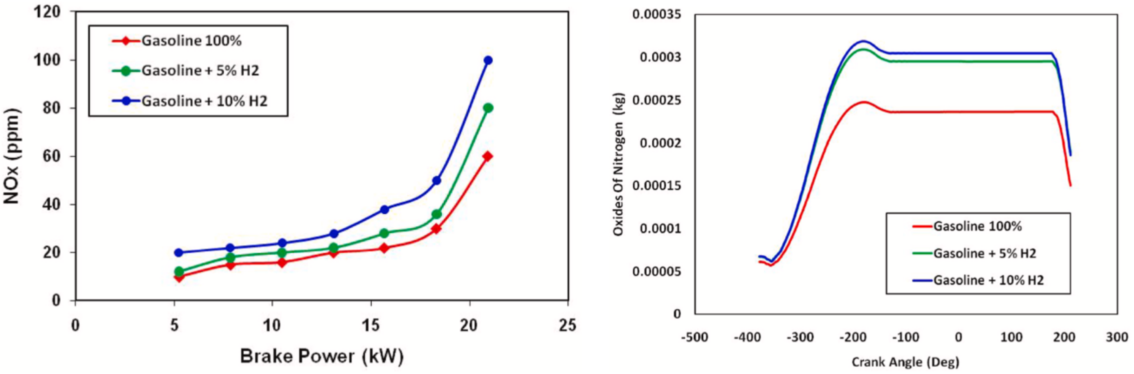

Figure 25. Analysis of NO_x emissions for the different cases **[23]**

The reason that brings to those results actually is the same as for the previous, the very fast combustion of hydrogen leads to an increase in the cylinder and cycle temperatures. In the 100% gasoline case, the lower flame speed of the fuel brings to a more controlled combustion, instead the hydrogen fuel completely burns and for the rapid flame speed and enhance the formation of NO_x.

Lastly, the pressure inside the cylinder is plotted in Figure 26, where the introduction of hydrogen leads to a rise in the pressure all over the cycle. The reason to this, as the authors explained, is related to raid combustion rate of the H_2 and the high flame speed.

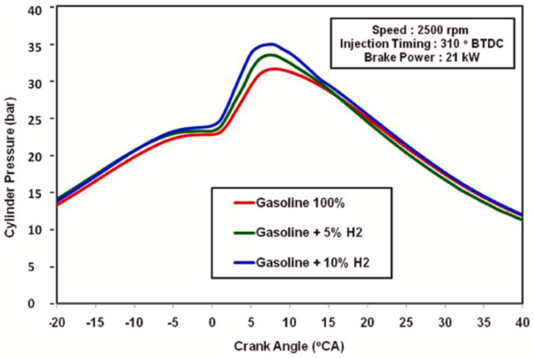

Figure 26. Cylinder pressure for the complete cycle **[23]**

If the dual-fuel application considered is the diesel-hydrogen one, instead, Akhtar et. al [24] investigates the combination of those two fuels together in a 4.4 L, 4-cylinder Joseph Cyril Bamford limited (JCB) heavy-duty diesel engine using extensive one-dimensional combustion modelling. The engine speed used for the study were varied from 900 to 2200 rpm, a hydrogen fraction ranging from 0 to 17.5% was introduced by port injection in the cylinder. An EGR system was implemented and regulated to control the NO_x emissions. Then the impact on brake power, torque, efficiency and emissions have been evaluated.

Moving on the results, Figure 27 represent the changing of both brake power and torque on the engine speed.

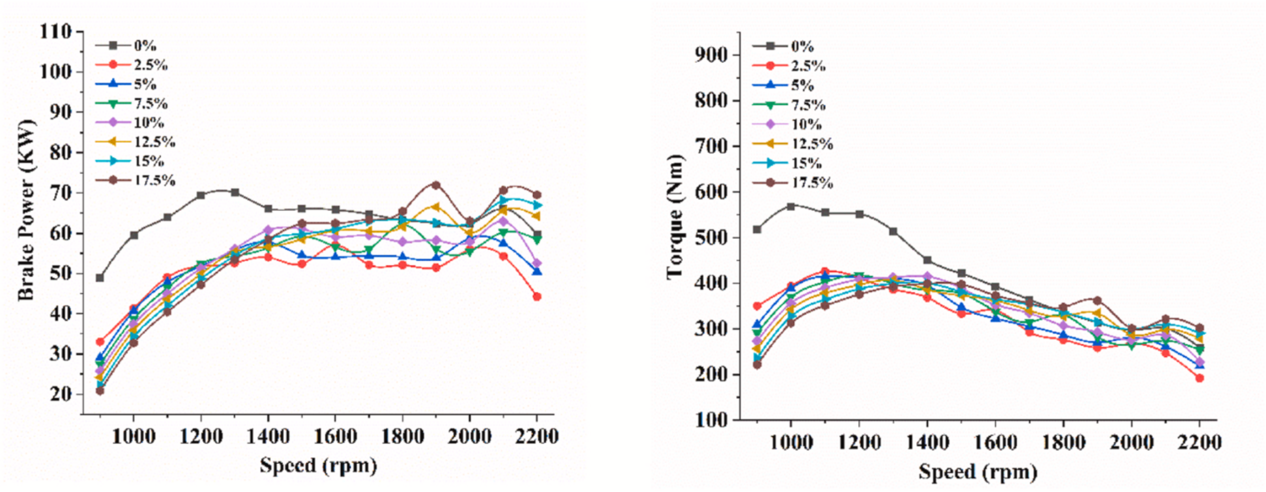

Figure 27. Comparison of Brake Power and Torque on different engine speeds **[24]**

What visible from the results is that hydrogen enrichment has led to a substantial impact on both the parameters analysed, but also the engine speed plays a relevant role. At a speed up to 1600 rpm, the increase in the hydrogen fraction bring to a reduction in both brake power and torque. The meaning that the author gave to this result is related to the properties of the hydrogen that, at low speed could be an obstacle to the ignition. This leads to incomplete combustion, that reduce the energy coming from the fuel and so the useful work, resulting in a deteriorating brake power. Moreover, the geometry and setting of the engine were tailored for the diesel fuel, with different properties from the hydrogen. Considering instead what happened at high speed, after 1700 rpm, when the combustion process is more forceful and efficient, the presence of hydrogen led to better performance. The reasons defined by the authors mainly follow the same concept expressed before, related to the high reactivity of the hydrogen, that, thanks to the faster combustion, reduced burn duration, an increase fraction of fuel chemical energy has been converted in mechanical work. Also, the high flame speed of this element helps to facilitate premixed burn propagation in condition with excessive air presence. However, the surplus of hydrogen, over 20%, could lead to a reduction in power, efficiency but also to knock phenomenon inside the engine.

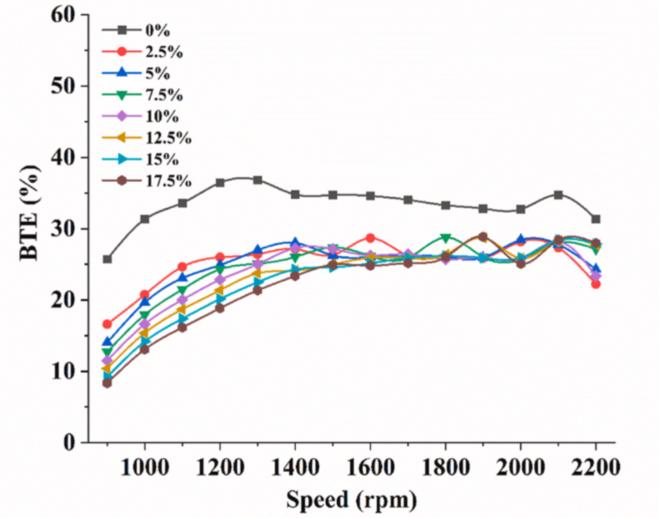

Figure 28. Comparison of BTE on different engine speeds **[24]**

Going on with the analysis with the variation of the efficiency due to hydrogen increment, Figure 28 shows the results for different engine speeds. The increase in hydrogen fraction leads to a reduction in the efficiency at low speeds, then all increased reaching a saturation point around 1600 rpm, when the different fraction of hydrogen reaches close values that are not far from the efficiency of the diesel fuel alone.

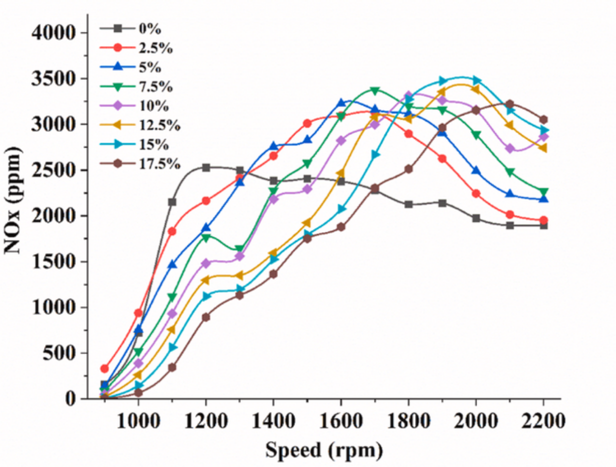

Figure 29. Comparison of NO_x on different engine speeds **[24]**

In Figure 29 are represented the results bout the emission of NO_x, comprising both NO and NO_2, on the different hydrogen fraction and engine speeds. The results show that there is a high dependence on the speed. Indeed, at speeds up to 1300 rpm, the higher hydrogen fraction leads to a reduction in general emissions compared to pure diesel. The explanation that the author gave to this trend is related to the lean-burn nature of hydrogen, that reduces the in-cylinder temperature and combining this to the lower activation energy on the same, limit NO_x formations. Moreover, the ignition delay and combustion duration combined with unstable flame propagation at low speeds, bring to high heat losses to the walls that lowers the temperatures. On the other hand, the opposite trend is visible for high speeds, where for high engine speeds the emissions increase as the hydrogen fraction increases. The reasons that could lead to those results are also explained by the authors, like the higher combustion efficiency that is experienced and the deeper energy release that generates higher temperature.

After that, the article is continued with an interesting analysis of the effect of EGR on the emissions and fuel consumption for the case studied. The results, shown in Figure 30, are related to the engine speed of 2200 rpm, where the addition of hydrogen increases significantly the emissions.

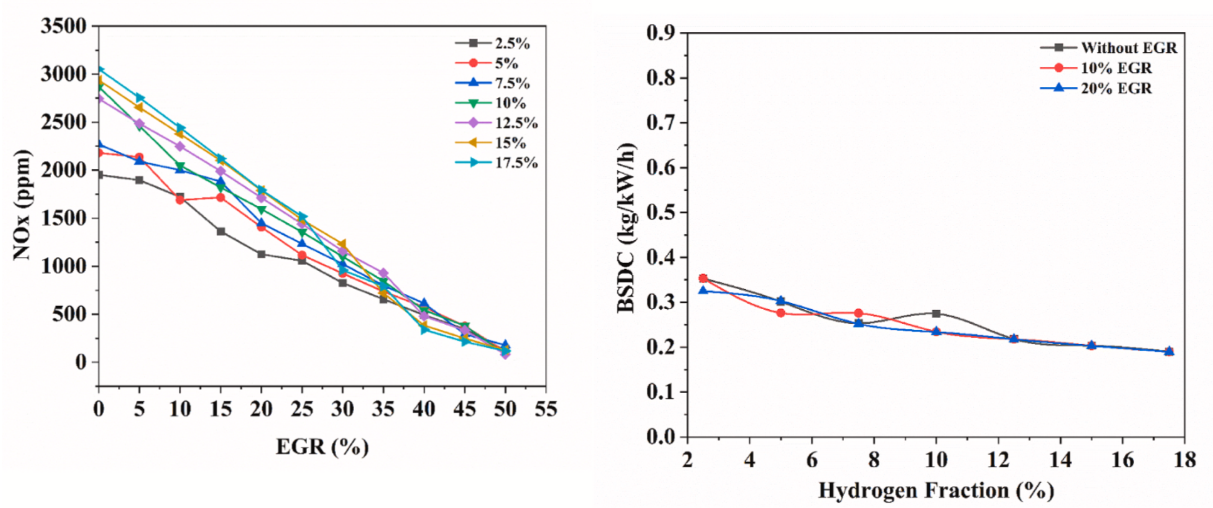

Figure 30. Comparison of NO_x on different EGR percentage (on the left), and brake specific diesel consumption (BSDC) on different hydrogen fractions **[24]**

The considerations done in the article related to these results are the following. Firstly, in the entire represented range of EGR, the emissions reduce moving to higher values, following what is the function of the EGR. However, the function of this device leads also to the lowering in the oxygen concentration, that is positive if well programmed. Instead, if there's an excess this could bring to incomplete combustion and misfiring due to oxygen deficiency. In the image above, the stable combustion is experienced for EGR values around 20-30%.

The second observation done by the authors, moving to the right plot, is that the BSDC is reduced with increasing values of EGR and lower hydrogen fraction. The authors expressed several factors that have led to those results. The EGR reduces in-cylinder temperatures, and so the heat loss to the chamber walls. Moreover, less pumping losses in the intake manifold due to increased gas density and pressure.

As a conclusion for this part, it is possible to state that the correct control of the EGR system could bring to an important reduction in NO_x emissions, unlocking the potentials of dual-fuel applications but also to just hydrogen fuelled engines, that is one of the main challenges for this element.

Going out for the automotive sector, but remaining in the transport one, the application of dual fuel with hydrogen is particularly study for naval application. Cameretti et. al [25] investigated several strategies to improve oxidation of ammonia in a dual-fuel medium speed marine engines, more specifically a 4-stroke, turbocharged, 6-cylinder and 4-valves engine. In the article, several combinations of NH_3/H_2 are tested to examinate the combustion development and the emissions. The main reason for the addition of the hydrogen to the ammonia, the authors explain, is due to the improvement of the ammonia weak flammability. Indeed, the addition of hydrogen in the premixed charge allowed to achieve a complete ammonia oxidation and an important reduction of CO_2 for mixture with 20% of hydrogen. Moreover, an addition of just 10% of H_2, has been demonstrated to worsen the performance. Generally, the authors defined that for an improvement of performance is necessary an addition of more than 10% of hydrogen to the ammonia. On the other hand, as for the other articles already analysed, the addition of hydrogen led also to an increase to NO_x emissions.

Table 7 shows the main parameters used and the different test cases studied in the article. Among the different cases, the one with the addiction of hydrogen is more relevant for this thesis, but the other are also important in order to compare the performance and emission of hydrogen with the conventional fuels. Moreover, the base case is necessary in the article for the validation of the CFD model with the experimental data.

CASE	PREMIXED BLEND	ENERGY INPUT [KJ]	CH4 MASS [MG/CYCLE]	H2 MASS [MG/CYCLE]	NH3 MASS [MG/CYCLE]	DIESEL MASS [MG]	DOI
BASE	CH_4	18.5	328	-	-	50	1.5° CA
1	CH_4/H_2 (60%-40%)	18.5	131	81		50	1.5° CA
2	NH_3	18.7	-	-	887	50	1.5° CA
3	NH_3	21.3	-	-	887	110	3.2° CA
4	NH_3	24.4	-	-	887	180	5.4° CA
5	NH_3/H_2 (95%-5%)	18.7	-	7	842	50	1.5° CA
6	NH_3/H_2 (90%-10%)	18.7	-	14	798	50	1.5° CA
7	NH_3/H_2 (80%-20%)	18.7	-	28	709	50	1.5° CA

Table 7. Main parameter of the different cases studied in the article **[25]**

Moving to the results of the analysis, the first comparison that has been done was on the base case, Cases 1 and 2 on pressure and Rate of Heat Release (ROHR), as represented in Figure 31.

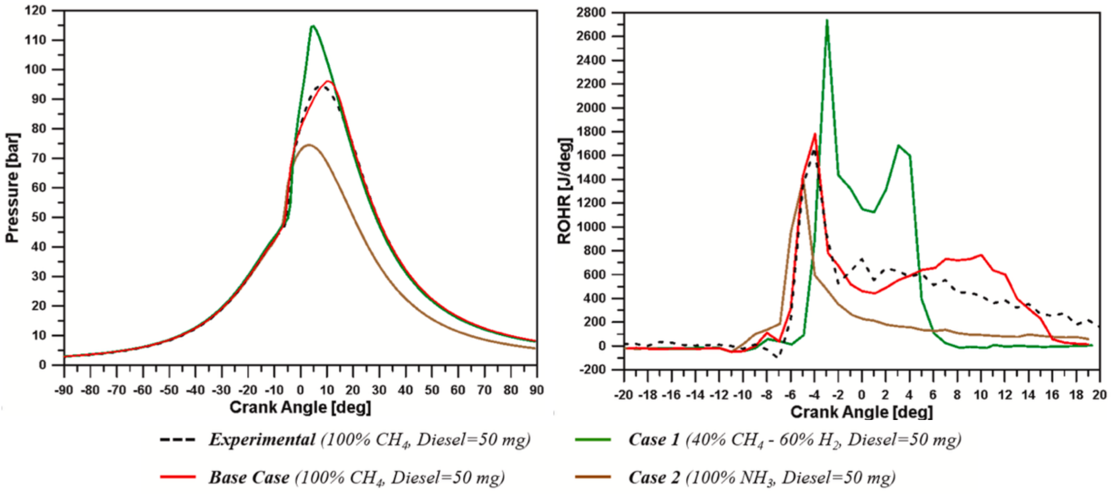

Figure 31. Comparison of pressure and ROHR for different case studies **[25]**

The first observation done by the authors on the results above, in particular for the Case 1, is related to the high peak pressure and fast decrease of the rate of heat release (ROHR) curve, due to the introduction of the hydrogen, that has high laminar flame speed.

After that, in the article, it is shown the comparison directly on different addition of hydrogen in the fuel, Figure 32. Analysing those results, from a general point of view it is possible to state that lower quantities of hydrogen worsen the performance of the engine with respect to only ammonia. The low amount of hydrogen works as diluent in that case, limiting mixture oxidation. From 10% of hydrogen, instead the performance starts to increase, with the peak at 20%, when it exceeds the baseline case.

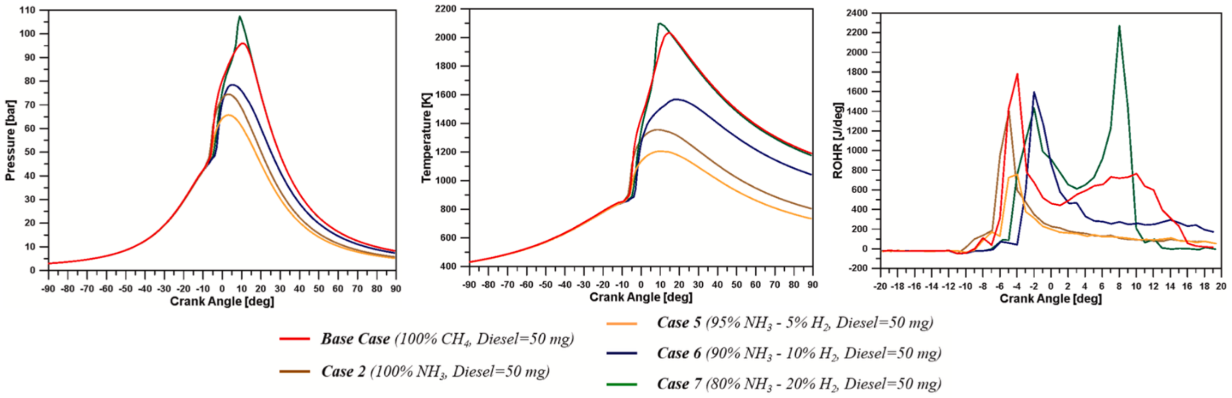

Figure 32. Comparison of pressure, temperature and ROHR for cases 2-5-6-7 **[25]**

However, as the authors suggest, the high diffusivity of the hydrogen may interfere with the diesel-air charge needed for the start of the combustion. Moreover, looking at the ROHR, Case 7 present a second peak, leading to a strong acceleration. Therefore, in Case 6 the combustion improves and in the first peak the combustion is slightly retarded compared to Case 7.

The results in terms of emissions are represented in the figure below, they show an important result: the introduction of hydrogen in the fuel, from 10%, reduce the CO_2 emissions without affecting the diesel oxidation, as confirmed by the complete conversion of CO. From these results the authors assert that this could be an "*opportunity for the reduction of GHG in marine applications*".

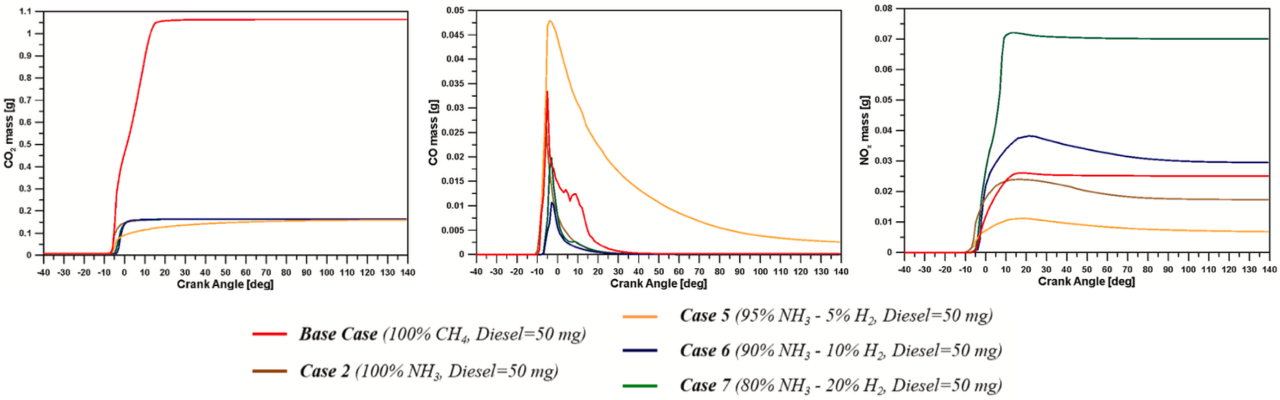

Figure 33. Emissions performance for cases base-2-5-6-7 **[25]**

However, the main problems associated with the hydrogen remains the NO_x emissions, that also in this application increase as the hydrogen fraction increases. But should be also considered that in this article the ATS were not taken into consideration.
Then, the conclusions for the authors on the work are that mainly addition of hydrogen for marine application brought improvements, like CO_2 reduction of 84%, overcoming of ammonia and hydrogen slips and improved the performance of the original fuel.

Another study regarding this subject has been done by Berni et. al [26] who propose a numerical framework based on 0D, 1D and 3D tools for CFD analysis in an NH_3/H_2 ICE. The analysis focused on combustion efficiency, emissions, heat transfer and knock tendency for different combinations of NH_3 and H_2. The engine used for the study was a single cylinder, 4-strock derived from large heavy-duty diesel engine, characterized by a maximum specific power >2000 kW and a total displacement > 50000 cm^3. The parameters used for this analysis are described in detail below, and is interesting that, compared to the other articles previously described, here there is also the analysis of pure hydrogen for naval application.

FUEL	DIESEL	NH_3-H_2 100%-0%	NH_3-H_2 90%-10%	NH_3-H_2 80%-20%	NH_3-H2 80%-20%	NH_3-H_2 50%-50%	NH_3-H_2 0%-100%
NH_3 [MOL%]	-	100	90	80	80	50	0
H_2 [MOL%]	-	0	10	20	20	50	100
NH_3 [MASS%]	-	100	98.7	97.1	97.1	89.5	0
H_2 [MASS%]	-	0	1.3	2.9	2.9	10.5	100
ENERGY [J]	17.63	17630	17630	17630	17630	17630	17630
FUEL MASS [MG]	410	937.8	875.9	810.1	810.1	597	145.7
AIR MASS [MG]	11840	5674.6	5621.6	55652	13913	5382.7	4996.1
TOTAL MASS (AIR + FUEL) [MG]	12250	6612.4	6497.5	6375.3	14723.1	5979.7	5141.8
LHV [MJ/KG_{FUEL}]	43.25	18.80	20.13	21.76	21.76	29.53	121
ENERGY CONTENT, ϕ=1 [MJ/KG_{AIR}]	3.015	3.107	3.113	3.120	3.12	3.152	3.529
STOICHIOMETRIC AIR-FUEL RATIO [-]	14.34	6.05	6.42	6.87	6.87	9.02	34.29
EQUIVALENT RATIO [-]	0.5	1	1	1	0.4	1	1

Table 8. Fuel composition investigated in the article. **[26]**

Passing to the results of the article, the authors start comparing the in-cylinder pressure of different ST for different combinations of ammonia and hydrogen, here represented in Figure 34. For the selection of the timing, it was started from 720 CAD and then progressively anticipated of 5 CAD until the excessive reduction led to poor performance or knock. Indeed, the most anticipated case studies are 100mol%-0mol%, 90mol%-10mol% and 80mol%-20mol%, where the last simulation done led to a reduction in performance, also visible in Figure 35 in terms of Indicated Mean Effective Pressure (IMEP), that will be explained later.

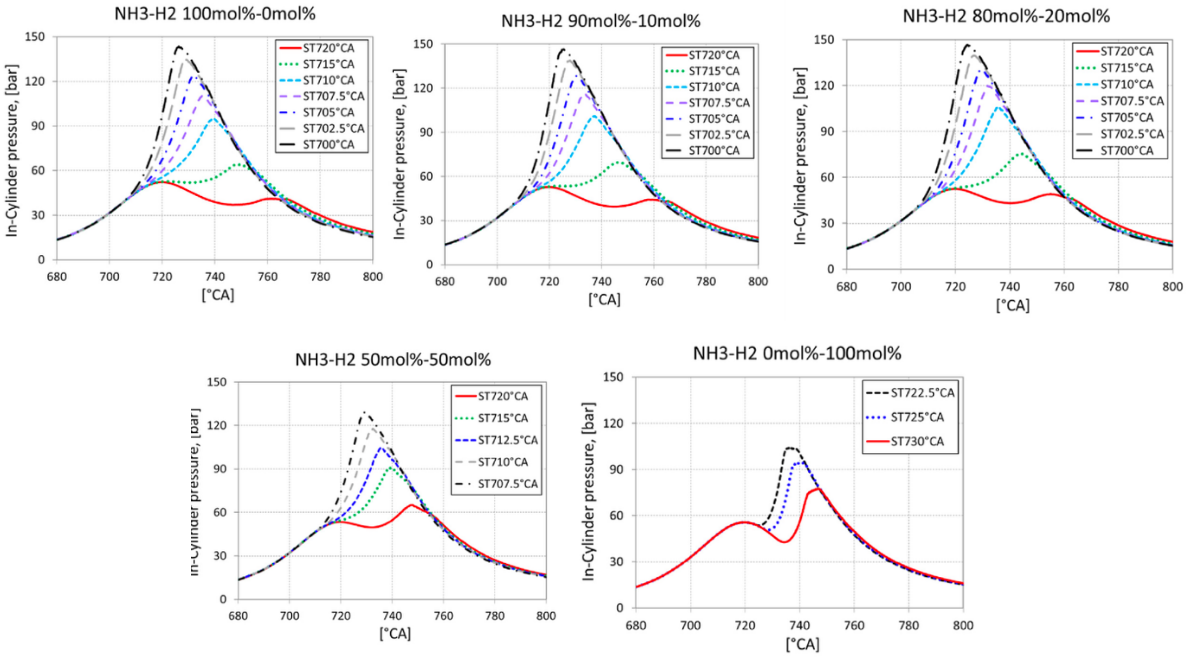

Figure 34. In-cylinder pressure comparison of different NH3-H2 and spark timing. **[26]**

The outcome of the images above is mainly that higher percentage of hydrogen leads to a higher reduction in performance and knock.

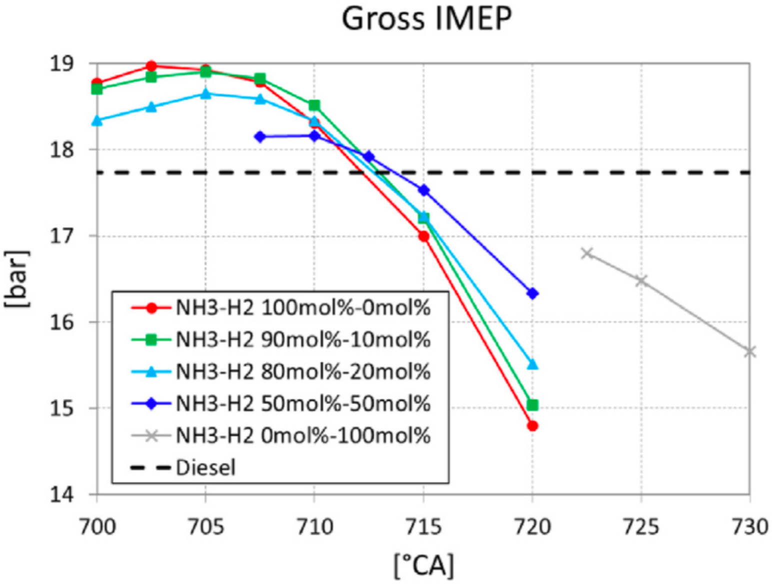

Figure 35. Performance analysis in term of gross IMEP for different combination of NH_3 and H_2. **[26]**

The figure above directly defines the performance associated to the different combinations of the two fuels, showing that increasing the percentage of H_2 the achievable performance, IMEP, decrease. Moreover, up to 50% by mole fraction of H_2 it is possible to recover the performance of the diesel fuel, with the right spark timing. Instead, for the case with 100% of H_2, it is not possible to reach the diesel in terms of performance.

Then, another important parameter is described in the article, the laminar flame speed (LFS) associated to the different combinations of fuels. This parameter will be also fundamental in the discussion of the *Results analysis* part.

Figure 36 show this parameter and the different thermodynamic states in which it's defined.

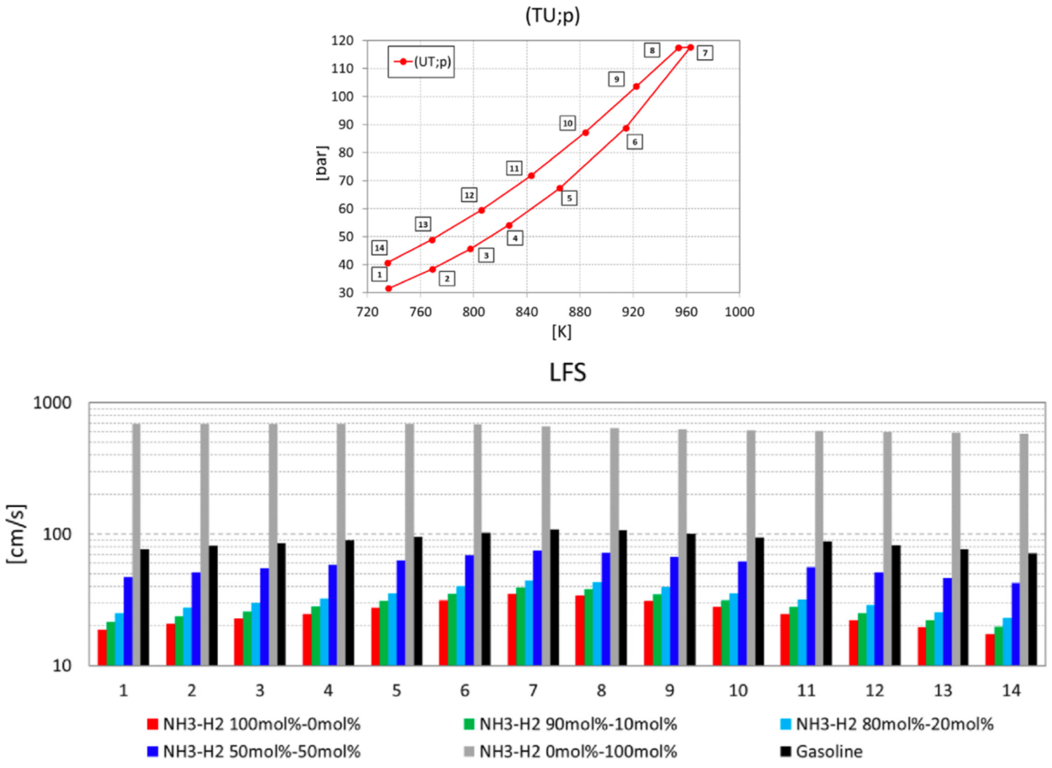

Figure 36. LFS for different combination of fuels and thermodynamic states. **[26]**

In the image is also present the LFS of the gasoline, to compare the case studies to that fuel. The combination of 80mol%-20mol% NH_3/H_2 shows values slightly higher than pure NH_3, but lower than gasoline ones. Instead, to reach the performance of gasoline, results shows that a percentage of H_2 higher that 50 % is necessary, leading to other drawbacks, as previously described, like a reduction in performance, auto-ignition and the occurrence of knock.

Moving to another interesting parameter to analyse, the article shows the heat transfer for different regions of the cylinder (head, piston, liner, total) fuelled in different ways, both for the entire cycle and the instantaneous value. These results are reported in Figure 37.

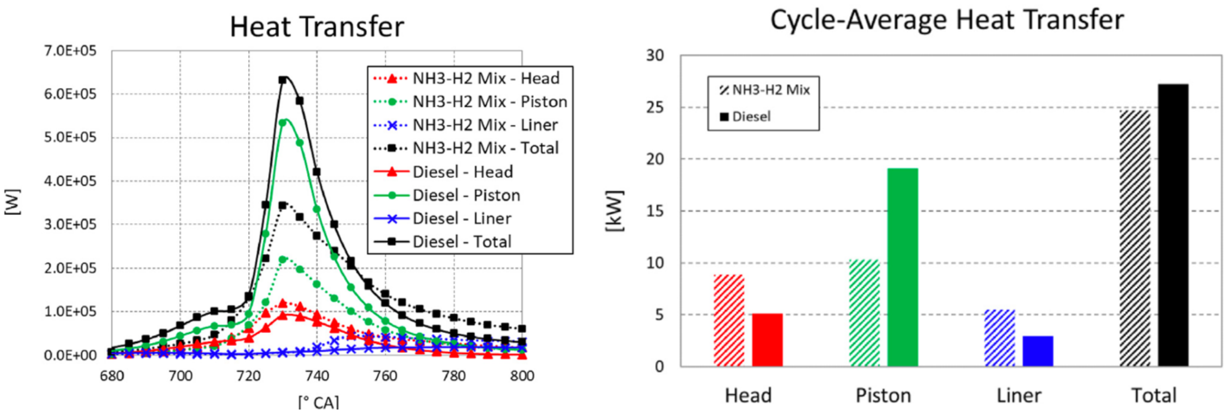

Figure 37. Heat transfer for different region of the cylinder and for different fuels. **[26]**

The first consideration of the results above is that, despite the average heat transfer between the cases is similar, the instantaneous instead is very different from a general point of view but also for the single regions. The reason for these results given by the authors is related to the change in the combustion mode, that leads the piston to not be invested by the hot jet and the heat transfer. On the contrary, due to the uniform flame propagation on each direction, there is an increase of the heat transfer on the other boundaries for the NH_3/H_2 cases. Lastly, the thermal tress changes even if the total heat transferred to the coolant remains comparable with the other fuels.
The analysis continues with the emissions, in particular the NO ones. The results, in mass fraction are represented in the figure below for different distances from the flame brush position.

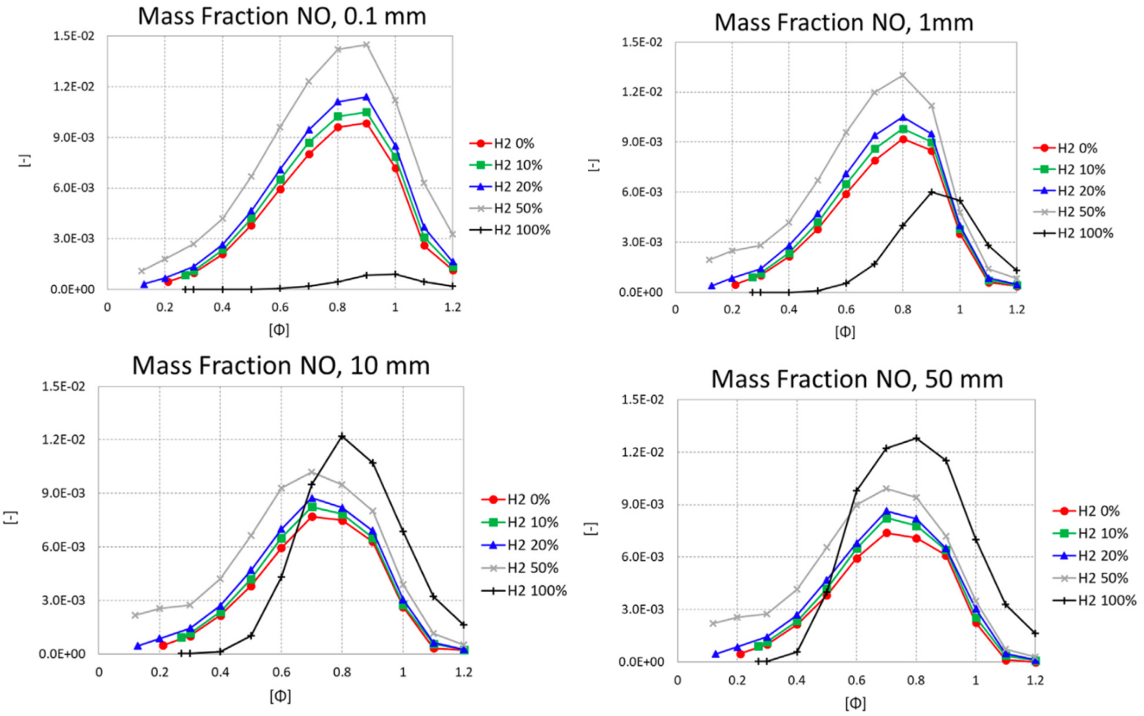

Figure 38. NO mass fraction for different H_2 percentage and distance from the flame brush. **[26]**

The first consideration on these results done by the authors is related to the fact that, also close to the flammability limit is not possible to eliminate or strongly reduce NO, compared to the stoichiometric conditions. There could be an important reduction of NO for pure H_2 when applied at lean conditions, but as already explained, pure H_2 would bring to other problems. Then, the main issue related to NH_3 is the presence of nitrogen that directly leads to NO_x formation, also at low temperatures. Instead, in other fuel, the emissions come from high combustion temperatures that made the N_2 present in the air reacting with the oxygen. The condition already described is clearly visible in the image, specifically for the peak region (equivalence ratio of 0.8), where for all the fuels containing NH_3, the NO concentration decreases with an increase in the distance from the flame brush. This result doesn't follow the temperature gradient, where the temperature is higher behind the flame front. Another confirmation of this comes from the pure hydrogen case, where the leaner concentrations lead to lower NO emissions due to low temperatures.
For what concern a reduction in NO for the combination of the two fuels with respect to the pure NH_3 case, a good solution that comes from the results was to use richer mixture, generally above 1.
In conclusion, the authors declare that the combination of ammonia and hydrogen could be a valid solution to replace the diesel in terms of performance, in particular the combination 80mol%-20mol%, but there are some limitations regarding the emissions of NO_x due to the presence of NH_3 that need further investigations.

Studies on H2ICE: parameters changed

Considering now studies made on H2ICEs running on pure hydrogen, there are a lot of scientific articles that show how the performance and emissions of those engines would change depending on what parameters are considered and modified. The main parameters analysed for these studies are the following:

- *Air-fuel ratio*, the air-fuel ratio (λ) is defined as the mass of air in the engine divided by the mass of fuel, and it gives an indication of the mixture present in the engine for cycle or work that it's doing.

$$Air - fuel\, ratio = \frac{Mass\ of\ air}{Mass\ of\ fuel} \tag{1}$$

- *Compression Ratio* (CR), defined as a ratio of the volume of the cylinder when the piston is at the Bottom Dead Centre (BDC) and the volume when the piston in at the Top Dead Centre (TDC).

$$Compression\, ratio = \frac{V_{BDC}}{V_{TDC}} \tag{2}$$

  The compression ratio is a critical factor that influences directly the engine thermal efficiency and combustion.
- *Jet features*, represent some general features of the injection nozzle, like the angle with respect to the walls and the injection timing.
- *Nozzle geometry*
- *Spark Timing*

In this section, from all the element listed above, the influence that they do on the output of the engine will be described, with the reference of previous studies.

Moving to the results coming from studies, Aljabri et. al [27] studied the influence of three of the mentioned parameters on the engine combustion performance and emissions on a single cylinder derived from the Volvo D13C500 engine. The first interesting results coming from the study was the effect of the CR. For this analysis, five CRs from 16.5 to 11.5 where selected, with λ=2.85. The results, Figure 39, show that a reduction in CR leads to a more retarded combustion, a reduction in Maximum Pressure Rise Rate (MPRR) and a reduction of the heat transfer losses.

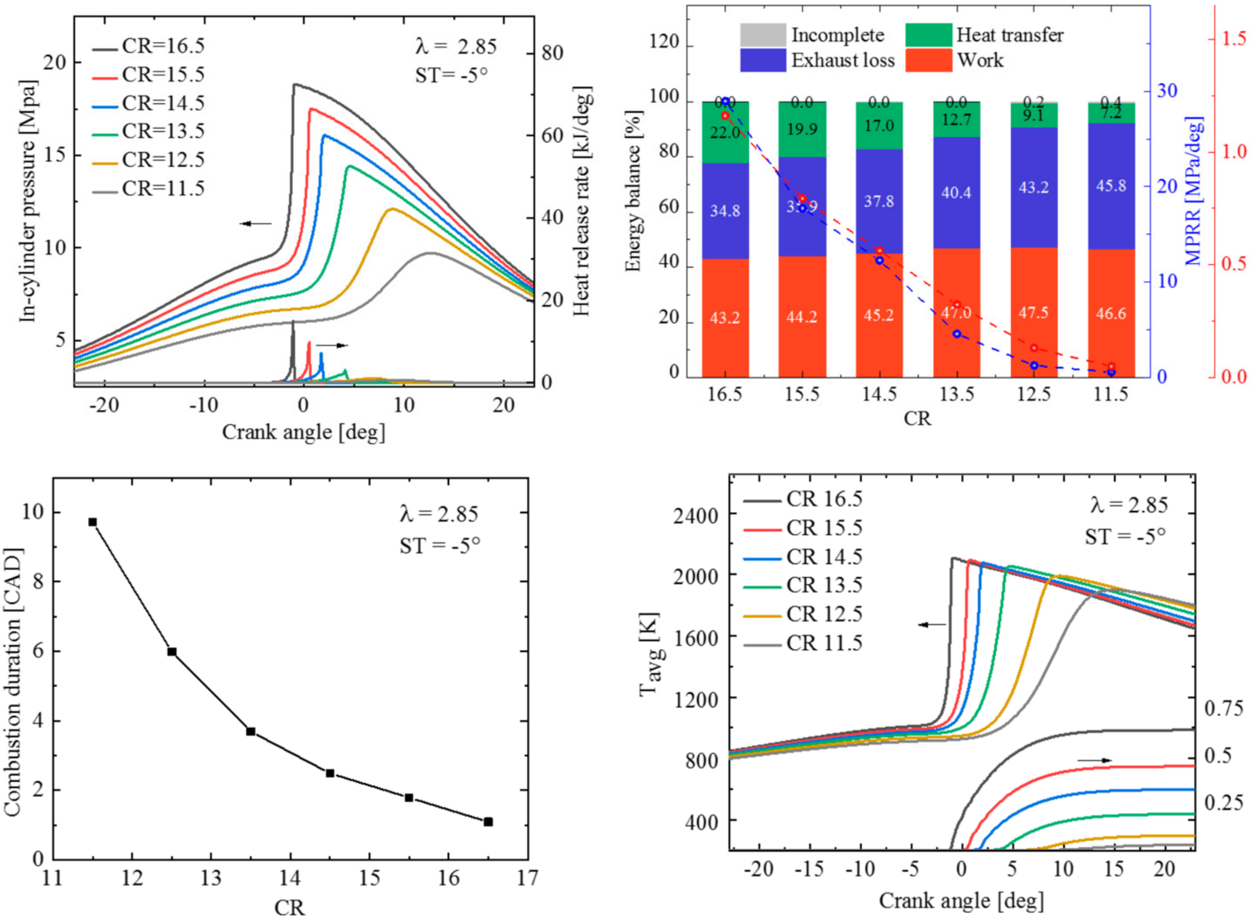

Figure 39. Effect of CR ratio on engine performance. **[27]**

The figure above also shows the combustion duration with respect to the CR, and the correlation is almost inversely proportional. Lastly the retarded combustion explained above is also visible in the temperature diagram, where for lower CR the combustion is retarded, this leads also to a reduction in NO_x emissions.

The article continues with the studied of the *air-fuel ratio*, related to auto-ignition. The results are reported in Figure 40.

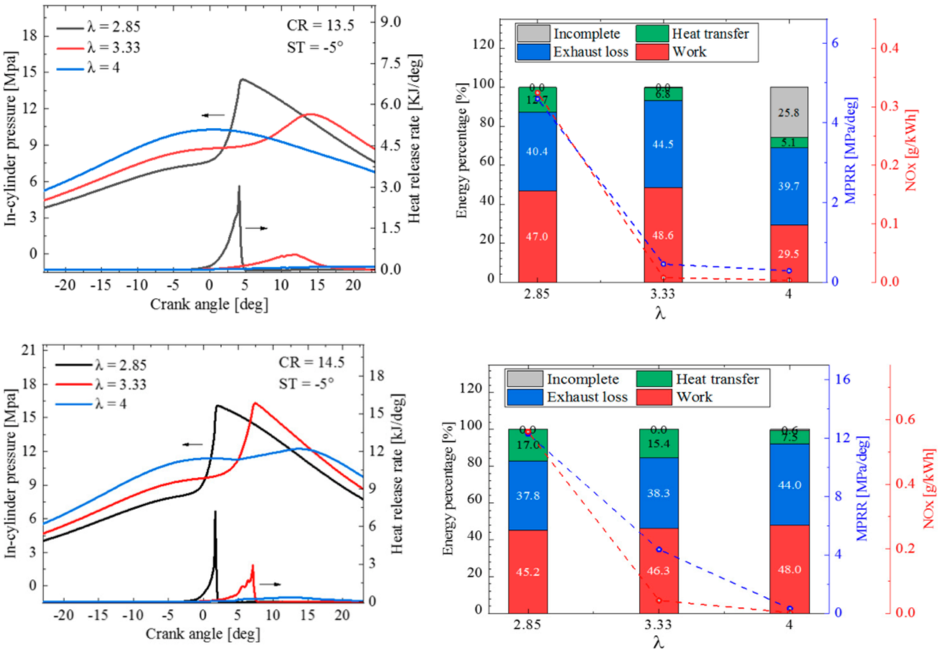

Figure 40. Effect of air-fuel ratio on engine performance. **[27]**

The case studies considered in the article were mainly two for the CR, 13.5 and 14.5, both with a ST=-5 CAD. The parameters of λ compared were 2.85, 3.33 and 4, then the total fuel mass was kept constant by adjusting the intake pressure.

The figure shows that increasing λ over 2.85 would delete auto-ignition phenomena in the cycle. However, the increase in λ also led to retarded combustion phasing and so incomplete combustion, bringing to higher exhaust losses. The authors also do not recommend working with λ lower than 2.5 due to ultra-fast flame speed that generates high-pressure rise rate.

The last parameter considered in the article was the ST. As baseline cases was used CR=13.5, λ=3.3 and 4. The results are presented in Figure 41.

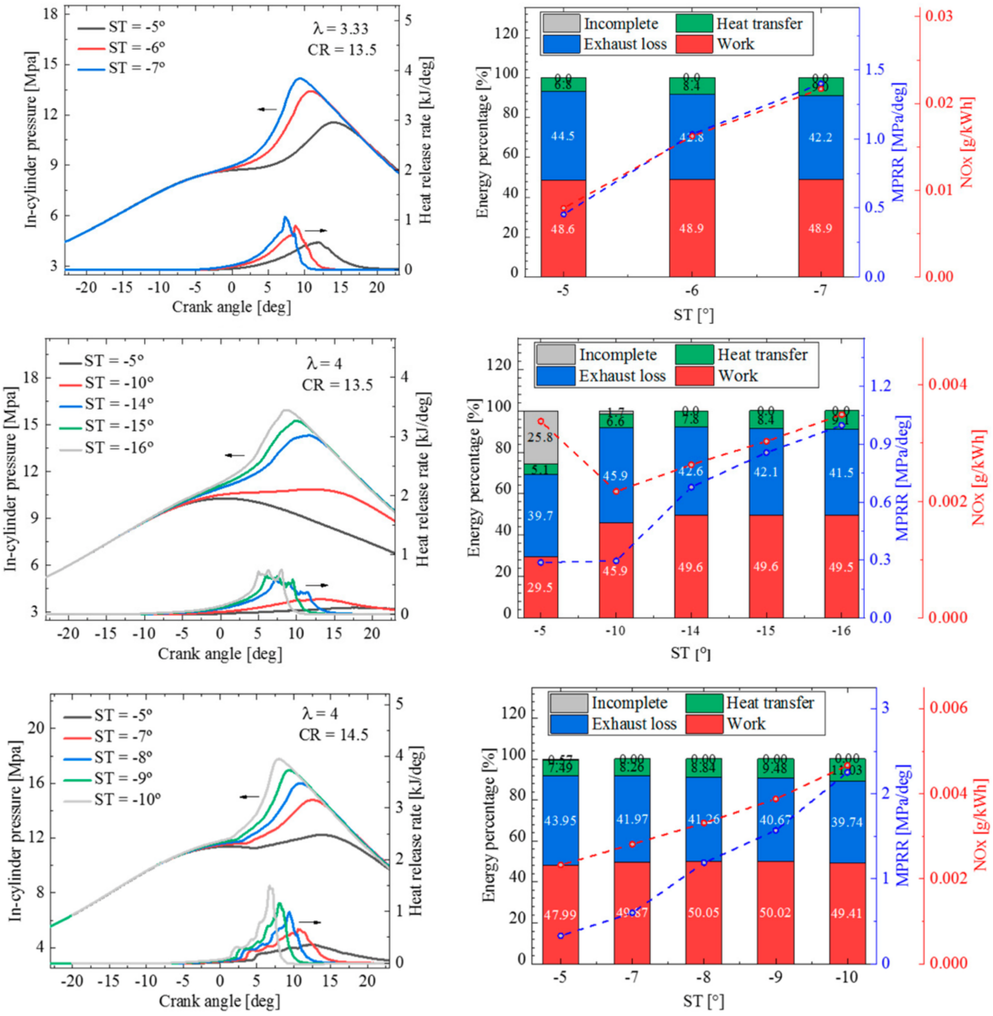

Figure 41. Effect of ST ratio on engine performance. **[27]**

From the image above the first consideration done by the authors is that advancing the spark timing the combustion and exhaust losses are reduced, instead the heat transfer ones increased due to the combustion anticipating. Also, the advancing of ST increases the maximum pressure rise rate (MPRR) due to the heat release of the combustion near to the TDC, leading to shorter combustion. In order to reduce the auto-ignition, the results show that it is preferable to choose higher CR. Lastly, the advancing of ST led to an increase in combustion temperatures, finishing in an increase in NO_x emissions, but remaining always below the Euro 6 regulations (0.46 g/kW-h).

The conclusions of the authors are that the optimal operating conditions are obtained with CR around 13.5-14.5 and a λ value around 4. These conditions lead to an easier regulation of ST to better optimize the combustion performance and avoid the phenomenon of auto-ignition.

On the same topic, Panthi et. al [28] examined the hydrogen combustion at leaner condition. In particular, the article used single cylinder coming from the 2.13 L 6-cylinder Volvo D13C500 diesel engine, modified by enabling only one of the cylinders and deactivating the remaining. Then the engine was converted to SI operation by removing the diesel injector with a spark plug. The operating conditions are listed in Table 9.

λ [-]	2	3	-
Spart Time [CAD aTDC]	-15	-20	-25

Table 9. Operating conditions. **[28]**

The first relevant result coming from this article is shown in Figure 42, where in-cylinder pressure and ROHR are compared for the different operating conditions of the work.

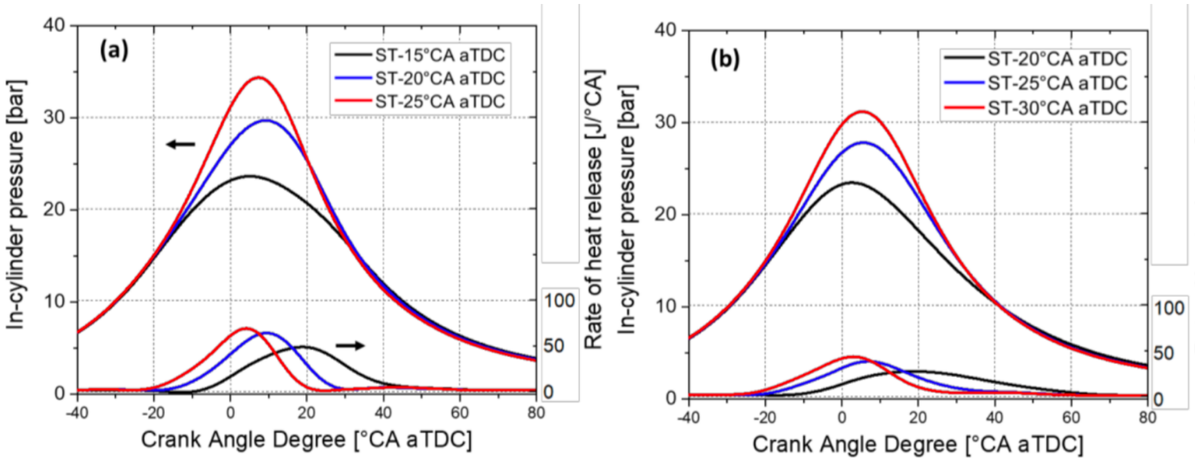

Figure 42. In-cylinder pressure and ROHR for λ =2.5 (a) and λ =3 (b). **[28]**

A consideration that can be done on the results is that the peak pressure for λ = 3 is lower than in the other cases. Then, in the article was reported that the peak pressure rise rate for λ = 2.5 at ST = -25 CAD aTDC was 0.95 bar/°CA and were below 0.95 bar/°CA for all other operating conditions. This, according to the authors, suggests that the flame propagation was dominant and no knocking or abnormal combustion behaviour was experienced throughout the combustion.

Another important results that also was reported in other articles is the combustion duration, that for this study is reported in Figure 43 as CA10-90, with CA10 and CA50. CA10, CA50, and CA90 defines the crank angle corresponding to 10%, 50%, and 90% of the cumulative heat release, respectively. Then, the combustion duration has been defined as the difference between CA10 and CA90.

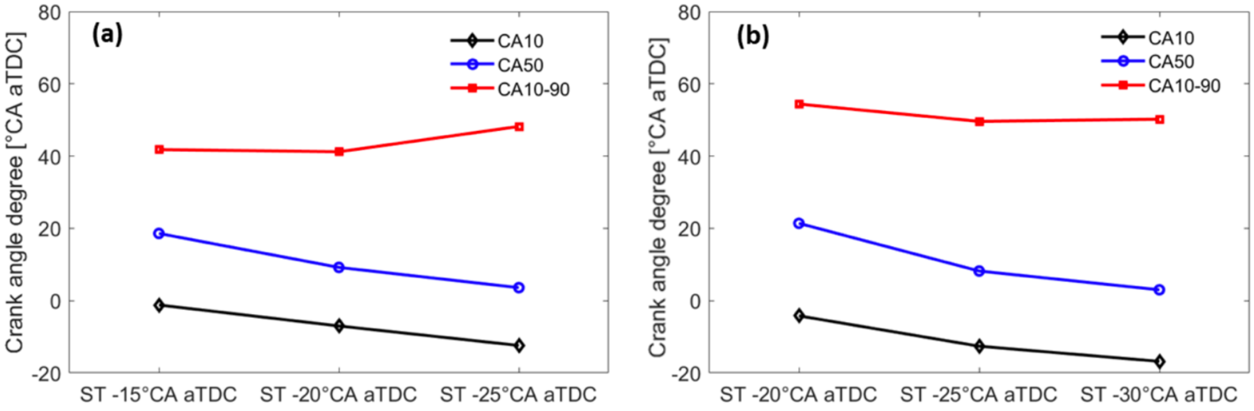

Figure 43. Combustion phasing and combustion duration for λ=2.5 (a) and λ=3 (b). **[28]**

Defined that, the results show a decrease of CA10 and CA50 with the advance of the spark timing, regardless of the λ value. Moreover, the minimum combustion duration is observed for λ = 2.5 at ST of -20 CAD aTDC and for λ = 3 at ST of -25 CAD aTDC.
Then the article shows some results that has been studied also for other works with the same subject, the flame front propagation speed, here represented on Figure 44.

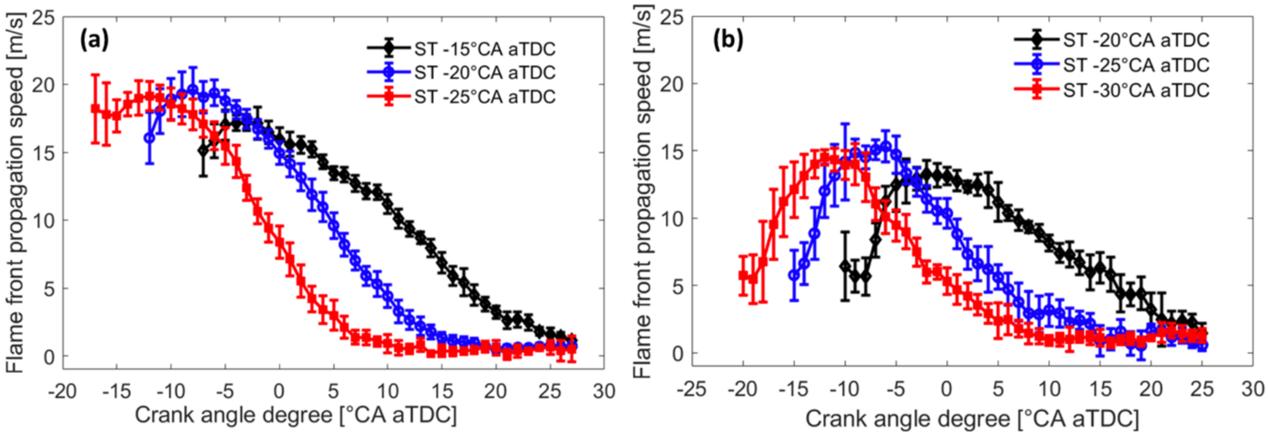

Figure 44. Flame front propagation speed for λ=2.5 (a) and λ=3 (b). **[28]**

The overall behaviour of flame front propagation speed is similar for both operating λ conditions, with the λ = 3 cases showing a slightly lower peak than the λ=2.5 cases. This, with other parameters, for the author confirm the optimal configuration of ST for the tested λ conditions for pure hydrogen combustion.

All the studies already mentioned and analysed focus on ST and injection timing. Instead, Zhao et. al [29] studied the combustion of an H2ICE mainly focusing on the achievement of the best mixing condition inside the cylinder, modifying also some injector features. In particular, the engine taken into account was a 6-cylinder 15L direct-injection spark-ignited engine, and the parameters used for the analysis were the number of holes in the injector nozzle and the swirl ratio.
The simulations were done with 1-4 and 8 holes, with a ST set at -5 CAD aTDC.

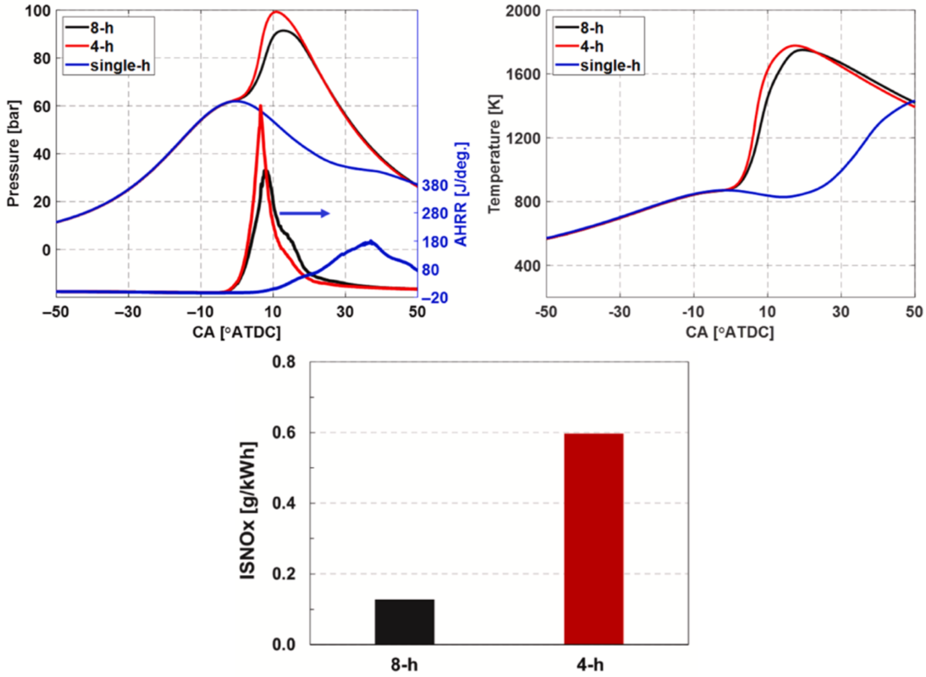

Figure 45. Pressure, AHRR, temperature and emission for different number of nozzle holes. **[29]**

Figure 45 shows the results of pressure, apparent HRR (AHRR), temperature and emissions for the different numbers of nozzle holes. The main comparison has been done on the 4 and 8-holes configuration, this because for the single-hole nozzle is visible from the pressure distribution an incomplete combustion. This due to the failure in reaching the proper mixture before the ST. Instead, the other cases reveal rapid increase of pressure and temperature, in particular for the 4-holes case, where higher values were reached, motivated by the author with a non-uniform distribution and higher air-fuel ratio. For the emissions analysis the single-hole case has not been considered due to the non-complete combustion and so the absence of meaningful results, but the 8-hole case demonstrates an 80% reduction in NO_x emissions, thanks to a more homogeneous mixture. The emissions are expressed in Indicated Specific NO_x (ISNOx), defined as the mass of NO_x over the gross indicated work on the compression and expansion stroke. These highlight the impact of mixing quality on combustion performance and emissions that the authors underline with this work.

Another interesting analysis done in the article is related to the impact of the swirl ratio (SR) of the combustion performance. The swirl ratio is a dimensionless number that quantifies the rotational velocity of the air-fuel mixture within the engine cylinder, and in this work the values considered were 0.5-2-4.

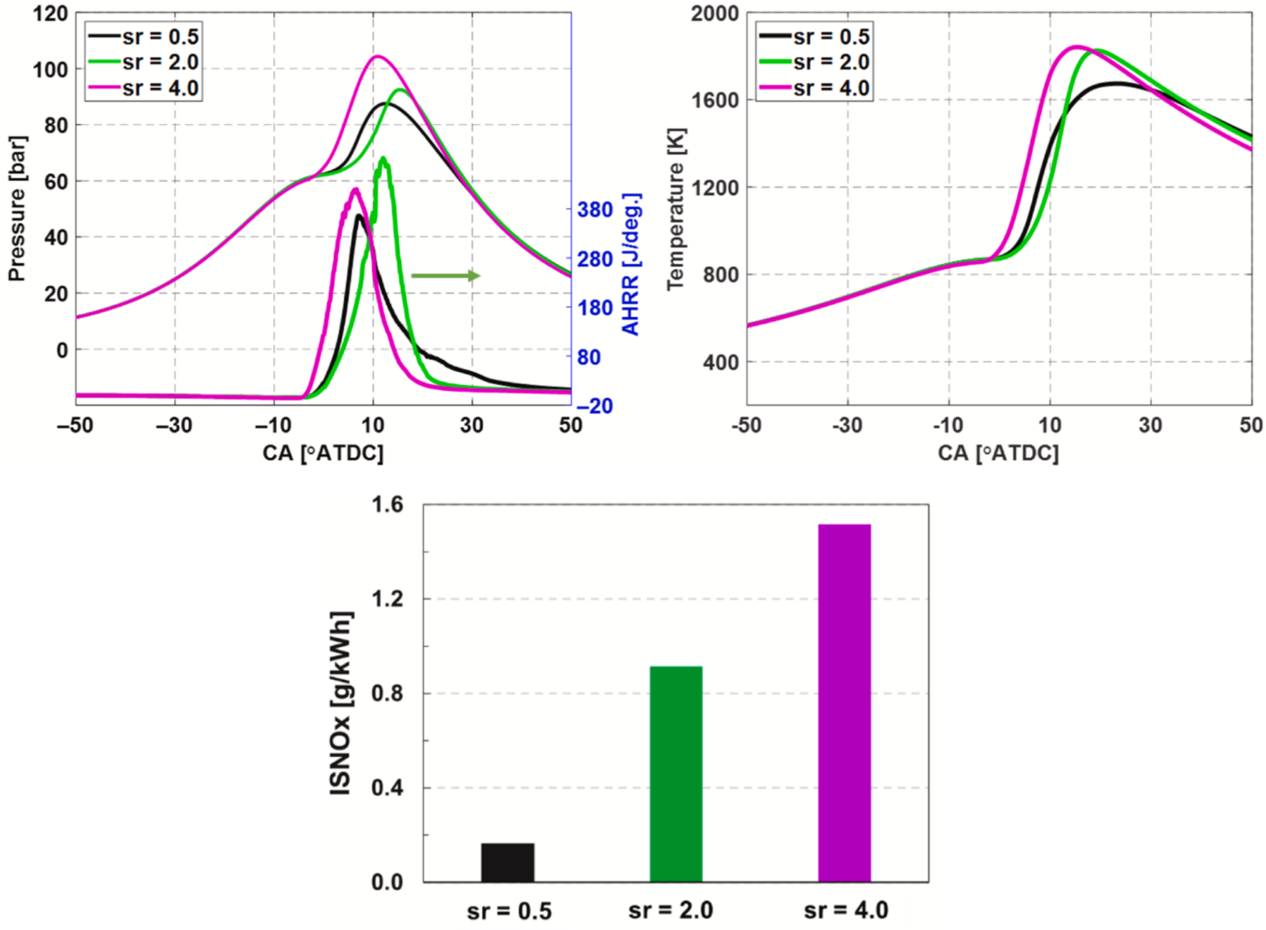

Figure 46. Pressure, AHRR, temperature and emission for different swirl ratios. **[29]**

The above figure compares the effect of different swirl ratios. The first visible result is that the highest swirl ratio leads to an earlier initialization of combustion, higher in-cylinder peak pressure and temperature. Then, after 10 CAD aTDC, the simulations done with a swirl ratio (SR) value of 2 had both more pressure and temperature, this explained by the fast flame development for high values of swirl ratio. However, SR=4 led also to higher emissions of NO_x. The conclusions from these results are that the increase in the SR impedes the homogeneous mixing of air-fuel, leading to incomplete combustion.

Lastly, an interesting analysis was on the comparison of the baseline configuration of the engine, coming from the 8-hole configuration with the baseline SOI timing and SR, and a complete homogeneous mixture in the cylinder reached before the combustion occurs, the mixture comparison is shown in Figure 47.

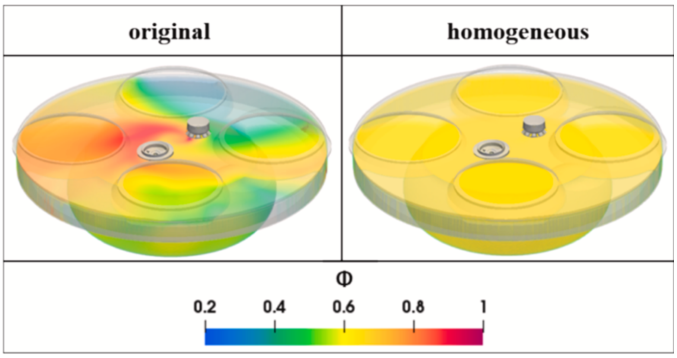

Figure 47. Comparison of the air-fuel mixture for the two compared cases. **[29]**

The most relevant result of this comparison is related to the emissions for the homogeneous case. Indeed, the results demonstrate that reaching a mixture with that level of homogeneity, should be possible to reduce the emissions of NO_x by 80% with respect to the original configuration.

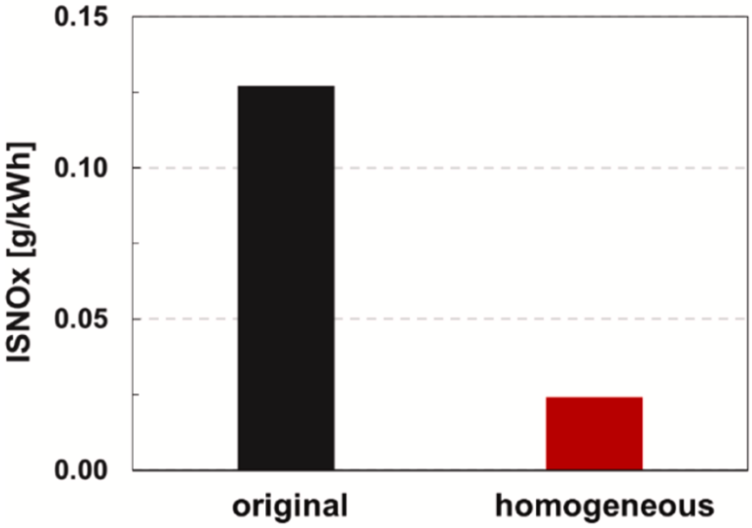

Figure 48. NO_x emissions related to the "original" and "homogeneous" configurations **[29]**

In conclusion the authors underline the importance of the mixing for both combustion performance, but more importantly on the emission of NO_x form the engine.

Validations of CFD combustion models used in hydrogen simulations

In the previous sections have been cited several articles that simulate the combustion inside the H2ICE based on different mathematical models that define the combustion phase in the engine working cycle.

This section will focus on the analysis of other scientific papers that used for their work those models, in particular on the way they have been validated from the experimental results.

This is needed because in this thesis those models will be used and compared, but unfortunately, no experimental results could be used, due to difficulties in obtaining them.

The models considered are the following and will be described in a more specific way in the next sections:

- SAGE model
- Extended Coherent Flame Model (ECFM)
- G-equation model

This section will be divided by them and will go through some validation examples present in the literature.

G-equation

Sfriso et al. [30] used the G-equation model for the heat transfer and the ignition, then combine it with the detailed chemistry model in order to predict the NO_x emission of an DI, SI, H2ICE.
Several numerical validations had been done to those models, starting from Figure 49, that show the comparison of in-cylinder pressure and a diagram of experimental pressure over CFD pressure.

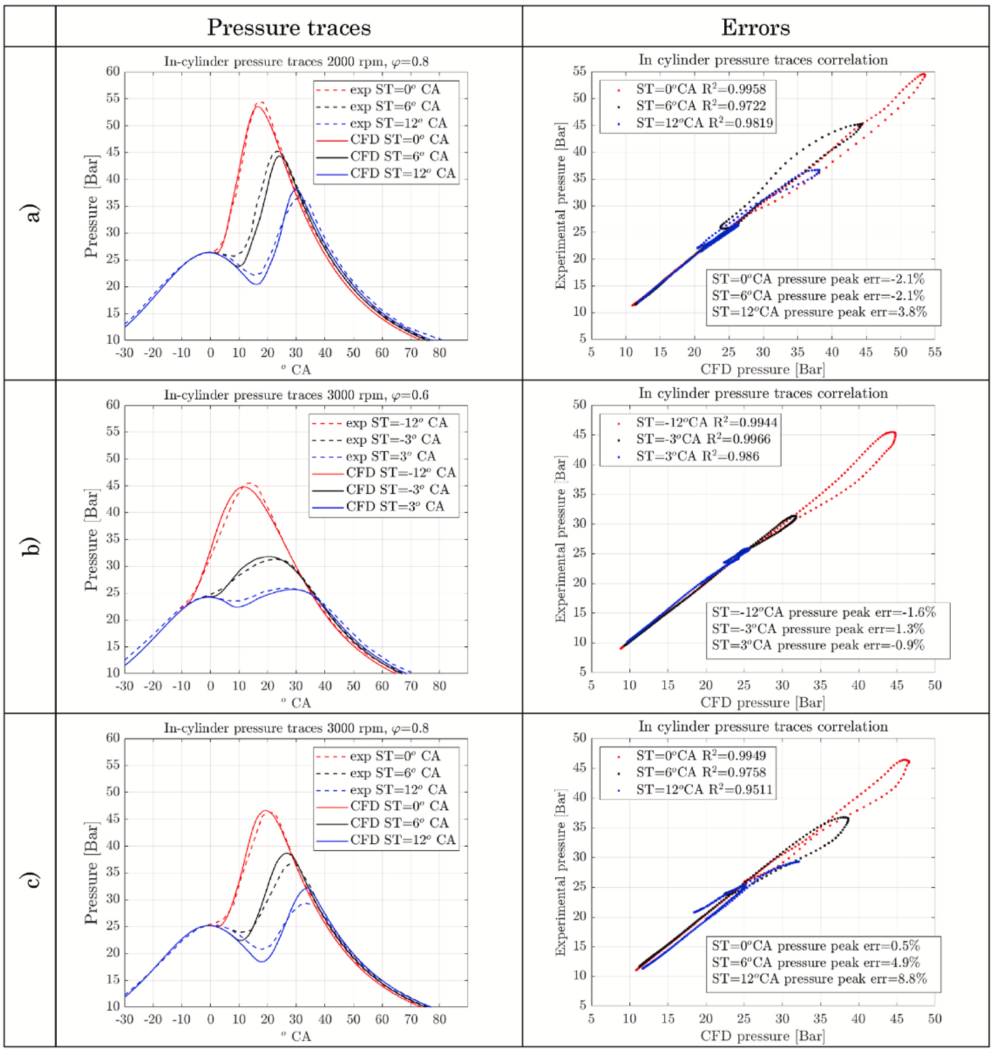

Figure 49. Comparison of experimental and simulated pressure data for different working conditions. **[30]**

As possible to see from the image, the model is able to reach a valid results close to the experimental one for all the test cases. The highest error occurs at the 3000 rpm - $\varphi = 0.8$ case, in particular for the most advanced spark. Instead, the best results occur at the $\varphi = 0.6$ case. The explanation done by the authors is related to the injection duration. Where longer injection led to lower time for the mixing.

Another study that used the G-equation as combustion model for the simulation was done by the same group, Sfriso et. al [31], who analysed different set up cases for an H2ICE. The used engine was a two-valve naturally aspirated engine originally fuelled with diesel, then modified to be run with hydrogen, with the substitution of the diesel injector with a spark plug.
The results of the model are shown in Figure 50.

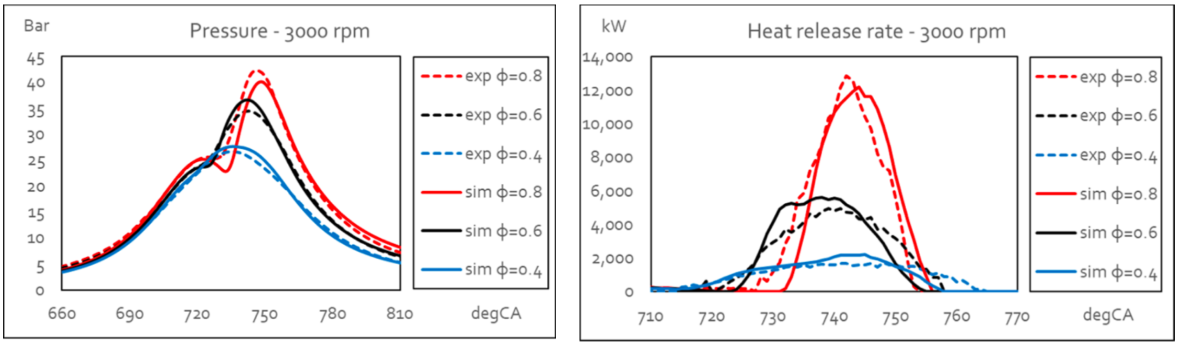

Figure 50. Validation of pressure and HRR. **[31]**

In the figure, combustion is slightly anticipated and delayed for φ =0.6 and φ =0.8, respectively, as confirmed by the apparent heat release rate profiles. But in general, the validation shows good agreement of the model with the experimental data, also with different equivalence ratio set ups.
Then the authors validated also some combustion parameter, like the MFB50, that is the time (in CAD) needed for 50% of fuel to burn, and combustion duration (also in CAD). Both these elements are visible in the figure below.

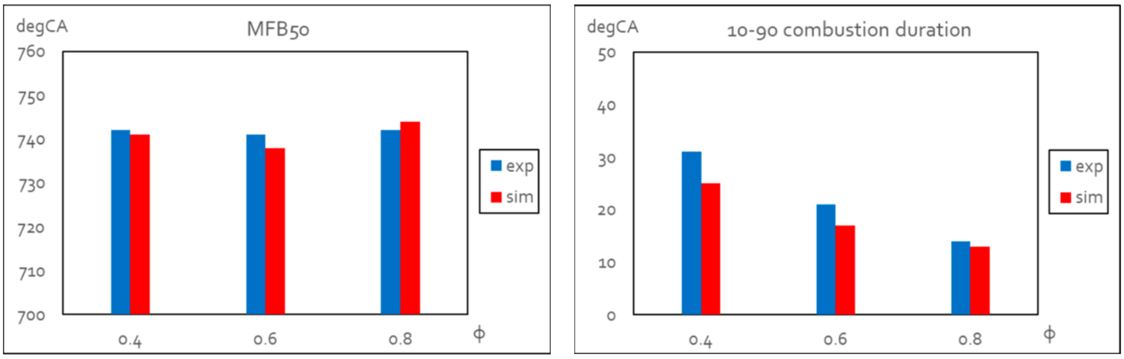

Figure 51. Validation of MFB50 and combustion duration **[31]**

What can be expressed from the Figure 51 is that also in this case the validation is acceptable with good correlation between experimental and simulation results. The comment that can be done on this is that the combustion is slightly anticipated and delayed for φ =0.6 and φ =0.8, respectively. This trend is confirmed by the apparent heat release rate profiles, previously shown in Figure 50.

Different approach has been done by Robbio et. al [32] who studied the combustion in a single cylinder research engine fuelled with diesel and hydrogen for a dual-fuel application, and compared the experimental results obtained through optical apparatus that allowed the visualization of the combustion process with the simulation prediction using G-equation model. The test cases were characterized by two different engine speeds of 1500 and 2000 rpm, and a low load level, corresponding to 2 bars of BMEP on light-duty vehicle.
Starting with the case with 1500 rpm and 2 bars of BMEP (defined in the article as *1500x2*), the comparison of experimental and numerical results is shown in Figure 52, where pressure and ROHR are compared.

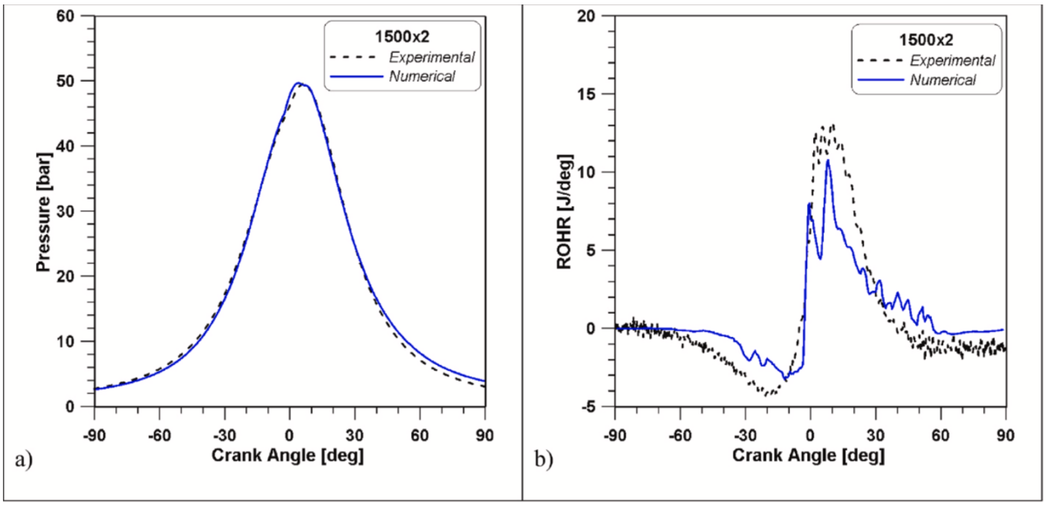

Figure 52. Comparison of pressure (a) and ROHR (b) for the 1500x2 case. **[32]**

The figure shows that the simulated results follow in a good way the experimental one for the pressure diagram, for the ROHR, there are some differences that can be explained by the use of different constants for the calculation of such variable. However, the authors defined acceptable those results on the ROHR due to the comparable order of magnitude, but most important for the change of gradient, that matched in a good way, leading to a correct simulation of the combustion process.

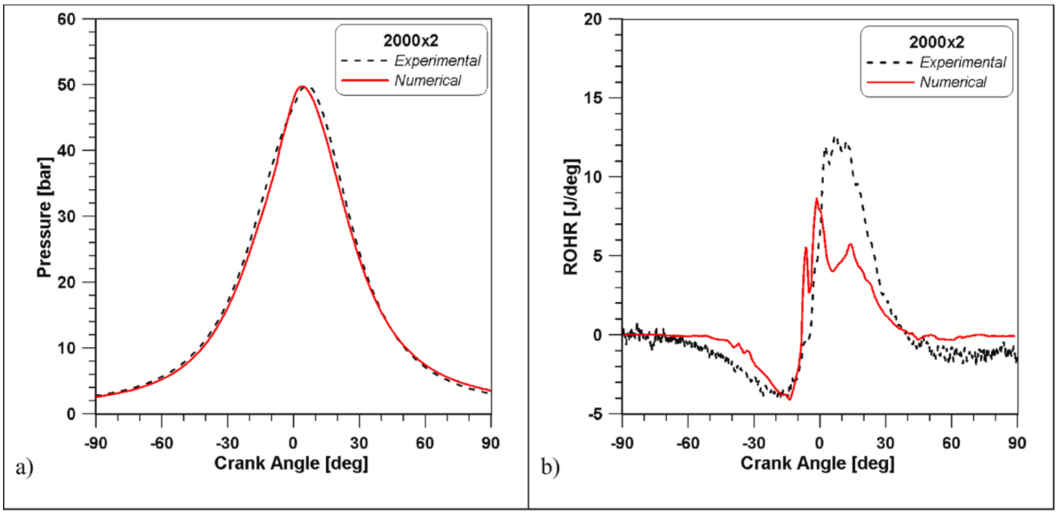

Figure 53. Comparison of pressure (a) and ROHR (b) for the 2000x2 case. **[32]**

From the figure above, that shows the 2000x2 case, almost the same consideration can be done regarding the comparison of experimental and simulated results, but in this situation the difference for the ROHR is higher and the problems explained previously for the other case here led to an increase of the differences. Furthermore, the first peak, occurring between 10 CAD bTDC and TDC and primarily attributed to diesel fuel ignition, and the second peak, which appears after TDC due to the main combustion event, are both accurately captured. Moreover, the numerical simulation reveals a distinct peak, likely resulting from the oxidation of the premixed air/hydrogen mixture originating from the crevice regions.

Another important comparison done in the article is related to the emissions. Indeed, the authors compared for the same cases the emissions of CO, CO_2, unburned hydrocarbons (UHC) and NO_x detected by the experiment and the one obtained from the simulation. The results are shown in Figure 54.

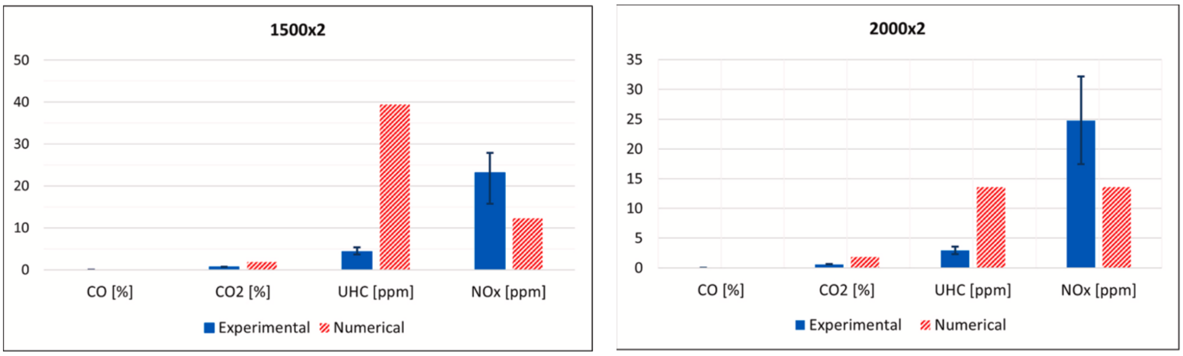

Figure 54. Comparison of the emissions for the case studies. **[32]**

The opinions on those results done by the authors are positive, CO emissions are not detected both by the experimental and simulated results, similar for CO_2 that are very low. Instead, for the UHC and NO_x, the first was overestimated by the model, meanwhile the other was underestimated. However, considering that the order of magnitude is the same, the authors consider the results acceptable.

SAGE

Moving to another combustion model, in this case one of the most used for the combustion in engines for the detection of autoignition.

For this reason, several authors adopted this model for the study of the combustion in H2ICEs, like Aljabri et. al [33], who compared SAGE and G-equation models for the study of the combustion in a cylinder coming from a 6-cylinder Volvo D13C500 heavy-duty diesel engine, that was converted to SI operation by replacing the diesel fuel injector with a spark plug and adding the port-fuel gas injectors in the intake manifold. The experiments were done with two main conditions, λ=2.5 and λ=3, and the validation of pressure is reported in Figure 55.

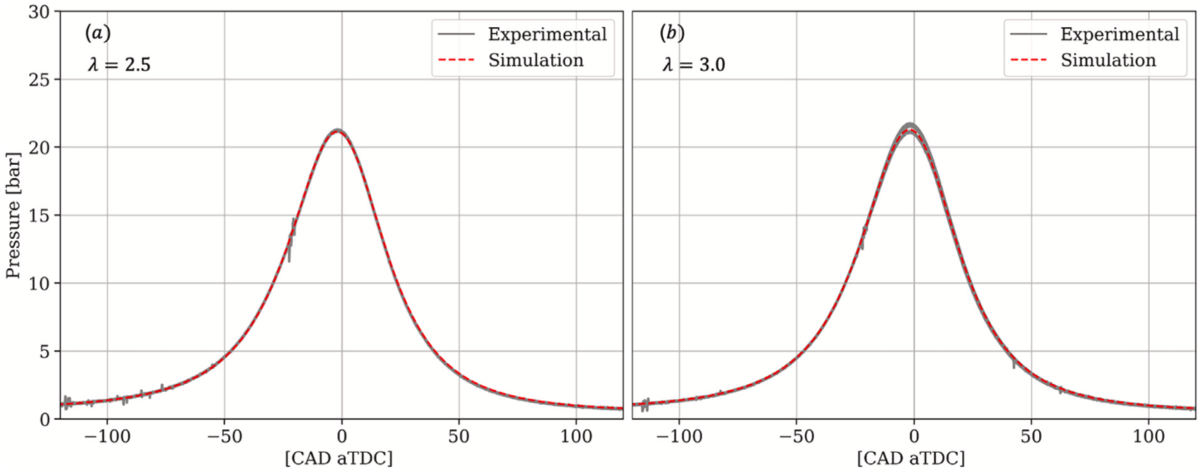

Figure 55. Validation of pressure for the two case studies. **[33]**

The results show for this case a good agreement with the experimental and the simulated data for both the lambda values.

Then, in this study, four different chemical kinetic mechanisms, that are the base of the SAGE model, have been analysed and compared with the experimental data for pressure and AHRR. The comparison is shown in the figure below.

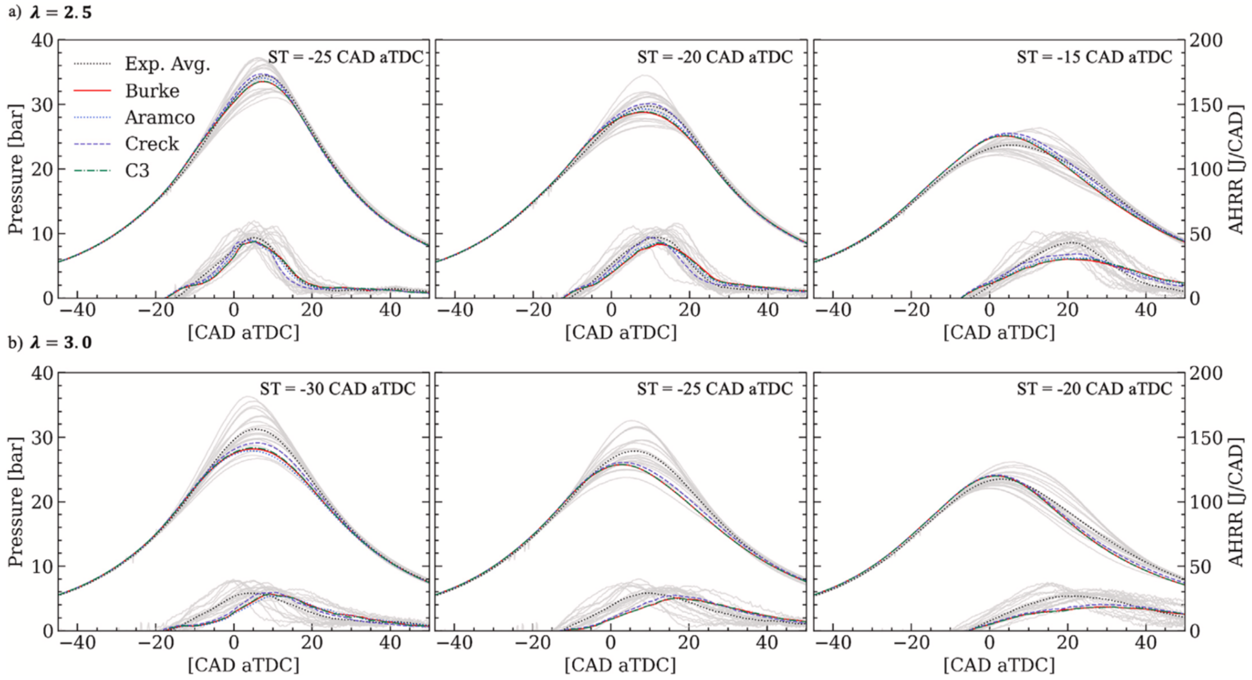

Figure 56. Comparison of pressure and AHRR for the different case studies and chemical kinetic mechanisms. **[33]**

The results presented above have come from 20 consecutive experimental cycles. In the λ=2.5 case, all the mechanisms show a good correlation with the average-experimental one for both pressure and AHRR. However, for the λ=3 case, all mechanisms under-predict both the peak pressure and the AHRR. The authors express that this trend manifests as a delayed AHRR, at earlier spark timings.

Other study that used SAGE model for the analysis of the combustion, and validate it, was done by Wei et. al [34] who considered a 4-cylinder 2.0L PFI H2ICE and validated the experimental data with the simulated one for an engine speed of 3000 rpm and different λ values: 0.6, 0.8 and 1.

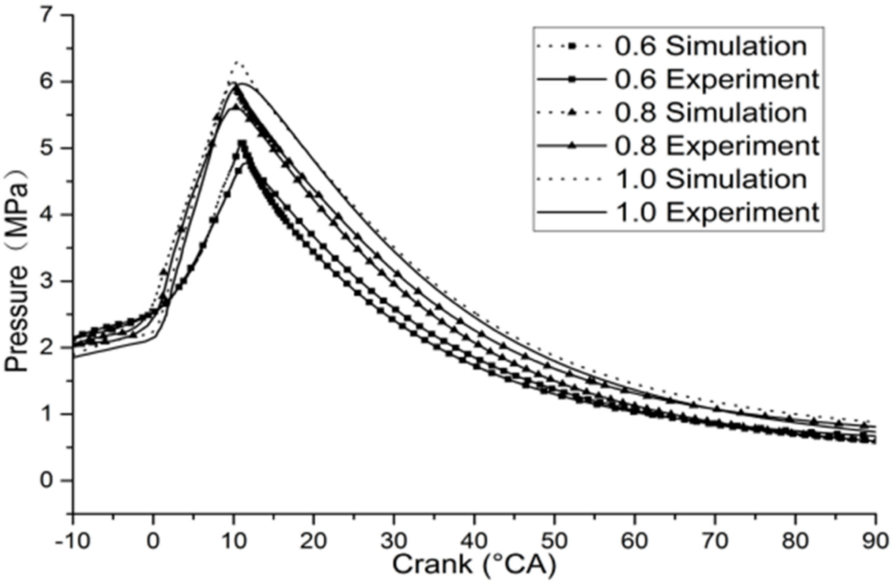

Figure 57. Pressure validation of experimental result with SAGE model. **[34]**

What can be seen from the figure above is that the simulated results match well the experimental ones, the peak value of pressure is slightly higher for the simulated results, leading to an average value, defined by the author, as 5%.

Similar to the articles reported for the G-equation model, also for the SAGE one there are some that validate it for dual fuel application, like Kumar et. al [23], already mentioned for the effect of the addition of different percentage of hydrogen in gasoline engine. In this section, the validation of the combustion model for the same case is discussed. The validation has been done, like the other articles, for in-cylinder pressure and HRR, both shown in Figure 58 with all the working conditions.

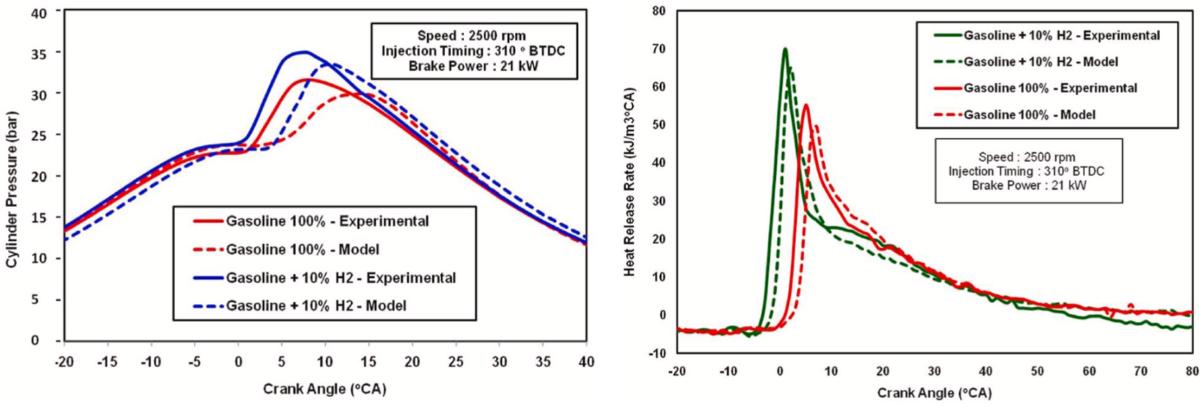

Figure 58. Validation of pressure and HRR. **[34]**

Starting with the analysis of the pressure diagram, there is a difference of about 2 bars pressure in both the cases as compared to the experimentally measured values, also experimental peak pressure is retarded compared to the predicted data. The reason given by the authors for these differences is related to the combustion model used and the assumption made for the fuel properties. Moreover, in the real combustion, there are variables that could affect the combustion itself, like turbulence, mixture distribution and intake change temperature. Variable changes that are not taken into account in the model.

Similar consideration could be done for the other diagram, related to the Heat Release Rate (HRR), that shows a slightly retarded behaviour with respect to the experimental one, but in conclusion the trends reach a good agreement with the experimental data, making the results acceptable.

ECFM

Lastly, the third combustion model considered for this thesis is the ECFM. The scientific works that adopts this model are not so much compared to the others, this is due to the more fitting of this model to other fuels, not hydrogen. But some of them are still present in the literature, like Knop et. al [35] that, indeed, modified the ECFM model to adapt it to work with hydrogen through the addition of a new laminar flame speed correlation and a new laminar flame thickness expression. The model has been validated with the experimental results for pressure and NO_x emissions. Figure 59 shows the validation done for two case studies, defined as *Cryogenic* and *Direct injection*. The first is a PFI engine set to test the model in almost homogeneous condition, the second is a direct injection (DI) engine, operated with a late injection strategy to validate the adaptation of the model to the most stratified experimental condition.

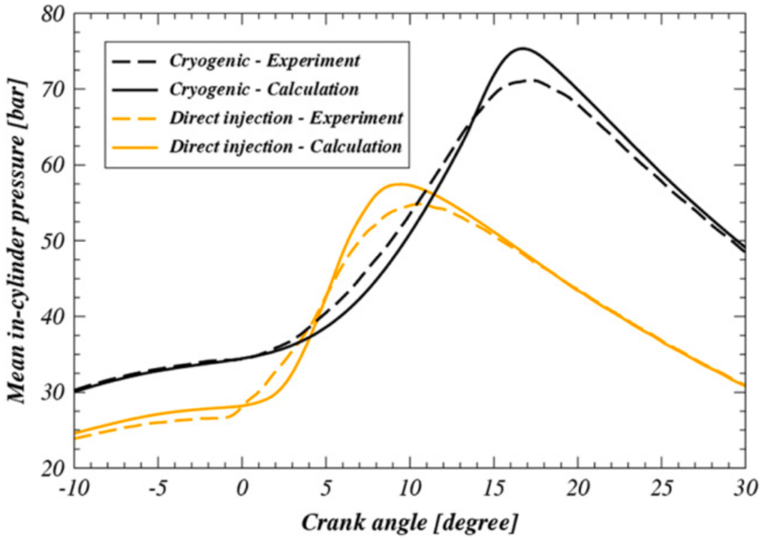

Figure 59. Pressure validation for the Cryogenic and DI cases. **[35]**

For the authors there is a good agreement with the experimental results for both cases. The overestimation before to combustion for the DI case is related, as explained by the author, to an uncertainty on the CR due the use of a theoretical one while the real should be lower, so fixing this problem reducing the compression ratio, this difference should be deleted. Then, the visible difference is also at the peak combustion phase, where the model develops a slow combustion in the beginning, and then speed it up at the peak point, leading to peak value higher that the experimental one.

Moving to a more recent study, Maio et. al [36] described the most important phenomena in SI H2ICEs using the ECFM model. The experimental results were obtained from a single-cylinder, 2.13L heavy-duty engine. The operating conditions used in the article are reported in Table 10.

Configuration	Spark Advance [CAD]	Air/Fuel Ratio [-]
PFI-MP3	18.2	2.4
PFI-MP9	13.4	2.4
PFI-MP15	7.3	2.4
PFI-MP4	16.8	2.4
PFI-MP7	12.6	2.1
PFI-MP10	8.8	1.8
DI-MP3	10.6	2.4
DI-MP5	8.1	2.1
DI-MP6	6.3	2.0

Table 10. Operating conditions, mainly divided by PFI with constant AFR, variable AFR and DI configuration. **[36]**

The validations done in the in-cylinder pressure for all the operating conditions are represented in Figure 60.

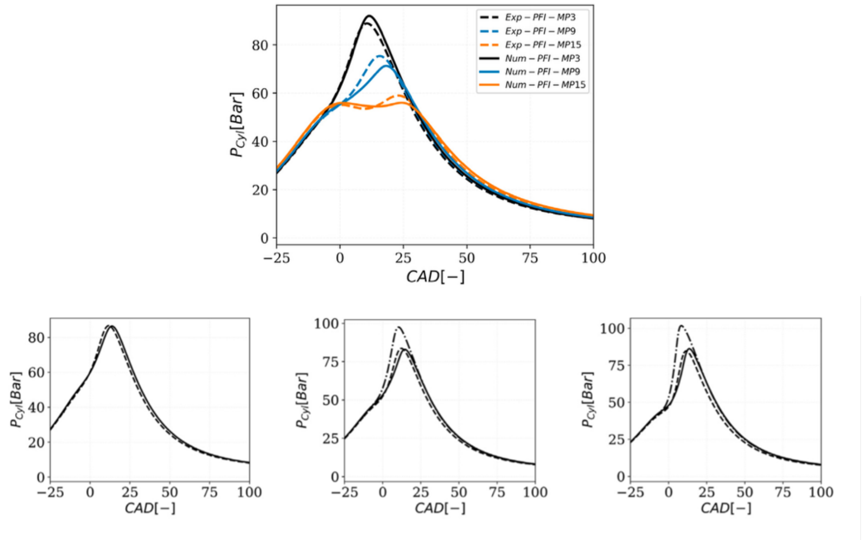

PFI-MP4 $\lambda = 2.4$ PFI-MP7 $\lambda = 2.1$ PFI-MP10 $\lambda = 1.8$

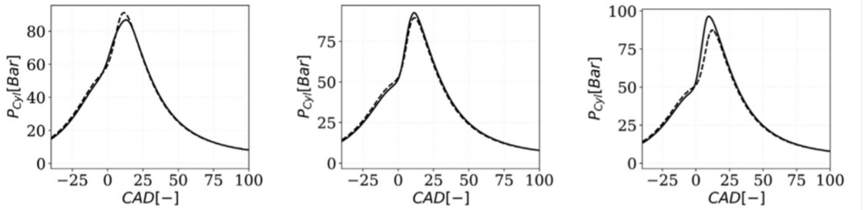

DI-MP3 $\lambda = 2.4$ DI-MP5 $\lambda = 2.1$ DI-MP6 $\lambda = 2.0$

Figure 60. Validation of all the operating conditions. Where not shown, the dashed line represents the experimental data, the continuous one the simulated ones and the dashed dotted line the simulated model with recalibration. **[36]**

Starting from the first group, the simulated results had a good match with the experimental ones using a calibration necessary for the model when hydrogen is used as fuel. Instead, for the other cases, the calibration has been done individually for each operating condition, that's why in the figure above, there are both the line representing the simulated results with a reference calibration (dashed lines) and the one that show the calibration done for each condition (dashed dotted). In particular, this work was necessary for the PFI condition with variation of λ.

The necessity of recalibration did for those cases is explained in the article as *"attributed to the absence of the impact of differential diffusion on the turbulent flame speed in ECFM"*. Also, this phenomenon is particularly significant for the H_2 combustion.

For the DI group of operating conditions, the model follow the experimental results in a good way, with main differences in the DI-MP6 case, where, according to the authors, there is an overestimation of the turbulent combustion velocity, like the PFI with varying AFR cases. Moreover, the use of the reference re-calibration led to an overestimation of the combustion speed for the richer points, that in the DI case is mitigated due to the similar mixture stratification profile produced by the H_2 injector, for all the working points.

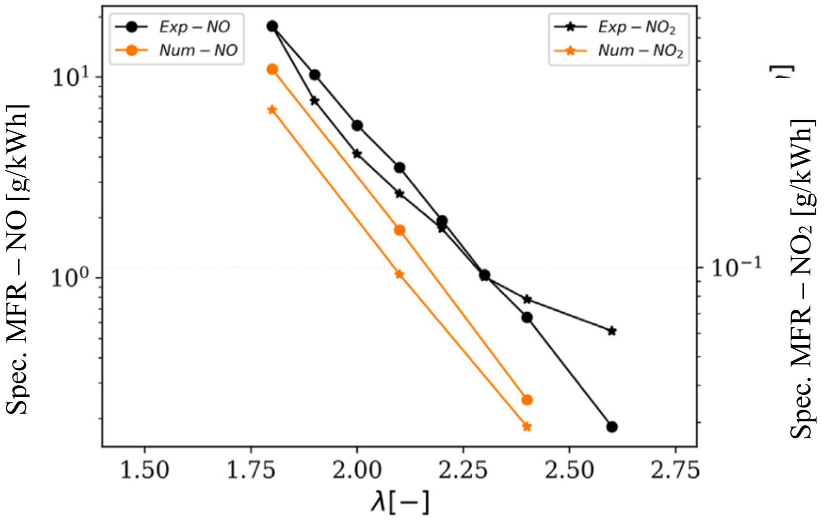

Figure 61. NO and NO_2 emissions, mass flow rate (MFR) validation for PFI cases. **[36]**

Lastly, Figure 61 represents the validation done also for the NO and NO_2 emissions. In particular the mass fuel rate (MFR) of the PFI cases, where, as visible from the figure, both NO and NO_2 predictions are under-predicted. NO is under-predicted by a factor between almost 2 and 3 while NO_2 by a factor between 2 and 5. This discrepancy is motivated by the authors as some limitation of NO_x prediction of the model.

Something interesting explained in the article is that, if increasing λ from 1.8 to 2.5, the emissions of NO and NO_2 would decrease by at least one order of magnitude, this shows the importance in emissions for the air/fuel ratio, that do not influence directly the emissions, but the equivalence ratio that is direct variable that control the emissions.

The last validation of the ECFM model that will be analysed was done by Sola et. al [37] who studied the influence of hydrogen in a SI Rapid Compression Expansion machine (RCEM), equipped with a passive pre-chamber. The study has been done both experimentally, with the use of an optical access on the RCEM, and through simulation with the application of the ECFM model for the combustion phase. In particular, the engine used comes from a horizontal, water-cooled, four-stroke, single-cylinder diesel engine (Yanmar NFD170).

The experiments have been done with two values of equivalence ratios: stoichiometric conditions (φ =1) and lean conditions ($\varphi = 0.625$). then, for the simulation, two chemical kinetic mechanisms have been chosen for the analysis, C3 V3.5 and GRI-Mech 3.0, but the comparison of this two will not be analysed. The main focus will be related to the validation of the ECFM model with the experimental data.

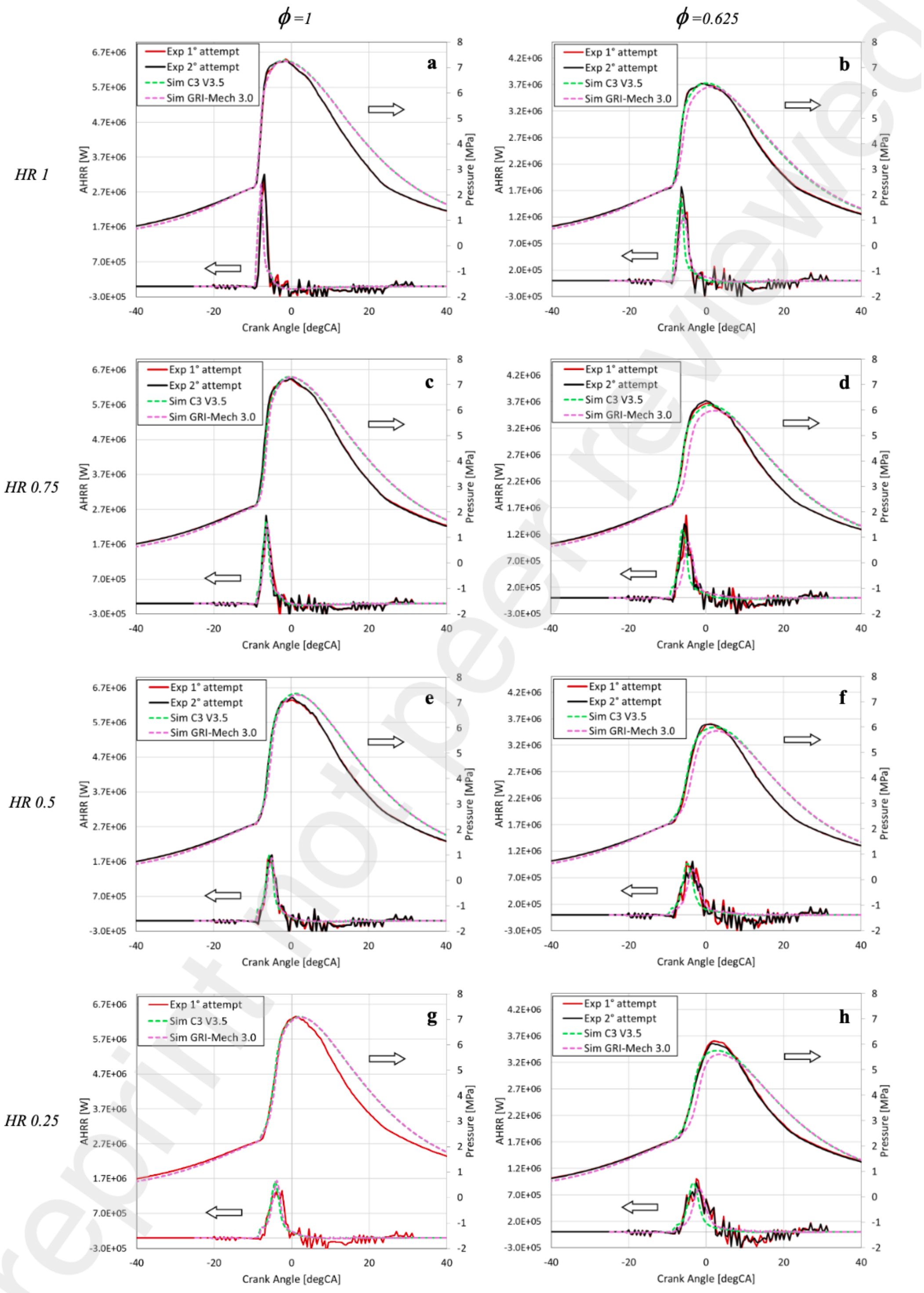

Figure 62. Validation of in-cylinder pressure and AHRR for all the kinetic mechanism and equivalent ratio used. **[37]**

The figure above shows the validation of in-cylinder pressure and AHRR for all the cases considered in the article, also there are different hydrogen ratios (HR), expressed in percentage in volume, considered and compared. Generally, the authors consider acceptable the correlation between experimental and simulated results. However, the best agreement is reached for the test cases in stoichiometric conditions. In particular, the major difference, present in the cases with lean mixture, is increased in the low hydrogen tests, when the mixture in completely in dependence on methane flame propagation.

Main differences could be seen for all the mechanisms used in the prediction of the AHRR, in particular for the oscillation present before and after the peak related to the ST.

Another significant parameter validated in the article is the Mass Fuel Burned (MFB), here reported in Figure 63.

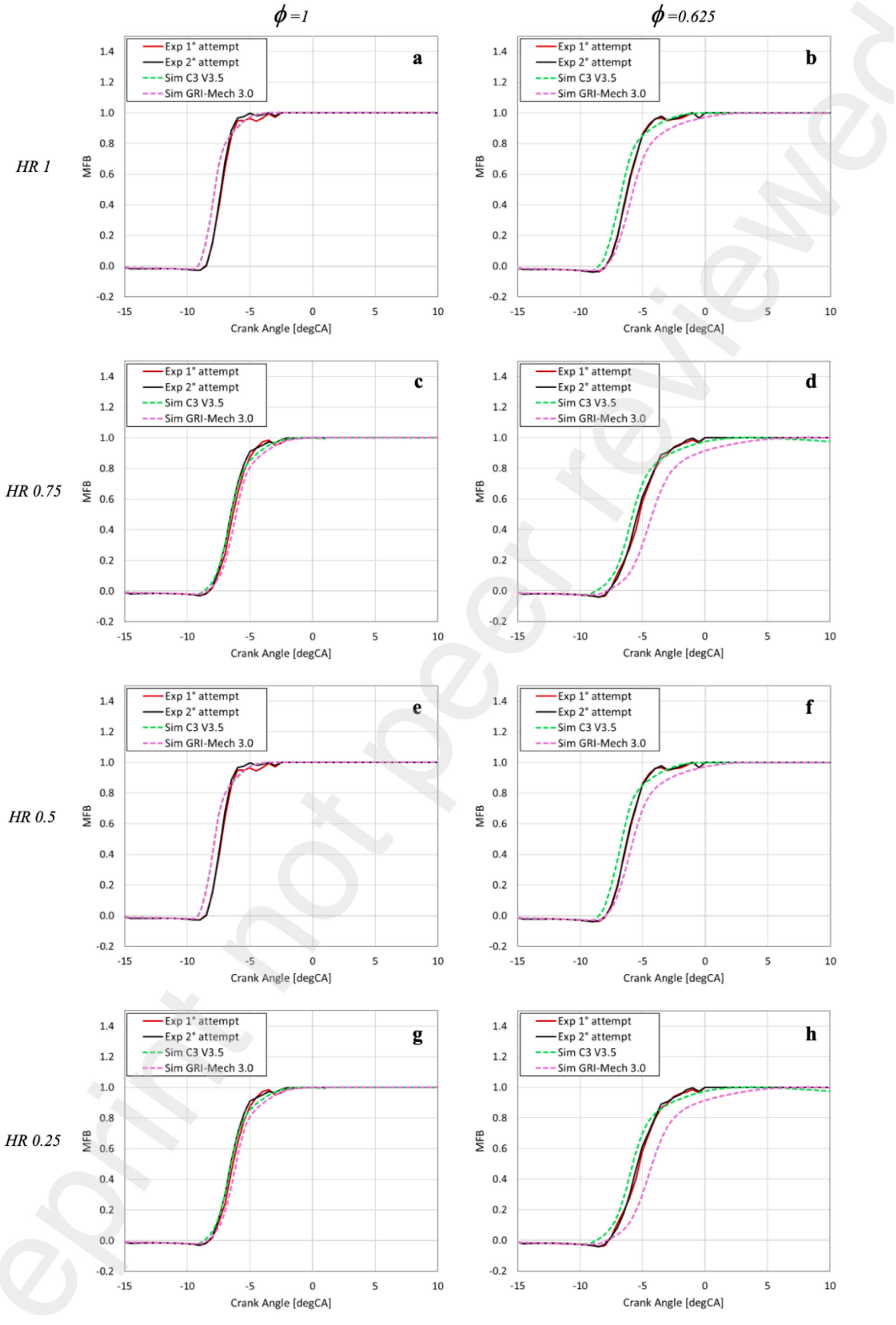

Figure 63. Validation MFB for all the kinetic mechanism and equivalent ratio used. **[37]**

Also in this case, the correlation between experimental and simulated results could be considered acceptable for this parameter.

Lastly, in the article, significant chart has been shown related to the validation of the data. Those charts are reported in Figure 64 and 65, that compare different elements between experiment and simulations.

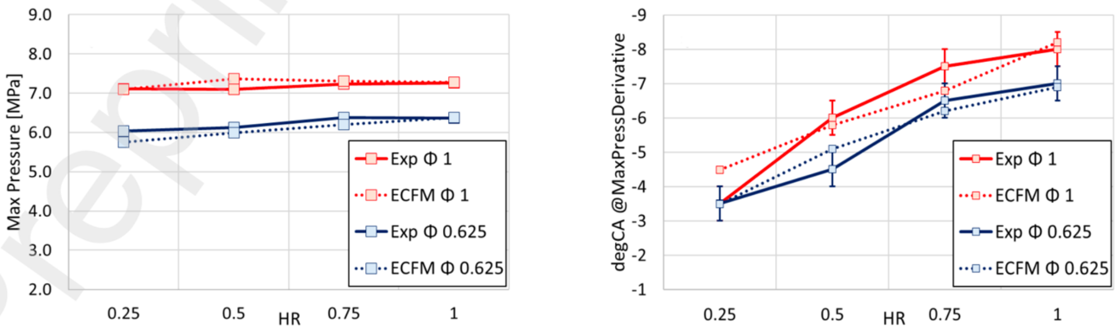

Figure 64. Comparison of experimental and simulated results for max pressure and CA corresponding to the max pressure, on the left, and the angle corresponding to the max pressure **[37]**

The figure above compares experimental and simulated data at the variation of equivalence ratio and hydrogen concentration, also for this study there is no significant discrepancy between the results. The main consideration done by the authors is that, for the max pressure predicted, in the stoichiometric case, the model predicts in a good way the pressure, instead the leaner case shows higher differences. Different considerations were done for the right chart, where for both curves the simulations predict the same trends, but the values are different and in a different way between the two conditions.

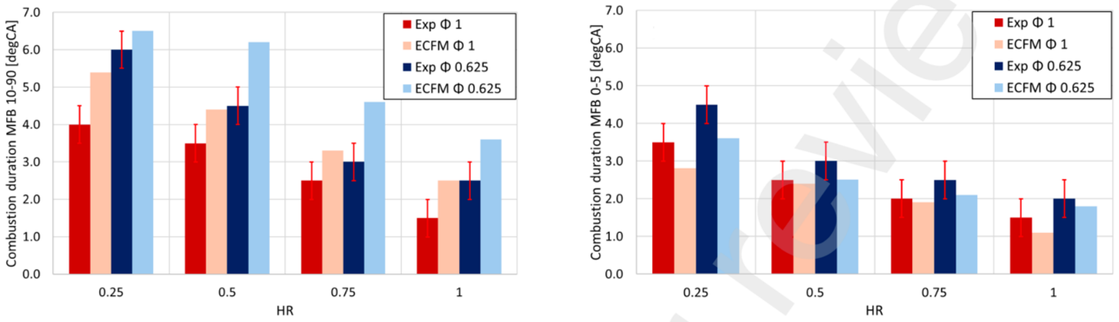

Figure 65. Comparison of experimental and simulated results for combustion duration and initial moment of flame propagation. **[37]**

Lastly, Figure 65 shows the comparison of the combustion duration for both simulated and experimental results. In particular, related to the duration in CAD between the points corresponding to 10% and 90% of the mass fraction burnt, to the left, and the combustion duration between two mass fractions burnt, to the right. The authors explains that for those parameters the differences between experimental and simulated results are higher partially due to the low experimental resolution during pressure acquisition. However, the trends of the different simulation have a good agreement with the experimental data, leading to the acceptance of the results.

Numerical setup

In this section, a description of the simulation settings and models used will be defined. Also, the aim of the thesis, with all the case studies will be analysed.

Combustion models definition

Now a description of the combustion models used, that are the ones already listed in the *"Validation of CFD combustion models used in hydrogen simulations"* section, will be done. The equations and features of the different models come from the CONVERGE Manual [38].

G-equation

Starting with the G-equation model, it’s mainly used to simulate premixed combustion, and it’s written in terms of the flame front tracking variable *G* and a progressive variable *C*.
This model is based on the tracking of the location of the flame front via the transport equation. The parameter G indicated the distance to the flame front and in particular:

- If G=0, this means that the flame front is in that location.
- If G<0, this means that the region is unburned.
- If G>0, the region is burned.

Figure 66 shows the representation of this.

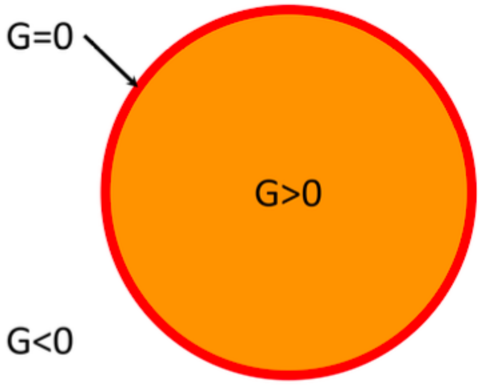

Figure 66. Image representative of the meaning of the parameter G **[38]**

This model, in the CONVERGE manual [38], is based on an important assumption, that the premixed turbulent combustion occurs in a *corrugated framelet* or in a *thin reaction zone regime*. This refers to how turbulent flames behaves under different conditions. When fuel and oxidiser are premixed before ignition and turbulence is present, the way the flame behaves depend on the turbulence intensity, representing how strong the turbulence is, and the flame thickness, how thick the reaction zone is. These elements define several regimes of turbulent combustions, that, following the classification done by the Peters diagram, a source of the G-equation model, are:

- Wrinkled framelet.
- Corrugated framelets.
- Thin reaction zones.
- Broken reaction zones.

The assumption done in the CONVERGE software [38] is that this model is in the second or the third of those regimes, that in particular have the following properties:

- In the *corrugated framelet regimes* the flame structure is similar to a laminar flame locally, the turbulence wrinkles the flame surface but does not penetrate the internal flame structure and the flame thickness is smaller than the lowest value in the Kolmogorov scale.
- In the *thin reaction zone regime*, the turbulence becomes stronger and small eddies interact with the preheat zone of the flame, however the reaction zone remains thin and is not fully disrupted. Also, the flame structure is slightly thickened, but the flame front is well defined.

The G-equation model works well in those two conditions but could be done some correction for the second regime to account for flame thickening.
After considering the necessary assumptions, the turbulent flame front could be tracked by solving for the mean of the parameter *G* the following transport equation.

$$\frac{\partial \rho \tilde{G}}{\partial t} + \frac{\partial \rho \widetilde{u_i G}}{\partial x_i} = -\rho D_t' \tilde{\kappa} \left| \frac{\partial \tilde{G}}{\partial x_i} \right| + \rho_u S_t \left| \frac{\partial \tilde{G}}{\partial x_i} \right| \tag{1}$$

and

$$\frac{\partial \rho \widetilde{G''^2}}{\partial t} + \frac{\partial \rho \tilde{u}_i \widetilde{G''^2}}{\partial x_i} = \frac{\partial}{\partial x_i}\left(\rho D_t \frac{\partial \widetilde{G''^2}}{\partial x_i} \right) + 2 \rho D_t \frac{\partial \tilde{G}}{\partial x_i} \frac{\partial \tilde{G}}{\partial x_i} - c_s \rho \widetilde{G''^2} \frac{\varepsilon}{k} \tag{2}$$

Where:

- S_t is the turbulent flame speed.
- ρ_u is the unburned density.
- k is the mean flame front curvature.
- ϵ is the turbulent dissipation.

Those equations define two version of the G-equation model, the first, defined by the first equation, do not solve the variance on *G* and is called in the software "*Peters flame speed model without G-equation prime*". The second, instead, solve the variance of *G* and is called "*Peters flame speed model with G-equation prime*".
For large eddies simulation, in the equation 2 an additional term, that compensate for kinematic restoration is considered.

$$\frac{\partial \rho \widetilde{G''^2}}{\partial t} + \frac{\partial \rho \widetilde{u_\iota} \widetilde{G''^2}}{\partial x_i} = \frac{\partial}{\partial x_i}\left(\rho D_t \frac{\partial \widetilde{G''^2}}{\partial x_i}\right) + 2\rho D_t \frac{\partial \tilde{G}}{\partial x_i}\frac{\partial \tilde{G}}{\partial x_i} - c_s \rho \widetilde{G''^2}\frac{\varepsilon}{k} - \rho\widetilde{\omega} \tag{3}$$

with

$$\widetilde{\omega} = c_2 (s_l \overline{\sigma})^2 \frac{C_S \Delta}{v''_\Delta} \tag{4}$$

Where:

- s_l is the laminar flame speed.
- C_S is the Smagorinsky constant.
- Δ is the filter width.
- v''_Δ is the sub-grid velocity fluctuation.
- c_2 is a proportionality factor evaluated as $c_2 = \frac{2}{Sc_\Delta \mathrm{b}_1^2}$, with b_1=2.

Going back on equation 1, the right-hand side is attributed to the averaged turbulent mass burning rate. Instead, the first term indicates the influence of curvature on the flame front, in particular the mean flame front curvature is defined as

$$\tilde{\kappa} = -\frac{\partial}{\partial x_i}\left(\frac{\partial \tilde{G} /\, \partial x_i}{\left|\partial \tilde{G} /\, \partial x_i\right|}\right) \tag{5}$$

Instead, the turbulent diffusion term D_t, in case of "*Peters flame speed model without G-equation prime*" is

$$D_t' = \frac{c_\mu k^2}{S_c \epsilon} \tag{6}$$

Where:

- k is the turbulent kinetic energy.
- c_μ empirical constant from the k-ε turbulence model. It calibrates the magnitude of turbulent viscosity or diffusivity.
- S_c is the turbulent Schmidt number, which is the ratio of turbulent viscosity to turbulent diffusivity. It characterizes how efficiently turbulence transports scalar quantities.

Instead, when the variance of *G* is solved, the turbulent diffusion term is defined as

$$D_t' = \sqrt{c_s \frac{kc_\mu}{2S_C} \widetilde{G''^2}} \tag{7}$$

To solve the original transport equation the level set approach is used [39]. It’s a numerical technique for tracking interfaces and shapes. This method represents a moving interface as the zero level set of a higher-dimensional function, typically denoted by $\phi(x,t)$. Instead, of tracking the interface directly, the function evolved over time.
The interface a time t is represented as:

$$\Gamma(t) = \{x, \phi(x,t)\} = 0 \tag{8}$$

Where ϕ is initialized as a signed distance function:

- $\phi(x,0)$=distance to the interface.
- ϕ>0 means outside.
- ϕ<0 means inside.

The evolution ϕ is governed by the Hamilton-Jacoby type ODE:

$$\frac{\partial \phi}{\partial t} + F\left|\overrightarrow{\nabla\phi}\right| = 0 \tag{9}$$

Where:

- ϕ is the set level function.
- F is the speed function, which can depend on position, curvature and time.
- $\left|\overrightarrow{\nabla\phi}\right|$ is the gradient magnitude of ϕ.

The set level method is well-suited for the G-equation model for the necessity to maintain and track the flame front.
Considering this implementation, the mean flame front position is defined as the location where $G(x,t) = 0$ in the solution of the transport equation. The interface divides the flow fields in the unburned region, defined by G<0, and the burned region, defined for G>0. Outside the flame surface, the equation that has to be satisfy is the following

$$\left|\frac{\partial G}{\partial x_i}\right| = 1 \tag{10}$$

SAGE

The second model that will be analysed is the SAGE model [38], that is a detailed chemical kinetics solver which uses a series of chemical reaction mechanism.
A chemical reaction mechanism is a set of elementary reactions that describe an overall chemical reaction, and they change depending on the fuel for the combustion. The SAGE model calculates the reaction rate for each elementary reaction while the CFD solver solves the transport equation.
More specifically, a multi-step chemical reaction mechanism could be written in the following form:

$$\sum_{m=1}^{M} \nu'_{m,i} \mathcal{X}_m \Leftrightarrow \sum_{m=1}^{M} \nu''_{m,i} \mathcal{X}_m \quad for\ i = 1,2,\dots,I \tag{11}$$

Where:

- $\nu'_{m,i}$ and $\nu''_{m,i}$ are the stochiometric coefficients for the reactants and products, respectively, for the species *m* and reaction *i*. *I* is the total number of reactions.
- $\mathcal{X}_m$ is the chemical symbol for species *m*.

Then, the net production rate of species *m* is given by

$$\dot{\omega}_m = \sum_{i=1}^{I} \nu_{m,i} q_i \, form = 1,2,\dots,M \tag{12}$$

where *M* is the total number of species and

$$\nu_{m,i} = \nu''_{m,i} - \nu'_{m,i} \tag{13}$$

The rate of progress parameter q_i for the i^{th} reaction is

$$q_i = k_{i,f} \prod_{m=1}^{M} [\mathcal{X}_m]^{\nu'_{m,i}} - k_{i,r} \prod_{m=1}^{M} [\mathcal{X}_m]^{\nu''_{m,i}} \tag{14}$$

In the previous equation, $[\mathcal{X}_m]$ is the molar concentration of species *m*, $k_{i,r}$ are the forward and reverse rate coefficients for reaction *i*. In the SAGE model, the forward rate coefficient is expressed by the Arrhenius equation as

$$k_{i,f} = A_i T^{\beta_i} exp\left(\frac{-E_i}{RT}\right) \tag{15}$$

where:

- A_i is the pre-exponential factor.
- β_i is the temperature exponent.
- E_i is the activation energy.
- R is the idea gas constant.

Moreover, the reverse rate coefficient could be calculated in a similar way following the previous equation, or from the equilibrium coefficient $K_{i,c}$.

$$k_{i,r} = \frac{k_{i,f}}{K_{i,c}} \tag{16}$$

The equilibrium coefficient $K_{i,c}$ is determined from the thermodynamic properties and is defined as

$$K_{i,c} = K_{i,p} \left(\frac{P_{atm}}{RT}\right)^{\sum_{m=1}^{M} \nu_{mi}} \tag{17}$$

where:

- P_{atm} is the atmospheric pressure.
- R is the ideal gas constant.
- T is the temperature.

Instead, the equilibrium constant is defined as

$$K_{i,p} = exp\left(\frac{\Delta S_i^0}{R} - \frac{\Delta H_i^0}{RT}\right) \tag{18}$$

Where Δ referes to the change that occurs in passing completely from reactants to products in the i^{th} reaction, specifically:

$$\frac{\Delta S_i^0}{R} = \sum_{m=1}^{M} \nu_{m_i} \frac{S_m^0}{R} \tag{19}$$

and

$$\frac{\Delta H_i^0}{RT} = \sum_{m=1}^{M} \nu_{m_i} \frac{H_m^0}{RT} \tag{20}$$

where:

- S is the entropy.
- H is the enthalpy.

With all the equation and parameters defined above, the SAGE model defines and solve the governing equations for mass and energy conservation for a given computational cell. The governing equation for the mass is the following.

$$\frac{d[X_m]}{dt} = \dot{\omega}_m \tag{21}$$

The governing equation for the energy instead is

$$\frac{dT}{dt} = \frac{\frac{dP}{dt} - \sum_m\left(\bar{h}_m \dot{\omega}_m\right)}{\sum_m\left([X_m]\bar{c}_{p,m}\right)} \tag{22}$$

where:

- $\dot{\omega}_m$ is the net production rate of species m and has been previously defined.
- $\bar{h}_m$ is the molar specific enthalpy of species *m*.
- $\bar{c}_{p,m}$ is the molar constant-pressure specific heat of species *m*.

The previous equation refers to the constant-volume combustion, in case of constant-pressure combustion the numerator of the RHS of the equation become just $\sum_m\left(\bar{h}_m \dot{\omega}_m\right)$.
It is important to note that the temperature obtained from previous equation 22 is used to update only the rate coefficients and is not used to update the cell temperature. The cell temperature, instead, is updated after the detailed chemistry calculation has converged using the computed species concentrations.

ECFM

Lastly, the ECFM model is a premixed combustion model used in particular for spark-ignite engines. This model is based on the definition of the flame surface density ($\sum$). It represents the amount of flame surface area per unit volume, in particular it quantifies how folded and stretched the flame front is due to turbulence. It's defined as

$$\sum = \frac{A_f}{V} \tag{23}$$

Where:

- A_f is the flame surface area.
- V is the volume containing the flame surface.

To determine the $\sum$, the ECFM model uses the fuel/air equivalence ratio in fresh gases, the composition and the temperature near the flame. The resulting $\sum$ is used to describe large scale burned/unburned stratification.
For the determination of the flame surface density the model is based on the following transport equation:

$$\frac{\partial \Sigma}{\partial t} + \frac{\partial u_i \Sigma}{\partial x_i} = \frac{\partial}{\partial x_i}\left(\frac{\mu}{Sc} \frac{\partial \left(\Sigma / \bar{\rho} \right)}{\partial x_i} \right) + \left(At_{sgs} + At_{res} + Curv_{sgs} \right) \sum - D + P_k \tag{24}$$

where:

- μ is the molecular viscosity.
- S_c is the Schmidt number.
- At_{sgs} is the flame surface production by turbulent stretch.
- At_{res} is the production by the mean flow dilatation.
- $Curv_{sgs}$ models the effect of the flame thermal expansion and curvature.
- D is destruction due to consumption.
- P_k is the source term.
- ρ_u is the density of the unburned gas.
- s_l is the laminar flame speed.
- $\tilde{c}$ is the mass progress variable.
- $\bar{c}$ is the volume progress variable.

In the previous transport equation, some elements are not variables but depend on the mass or volume variables. In the following they are defined.

$$At_{sgs} = \alpha K_t, \quad At_{res} = \frac{2 \partial \tilde{u}_i}{3 \partial x_i}, \quad Curv_{sgs} = \frac{2}{3} \frac{\rho_u}{\rho_b} s_l \frac{1 - \tilde{c}_\Sigma}{\tilde{c}_\Sigma} \Sigma, \quad D = \beta s_l \frac{\Sigma^2}{1 - \bar{c}}$$

The following image shows the scheme of the flame surface density progress variable $\tilde{c}_\Sigma$.

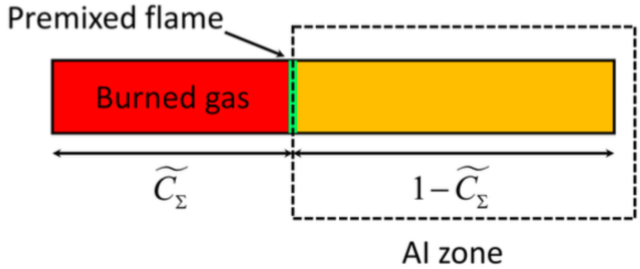

Figure 67. Scheme of the flame surface density progress variable **[38]**

The mass progress variable is defined as

$$\tilde{c} = \frac{\sum_i \tilde{Y}_i^b}{\sum_i \tilde{Y}_i^u + \sum_i \tilde{Y}_i^b} \tag{25}$$

Moreover, the burned gas fraction from autoignition $\tilde{c}_{ai}$ is defined as

$$\tilde{c}_{ai} = \frac{\tilde{Y}_{N2}^{b,ai}}{\tilde{Y}_{N2}^{b,ai} + \tilde{Y}_{N2}^{b,\Sigma}} \tilde{c} \tag{26}$$

Where $\tilde{Y}_{N2}^{b,ai}$ and $\tilde{Y}_{N2}^{b,\Sigma}$ represent the N_2 mass fraction from autoignition and premixed flame oxidation, respectively.

Going on, the autoignition progress variable c_{ai} is calculated as

$$c_{ai} = \frac{\tilde{c}_{ai}}{1 - \tilde{c} + \tilde{c}_{ai}} \tag{27}$$

Finally, the flame surface density progress variable $\tilde{c}_{\Sigma}$ and volume progress variable $\tilde{c}$ could be calculated in the following way:

$$\tilde{c}_{\Sigma} = \tilde{c} - \tilde{c}_{ai} \tag{28}$$

$$\overline{c} = \frac{\rho}{\rho_b} \tilde{c} \tag{29}$$

Lastly, the element that should be defined is the source term, that for the simulations done follow the Imposed Stretch Spark Ignition Model (ISSIM) and will be defined in the section related to the results analysis.

Software setup

In the following section the set-up, engine dimensions and parameters used for the simulations will be explained. Considering that the combustion model will be changed based on the simulation, here only the most important common parts will be explained.

Engine dimensions

Starting with the engine dimensions, Table 11 will show all of them.

PART	DIMENSION [m]
CYLINDER BORE	0.092
STROKE (2 TIMES THE CRANK RADIUS)	0.085
CONNECTING ROD LENGTH	0.16667
CRANK OFFSET	0.0037
SWIRL RATIO	0
SWIRL PROFILE	3.11

Table 11. Main geometrical engine components.

Moreover, for all the simulations done the engine speed used was maintained constant at 1500 rpm.

Simulation parameters

Moving to the parameters that define the simulations themselves, in Figure 68 all the time setting are reported.

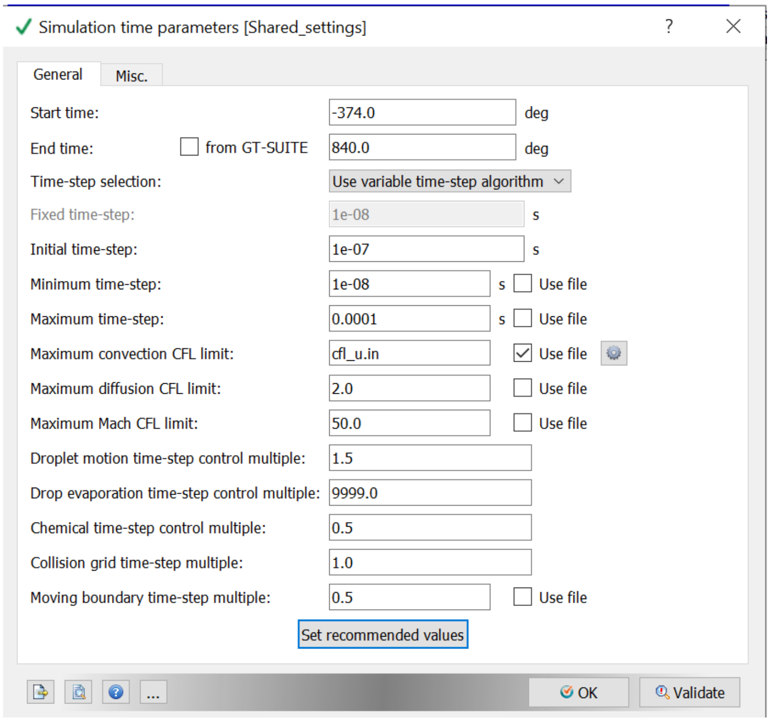

Start time: -374.0 deg

End time: ☐ from GT-SUITE 840.0 deg

Time-step selection: Use variable time-step algorithm

Fixed time-step: 1e-08 s

Initial time-step: 1e-07 s

Minimum time-step: 1e-08 s ☐ Use file

Maximum time-step: 0.0001 s ☐ Use file

Maximum convection CFL limit: cfl_u.in ☑ Use file

Maximum diffusion CFL limit: 2.0 ☐ Use file

Maximum Mach CFL limit: 50.0 ☐ Use file

Droplet motion time-step control multiple: 1.5

Drop evaporation time-step control multiple: 9999.0

Chemical time-step control multiple: 0.5

Collision grid time-step multiple: 1.0

Moving boundary time-step multiple: 0.5 ☐ Use file

Figure 68. Simulation time parameters.

Those parameters are the same used for all the simulations. Regarding the start and end time, the necessity of start very earlier and end lately is due to the fact that, for that type of simulations, with the TDC at 0 CAD, the results obtained from the first cycle could not be considered valid, they are needed for calibration, so at least a second one is needed, and those results will be analysed.

Boundary conditions

The boundary conditions related to the engine studied are reported in this section, however, before must be defined the regions in which the engine itself have been divided, that are:

- Cylinder.
- Intake.
- Exhaust.
- Injector.

All of them have been assigned to a boundary. In the following table all the boundary conditions with the relative type and region are reported.

BOUNDARY	TYPE	REGION
HEAD	Stationary WALL	CYLINDER
LINER	Stationary WALL	CYLINDER
PISTON	Translating WALL	CYLINDER
INTAKE PORT	Stationary WALL	INTAKE
EXHAUST PORT	Stationary WALL	EXHAUST
EXHAUST VALVE TOP	Translating WALL	EXHAUST
EXHAUST VALVE ANGLE	Translating WALL	EXHAUST
EXHAUST VALVE BOTTOM	Translating WALL	CYLINDER
INTAKE VALVE TOP	Translating WALL	INTAKE
INTAKE VALVE ANGLE	Translating WALL	INTAKE
INTAKE VALVE BOTTOM	Translating WALL	CYLINDER
INTAKE	INFLOW	INTAKE
EXHAUST	OUTFLOW	EXHAUST
H2 INTAKE	INFLOW	INJECTOR
PISTON SKIRT	Translating WALL	CYLINDER
INJECTOR HEAD	Stationary WALL	CYLINDER
TUMBLE FIXTURE	Stationary WALL	INTAKE
INJECTOR BODY	Stationary WALL	INJECTOR
PARK PLUG	Stationary WALL	CYLINDER

Table 12. Boundary conditions.

Region initialization and events

The region definition has already been explained before. However, this section is also related to the initialization of them, so the initial conditions that have been set are listed in the table below.

REGION	INITIAL PRESSURE [Pa]	INITIAL TEMPERATURE [K]	TURBULENT KINETIC ENERGY $[m^2/s^2]$	TURBULENT DISSIPATION $[m^2/s^3]$	SPECIES (mass fraction)
CYLINDER	103909.9	800	62.02	17183.4	H_2O (0.127641) N_2 (0.759002) O_2 (0.113357)
INTAKE	101229	309.15	62.02	17183.4	N_2 (0.77) O_2 (0.23)
EXHAUST	93275.1	800	62.02	17183.4	H_2O (0.127641) N_2 (0.759002) O_2 (0.113357)
INJECTOR	107957	309.15	62.02	17183.4	H_2 (1)

Table 13. Region and initial conditions.

Next the events have been set, in particular the opening and closure of the valves and injector. This lats one will change during the simulation, here is shown the timing for the standard condition.

- Intake valve opening: -374 CAD
- Intake valve closure: -140 CAD
- Exhaust valve opening: 130 CAD
- Exhaust valve closure: 364 CAD
- Injector opening: -137 CAD
- Injector closure: -103.5 CAD

As already explained before, the simulation needs at least two cycles, so the data provided in the list before should be shift by 720 degrees in relationship to the second cycle simulated.

Physical models

Regarding the physical models, the combustion one, will be varied in the simulations. However, all the simulations done have in common the combustion region definition, that has the following settings:

- It's cyclic
- The period will be of 720 degrees
- Start time: -30 CAD
- End time: 130 CAD

Another setting in common was the turbulence model used, in particular it was the RANS k-ϵ model, all the model's parameters are shown in the Figure below.

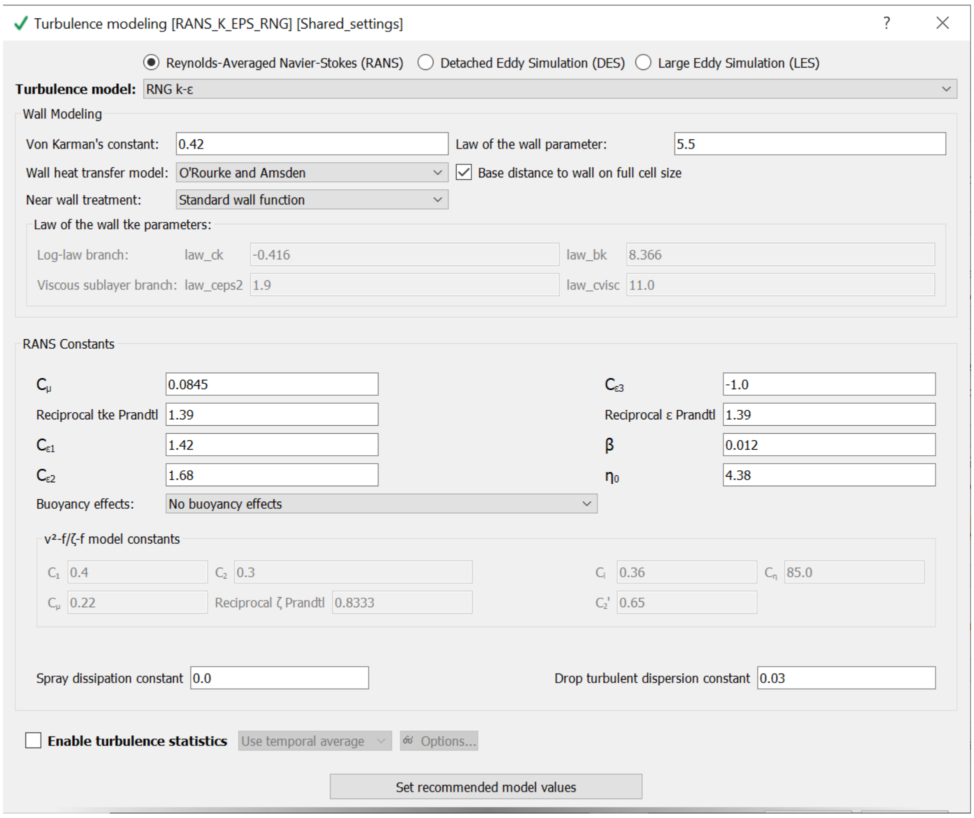

✓ Turbulence modeling [RANS_K_EPS_RNG] [Shared_settings]

● Reynolds-Averaged Navier-Stokes (RANS) ○ Detached Eddy Simulation (DES) ○ Large Eddy Simulation (LES)

Turbulence model: RNG k-ε

Wall Modeling

Von Karman's constant: 0.42

Law of the wall parameter: 5.5

Wall heat transfer model: O'Rourke and Amsden

☑ Base distance to wall on full cell size

Near wall treatment: Standard wall function

Law of the wall tke parameters:

Log-law branch: law_ck -0.416 law_bk 8.366

Viscous sublayer branch: law_ceps2 1.9 law_cvisc 11.0

RANS Constants

C_μ 0.0845

$C_{\varepsilon 3}$ -1.0

Reciprocal tke Prandtl 1.39

Reciprocal ε Prandtl 1.39

$C_{\varepsilon 1}$ 1.42

β 0.012

$C_{\varepsilon 2}$ 1.68

η_0 4.38

Buoyancy effects: No buoyancy effects

v²-f/ζ-f model constants

C_1 0.4 C_2 0.3 C_l 0.36 C_η 85.0

C_μ 0.22 Reciprocal ζ Prandtl 0.8333 C_2' 0.65

Spray dissipation constant 0.0

Drop turbulent dispersion constant 0.03

☐ **Enable turbulence statistics** Use temporal average

Table 14. Turbulence model settings.

Grid control

Last setting that will be analysed is the gid control and the mesh definition. Starting with the base mesh size, it was defined as 0.004 m in the three directions.

Then, to capture the combustion of the hydrogen both Adaptive Mesh Refinement (AMR), that could be changed in time, and fixed embedding, mesh refinement permanent during the entire simulation, have been set.

Starting with the AMR, it should be set for specific region, during a time interval. Also, must be defined a variable that activates it, that could be pressure, temperature etc. Then, must be defined the activation value related to that variable, that is a threshold value. When the activation value would be overcome, then the AMR will start.

Lastly the max embedding level should be set, it defines the max dimension of the cells, and it defines in this way:

$$\frac{Base\ grid\ size}{2^{max\ embedding\ level}} \tag{30}$$

For all the regions chosen the max number of cells that could be created was limited to 10^7. Below is reported a table with all the setting regarding the AMR.

MODEL	REGION	VARIABLE	MAX EMBEDDING LEVEL	SUB-GRID CRITERION	TIMING
SAGE	Cylinder	Velocity	3	1 m/s	Permanent
		Temperature	4	2.5 K	Cyclic Start: -30 End: 130 Period: 720
	Intake	Velocity	3	1 m/s	Permanent
G-EQUATION	Cylinder	Velocity	3	1 m/s	Permanent
	Intake	Velocity	3	1 m/s	Permanent
ECFM	Cylinder	Velocity	3	1 m/s	Permanent
		Temperature	4	2.5 K	Cyclic Start: -30 End: 130 Period: 720
	Intake	Velocity	3	1 m/s	Permanent
	Cylinder Injector	Progress variable $\tilde{c}$ (defined in the previous chapter)	3	Embedded between 1e-5 and 0.8	Permanent

Table 15. AMR settings.

Then, the fixed embedding has been set. This setting is the same for all the simulations done and in the table below all the parameters are reported.

ENTITY TYPE	REGION	BOUNDARY	MODE	EMBEDDING LEVEL	EMBED LAYERS
BOUNDARY	-	Piston skirt	Permanent	3	1
BOUNDARY	-	Exhaust valve angle	Permanent	3	1
BOUNDARY	-	Intake valve angle	Permanent	3	1
BOUNDARY	-	Tumble fixture	Permanent	2	1
REGION	Injector	-	Permanent	4	-
CYLINDER (BUILD UP CYLINDER)	-	-	Cyclic Start: -137.5 CAD End: -100 CAD Period: 720	3	-
SPHERE 1 (BUILD UP AROUND THE SPARK PLUG) SMALLER RADIUS	-	-	Cyclic Start: -30 CAD End: -5 CAD Period: 720	6	-
SPHERE 2 (BUILD UP AROUND THE SPARK PLUG) BIGGER RADIUS	-	-	Cyclic Start: -30 CAD End: -5 CAD Period: 720	5	-
CYLINDER	-	-	Permanent	2	-

Table 16. Fixed embedding settings.

Aim of the project

The aim of this project is to compare the results obtained in different conditions of ST and air/fuel ratio for the models previously discussed. That analysis will be done firstly for the variables like pressure, temperature, heat release rate (HRR) and others correlated to them that directly affect the performance of the engine. This part of the analysis will be called "Performance". Moreover, there will be a part related to the study of how the different models predict the NO_x emissions, that, as already explained through previously scientific research in the *"Introduction"* section, is the most challenging part for the development of the H2ICEs. More details will be explained in the next part related to the analysis of the results.

Unfortunately, wasn't possible to obtain experimental results to compare with the ones obtained through the simulations, so this project will be more focus on the correlation between the trends obtained from the simulation and the differences present in the governing equations of the models. This is done in order to both understand better how the different models are defined and what are the conditions in which them predict similar values or not working with hydrogen as fuel. Indeed, those models have been already studied and validated for other fuels like diesel, gasoline and ammonia. However, the hydrogen, been a very small particle is difficult to register, and those models tend to still have some difficulties if not well calibrated.

Case studies

All the results that will be analysed in the following section come from the example models of H2ICE already existing in the CONVERGE software. Those cases use the same cylinder with the same geometry.
For the study related to this work the parameters that will be changed are the combustion models, in particular the first part is related to the comparison of three of them, the SAGE, the G-equation and the ECFM. Those comparisons will be done without modifying the parameter related to the example cases, that are:

- ST = -25 CAD, this is related to the first cycle, but as already said the results related to that are not valid, so the actual spark time considered will be 695 CAD. However, from now on that case will be called as “ST -25 case”.
- Air/fuel ratio equal to 2.

After that comparison there will be the study of the models with the change of both ST and λ value, but, as will be explained, only for the SAGE and G-equation models. For that part the conditions that will be taken into account for the analysis will be the following:

- ST = -25 CAD, standard condition one.
- ST = -20 CAD, that correspond to 700 CAD for the second cycle and will be called “ST -20 case”.
- ST = -30 CAD, that correspond to 690 CAD for the second cycle and will be called “ST -30 case”.
- λ = 2.0, that will be called “standard mixture condition”, with no change in the port injector timing.
- λ = 1.7, that will be called “richer mixture condition”, where the injector port closure has been changed to -97 degrees for the first cycle.

All of those parameters will be compared each other, firstly the different ST maintaining constant the λ value, and then the different λ, maintaining constant the different ST.
Lastly, will be analysed the behaviour of the G-equation models for different values of the constant b_1, that is the most influent in the definition of the turbulent flame speed, parameter that is at the base of the model itself.

Results analysis

Comparison of the three models

Standard mixture condition (λ=2.0)

The first analysis done has air/fuel ratio 2.0, this condition will be defined as “Standard condition” from now on in order to recognize it.

Performance

Starting with the analysis of the results obtained from the simulations, the first parameter compared for the different models is the in-cylinder pressure. Figure 69 shows the difference for the three models.

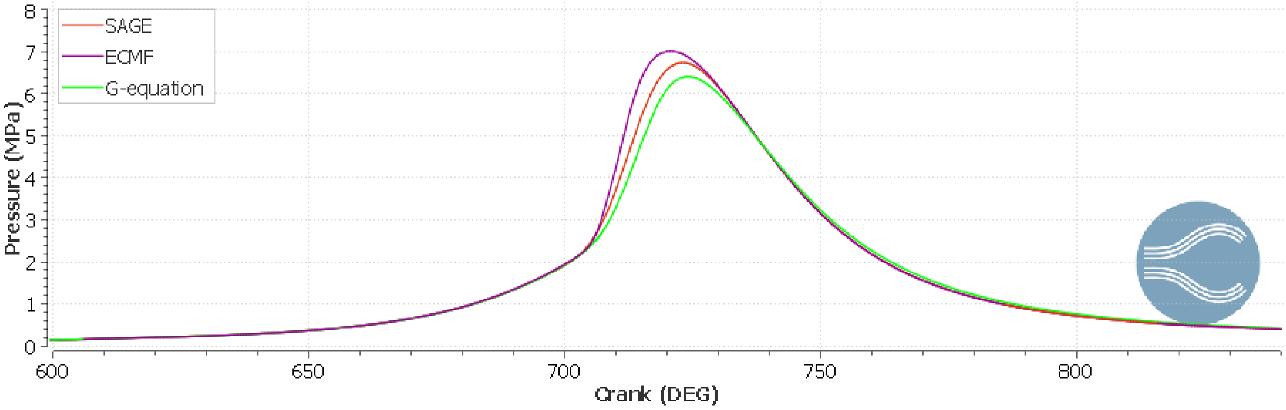

Figure 69. Comparison of the in-cylinder pressure evolution for the three models in standard mixture conditions

The main differences that can be seen are related to the peak values and the delay for the beginning of the combustion. The ECFM model has both higher peak value and steeper slope, followed by the SAGE model and then the G-equation one.

The same behaviour can be seen in the temperature field, represented in Figure 70. The image refers to the "mean temperature" because it represents the mean of all the temperatures estimated for all the cells that build the mesh of cylinder.

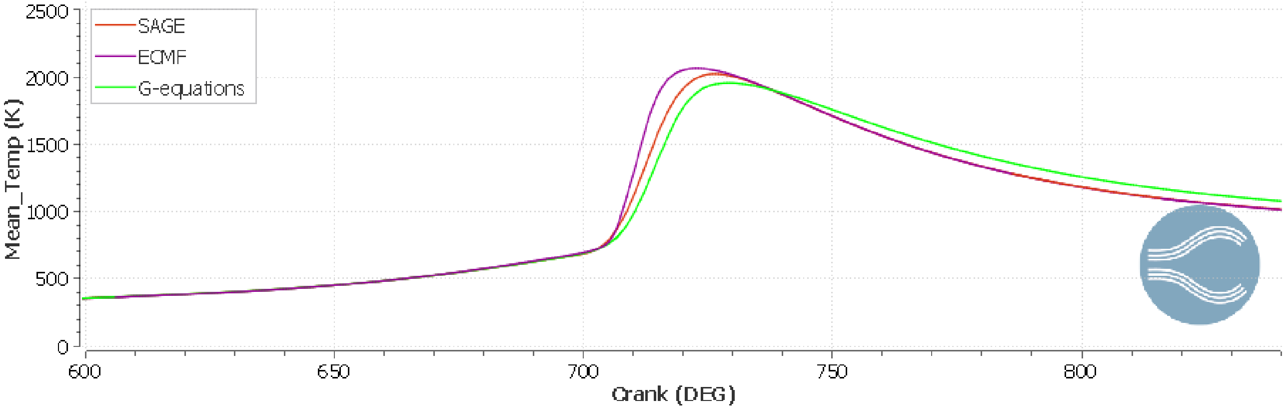

Figure 70. Comparison of the in-cylinder mean temperature evolution for the three models in standard mixture conditions

Also in this case, the most impact difference in the models is the difference in peak values, like for the in-cylinder pressure, the ECFM model predicts a higher value of temperatures, then the SAGE and lastly the G-equation one.

In order to explain this phenomenon, a possible way is to analyse the difference in the HRR and heat release (HR), in particular the integrated heat release (IHR). This due to the direct correlation between them, pressure and temperature.

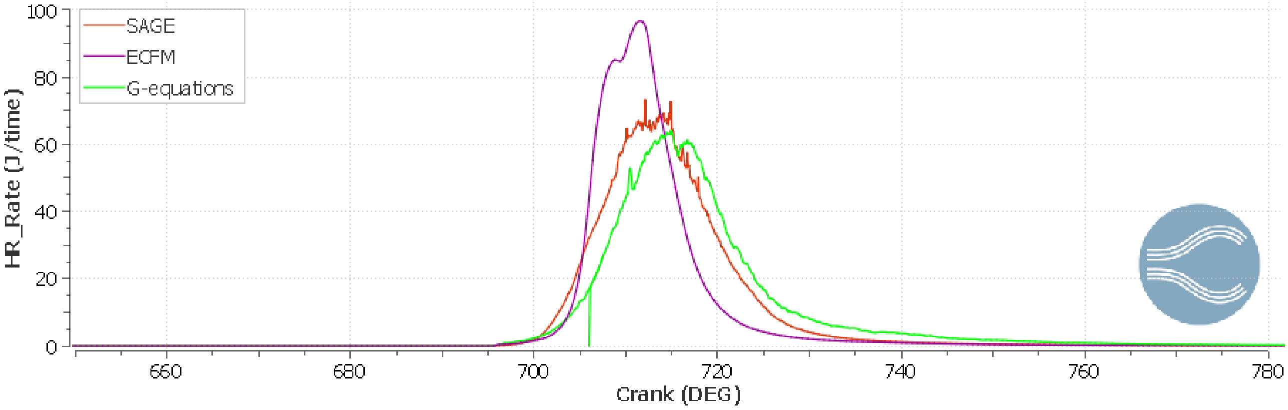

Figure 71. Comparison of the HRR in-cylinder evolution for the three models in standard mixture conditions

Looking at the Figure above is visible that the ECFM model gives a value of HRR significantly higher with respect to the other two models. Also, the shape of the diagram is smoother, and the slope in the increasing and decreasing phase is steeper. However, also the SAGE and the G-equation models show differences, but less significant with a general shape and turbulence fluctuation around the peak time that could be considered comparable.

Similar consideration could be done looking at the diagram of the HR, in Figure 72. For this plot the cycle considered is the first, this is necessary due to the main problem that, after the first cycle, the residual heat, visible after 30 CAD, is the starting point of the second cycle, so they don't start all from the same level at the next combustion, leading to possible errors. However, this plot could be considered acceptable due to the necessity of understanding the trend of the models and to give a qualitative analysis of the simulations.

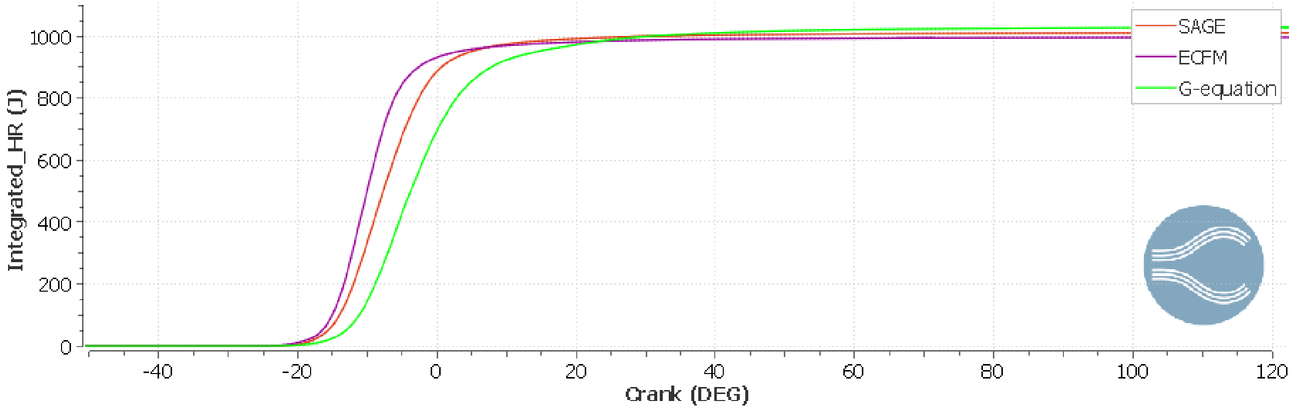

Figure 72. Comparison of the in-cylinder HR evolution for the three models in standard mixture conditions

The image confirms what was expressed for Figure 71, the slope of the curve for the ECFM model is steeper but after the combustion the energy realised is lower than the other two.

The differences in HRR and IHR could be explained by two main factors that differentiate the models. The first is the way they define the spark, that could lead to different timing and energy absolute value. Instead, the second is the effect of the turbulence on the different models, that will be studied later.

Starting with the modelling of the spark, the SAGE model defines it using the ENERGY SOURCE MODELING, where the software solves the energy equation for compressible flows

$$\frac{\partial \rho e}{\partial t} + \frac{\partial u_j \rho e}{\partial x_j} = -P\frac{\partial u_j}{\partial x_j} + \sigma_{ij}\frac{\partial u_i}{\partial x_j} + \frac{\partial}{\partial x_j}\left(K\frac{\partial T}{\partial x_j}\right) + \frac{\partial}{\partial x_j}\left(\rho D\sum_m h_m \frac{\partial Y_m}{\partial x_j}\right) \tag{31}$$

where:

- ρ is density
- Y_m is the mass fraction of species m
- D is the mass diffusion coefficient
- P is the pressure
- e is the specific internal energy
- K is the conductivity
- h_m is the species enthalpy
- σ_{ij} is the stress tensor
- T is the temperature
- S is the energy source term, that for the simulation done, was set as fixed value of 0.02 J

Note that, as in the simulations done the turbulence models was activated, the *conductivity* is replaced by the *turbulent conductivity* [38], defined as

$$K_t = K + c_p \frac{\mu_t}{Pr_t} \tag{32}$$

where:

- c is the specific heat at constant pressure,
- μ is the turbulent viscosity
- Pr_t is the turbulent Prandtl number

The SAGE model, as it's based on chemical reactions, uses the equations that represent the conservation of internal energy in a compressible fluid, and it accounts mechanical effects and thermal conductions, but also chemical species diffusion and the external source term that is fixed. Moreover, the energy is divided in two sources, one for the *break-up phase* and the other for the *glow and arc phase,* with an overlap of the effects in the first 0.5 CAD after the spark, leading to the sum of the energy for that period.

The ECFM model, instead define the source through the *Imposed Stretch Spark Ignition model* (ISSIM), that simulate the reaction rate due to the flame surface density (FSD) starting at the instant of the ignition, representing the electrical circuit energy deposition, the flame surface and mass deposition.
The circuit is divided in two parts, the primary one includes the primary inductance and the batteries, the secondary circuit the spark plug and the second inductance. When the switch turns on, the energy is stored in the primary inductance and almost the 60% of the energy is passed to the spark plug, the remaining part is dissipated through the secondary inductance. Also, the amount of energy transferred to the secondary circuit for the simulation done was set at 0.04 J.
Unlike the SAGE model, the ECFM uses different equations for the three spark phases. The *breakdown* and the *arc phase*, the shorter, are modelled using an instantaneous energy value, defined as

$$E_{bd} = \frac{V_{bd}^2}{C_{bd}^2 d_{ie}} \tag{33}$$

where:

- V_{bd} is the breakdown voltage, approximated by the Paschen's law [40]
- C_{bd} is a constant equal to 1.5 E6
- d_{ie} is the inter-electrode distance, defined as 1mm

Then, the *glow phase,* that is longer than the others, is defined solving the electrical circuit ordinary differential equations (ODE).
After those calculations, the total energy received by the gas is defined as the sum of the energy received in the breakdown phase (E_{bd}) and the one during the glow phase.

$$E_{ign} = 0.6E_{bd} + \int_{tspk}^{t} V_{gc}\, i_s \, dt \tag{34}$$

In the equation above i_s represent the current and V_{gc} represent the gas column voltage, defined as

$$V_{gc} = 40.46 l_{spk} i_s^{-0.32} p^{0.51} \tag{35}$$

Using l_{spk} as spark length and p as pressure.

Lastly, for the G-equation model the *Passive source model* is used. The passive source model is based on the following general transport equation

$$\frac{\partial \rho\phi}{\partial t} + \frac{\partial \rho u_i \phi}{\partial x_i} = \frac{\partial}{\partial x_i}\left(\rho D \frac{\partial \phi}{\partial x_i}\right) + S \tag{36}$$

where:

- u_i is the velocity
- ρ is the density
- D is the diffusion coefficient
- ϕ is the passive selected
- S is the passive source term

In CONVERGE [38], a passive is the abbreviation for a "passive scalar", that is one of the two possible scalar quantity calculated by the software. A scalar is a calculated quantity that is collocated in space and time with mass, momentum, energy, and species. The only difference between a scalar and a passive is when the quantity is solved within the time-step. Passives can be non-transport passives or transport passives. Moreover, in CONVERGE scalars and passives have several different uses. Some may indirectly affect the transport equations through a parameter in a source term, like in this case.

Form the general equation of the passive source model, for the G-equation model the passive used is the mean of the non-reactive scalar component G, leading to the final form of the transport equation already explained in equation 1.

All three models describe in a different way the ignition phase, with different equation, but could be found some parameters in common that could give a possible explanation to the differences in the results obtained. Looking at the equations, there are few parameters that are shared between models. In particular, the most repeated ones that influence the combustion ignition for the models are:

- Pressure (mainly SAGE and ECFM)
- Temperature (mainly SAGE)
- Density (mainly SAGE and G-equation)

In particular it must be taken into accounts that the influence is done for those variables at the spark time, that for the simulation done was 695 CAD (-25 CAD for the first cycle).

Starting with the analysis of the pressure at the ST, Figure 73 shows its values for all the models.

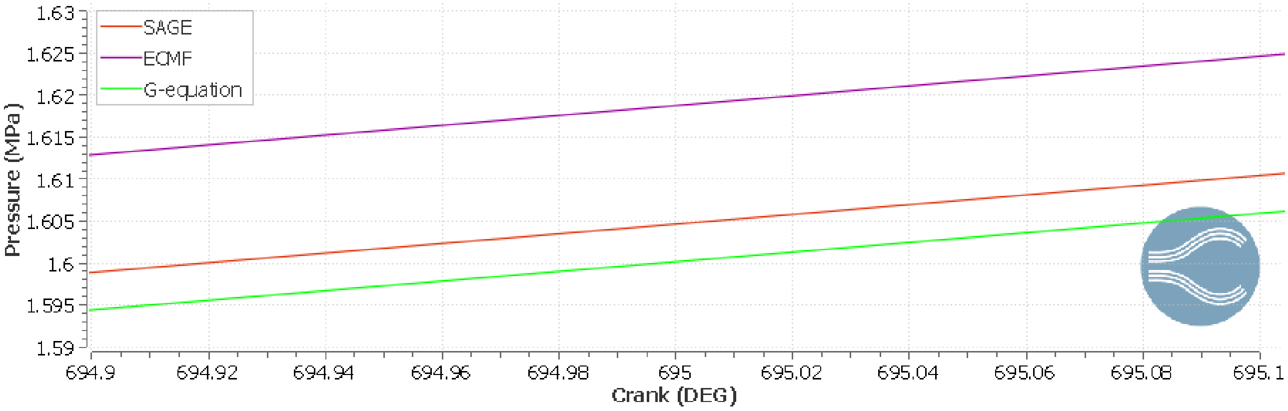

Figure 73. Zoom of the pressure at the ST for the three models in standard mixture conditions

In the image above it is possible to see the same behaviour presented also at the peak pressure, reached after the ST. This defines a possible reason of why the ECFM model give high differences between the other model, due to the prediction of higher values also outside of the combustion phase.

Moving to the temperature distribution at the ST, shown in Figure 74, the previous behaviour is even bigger. With a huge difference between the ECFM model with the others.

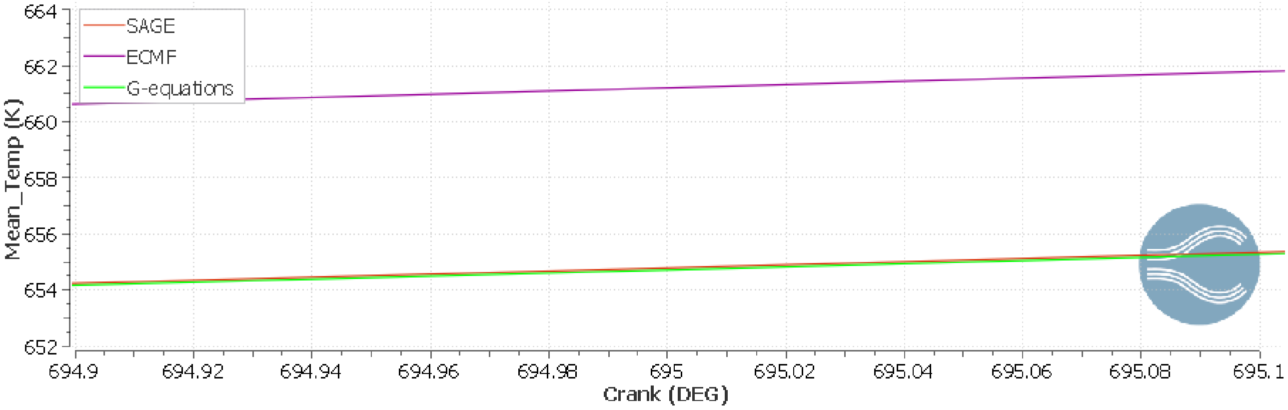

Figure 74. Zoom of the mean temperature at the ST for the three models in standard mixture conditions

For considering the dependence of the models to those parameters, in particular to the pressure for the ECFM model. The trend of maximum values reached at the peak of the combustion is maintained. However, regarding the SAGE and the G-equation models, the difference is very low at the ST, showing that the temperature has different influence. Indeed, looking at the equation and the way the models are defined, the G-equation model mainly depends on some turbulent parameters, like turbulent dissipation or turbulent kinetic energy (TKE), that influence the temperature change, but the model is not directly dependent on it. Instead, the SAGE model, based on reaction mechanisms, have a direct correlation with the temperature that gives high influence on the results.

Last parameter considered is the density, that, looking at Figure 75, show almost the same difference between the models.

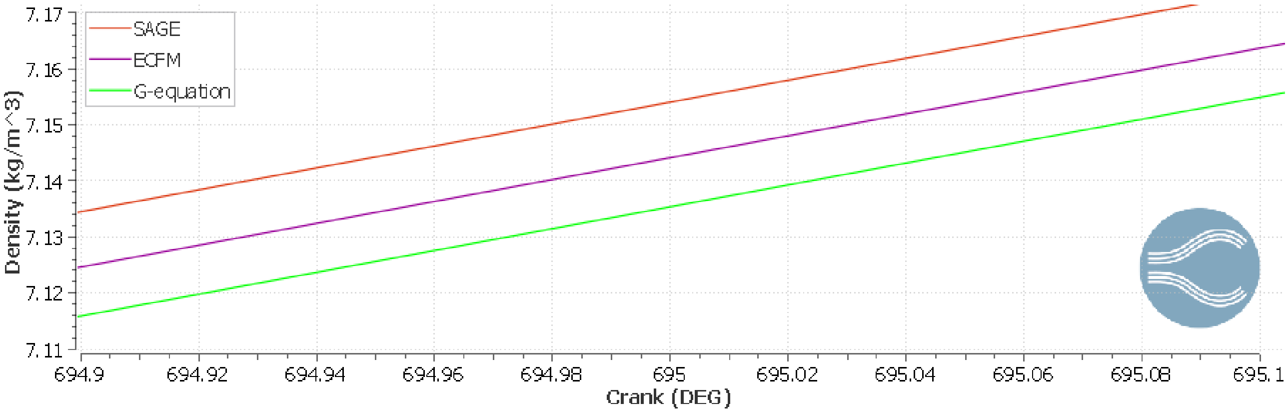

Figure 75. Zoom of the density at the ST for the three models in standard mixture conditions

In this diagram the order of the models is different, the SAGE model predict higher results than the others. This difference with respect to the other diagram previously shown, could be explained considering how the models predict the different variables, indeed both G-equation and ECFM models are based on transport equations, instead the SAGE one, based on the chemical reactions, is possible that create more discrepancy with the others for results directly related to the chemistry of the combustion.

Returning to the analysis of the HRR, it is interesting to see how the different model predicts the ST. In Figure 76 this is shown and is visible that for the three models the prediction of the time when the spark occur is different, even though the time set for all the models was the same.

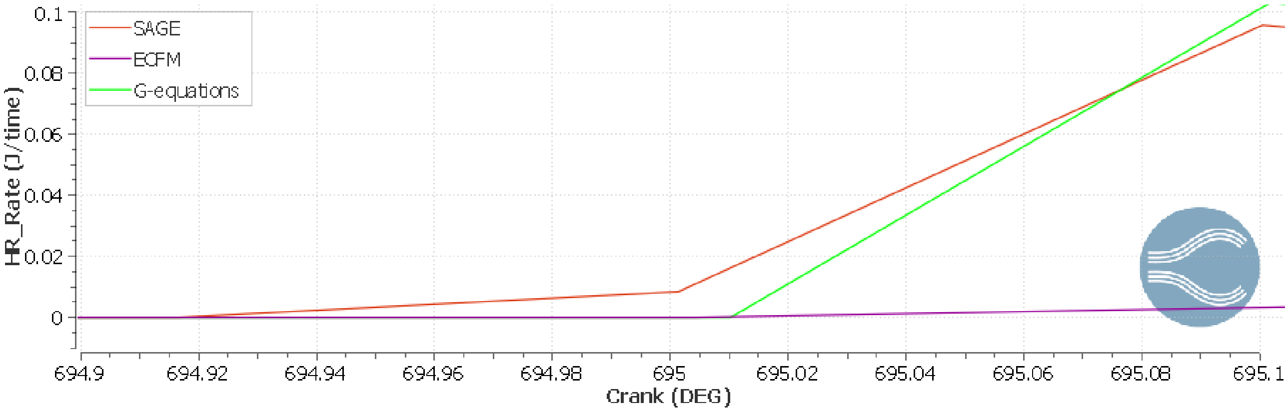

Figure 76. HRR at the ST for the three models in standard mixture conditions

In the image above the SAGE model starts the combustion 0.03 CAD before the time set, instead in the ECFM model, the spark occurs at 695 CAD, as set, but with a very low slope, that will actually start rising only after 0.7 CAD.

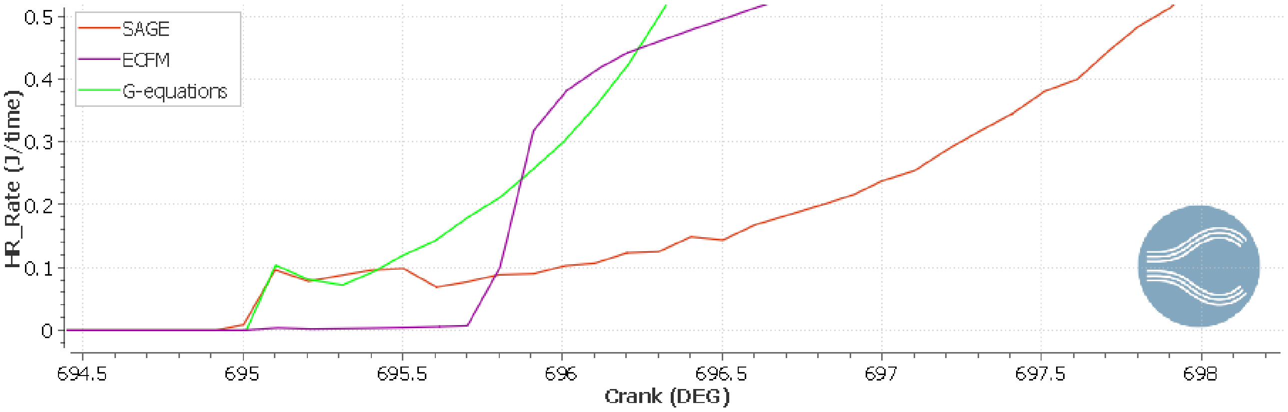

Figure 77. HRR of the three models at the ST and the start of the combustion phase in standard mixture conditions

Figure 77 is important to underline how the different models propagate the energy, and this could be a possible explanation of the results that are shown in previous diagrams like pressure and temperature. Looking at the different curves, the one that has a more continuous development seams the G-equation one, that starts exactly at the ST set and grows in an almost parabolic shape.

A possible reason for the different behaviour of the curves is that, due to an earlier ST or low fuel quantity, the SAGE model needs more time to develop the heat and start the combustion, knowing that it’s based on the chemical reactions. Instead, G-equation model predicts a fast propagation of the flame front already at the ST. However, going back on Figure 71, the heat released by the SAGE models grows faster that the G-equation one in the following CAD, showing a switch of the two behaviours. Lastly, the ECFM model give the most different result among the others probably due to the general difficulties to detect the combustion of hydrogen, the reason could be the low mixing and the small dimension of the H_2 particles, indeed this model is mainly used for the analysis of other fuels like gasoline.

This behaviour also could be the reason of why the peak of the models are shifted toward the right, the different moment and way the models start the combustion effects the energy released in time and then the moment the models reach the peak values of both pressure and temperature.

Another element that could affect the results is the turbulence, defined for all the cases using the RANS models. In particular, one of the elements that influences mostly the results is the Turbulent Kinetic Energy (TKE), that represents the mean kinetic energy per unit mass associated with eddies in a turbulent flow. This parameter doesn’t have a direct correlation with temperature and pressure, but an increase in TKE leads to higher turbulence and a faster propagation of the flame. This phenomenon influences the three models is a different way.

The SAGE model is not directly affected by it, indeed it doesn't enter in the chemistry solver directly. However, TKE influence the turbulent viscosity, which influences how species and energy are transported.

Instead, for the G-equation, the TKE is directly present in the equations that govern the model, in particular in the calculation of turbulent flame speed (S_t), that in the CONVERGE software [38] is defined through the Peters model.

$$s_t = s_l + u' \left\{ -\frac{a_4 b_3^2}{2b_1} D_a + \left[\left(\frac{a_4 b_3^2}{2b_1} D_a \right)^2 + a_4 b_3^2 D_a \right]^{1/2} \right\} \tag{37}$$

where:

- u' is the root mean square of the turbulent velocity fluctuation
- s_l the laminar flame speed
- a_4, b_1 and b_3 are modelling constants that for the simulations done were defined as 0.78, 3 and 1, respectively.
- D_a is the Damkohler number

This last parameter (D_a) is defined as

$$D_a = \frac{s_l l_t}{u' \delta_l} \tag{38}$$

where:

$$\delta_l = \frac{\left(\lambda / c_p\right)_o}{(\rho s_l)_u} \tag{39}$$

In this equation λ is the molecular conductivity and the subscript o indicates a cell value, the subscript u indicates the unburned region value.

Lastly, in the definition of the Damkohler number

$$l_t = C_\mu^{3/4} \frac{k^{3/2}}{\varepsilon} \tag{40}$$

where is present the TKE (k).

For the ECFM model, the TKE is used to compute the turbulent flame surface density $\sum$

$$\frac{\partial c}{\partial t} + \vec{u} * \nabla c = S_l \sum \tag{41}$$

where $\sum$ is a function of TKE, turbulent dissipation and ∇c.

In conclusion the models that are most influenced by the TKE are the G-equation one and the ECFM. Looking at the diagram of the TKE for the three models, the differences are very low and mainly in at the peak at 600-620 CAD, as shown in Figure 78.

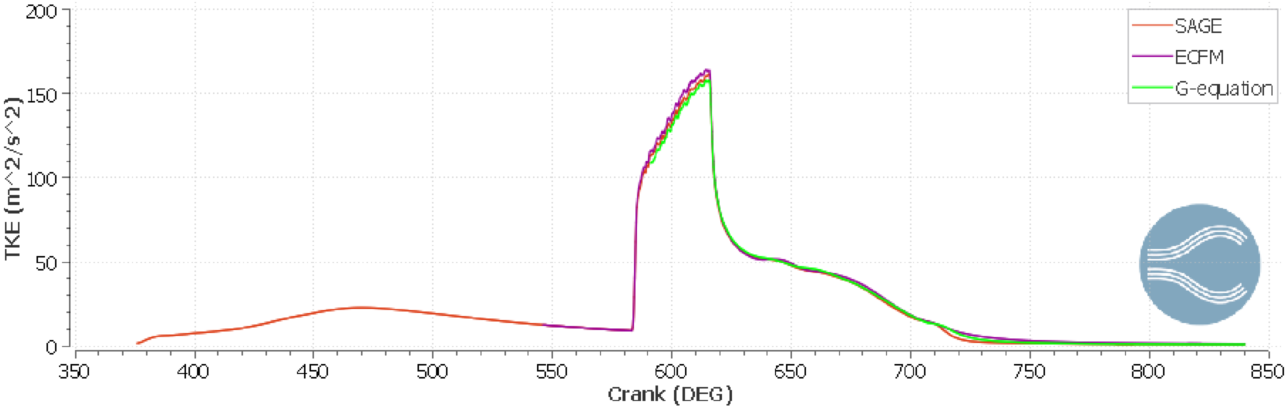

Figure 78. Comparison of the in-cylinder TKE of the three models in standard mixture conditions

However, the focus of the analysis should be on the moment of peak pressure and temperature. Indeed, the figure below represents the TKE at the moment of the peak values of P and T, that for the three models are between 720 and 730 CAD.

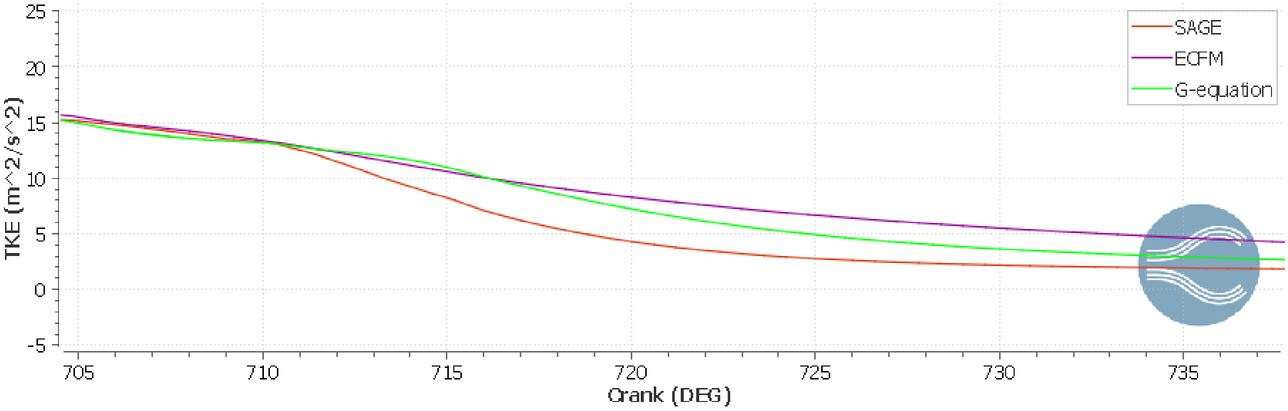

Figure 79. Zoom of in-cylinder TKE at the peak of the combustion phase for the three models in standard mixture conditions

What can be observed from the diagram is that the ECFM model has the highest value, maintaining the trend present also for the other parameters, followed by the G-equation model. The SAGE model, in this diagram predicts the lowest values, but in the pressure and temperature diagram it's higher than the G-equation. This could be related to the fact that the SAGE model is the one less influenced by the TKE and considering the general concept at the base of the model, it ignores the effect of turbulence on reaction rates.

The same consideration is extended also for the TKE at the ST, when the difference with the models is proportionally the same.

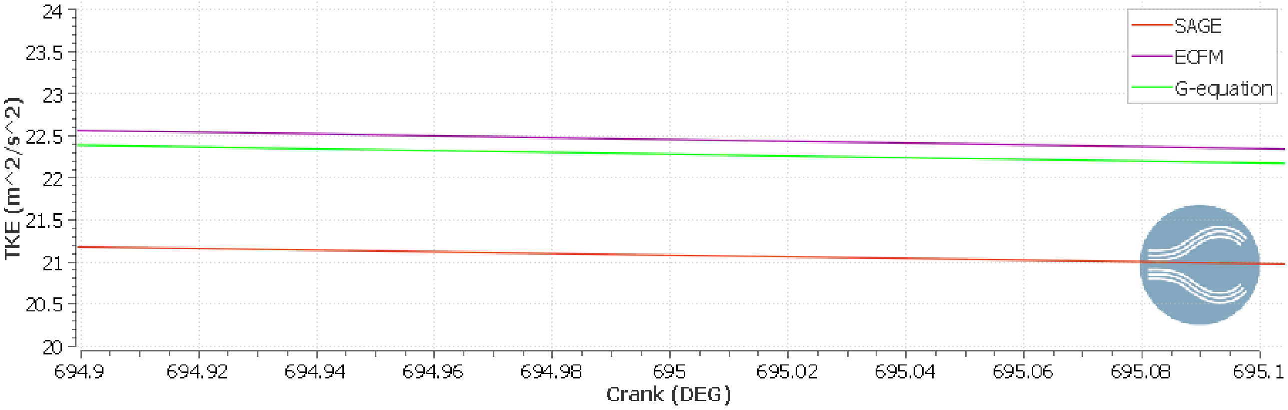

Figure 80. Zoom of the in-cylinder TKE at the ST for the three models in standard mixture conditions

NO_x emissions

Moving to the analysis of the emissions predicted by the different models, the NO_x estimation has been done using the *extended Zeldovich mechanism*, that is a chemical mechanism that describes the oxidation of nitrogen and NO_x formation, first proposed by the Russian physicist Yakov Borisovich Zeldovich in 1946 [41]. The reactions are the following, where k_1 and k_2 are the constants in the Arrhenius law:

$$N_2 + O \overset{k_1}{\leftrightarrow} NO \ + \ N$$
$$N + O_2 \overset{k_2}{\leftrightarrow} NO \ + \ O$$

The reaction above describes the mechanism, but in case of fuel-rich conditions, due to lack of oxygen, the second reaction becomes obsolete and a third is included, this defines the **extended Zeldovich mechanism** (with all three reactions)

$$N + OH \overset{k_3}{\leftrightarrow} NO \ + \ H$$

In particular, that is the one used by the software for the NO_x emissions calculation.

For the analysis of the emissions, it is important to understand how the different constants are calculated, starting from the Arrhenius law [42], that defines the constants in this way:

$$k_x = Ae^{\frac{-E_a}{RT}} \tag{42}$$

This is the equation where the factor A is considered temperature-dependent, but some studies explicit it through the modified Arrhenius equation:

$$k_x = AT^n e^{\frac{-E_a}{RT}} \tag{43}$$

where:

- A is the pre-exponential factor (specific to each reaction).
- T is the absolute temperature.
- N is an empirical temperature exponent.
- E_a is the activation energy.
- R is the universal gas constant.

Following the equations defined above, the dependence on the temperature is very high, leading the smallest difference in temperature to an important variation in the calculation of the NO_x mass for the different models.

Indeed, all the models are based on different equations and also the way they calculate the temperature is deeply different.

Starting with the SAGE model, the temperature is directly computed by solving the energy equation, fully coupled with detailed chemical reactions and used detailed reaction mechanisms involving many species and reactions, which are solved together with mass and energy conservation equations. So, the temperature rise comes from the heat release of the chemical reaction itself, not from specific equations.

The ECFM model, instead, uses a flame surface density (FSD) approach, it calculates temperature based on a progress variable that tracks the local state of combustion, similarly to a lookup-based or tabulated approach. All the model is built around a progressive variable c, that if is equal to zero represents the unburned gas, if it is equal to one it is the fully burned gas. The temperature, then is interpolated between unburnt and burnt gas temperatures through the following law:

$$T = T_u + c(T_b - T_u) \tag{44}$$

where:

- T_u is the unburnt mixture temperature
- T_b is the burnt gas temperature

Moreover, the variable c changes according to the transport equations that took into account diffusions mechanisms and source terms, that is related to the flame surface density $\sum$ and the laminar flame speed S_L (that will be analyse later), following the equation:

$$\frac{\partial c}{\partial t} + \vec{u} * \nabla c = \dot{\omega} = \rho * S_L * \sum \tag{45}$$

Lastly, the G-equation model assumes a thin flame front separating unburned and burned gases, then assigned a fixed unburned and burned temperature, then the flame front is tracked using the G-equation:

$$\frac{\partial G}{\partial t} + \vec{u} * \nabla \mathrm{G} = \mathrm{S_L}|\nabla \mathrm{G}|$$

where G=0 represents the flame location. Then the temperature field is reconstructed using an interpolation but not solved. The interpolation is similar to the one used by the ECFM model, but instead of the c variable, here a function dependent on the G factor is considered.

$$T = T_u + H(G) * (T_b - T_u) \tag{46}$$

Moving to the analysis of the results, considering all the differences for the models explained, the first important comparison that will influence the total NO_x emissions is the temperature, already shown in Figure 70.

What can be seen from that diagram is that all the models predict different peak temperatures for the combustion, in particular the ECFM model gives higher value compared to the others. However, after the combustion (from 740 CAD) the SAGE and ECFM model predict the same decreasing profile, meanwhile for the G-equation model the peak is lower but also the slope after the combustion is less steep. Moreover, the different peaks have also delayed each other, showing a different prediction of the peak combustion temperature in time, not only in absolute value.

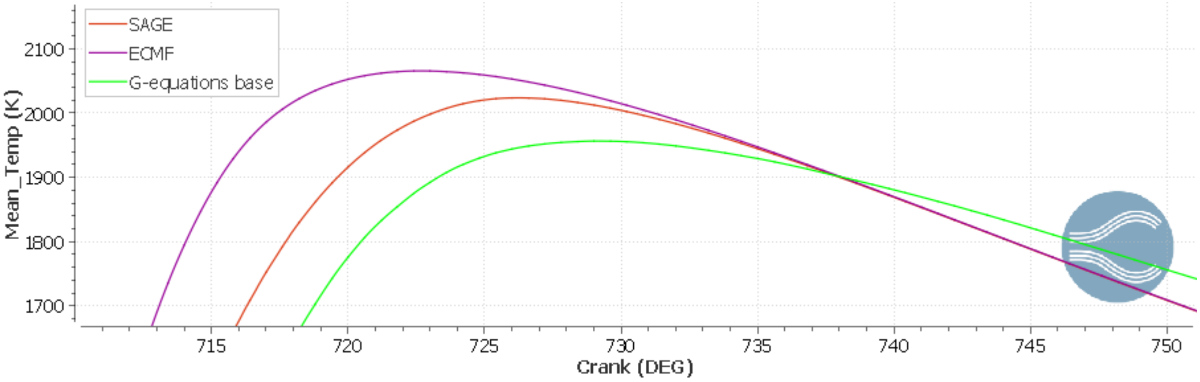

Figure 81. Zoom of the peak values of the temperature for the three models in standard mixture conditions

Figure 81 show a zoom of the different peaks for all three models, to underline the difference in prediction of the peaks. The peaks values are the following:

MODEL	PEAK TEMPERATURE [K]
SAGE	2023.47
ECFM	2065.36
G-EQUATION	1956. 29

Table 17. Peak values of the mean in-cylinder temperature for the three models in standard mixture conditions

The difference in peak values predicted varies from 42 K for SAGE and ECFM, to 109 K for ECFM and G-equation. Those differences give high influence on the estimation of the NO_x values, as previously described for the Zerdovich mechanism.
The results for the emission of in-cylinder NO_x are represented below in Figure 82.

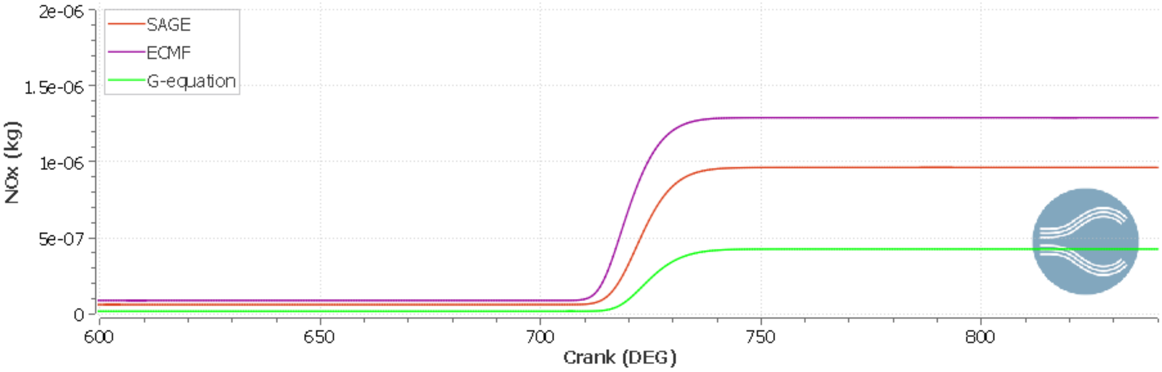

Figure 82. NO_x emissions in the combustion chamber

The results are shown in Kg, usually for the analysis of the emissions those data are expressed in Part Per Million (ppm), and considering this unit of measure, the following are the results of NO_x emissions predicted by the different models after the combustion phase:

MODEL	PEAK NO_x [ppm]
SAGE	0.963
ECFM	1.29
G-EQUATION	0.425

Table 18. Peak NO_x emissions values for the different models in standard mixture conditions

The results in the table above underline the high sensitivity of the NO_x emission from the temperature, leading a difference of 109 K (ECFM and G-equation models) to emission value of the ECFM model that is 3 times higher with respect to the G-equation ones.

Richer mixture conditions (λ=1.7)

The same simulation has been done with another quantity of fuel, in this case more than the standard condition, reaching an air/fuel ratio equal to 1.7, to see how it would influence the results for the different models. This condition will be defined as “richer mixture condition” and will be called like this from now on. The comparison of the mass of H_2 present in the chamber before the combustion for the two cases is shown in Figure 83, the difference at the combustion instant is about 1.67 E-6 kg.

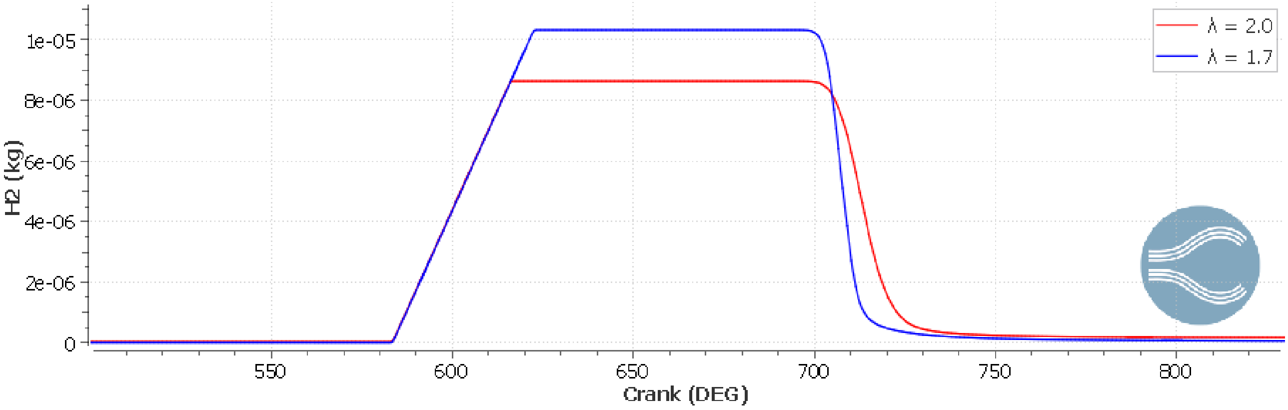

Figure 83. H_2 mass in the cylinder for the different air/fuel ratio considered

Performance

Starting, as before from the comparison of the pressure evolution, it is reported in Figure 84.

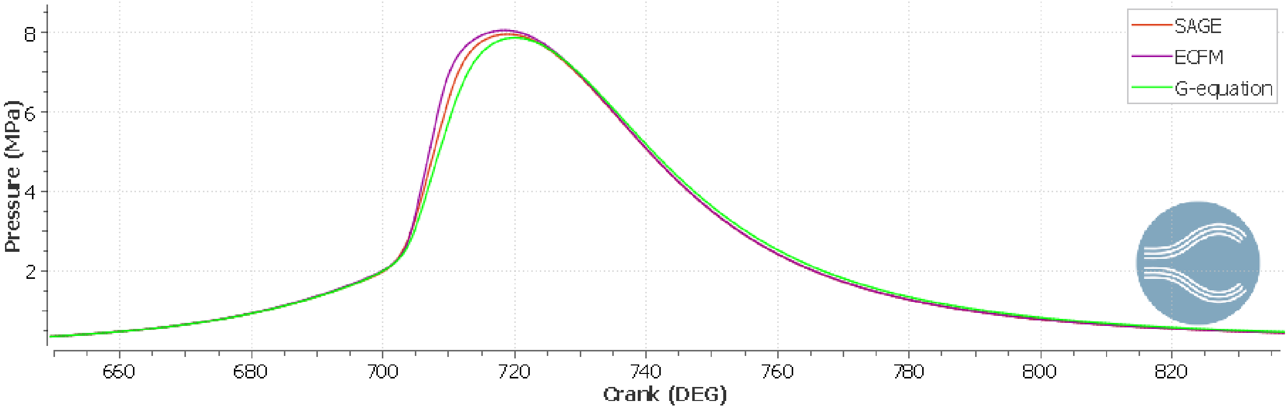

Figure 84. Comparison of the in-cylinder pressure for the three models in richer mixture conditions

From the image is possible to see that, with respect to the standard case previously studied, the models predict more close pressure curves for this condition, leading to the conclusion that, for $\lambda = 1.7$ all three models predict closer values each other. An explanation that could be done for those results is due to the higher fuel present in this simulation, indeed this would lead to more mixing and easier prediction of the results for all the models, independently of how they predict them. Moreover, higher mass of fuel means also more fast and robust flame, that is better predicted by all the models, instead for leaner mixture, the chemistry becomes crucial and difficult to predict.

Same consideration could be done for the temperature evolution through crank angles.

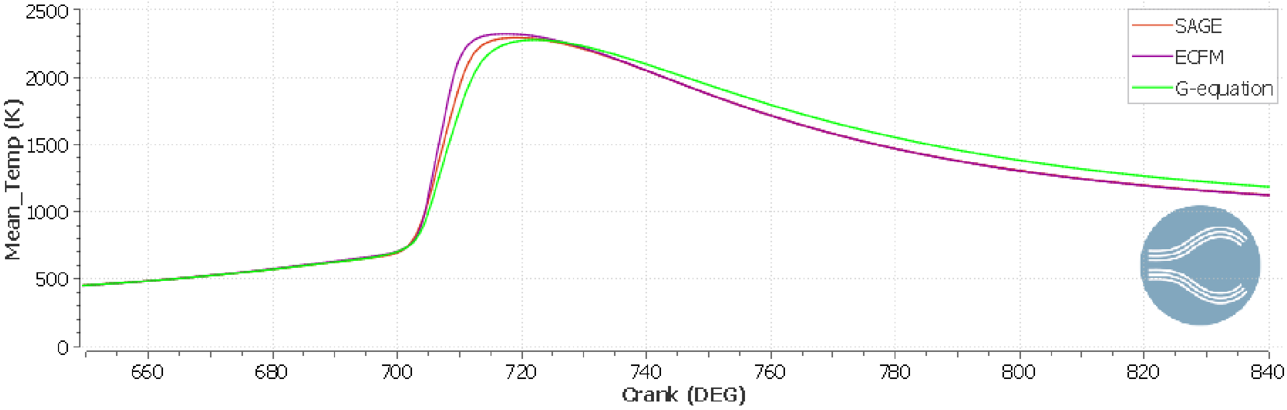

Figure 85. Comparison of the in-cylinder mean temperature for the three models in richer mixture conditions

The order of the different models remains the same, with the ECFM that still predicts higher values, followed by the SAGE and the G-equation models.

Different considerations could be done for the HRR, where the difference between models is highly visible, in particular with the ECFM one, like the previous case. Also, in this comparison the curve related to the ECFM model is smoother, steeper and reach higher values with respect to the other models. Moreover, in Figure 86 it is also well visible that the SAGE and the G-equation models, having different values, the curves are almost parallel each other, underling a close behaviour, instead for the ECFM model the curve is different both in values and shape.

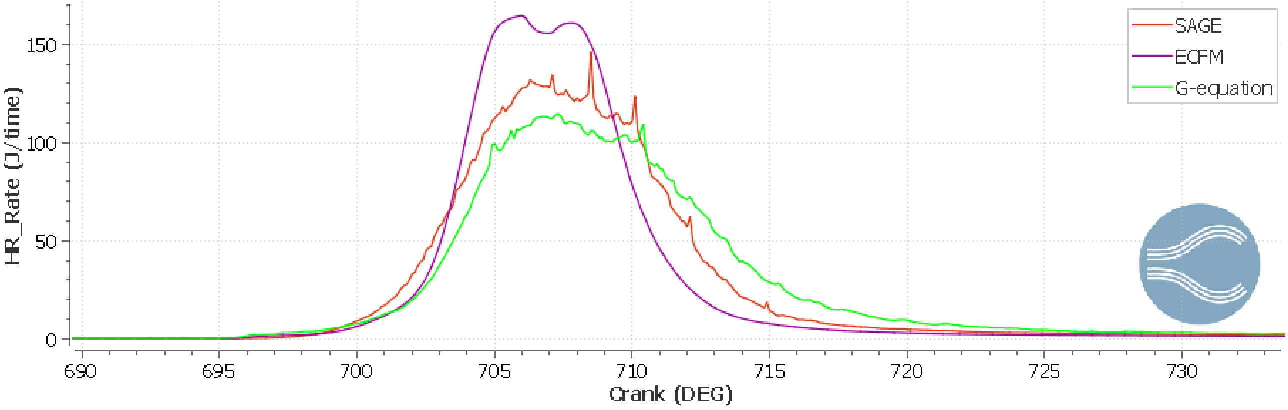

Figure 86. Comparison of the in-cylinder HRR for the three models in richer mixture conditions

For what concern the diagram related to the IHR, figure below, the results are close to the one of the previous case, with the ECFM model that still has higher slope at the beginning of the combustion but is the first that saturates the energy value, instead SAGE or even more G-equation models has slower increase in values (slope that is the HRR, so coherent with Figure 86) but finished with the higher energy content released after the combustion phase.

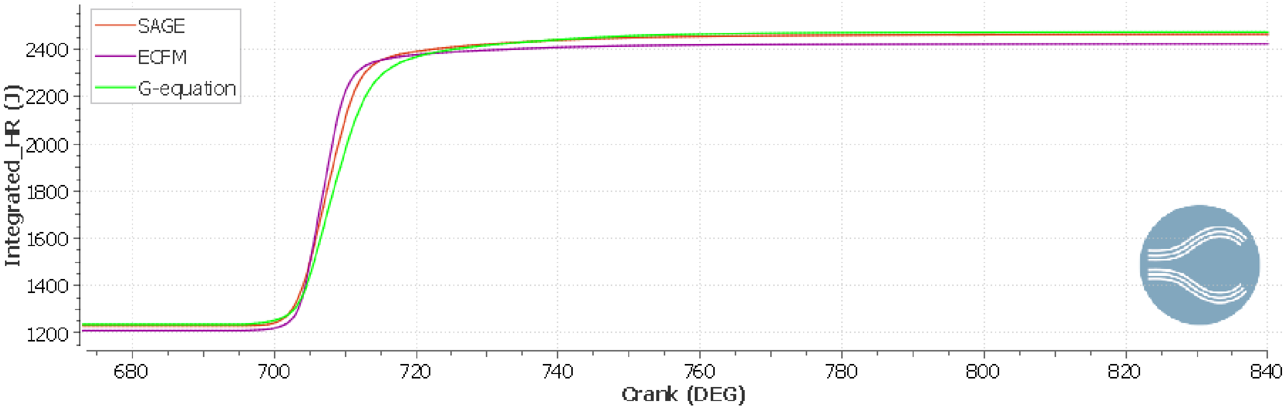

Figure 87. Comparison of the in-cylinder IHR for the three models in richer mixture conditions

Following the analysis done in the previous section, the values that influence the diagrams shows until now are the one at the ST for pressure, temperature and density. The first two are shown in Figure 88 and it could be seen that there are no significant differences form the standard case with $\lambda = 2.0$.

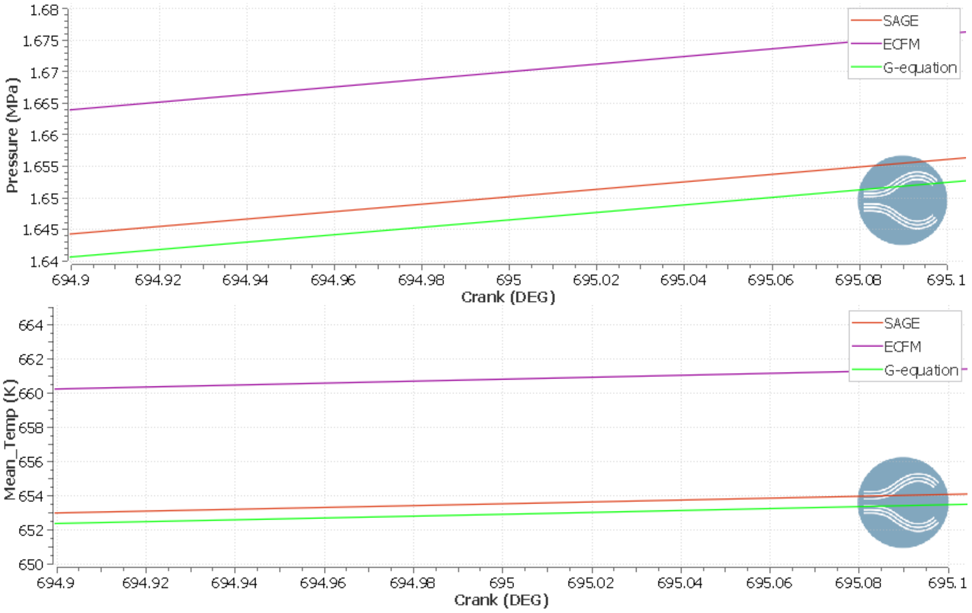

Figure 88. Comparison of the in-cylinder pressure and mean temperature at the ST for the three models in richer mixture conditions

The diagrams above show that, as expected, the ECFM model still has higher values for both pressure and temperature at the ST, giving another element to explain the result of the same at the peak of the combustion.

The main differences in the values at ST is visible in the following figure representing the density. Indeed, in this case the ECFM model has the higher value, instead of the SAGE one. However, the differences are very small but help anyway to understand the trends of the models and how them react to different air/fuel conditions.

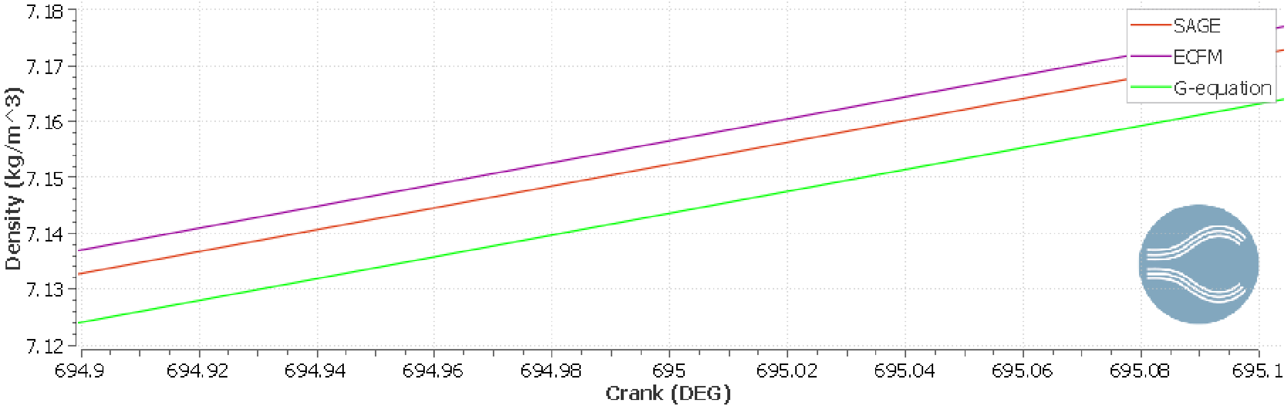

Figure 89. Comparison of the in-cylinder density at the ST for the three models in richer mixture conditions

Continuing to the analysis of the different parameters at the ST, the HRR is the next important variable, represented in Figure 90.

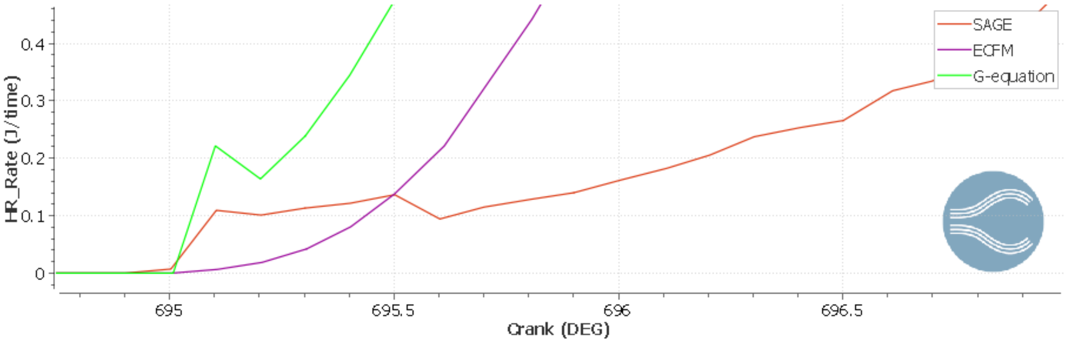

Figure 90. Zoom of the HRR at the ST for the three models in richer mixture conditions

In this case all the models have the correct ST, with a small advance for the SAGE one. However, this underlines the effect of the fuel, indeed for the λ = 2.0 case, with a leaner quantity of fuel, the models had difficulties in the prediction of the correct instant for the ST. Instead, with higher fuel is easier for all the models to predict the correct ST for the energy release.

There are still some differences in the way the models develop the HRR, the SAGE one show also in this condition the less slope for the HRR curve, the G-equation one is also in this case the one that predict with steeper slope and the ECFM is almost parallel to it, but less steep.

Moving the analysis to the turbulence parameters of the models, the first that has impact in the results is the TKE, shown in the figure below.

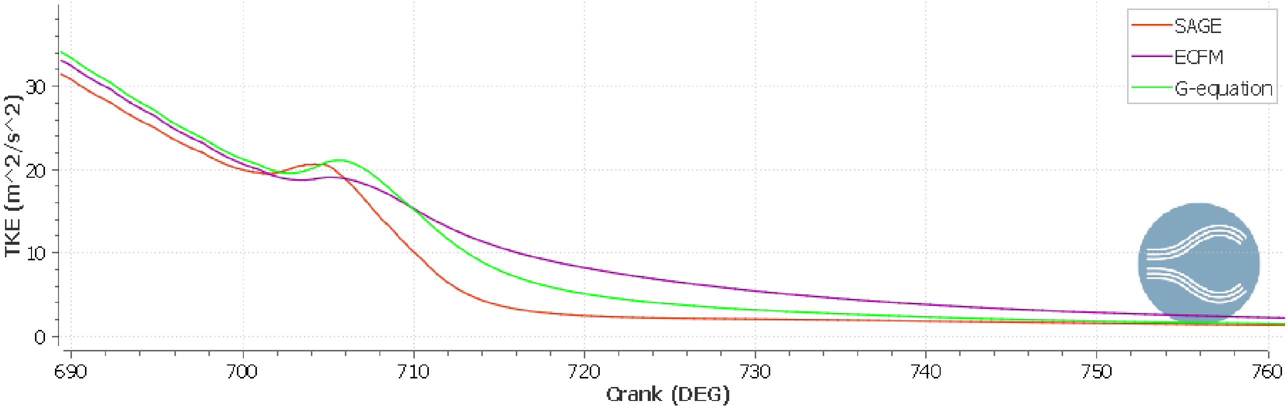

Figure 91. TKE of the three models for the owl combustion phase for the three models in richer mixture conditions

In the image could be seen both the values at the ST, that occur at 695 CAD, and the peak of the combustion phase. Starting with the first, the G-equation model has higher values than the others, followed by the ECFM and then the SAGE one, more far from the other two. This could be explained considering that the SAGE model is the only one that doesn't work directly with the turbulence but with the chemistry, instead both ECFM and even more the G-equation models base their constitutive equation on the turbulence parameters, where the TKE is one of the most relevant. This is coherent also with the previous case with λ = 2.0, while the switch in values for the G-equation and ECFM model is very small and could be done to external parameters.

NO_x emissions

Next there's the study of the emissions for the three models in the richer mixture condition. Starting with the peak temperature values, that are the main influence in the NO_x formation during the combustion, also in this case the differences are visible but less significant with respect to the previous case. The ECFM model is the one that still has higher values, followed by the SAGE and then the G-equation one.

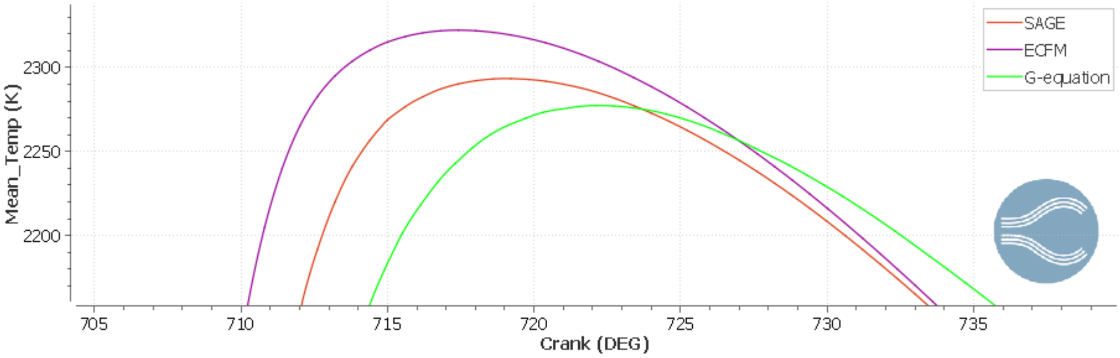

Figure 92. Zoom of the peak values of the temperature for the three models in richer mixture conditions

The differences in Figure 92 are then transferred to the NO_x emission, shown below, and is possible to see that the differences in values between models is lower than the other case with λ = 2.0. This confirms the previously done consideration in which, due to higher fuel, all the models work in a more favourable conditions to the definition of some parameters and the results are closer each other.

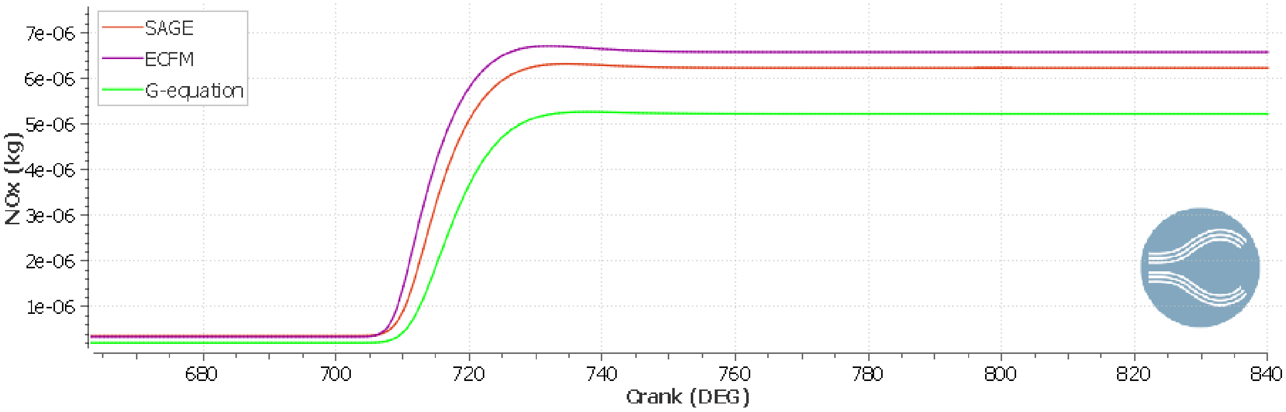

Figure 93. NO_x emissions comparison for the three models in richer mixture conditions

In particular what is more clear in the analysis of the results for the richer mixture condition is that, for all the variables related to the chemistry, like density and NO_x emissions, all the models predict values that are close each others, and considering than only the SAGE model is a solver based on the chemistry mechanism, the quantity of fuel is one of the more influent variable for the results quality for all the models considered, but in particular for the G-equation and ECFM ones.
Reported below are the main data related to the influence of temperature to the NO_x emissions for the simulation analysed.

MODEL	PEAK TEMPERATURE [K]	NO_X EMISSION [ppm]
SAGE	2293.6	6.23
ECFM	2322.1	6.58
G-EQUATION	2277.3	5.23

Table 19. Comparison of peak values of temperature and NO_x emissions for the three models in rich mixture conditions

Comparison of SAGE and G-equation models for fixed lambda, different ST

Standard mixture conditions (λ=2.0)

From now on the comparison for different ST values will be done only on the SAGE and G-equation models, the reason is related to the high difference in results obtained with the ECFM one and, because comparing the definition of the three models, the SAGE and G-equation have the highest differences in constitutive equations. This allows us to focus more on the model differences.
Moreover, as will be seen, the number of curves on the plots will be a lot, adding other could have only put more confusion and lass clearance in the figures proposed.

Performance

The study of the results is now moved to the analysis of the difference in the models SAGE and G-equation for a fixed value of air/fuel ratio of 2 at the moment of the combustion and changing the spark time in two more values: -20 and -30 (with -25 as the standard condition shown in the previous sections). Those ST are referred to the first cycle, but the cycle shown is the second one that gives the right results, so the ST should be shifted by 720 degrees, leading to the following condition:

- Case ST -20: ST = 700 CAD
- Case ST -30: ST = 690 CAD

All of them considering at 720 CAD the TDC.

The first element of comparison, like in the previous sections, are the pressure and the temperature distributions in time. Starting with the pressure, represented in Figure 94, the main trend that can be seen is that with an increasing of the Spark Advance (SA) the pressure is higher for both the models, and in the same way, for a spark retarded, the pressure is lower. This behaviour is predicted by both the models but is visible that the difference in values is variable. Same consideration could be done regarding the time for the peak pressure value, indeed both models reach the peak almost at the same time with difference in peak values.

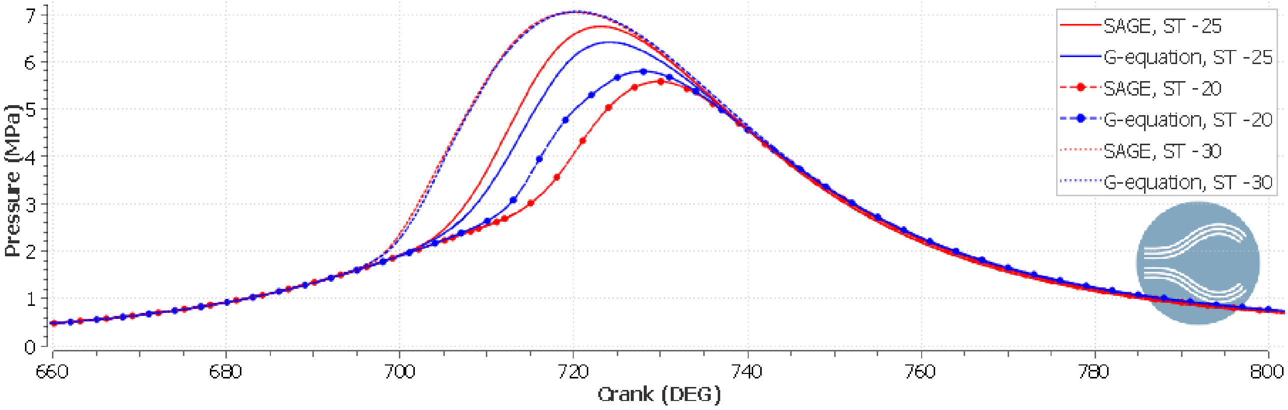

Figure 94. Comparison of the in-cylinder pressure evolution for the SAGE and G-equation models, different ST in standard mixture conditions

The main change in how the models predict the pressure is related to the ST -20 case, in that simulation there is a high delay for the SAGE model that leads to a switch in the position of the curves, where for all the other simulation the SAGE model predicts always the higher values.
The ST -30 case is also interesting because the difference in the models is very low, almost null for all the simulation time.
The same behaviour is also shown in the temperature distribution, Figure 95, where the trends present in the pressure diagram are maintained.

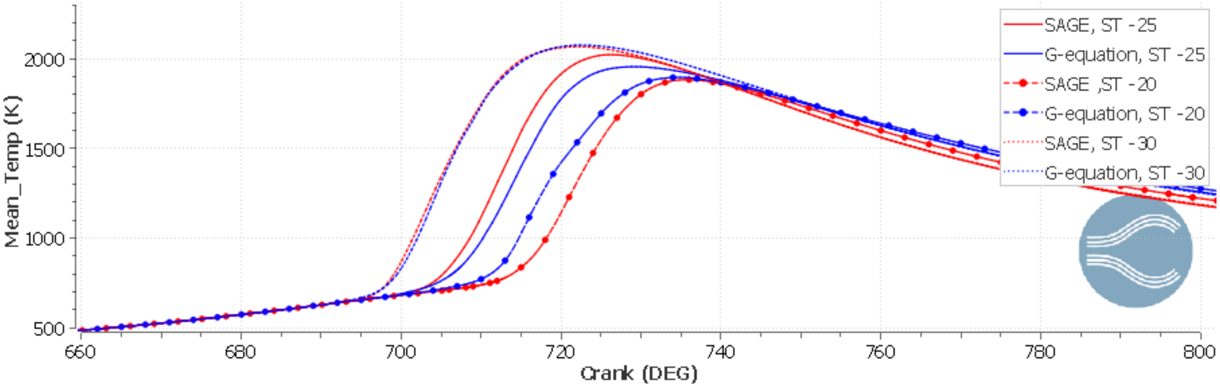

Figure 95. Comparison of the in-cylinder mean temperature evolution for the SAGE and G-equation models, different ST in standard mixture conditions

After the analysis of the two diagrams above, those are the main consideration on the differences between the models.

- For ST -30 the models show a very close behaviour, predicting both higher pressure and temperature due to the SA, but also having very similar results.
- For ST -25 the differences have been already explained in the previous chapter, but the main observation is that there is a delay between the models that is maintained for the entire combustion phase. However, the peak value is reached at the same time.
- Lastly, for ST -20 there is a change in the order of the models, the G-equation one reach for all the simulations higher values. The SAGE model shows an important delay in the pressure and temperature rise.

The reasons that lead to those results could be several. Following the analysis done on the three models, the element that is directly correlated to the pressure and temperature is the HRR, that for all the simulations done is shown in the figure below.

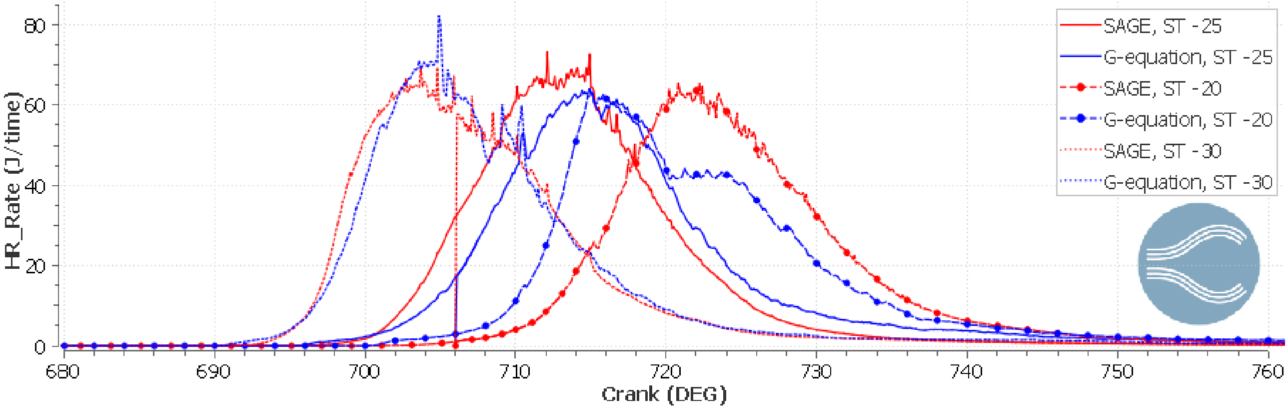

Figure 96. Comparison of the HRR evolution for the SAGE and G-equation models, different ST in standard mixture conditions

What could be seen from this picture is that the correlation with the pressure and temperature diagram is the same, but this could help to understand in particular the behaviour of the ST -20 case, when the values of the models were the opposite. The HRR of the G-equation model for the ST -20 is overlapped to the one of the ST -25 case, being anticipated with respect to the SAGE one. From another point of view, it is possible to state that the SAGE model for the ST -20 case release the heat later with respect to the G-equation model. In particular, this last sentence is supported by the view of the HRR at the instant of the ignition, like Figure 97 shows.

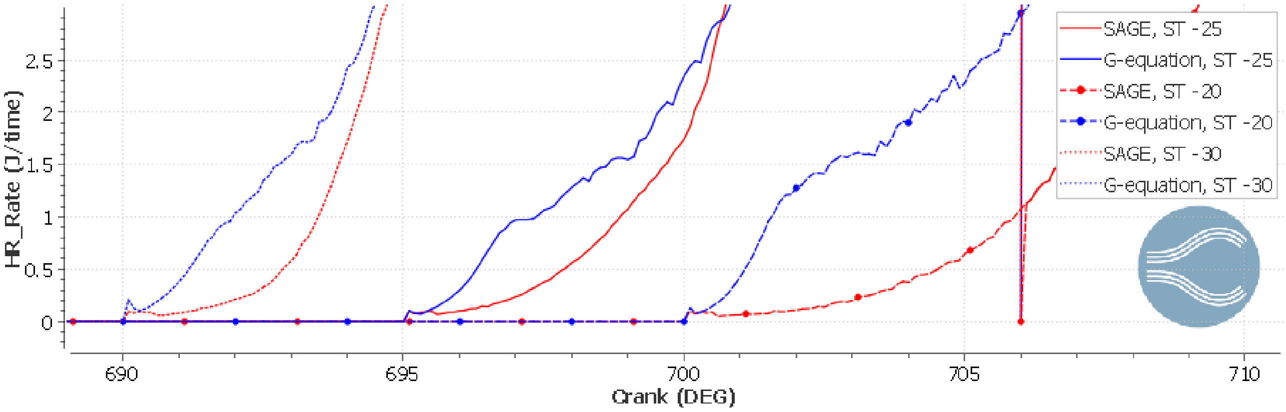

Figure 97. Zoom of the HRR at ST for the SAGE and G-equation models, different ST in standard mixture conditions

From the diagram it is visible that the models for all the cases predict the ignition at the set time. But, after the ignition instant, the speed of growing of the HRR change. For the G-equation model the slope of growing is almost the same for all the simulations, with a less smooth curve retarding the spark. Instead, for the SAGE model the difference between the cases is more important, with a reduction in the slope of the curve, especially for the ST -20 case, then the difference with the G-equation model is higher. This last trend (ST -20) is different from the one of the previous cases, where, in the first two (ST -30 and ST -25) the trends of growing are higher for the G-equation at the beginning, but after few degrees change and the SAGE model predicts higher values. For the third simulation, instead the slope of the SAGE model is particularly lower that the other one, leading to a huge gap in values that is not filled, finishing with an anticipated peak HRR for the G-equation model. Now it is important to point out that, as declared and justified before, for the analysis of the results will always be considered only the second cycle, because it’s the more accurate one and for that simulation, the first is needed for calibrations. However, in the ST -20 case, the two cycles show different results, in particular Figure 98 show the pressure and temperature for this simulation in the first simulated cycle.

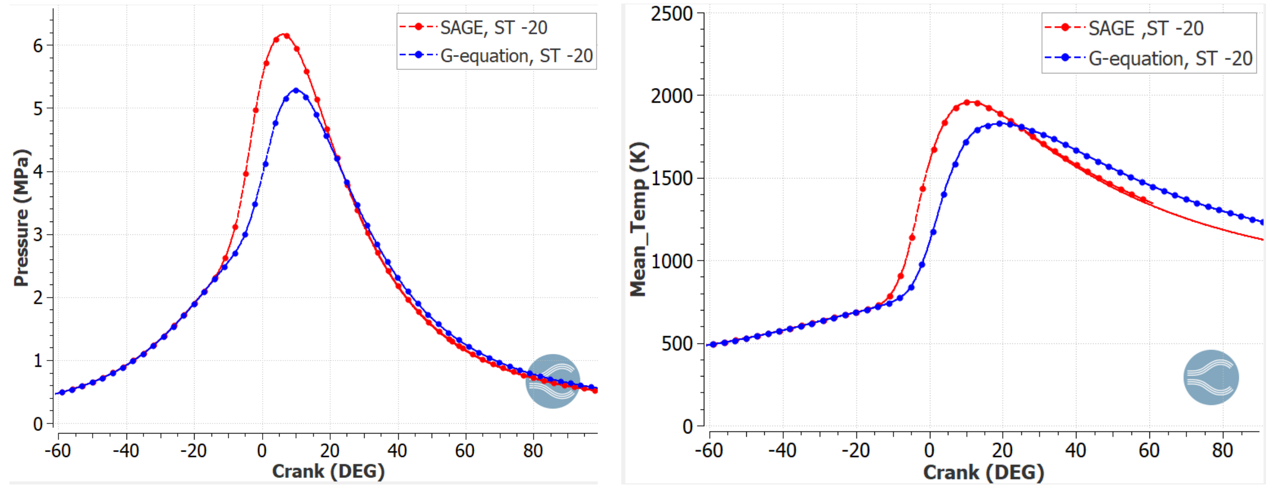

Figure 98. Comparison of pressure and temperature evolution for SAGE and G-equation models at ST = -20 CAD in standard mixture conditions

The image above shows that actually the SAGE model has higher results and anticipates the G-equation one in the first cycle. This is important to be underlined to give a complete analysis of the different models and also to express how much sensitive the simulations are with a hydrogen, being an element small and very difficult to be predicted.

Moreover, the differences of the two cycles could also be due to the residual energy after the first combustion, that can be seen from the IHR diagram, in the figure below.

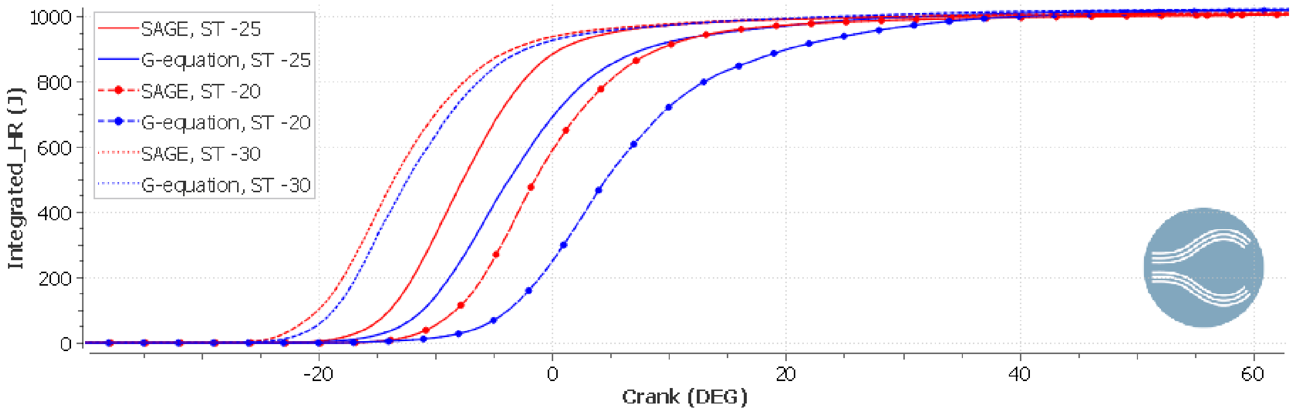

Figure 99. Comparison of the HR evolution for the SAGE and G-equation models, different ST in standard mixture conditions

Here also in the ST -20 case the energy released is higher for the SAGE model, following the behaviour of the other simulations. However, after the combustion the total energy released is higher for the G-equation model in all the simulations, so at the beginning of the second cycle, this model starts with higher energy with respect to the other. This is another reason to the switch in peak values for the ST -20 case for the two models. Indeed, in Figure 100 the HR at the spark for the second cycle is represented to show the differences in energy at the begin of the combustion.

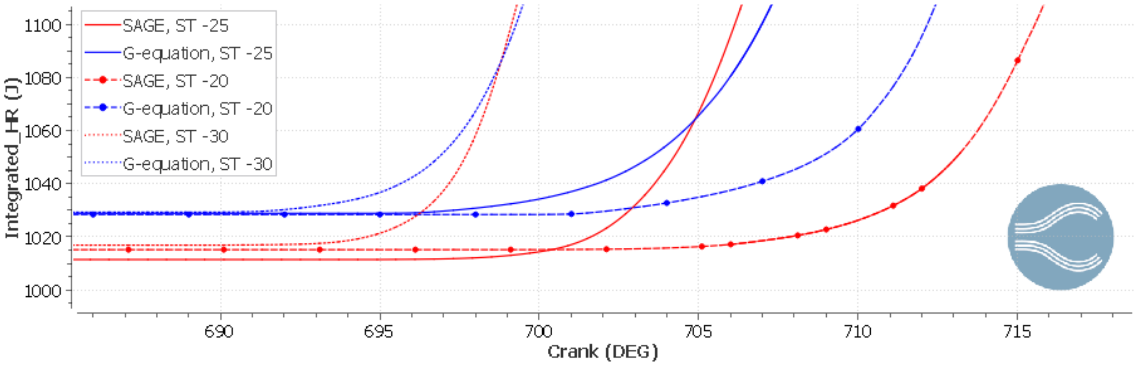

Figure 100. Zoom of the HR at ST for the SAGE and G-equation models, different ST in standard mixture conditions

As can be seen above, the G-equation model has higher IHR for all the simulations done before the ST, and at the instant of the second cycle, also due to higher slope of the G-equation curve, the difference in the two models has not been filled by the SAGE model.
However, it is also visible that the slope of the IHR for the SAGE models in the ST -20 case is lower than the others of the same model. This factor is consistent with the reason of why the first cycle is not considered as reliable results. The combination of the two factors described produced the pressure and temperature distribution shown in Figures 94 and 95.

Going on with the analysis, in the previous section, to explain the differences between the model behaviour has been considered also the influence of the density variation, element that is important for both SAGE and G-equation models for the definition of the spark. Below are scheduled the values of density at the different spark time for all the models and simulations, for this comparison has been chosen to use a table due to the higher number of results. Values that would influence the peak reached and that will be show next.

ρ [kg/m^3]	ST -20	ST -25	ST -30
SAGE	8.15	7.15	6.62
G-EQUATION	8.13	7.13	6.21

Table 20. Comparison of density values at St for the SAGE and G-equation models, different ST in standard mixture conditions

However, for the comparison of these simulations there are differences is the density variation, but, as also shown in Figure 101, are very low. In order to actually see the differences is necessary to highly zoom the diagram, as the same picture shows.

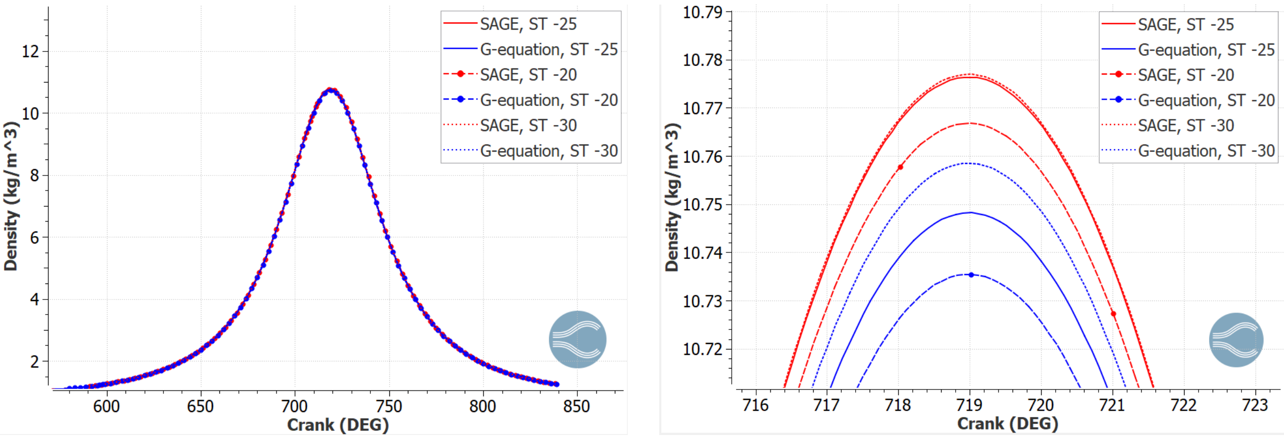

Figure 101. Density evolution (left) and peak value of density (right) for the SAGE and G-equation models, different ST in standard mixture conditions

The figure above shows that the SAGE model predicts always a higher peak value of density compared to the G-equation one. However, independently of the model, the rule that could be state is that the later the ignition, the lower is the density reached. This general rule is validate considering the ideal gas law.

$$\rho = \frac{P}{RT} \tag{47}$$

At later ignition, the volume of the chamber is lower, and so the pressure is higher, leading to higher density at the spark time. Instead, the density after the spark, so during the combustion, could decrease due to heat release and gas expansion. Therefore, in case of higher initial density, like ST -20 case, the rapid expansion due to later ignition could reduce decrease peak pressure, limit the mechanical work and so reduce post-combustion density.

Moving to the comparison of the turbulence parameters, the first that has impact on the results is the TKE, shown in the figure below for the entire combustion phase, for all the ST.

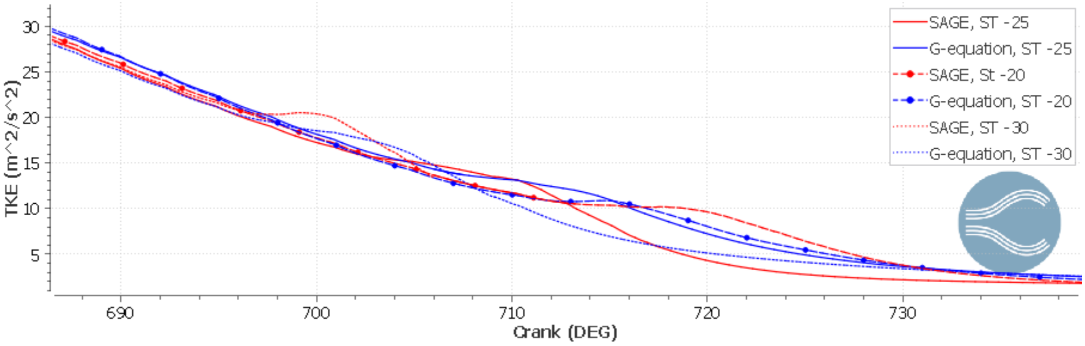

Figure 102. TKE evolution during combustion phase for the SAGE and G-equation models, different ST in standard mixture conditions

The behaviour of the TKE is similar to the one already studied for the comparison of the three models in the previous sections, with a decreasing trend during the combustion. However, it could be seen that for all the simulations done, after the ST with a small delay, all the curves show an increase in values with a peak. This peak is always predicted later by the G-equation model with also lower value. The only curves that have different trends are related to the ST -20 case, where the SAGE model is still the one that predict higher values during the peak, but delayed with respect to the other model in that case, this is another confirm to the differences present in that specific simulation, visible also in the pressure and temperature evolution.

***k* [m^2/s^2]**	**ST -20**	**ST -25**	**ST -30**
SAGE	17.75	21.08	25.47
G-EQUATION	17.68	22.27	25.09

Table 21. TKE values at ST for the SAGE and G-equation models in standard mixture conditions

In Table 5 are represented the values of TKE for all the simulation at the ST and could be seen that the ST -25 case is the one that show the highest difference in values. This could be correlated to the difference also in peak pressure, that, considering the absolute value (and so not taking into account the swish in values for the ST -20 case), for the ST -25 case is the highest between the simulations done.

Other possibilities to explain the trends visible in the pressure and temperature diagrams could be done considering the definition of the models itself. Indeed, in the three simulations done the spark occur at different moments with different conditions:

- The simulation done at ST = -30 and -25 CAD starts with lower values of pressure, temperature and more time available for the combustion to complete.
- The case with ST = -20 CAD starts at higher pressure, temperature and less time to complete the combustion.

Based on the definition of the SAGE model, it has higher benefits in the earlier simulations, due to more time to evolve chemical reactions, even if they start slowly due to lower pressure and temperature (visible from the HRR diagram at ST). Meanwhile, the G-equation model, being primarily driven by flame speed, is limited under low-temperature, low-pressure conditions. On the other hand, in late combustion (ST -20 case), in ignition condition hotter and denser, the G-equation model overcome the SAGE due to an increase in the flame propagation and laminar flame speed. Moreover, G-equation model is not constrained by the chemistry and can overpredict combustion speed under high pressure and temperature conditions. Instead, the SAGE model, in situation of late ignition and low combustion time could lead to a reduction in parameters prediction. This is coherent looking at the study on the laminar flame speed done, that, as shown in Figure 103, during the peak of combustion is higher for the ST -20 case with respect to the others, leading to an increase of the parameter prediction of the G-equation model, that lead to the results already studied.

Moreover, the results obtained in this case are correlated to the pressure evolution diagram, indeed a high value of the S_l comes from a lower pressure one, and in those cases the ST -20 case is the line that show higher laminar flame speed but lower pressure. This is visible also at the ST, with the higher values. For the other two cases the situation is pretty the same.

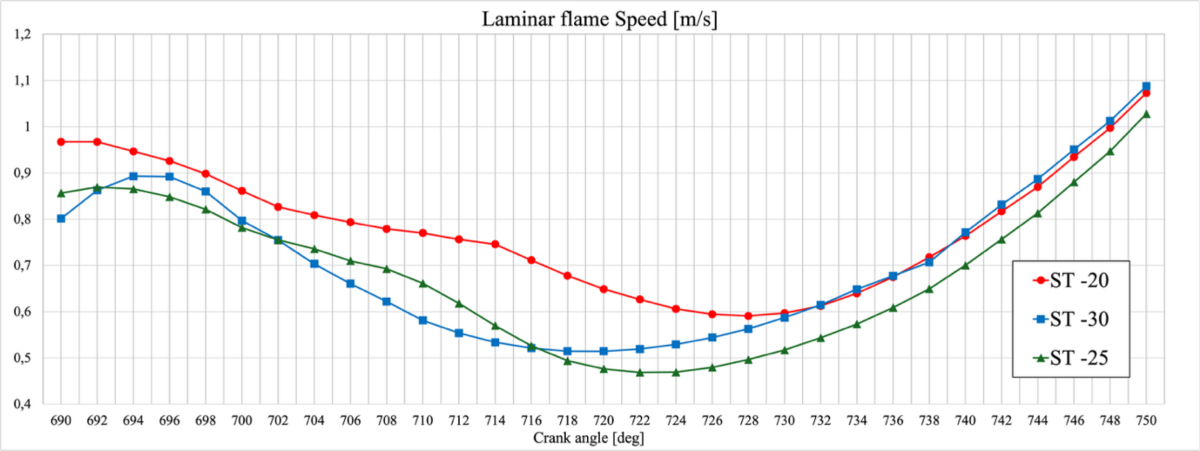

Figure 103. Laminar flame speed for the G-equation models, different ST in standard mixture conditions

The data of this diagram comes from the analysis of the 3D results of CONVERGE. The software doesn't obtain directly the data of laminar flame speed over the time, they must be taken from the spatial distribution of it and make an average over the cylinder, as done for this data. Moreover, the laminar flame speed and laminar flame thickness results are considered qualitatively comparable for both SAGE and G-equation due to the fact that the chemistry solver present in the software is the SAGE model itself, that is needed for the calculation of the TLF table. A data table that has laminar flame speed tabulated a function of mixture fraction, temperature, pressure and equivalence ratio. Reported below is the table that shows all the inputs parameters that defines the TLF table.

Pressure [MPa]	Temperature [K]	Equivalence ratio	Fuel mass fraction
1,5	300	0.3	1
2	400	0.4	-
2.5	500	0.5	-
3	600	0.6	-
3.5	700	0.7	-
4	800	0.8	-
4.5	900	0.9	-
5	1000	1.0	-
5.5	1100	1.1	-
6	1200	1.2	-
6.5	-	1.3	-
7	-	1.4	-
7.5	-	1.5	-
8	-	1.6	-
-	-	1.7	-
-	-	1.8	-
-	-	1.9	-
-	-	2.0	-

Table 22. Input values of the TLF table

Starting from the values of this table, for all the possible combination of them the values of S_l and δ_l are defined by the software.

The figures that follow are the comparison for the different simulations and models for laminar flame thickness, length scale and turbulent velocity fluctuation. All of them needed for the calculation of the turbulent flame speed, another important parameter to be studied in the comparison of the models.

Starting with the laminar flame thickness, that is the measure of the distance over which temperature and species gradients occur in the flame front, it represents the width of the reaction zone. Also, this parameter is considered the same for both SAGE and G-equation models for the same reason of the laminar flame speed. The correlation presented between the laminar flame speed and the flame thickness could be described as inversely proportional, indeed with the proper simplification, the S_l could be expressed in this way.

$$S_l = \frac{\alpha}{\delta_l} \tag{48}$$

where:

- α is the thermal diffusivity, a parameter that depends on the mixture transport and thermodynamic properties.

The main trend that can be seen looking at the figure below is that, after the combustion, the simulation ST -25 is the one with higher flame thickness, instead ST -30 is the one with less flame thickness. The reasons that lead to these results are several, from the conditions like temperature and pressure or the chemical properties of the hydrogen.

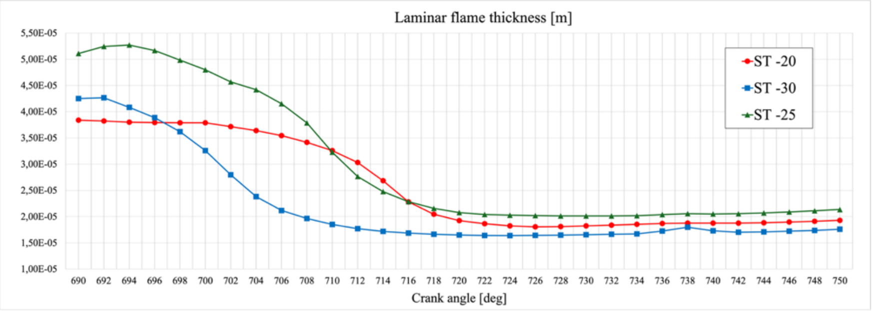

Figure 104. Laminar flame thickness for G-equation model at different ST in standard mixture conditions

Then, the other element needed for this part is the turbulent *length scale*. This parameter represents the size of the largest eddies in a turbulent flow and is important because it gives the idea of which the turbulent velocity fluctuations are correlated and is fundamental for the calculation of the turbulent flame speed. For the simulations done, Figure 105 shows the correlation of the length scale for the different models and simulations.

What visible from the image is that for most of the combustion time the G-equation model predicts higher values of the length scale.

The reason to the different results obtained could be found in the correlation between the turbulence parameters and the combustion ones for the different models, indeed they address the influence of turbulence parameters on combustion, then use turbulence characteristics as input parameters. In particular, combustion affects the mean density field, with density variations affecting turbulence, leading to different results in turbulence parameters. This is another important reason to the study of the density evolution in time for the different models.

However, the simulations with the SAGE model for the ST -20 case show a little difference that could be linked to the difference in the pressure and temperature diagram that have already been explained. Moreover, a common trend for the two models is that the earlier the ST, the higher the values predicted. This trend could be due to the influence of the TKE, that as a direct correlation with the length scale.

$$L \sim \frac{k^{3/2}}{\epsilon} \tag{49}$$

where k is the TKE and ϵ the turbulent dissipation rate. Therefore, with an increase of the TKE there is a decrease of the length scale, and considering the decreasing trend of the TKE, expressed in Figure 102, with earlier ignition the TKE is higher, leading to higher length scale.

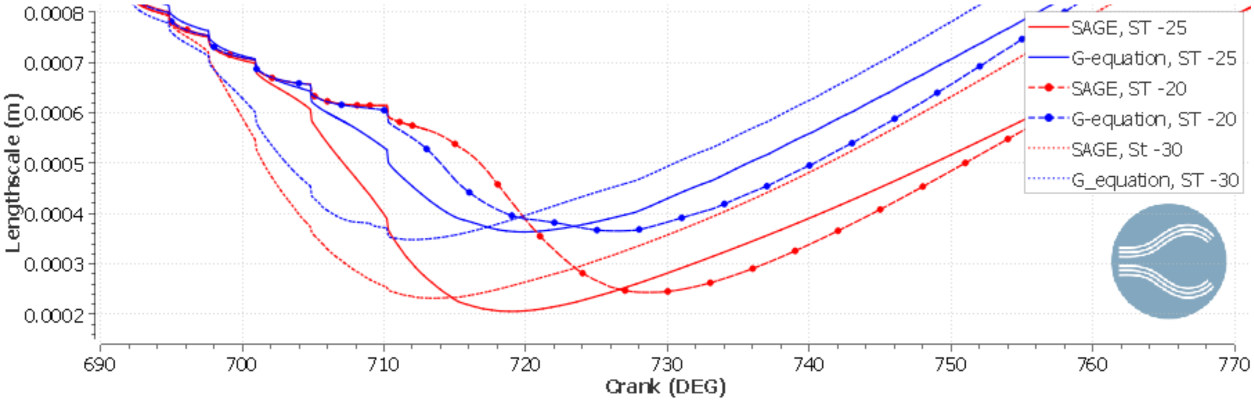

Figure 105. Length scale of different models for the SAGE and G-equation models, different ST in standard mixture conditions

Last parameter needed is the *turbulent velocity fluctuation* that represent the deviations of fluid velocity from its mean value due to turbulence. For the results obtained by the two models the difference could be explained in the same way as for the length scale. However, the difference in the results obtained by the different simulation showed that almost all the time, the late ST led to higher results during the combustion. Instead, after the ST, the results are the same of the length scale, with higher values for earlier spark. Also, in this case the reason is in the correlation between the turbulence parameters, indeed there's a direct correlation firstly with the length scale, because larger turbulence structure could lead to larger fluctuations, but there's also a correlation with the TKE, that, as the name says, is a kinetic energy, so depended on the velocity.

$$k = \frac{1}{2}\left(\overline{u'^2} + \overline{v'^2} + \overline{w'^2}\right) \tag{50}$$

where u', v' and w' are the velocity fluctuations in the three directions. Therefore, the correlation seen for the length scale with the TKE is the same also here for the turbulent velocity fluctuation.

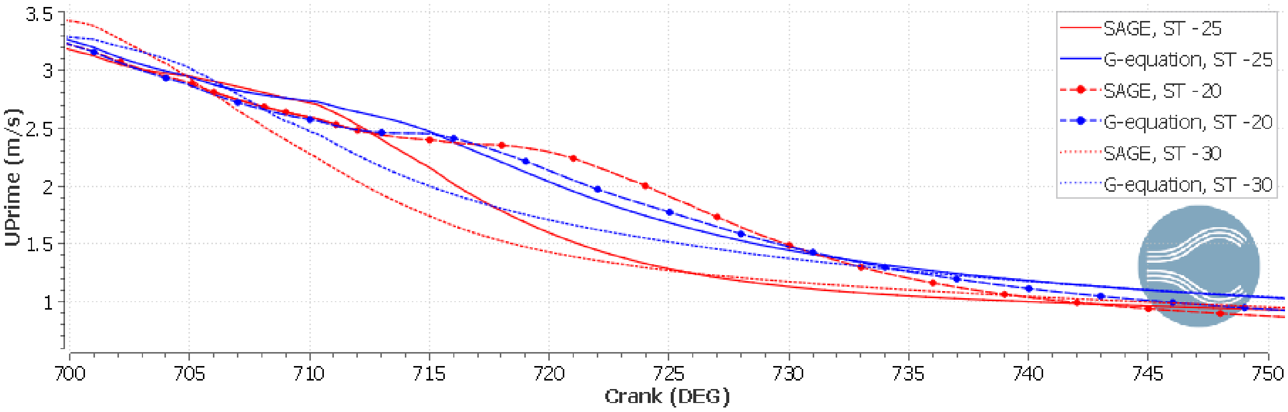

Figure 106. Turbulent velocity fluctuation for the SAGE and G-equation models, different ST in standard mixture conditions

Figure 107 shows what happens for the turbulent velocity fluctuation after 750 CAD when the combustion is over.

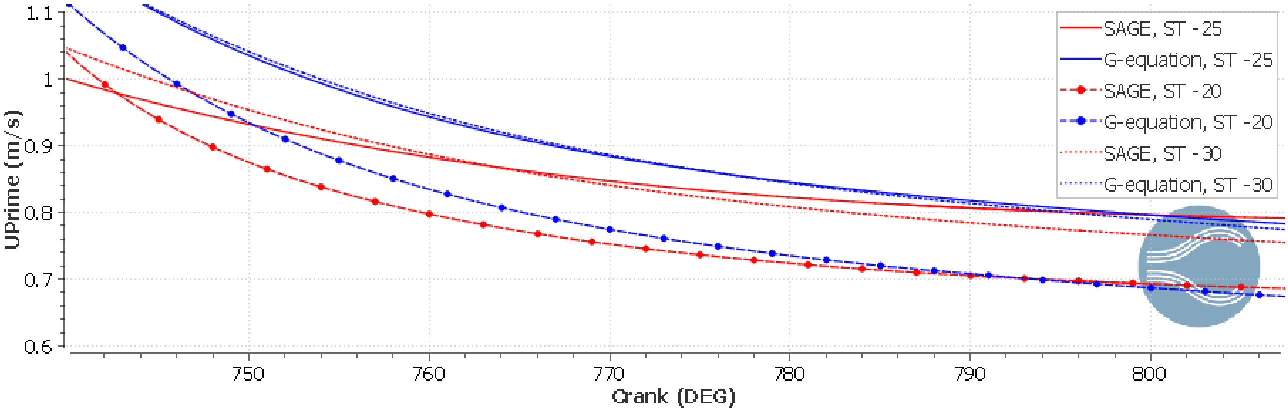

Figure 107. Zoom of the turbulent velocity fluctuation at the end of the combustion phase for the SAGE and G-equation models, different ST in standard mixture conditions

The trend visible in the figure above is that the different models for all the simulations tends to get closer and the lines become almost overlapped, with the ST -20 case being the one with the closed lines. However, looking at the trends of the simulations, the ST -30 and ST -25 converge to a value around 0.8 m/s, instead the ST -20 case has lower values that separates it from the other simulations, under 0.7 m/s.

After the analysis of all the parameters necessary to the definition of the *turbulent flame speed*, a qualitative plot of the turbulent flame speed itself could be defined, starting with the definition already done in the first section of the results analysis. The equation 37 was only valid for the G-equation model, that defines and calculate itself the turbulent flame speed, instead, for the SAGE model it is necessary to use a simplified equation that could only give a qualitative plot and correlation of this parameter between models.

SAGE model, with proper simplification yields the turbulent flame speed as

$$S_t = S_l \sqrt{Re_t} \tag{51}$$

where S_l is the laminar flame speed and Re_t is the turbulent Reynolds number, defined as

$$Re_t = \frac{u'L}{\nu} \tag{52}$$

where:

- u' is the turbulent velocity fluctuation of the flow.
- L is the length scale.
- ν is the kinematic viscosity.

In this equation the TKE, expressed as k, is the parameter that directly defines the turbulent velocity.

$$u' = \sqrt{\frac{2}{3}k} \tag{53}$$

The kinematic viscosity then could be expressed as

$$\nu = S_l \delta_l \tag{54}$$

where δ_l is the laminar flame thickness. The final correlation is the following.

$$S_t = \sqrt{\frac{S_l u' L}{\delta_l}} \tag{55}$$

Figure 108 shows the results of the above equations and the obtained values of turbulent flame speed for the simulations done. Is important to underline that the equations used for the calculation of different variables, like the turbulent flame speed, are useful to define *qualitative* correlation between the different simulations. However, from e *quantitative* point of view the order of magnitude is the same but it must be taken into account that there are a huge number of other parameters that contributes to the definition and variation of those variables. Indeed, the scale in which the S_t of the two models is obtained is different, due to this the comparison will be done on the trends that the curves shown and not on the values obtained.

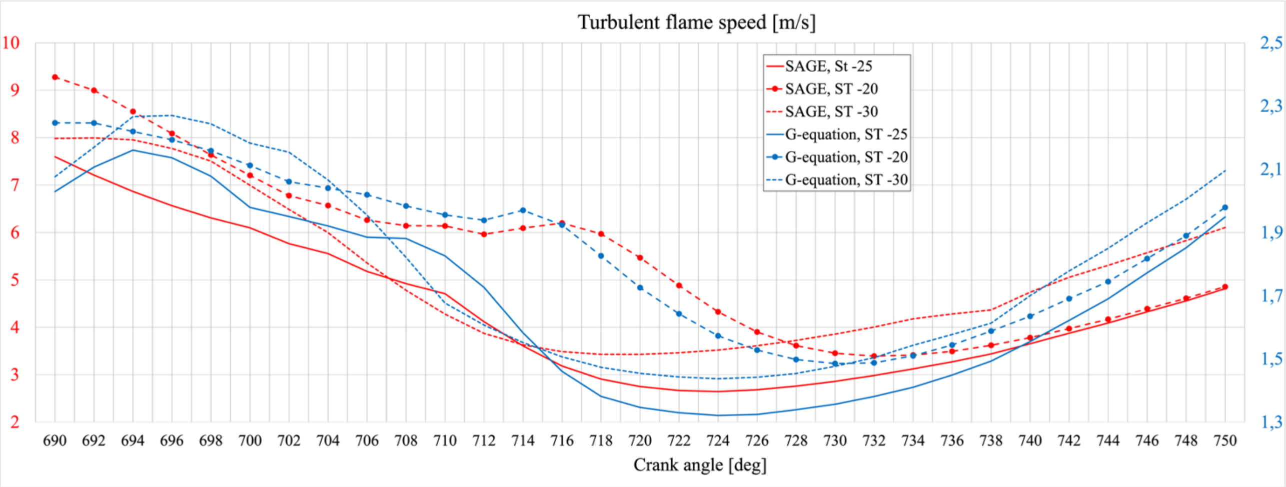

Figure 108. Turbulent flame speed comparison for the SAGE and G-equation models, different ST in standard mixture conditions

The trends obtained for the turbulent flame speed are quite close to the one obtained with the laminar one but there's the possibility to analyse also the difference for the two models used. What can be observed from this point of view is that for all the simulations the trends are quite close each other, but with differences. For all the simulations done, between the two models there are crossing points of the curves, showing that the slopes predicted by the G-equation models is higher both in the increasing and decreasing direction. Moreover, looking at the values on the lateral scale, the SAGE model yields curves with big difference between the higher and lower values predicted during the entire combustion phase, this is also due to the approximate way in which it's calculated but still is correlated with the results previously shown, like length scale and turbulent velocity fluctuation, where the SAGE model has higher decreasing phases with lower values reached with respect to the G-equation model.

This analysis on the effect of pressure, temperature and turbulence parameters on the SAGE and G-equation models could also be used to explain why in the earliest case (ST -30 CAD) the results of the two models are very close each other's. In particular, in that case both models operate in disadvantageous condition, but those limitations led to a convergence of the results. For the SAGE model, the spark occurs in cold condition, with respect to the other simulations, and so lower chemical reactions, that can be completed in more time. Instead, for the G-equation model, low pressure and temperature led to lower laminar flame speed (Figure 103), so the flame font advance slower, matching the rection time of the SAGE model.

NO_x emissions

Next comparison done for the emissions is related to the analysis of how different spark time influence these parameters for the models.

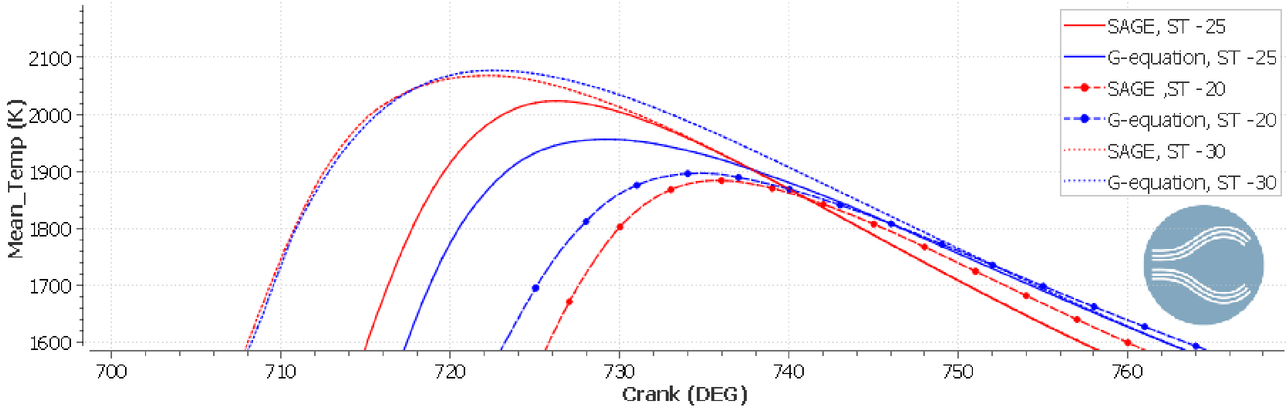

Figure 109. Zoom of mean temperature comparison for the SAGE and G-equation models, different ST in standard mixture conditions

Starting with the comparison of the peak values of the in-cylinder temperature, visible from Figure 109. It shows that with more anticipated ignition, the temperature rise, as already discussed, but also the highest difference in temperature prediction between the models is reached. Indeed, the ST -25 case is the one that shows the highest differences in temperature prediction for the two models. However, in the ST -20 case the values of SAGE and G-equation models are switched, with also a switch in the NO_x prediction.

The NO_x emissions are represented in Figure 110, and the results are coherent with the predictions.

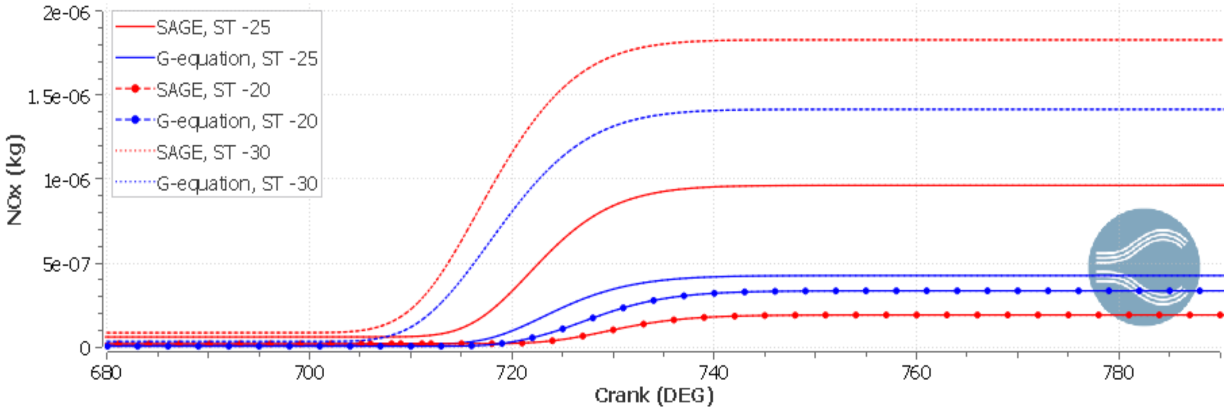

Figure 110. NO_x emissions for the SAGE and G-equation models, different ST in standard mixture conditions

Due to the difference in values, the correct discrepancy between the results for the case with ST -20 is not properly shown, that is the one with high difference in peak values. For that reason, Figure 111 represents only that specific case.

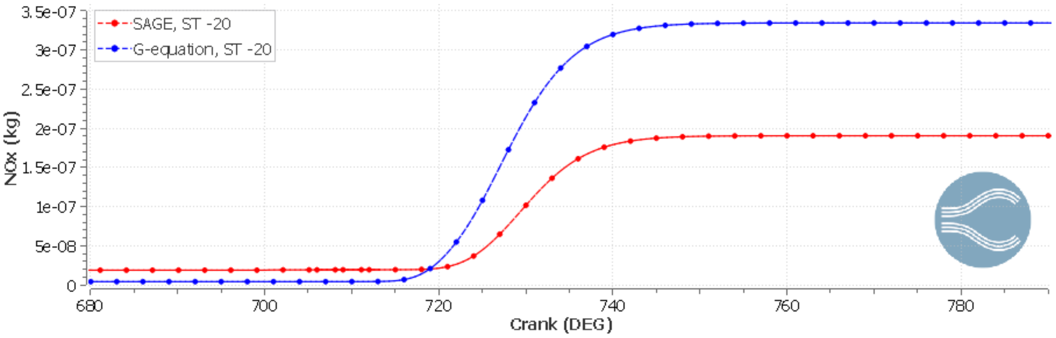

Figure 111. Focus of NO_x emissions for SAGE and G-equation models, ST = -20 CAD in standard mixture conditions

To analyse the results in a more accurate way, the peak values for the different cases and the differences in results are reported in the following table.

MODEL	PEAK TEMPERATURE [K]	DELTA TEMPERATURE [K]	PEAK NO_X EMISSION [PPM]	DELTA EMISSION [PPM]
SAGE, ST -25	2023.47	67.18	0.963	0.538
G-EQUATION, ST -25	1956.29		0.425	
SAGE, ST -20	1884.19	17.13	0.190	0.145
G-EQUATION, ST -20	1897.06		0.335	
SAGE, ST -30	2068.06	8.89	1.83	0.41
G-EQUATION, ST -30	2076.95		1.42	

Table 23. Data of comparison of peak values for temperature and NO_x emissions, for the SAGE and G-equation models, different ST in standard mixture conditions

The table above underlines the correlation between the temperature and the NO_x emissions as analysed before. Moreover, it shows that for both temperature and emissions, for ignitions of -25 CAD or later (like -30 CAD) the values predicted by the SAGE model are always higher than the one from the G-equation model. Instead, for the case with the ignition at -20 CAD, the values of both temperature and emissions are higher for the G-equation model, as also represented in the diagrams and explained in the previous section.

Richer mixture condition (λ=1.7)

In the next part the analysis of the results obtained with a lower value of air/fuel ratio will be discussed. Also, this comparison will be defined as "Richer mixture conditions"

Performance

Starting with the analysis of the performance and following the sequence of results studied in the previous sections, Figure 112 shows the pressure evolution over time. Here, the first comment that could be done is that for all the simulations, both SAGE and G-equation models predict very similar values. This mean that with richer mixture, both models work more closer each other's in all the ST considered for this analysis. Considering the equations and elements that govern the models, a possible explanation is that, for the SAGE model, with higher hydrogen in the chamber, the mixture is more homogeneous. Instead, the results of the G-equation model don't depend directly on the mixture, but with higher fuel, the flame propagation will be higher.

Moreover, looking at the different simulations, without considering which model, ST -30 and ST -25 don't have high difference peak values of pressure, showing a possible saturation of the peak value reachable in that specific condition.

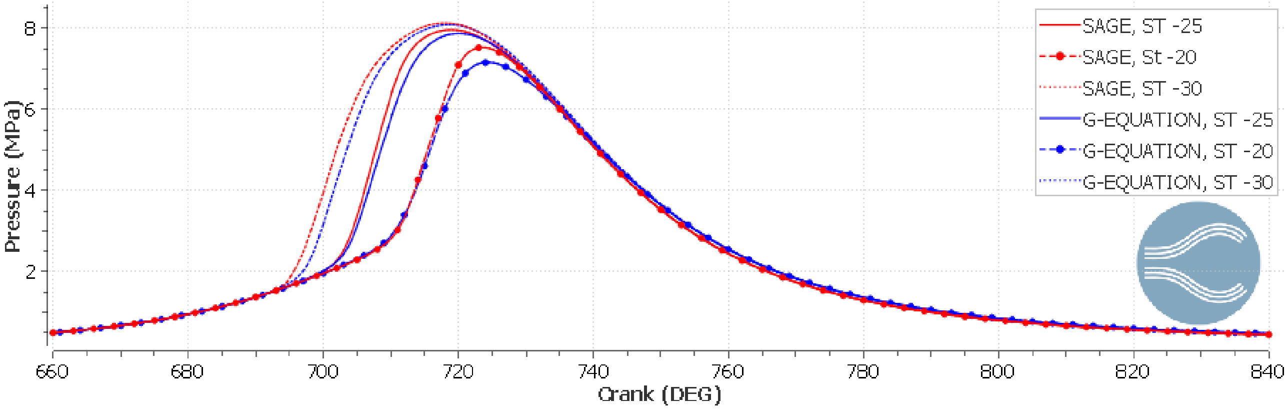

Figure 112. In-cylinder pressure evolution for the SAGE and G-equation models, for different ST in richer mixture conditions

The pressure evolution shows a close peak value of the simulation for ST -25 and -30 CAD, with SAGE model that predicts always higher values and anticipates the pressure increase with respect to the G-equation model. Moreover, in this simulation, for ST -20 case the SAGE model still predicts higher values than the other, while for $\lambda = 2.0$ the results were the opposite only for that specific case. A possible reason to this phenomenon is that, for leaner mixture and later ignition, the SAGE model, based on chemical reaction doesn't have enough time to premix the chemical elements and so has a strong reduction in results values, finishing to be lower that the G-equation model ones.

However, very similar behaviour is visible for the temperature evolution, shown in Figure 113.

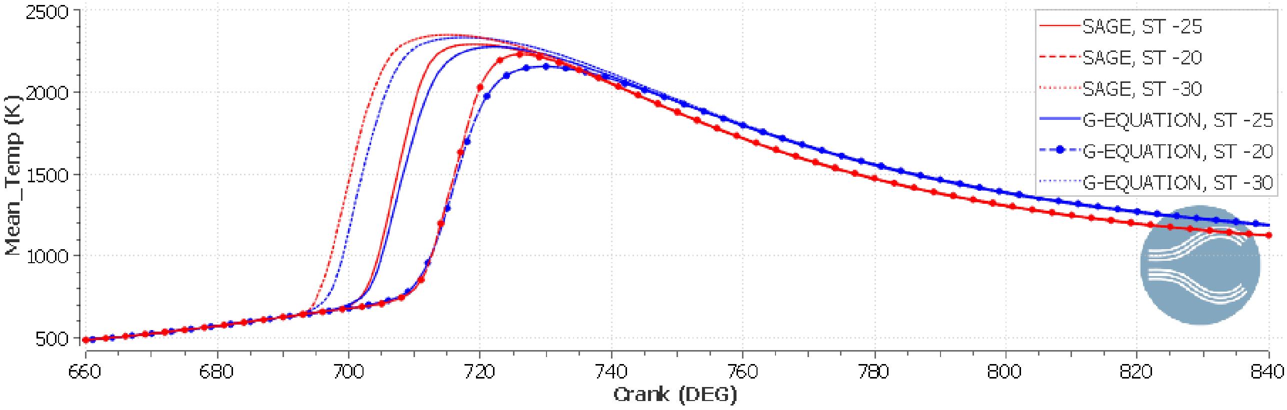

Figure 113. In-cylinder mean temperature evolution for the SAGE and G-equation models, different ST in richer mixture conditions

During the combustion phase, the results could be considered the same as for the pressure diagram, but looking at the end of that phase, after 740 CAD, is clearly visible that the G-equation model has higher values of temperature with respect to the SAGE model, for all the simulations done.

Returning to the main difference visible in those results, the element that shows in the best way this behaviour is the HRR, where, as could be seen in the next image, the peaks of combustion for the three simulations happen almost at the same time, with a small delay for the ST -30 case.

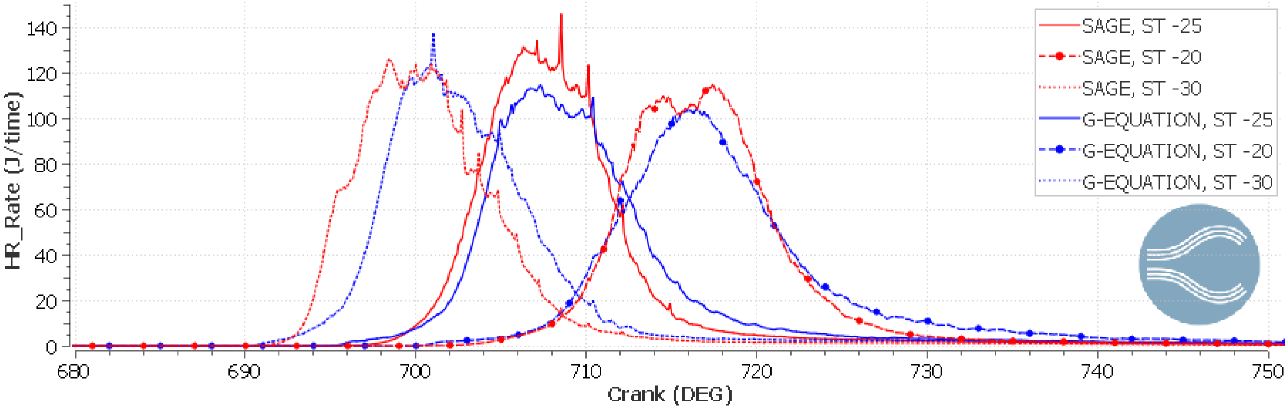

Figure 114. HRR for the SAGE and G-equation models, different ST in richer mixture conditions

Another element that underlines the difference for the two models is the HRR at the ST instant, shown in Figure 115.

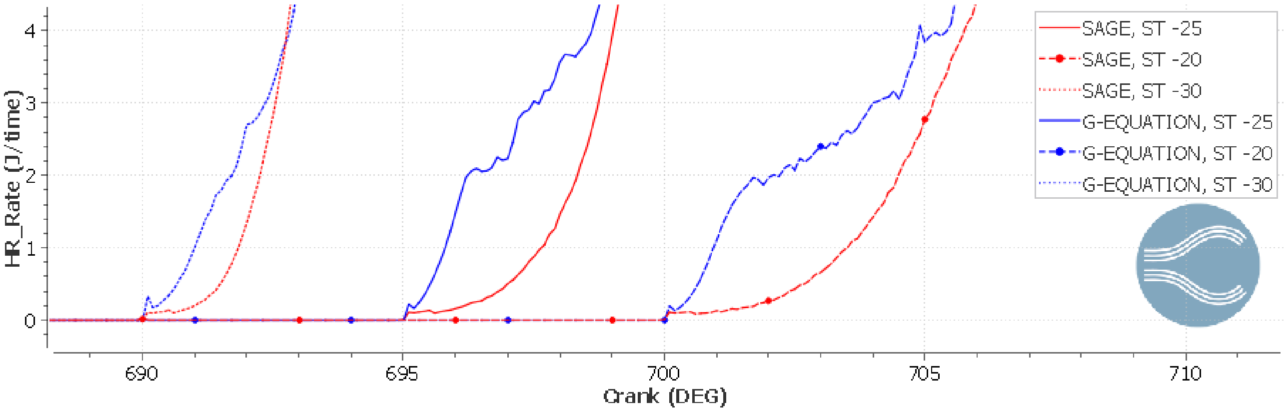

Figure 115. Zoom of HRR at the ST for the SAGE and G-equation models, different ST in richer mixture conditions

The figure above shows that, as expected, the HRR grows very fast for all the simulations that have been done. This is due to the richer mixture and so the higher fuel present in the chamber at the moment of the spark. Moreover, the difference in how the HRR of the two models grow in this figure is closer to the one seen for the standard condition one. However, for this simulation the main changes are visible not at the ST but after that, on the different way the models predict the combustion peak values.

Moving to the IHR diagram, an important consideration is that all the curves, of the same simulation for different models are closer each other. Moreover, this diagram shows in a stronger way that in this case, opposite to the previous simulation done with standard conditions, the ST -30 simulation gives higher difference in results, as visible also for all the previous diagrams.

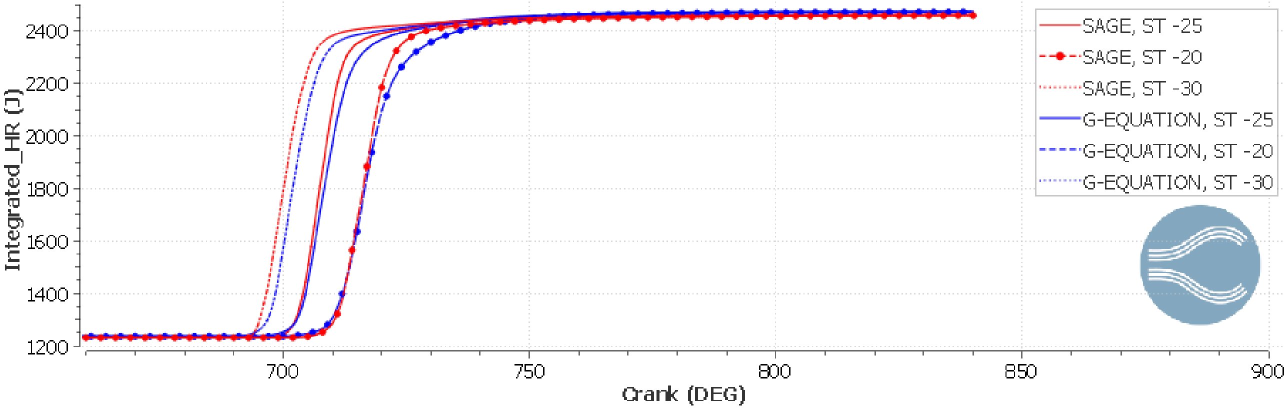

Figure 116. HR for the SAGE and G-equation models, different ST in richer mixture conditions

A possible reason to the difference in ST -30 case could be found in the condition in which the spark occurs. Indeed, with an early ignition, temperature and pressure are lower, there is more time for pre-ignition chemistry and also autoignition to occur. Those events, that are modelled by the SAGE model, could be predicted, however, the G-equation model does not consider them, being purely geometric. This leads in this specific case to have the highest difference in the model's prediction for the ST -30 case.

Considering also the other simulations, the conditions in which they occur influence the results, in particular:

- For the ST -20, the ignition happens late, leading to less time for pre-ignition or autoignition effect to develop and the combustion is mostly flame-propagation dominated, so both models behave in similar way and give similar results.
- For the ST -25, the ignition occurs a little earlier, with more influence from the compression heating and the detailed chemistry model, SAGE, starts to be affected more by those phenomena.

As seen in the previous section, after the first cycle there's a residual energy that is the starting point of the second one, and this has been considered a possible reason to the pressure and temperature distribution. The same happens in this simulation, as can be seen from Figure 117, but in this case the SAGE model for the ST -20 simulation has higher slope in the increasing phase in the heat release, reaching the same values as the G-equation. This could be due, as already said, to the richer mixture in the cylinder that bring the SAGE model to work in a more favourable condition.

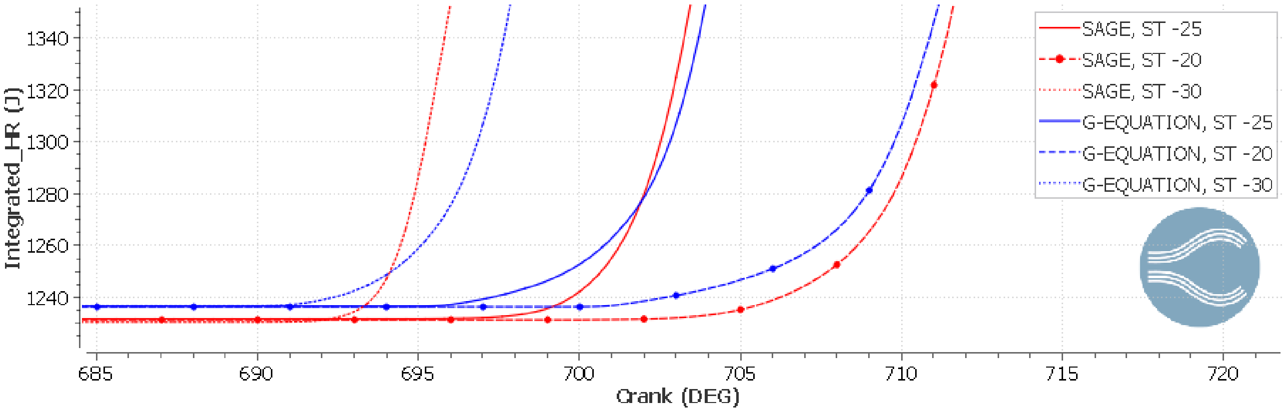

Figure 117. Zoom of HR at the ST for the SAGE and G-equation models, different ST in richer mixture conditions

Another parameter found in the previous sections that link those models is the density, that also in this case doesn't show important difference. The SAGE model still predicts higher values, and earlier ST lead to higher densities in accordance with what already said for the standard condition, that the density after the spark starts at higher values for later ignitions, but could decrease due to heat release and gas expansion during the combustion phase.

The table below reports the density values for the different simulations in order to show that, although the differences are very low, all the cases start at different density values.

ρ [kg/m^3]	**ST -20**	**ST -25**	**ST -30**
SAGE	8.15	7.15	6.23
G-EQUATION	8.14	7.14	6.21

Table 24. Comparison of density values at ignition, for the SAGE and G-equation models, different ST in richer mixture conditions

The table underlines that for the simulations done with a richer mixture, the differences in density predicted by them are very small, the ST -30 case is still the one that shows higher differences but negligible with respect to the one of the standard conditions.

Moreover, Figure 118 shows also a focus on the peak values and there is something interesting. The density predicted by the G-equation model for the ST -30 case is the same as for the ST -25 case, the curves are overlapped. This could mean that the G-equation model, for that specific simulation and the relative conditions, leads to less accurate results, because also without experimental results, should be not possible that simulation with different ST leads to the same density evolution over time.

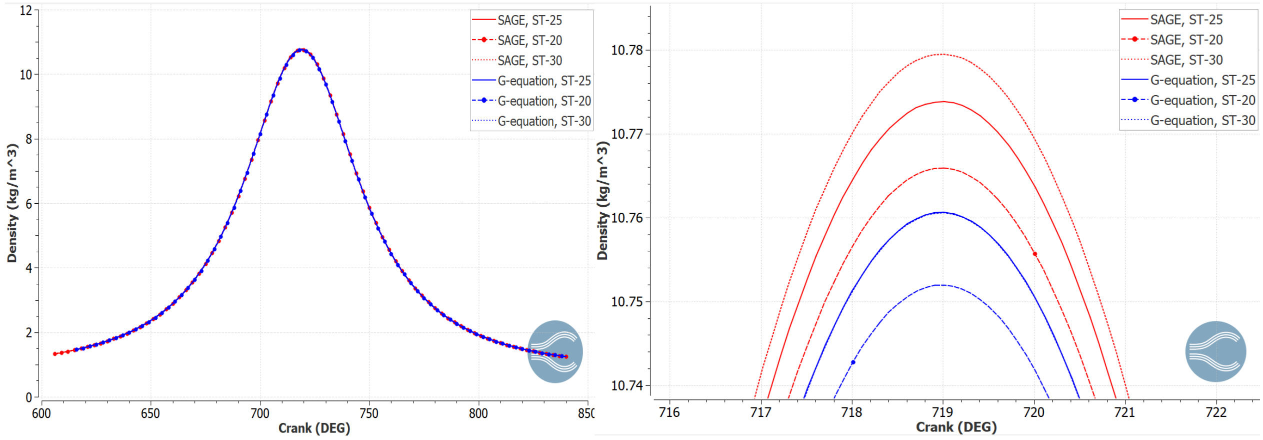

Figure 118. Density evolution (left) and peak values (right) for the SAGE and G-equation models, different ST in richer mixture conditions

The same situation was also present for the density evolution in the ST -30 case, but in the standard condition it was the SAGE models that predicted the two cases with the curves very close each other, reported in Figure 101.

Moving to the analysis of the turbulence parameters and starting with the TKE, Figure 119 shows its behaviour during the combustion phase for all the simulations.

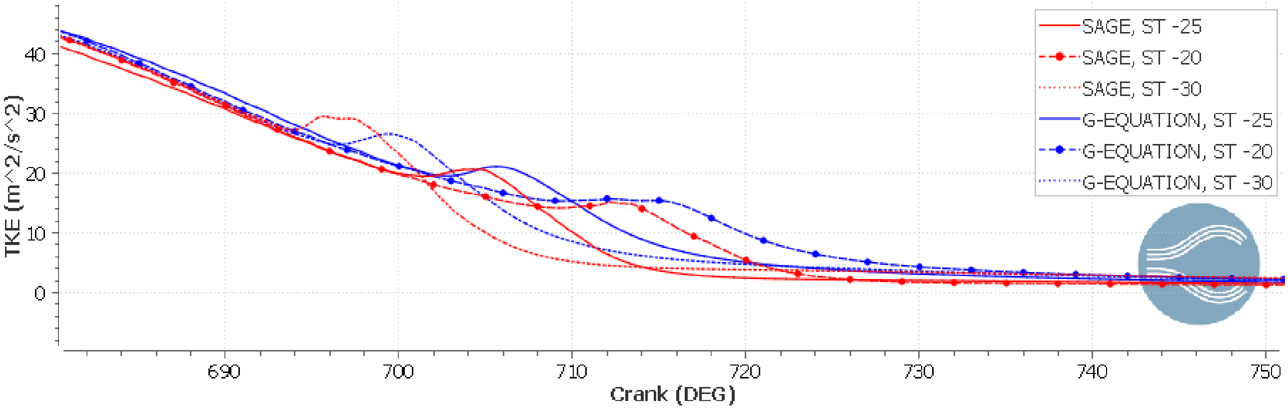

Figure 119. Comparison of TKE for the SAGE and G-equation models, different ST in richer mixture conditions

The image shows the same trend already analysed for the standard condition simulation, when after the ST the TKE has a peak value. However, in this case those peaks are clearly visible and close between models. The G-equation one continues to have some delay in the prediction and seams that, with later ST, this delay is reduced, reaching an almost overlapped curves for the ST -20 case. Moreover, also the values at ST for the different models compared are closer in this case. All of them scheduled in the table below.

***k* [m^2/s^2]**	**ST -20**	**ST -25**	**ST -30**
SAGE	19.79	24.82	31.66
G-EQUATION	21.14	26.88	31.54

Table 25. Comparison of TKE values for the SAGE and G-equation models, different ST in richer mixture conditions

From the data of the table, it is possible to see that there are still some differences between the models for the different cases, in particular for the ST -20 and ST -25 cases, that have some visible differences also in the other diagrams. Instead, for the ST -30 case the value at spark time is almost the same, this is another confirmation that the conditions in which that case operate are optimal for both the models to get closer each other and predict similar values.

Continuing the analysis with the laminar flame speed, Figure 120 shows the temporal evolution during the combustion phase, from the ST to the end.

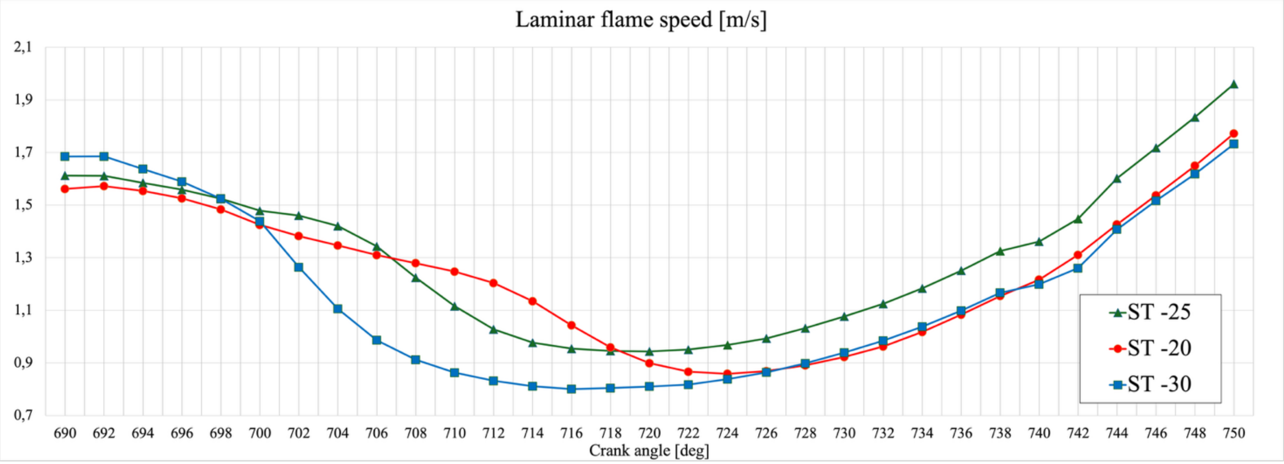

Figure 120. Laminar flame speed for the G-equation model, different ST in richer mixture conditions

The first comment that could be done is that the all the simulations have at the beginning of the combustion a peak of speed. Those peaks are shifted due to the different ST, so the later the ignition, the later the peak. In the figure above the more visible is the one of the ST -20 case that is the latest one, but at the beginning is possible to see the same behaviour also for the ST -25 case.
Some similarities between the curves are that all of them, after the ignition show the same behaviour. Moreover, the cases ST -20 and ST -30 after 726 CAD have very close values each other, but in the ST -25 case the results evolve in parallel with the other, with very small differences.
For the calculation of the S_t, like as been done before the parameters needed are the laminar flame thickness, the turbulent lengthscale and the turbulent velocity fluctuation.
Starting with the first, shown in the figure below, what could be seen in that after the spark all the values reduce to almost the same.

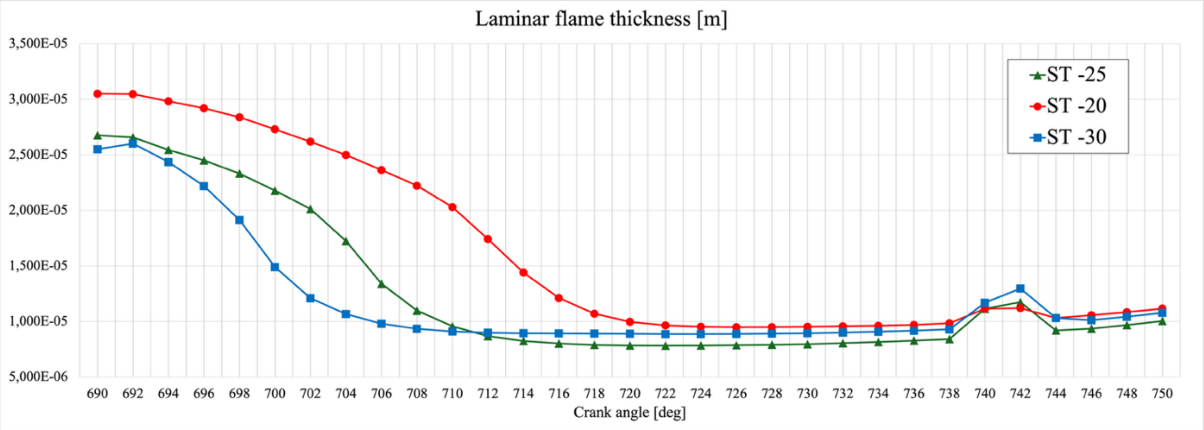

Figure 121. Laminar flame thickness for the G-equation model, different ST in richer mixture conditions

The values here are almost coherent with the one related to the laminar flame speed, due to the correlation between those two parameters, that could be seen properly when both diagrams have stabilized, after 726 CAD. Before that, during the ST and the combustion phase there are several differences between the equations that correlate S_l and δ_l, but as already said, the elements that influence those variables are a lot and especially in a highly turbulent phase like the combustion one, those laminar parameters should have some discrepancies.

Moving to the analysis of the length scale, Figure 122, the values for the different simulations and models are present and the first observation is related to the fact that after the combustion, the SAGE model predicts lower values for all the simulations. However, the trend that is common to all curves is that, after the ignition and a small delay, all curves as a decreasing phase and after that they grow almost parallels each other.

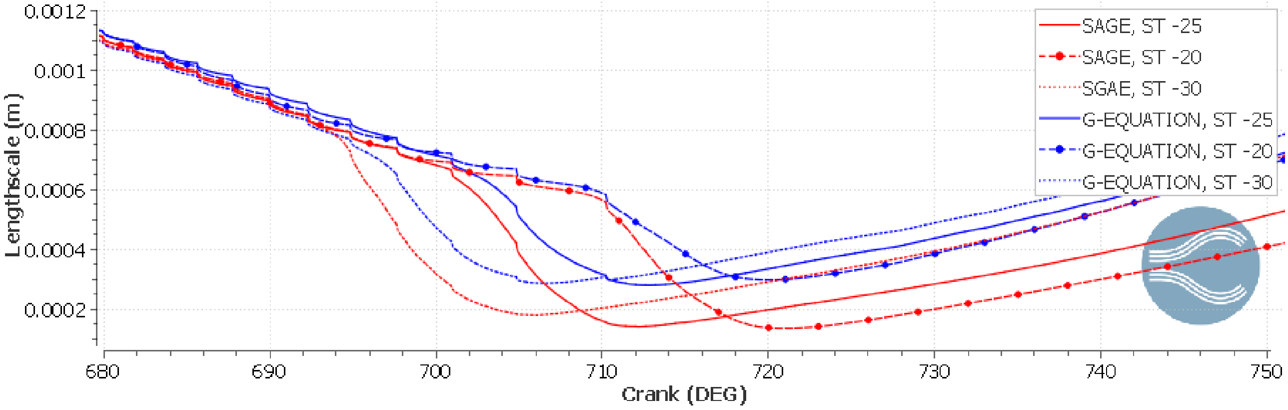

Figure 122. Length scale for the SAGE and G-equation models, different ST in richer mixture conditions

This behaviour was also presented in the previous section for the standard condition, but less clear. Moreover, the difference between models for all simulations is almost the same, with the SAGE model that, during the decreasing phase has a steeper curve and reaches lower values, but the difference of values with the G-equation models is almost constant for all simulations.

The last parameter necessary to the calculation of the S_t is the turbulent velocity fluctuation, shown in Figure 123.

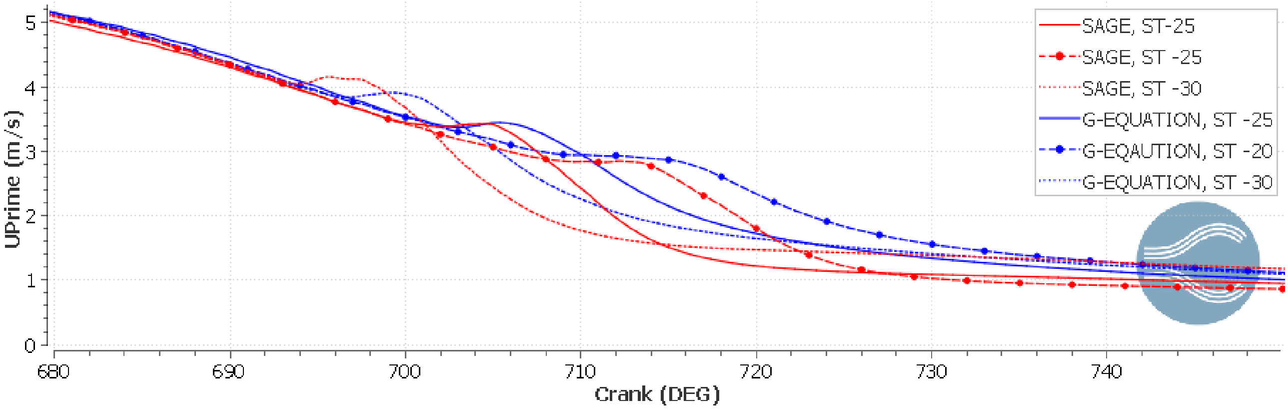

Figure 123. Turbulent velocity fluctuation comparison for the SAGE and G-equation models, different ST in richer mixture conditions

The trend of the different curves presented in this figure shows some correlation with the one of the previous length scale diagrams, indeed after the ignition all the simulations report a first peak value and then a reduction that at the end of the phase leads to a constant value. The main difference in models that could be seen here is that the later the ignition, the better the two models predict the same value, in particular the peak value after the ST. For the ST -30 case there is a delay between the models in how they predict that initial peak that become smaller for the other simulations. The same delay influence also the results in the decreasing phase, but remaining always not too far each other, similar results obtained for the standard condition in the previous section.

From the results evaluated in the previous figures it is possible to obtain the trends of the turbulent flame speed for the different simulations done with the SAGE model. Instead, as already explained, the one related to the G-equation model has been calculated by the software trough equation 37.

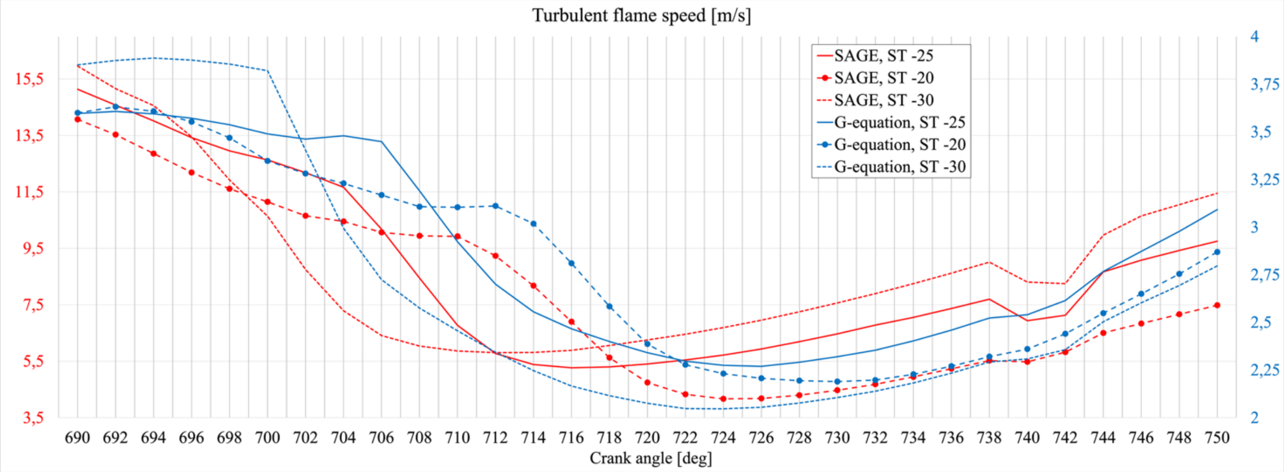

Figure 124. Turbulent flame speed for the SAGE and G-equation models, different ST in richer mixture conditions

Represented in Figure 124 are all the curves for all the simulations done. Considering the differences in values what could be compared also in this case are the different trends shown. The main trend that could be seen is that the curves related to the same simulation have different slopes and the curves meet at a “virtual point”, considering that they could not meet due to the difference in scale. Those points suggest the different behaviour of the different models at the peak value of the combustion, differences that are visible in the pressure and temperature distribution.

The figure below shows actually those differences at the peak values on how the two models reach it, with different slopes and curve shapes.

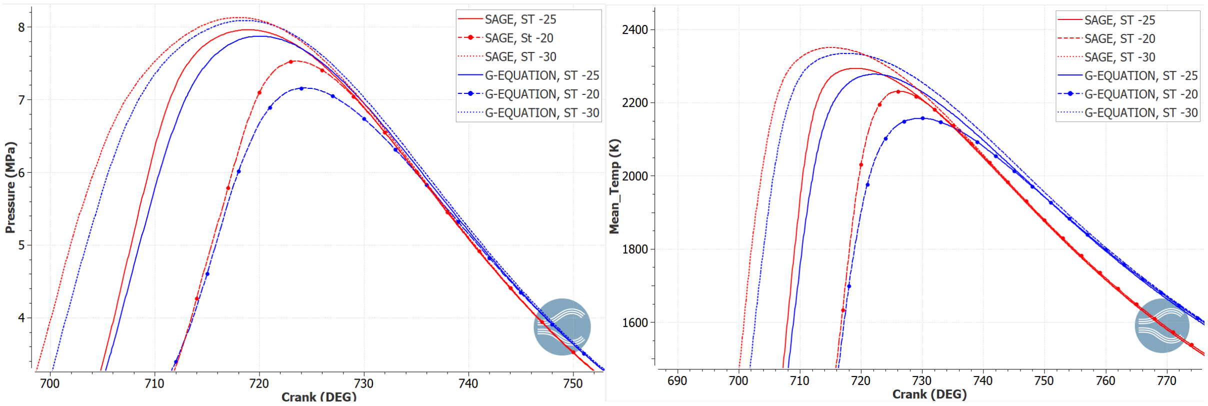

Figure 125. Zoom of pressure and mean temperature evolution for the SAGE and G-equation models, different ST in richer mixture conditions

Moreover, the trends found in the other parameters, with a first increase right after the spark and then a strong decrease of values, shifted for the relative ST, are presented also in this case. This is clearly visible for both models, with the G-equation one that has more accentuated peaks with respect to the SAGE one.

Something that could also be seen from the comparison is that, as said all the curves related to the same simulation meet in a virtual point, but in the other degrees they are almost parallels, and this could be an element that correlates the results between them.

Looking at the results of the same model, instead it is possible to see that for the SAGE model, the behaviour of the curves is almost the same, just shifted between them, with the S_t of the different cases after the ST with a clear order, the ST -30 case is the one that shows higher values, followed by the ST -25 and then the ST -20. Instead, for the G-equation model, this is not completely true, indeed at the beginning of the combustion also for this model the simulation has some peaks with the same rule according to which the earlier ignition has higher peaks, but after the decreasing phase, the ST -30 and the ST -20 case reach almost the same values, with the ST -25 gives higher results far from the others.

NOx emissions

Moving to the analysis of the NO_x emissions for the different simulations, the first prediction that could be done is that, as the amount of fuel is higher, the emissions will also increase with respect to the standard condition's simulations. However, the temperature diagram has already been shown in Figure 126, but for this part is crucial to look deeply at the differences in peak temperatures reached for the different simulations.

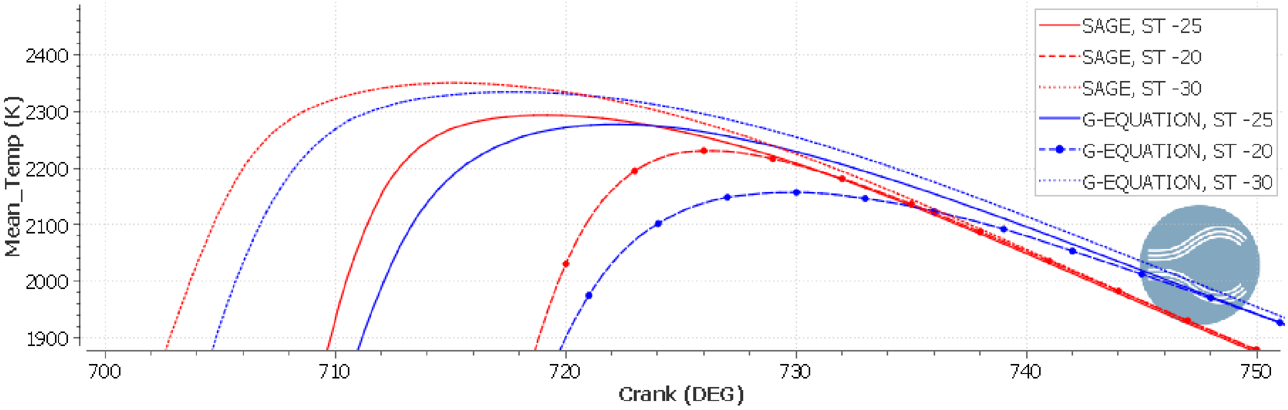

Figure 126. Zoom of peaks of mean temperature for the SAGE and G-equation models, different ST in richer mixture conditions

The figure above shows the peak values of mean in-cylinder temperature for all the simulation done and the main difference that could be seen is related to the ST -20 case.
Next, the NO_x emissions are reported in the following image.

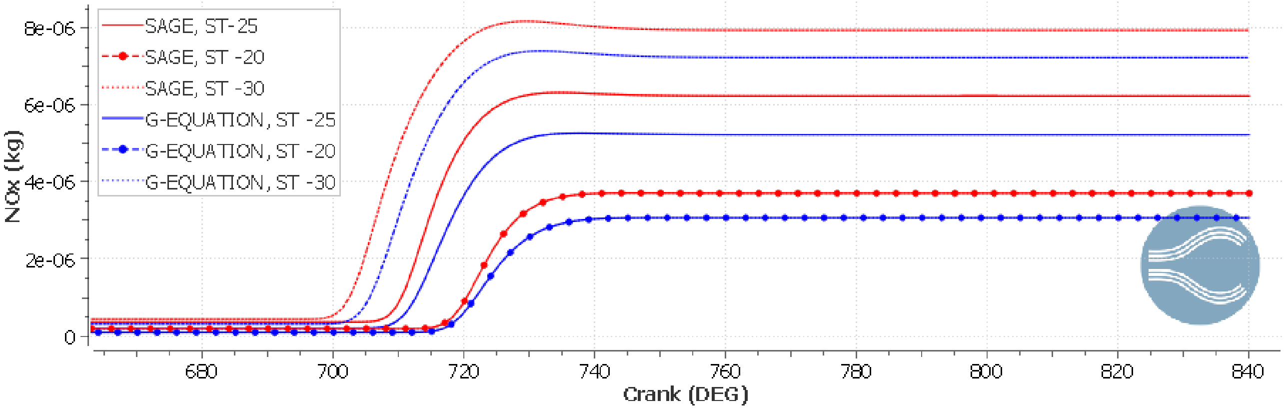

Figure 127. NO_x emissions comparison for the SAGE and G-equation models, different ST in richer mixture conditions

Looking at the diagram the main consideration that could be done is that earlier ignition leads to higher emissions, that is what already happened for the standard condition simulations. However, related to the difference of the models, the ST -25 case is the one that shows the higher difference in prediction of emissions, although it was not the highest difference in temperature peaks. This underlines that not only the temperature influences the prediction of NO_x emissions.
To better compare the different results obtained, the table with all the important parameter is reported below as already done in the previous sections.

MODEL	PEAK TEMPERATURE [K]	DELTA TEMPERATURE [K]	PEAK NO$_X$ EMISSION [PPM]	DELTA EMISSION [PPM]
SAGE, ST -25	2293.2	15.9	6.236	1.008
G-EQUATION, ST -25	2277.3		5.228	
SAGE, ST -20	2230.6	73.5	3.706	0.637
G-EQUATION, ST -20	2157.1		3.069	
SAGE, ST -30	2350.4	16.5	7.945	0.711
G-EQUATION, ST -30	2333.9		7.234	

Table 26. Comparison of peak values of temperature and NO$_x$ emissions for the SAGE and G-equation models, different ST in richer mixture conditions

The table above confirms what already said about the differences in the models, indeed the ST -20 case is the one that shows the highest difference in temperatures, however, is not the one with the highest difference in NO$_x$ emission, that is the ST-25 case. A possible explanation of these results could be related to the difference in the condition in which the three simulations develop. The ST-20 case starts later than the others, at higher temperature and pressure conditions, with a rapid and intense flame propagation that emphasizes the differences in the combustion models. However, in the ST-25 case, the situation is an intermediate between early (ST -30) and late (ST -20), and in that condition the chemical reactions play a significant role in the definition of the results related to the chemistry, like the emissions of pollutant gases. Therefore, the SAGE model could predict on a complete way the variation in chemical elements, while the G-equation models is a less accurate way, leading to the highest difference in the results, that could also be due to the richer mixture in which those simulations develop.

Comparison of SAGE and G-equation models for different lambda, fixed ST

After the discussion of the differences in results obtained for the simulations with the same λ, changing the ST, this section will compare the results for the same value of ST but changing the air/fuel ratio, in order to understand how this parameter influence the models.

ST = -20 CAD

Performance

Starting with the analysis of the performance results for the latest ignition simulation, Figure 128 shows the pressure evolution.

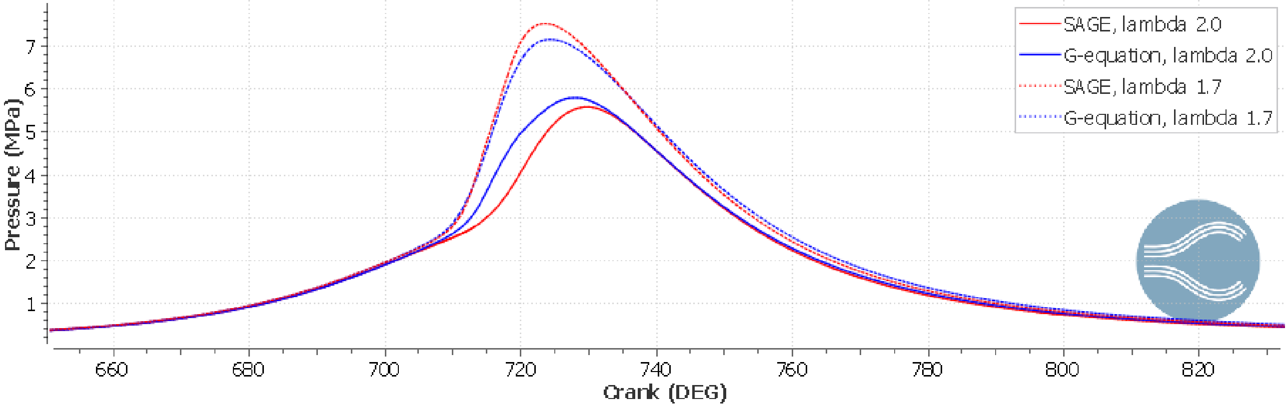

Figure 128. In-cylinder pressure comparison for the SAGE and G-equation models, different mixture conditions and ST = -20 CAD

This diagram shows the mayor differences found in all the simulations done, that has been already explained in the previous section, related to the switch in values for the case of λ = 2.0. However, what could be noticed is that the simulation with λ = 1.7 has higher pressures, as expected for the presence of more fuel, but also more closer curves of the two models, that have an important difference in the peak values, but in the remaining part of the diagram the curves are almost overlapped, showing that those are for sure more favourable condition for both models to obtain the same results. Or could be that both models are in a complex condition to predict, due to the fast and strong combustion, due to the later ignition, and then both limitations lead to the same results.
Another element of comparison is that the peak of the results from the two values of λ compered are shifter toward the right, representing a peak of combustion for both the models, like both as limitation in the prediction of the results in that specific case, probably related to the lower amount of fuel.
Same consideration could be done also looking at the temperature evolution for the simulation considered, Figure 129. The feature that remains also in this diagram and that is relevant to underline is that in the λ = 1.7 case also the spark time is predicted the same for both models.

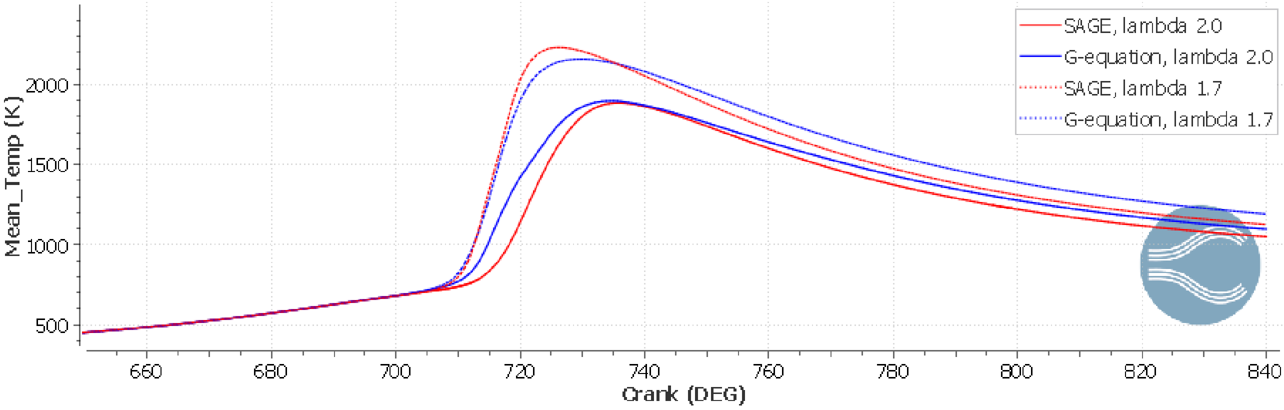

Figure 129. In-cylinder mean temperature comparison for the SAGE and G-equation models, different mixture conditions and ST = -20 CAD

Then, this last consideration, related to the spark time, is important because will be reflected at the peak value, in particular if both models predict the ST at the same instant, then also the peak value will be reached at the same moment. Instead, like in the λ = 2.0 case, the shifts in the ST prediction are then extended also to the timing of the peak values reached.
This could be also seen in the HRR diagram, shown in the figure below, where the standard mixture case has shifted values, instead the richer one has the HRR curves close each other.

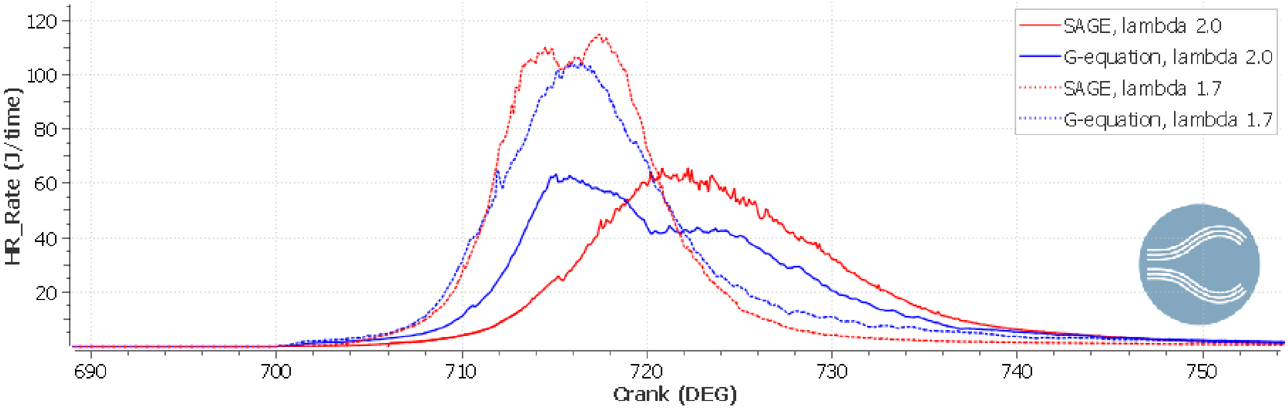

Figure 130. HRR comparison for the SAGE and G-equation models, different mixture conditions and ST = -20 CAD

Moreover, the image shows clearly that the simulations done with different air/fuel ratio, having the same ST, the curves of HRR are shifted, with the one related to the richer mixture clearly earlier that the other. This could be due to the mixture itself, higher presence of fuel gives more possibility for the flame to propagate and the heat to be released. Other reason could be found in the IHR diagram, next figure, that represents the sum of all the energy, also coming also from the previous cycle.

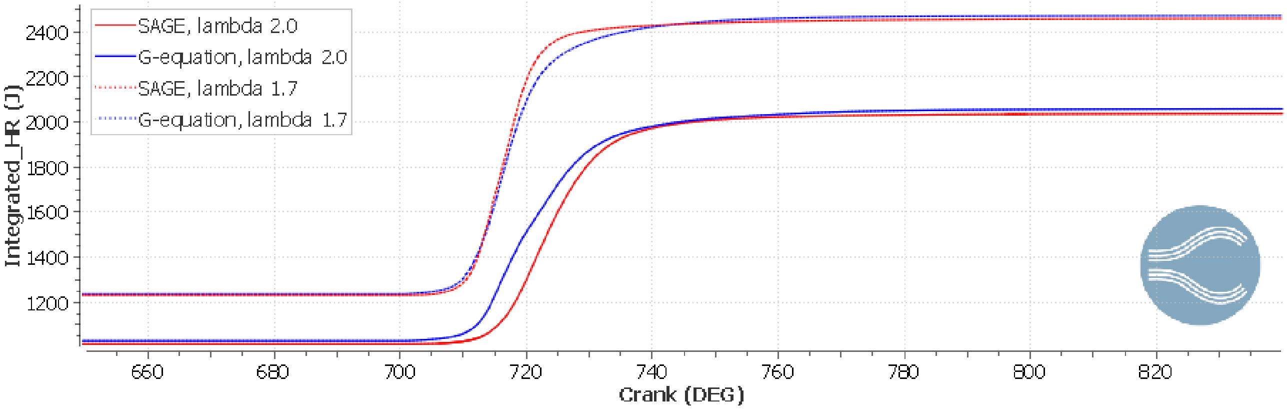

Figure 131. HR comparison for the SAGE and G-equation models, different mixture conditions and ST = -20 CAD

In the figure above the different starting points of the simulation compared are clear, and this could also be a reason to the shifted values obtained. However, the higher differences in the model's prediction for the $\lambda = 2.0$ case is visible, in particular in the first part of the combustion.
Moving to the analysis of the turbulence parameters, the first that gives important discussion is the TKE, in Figure 132.

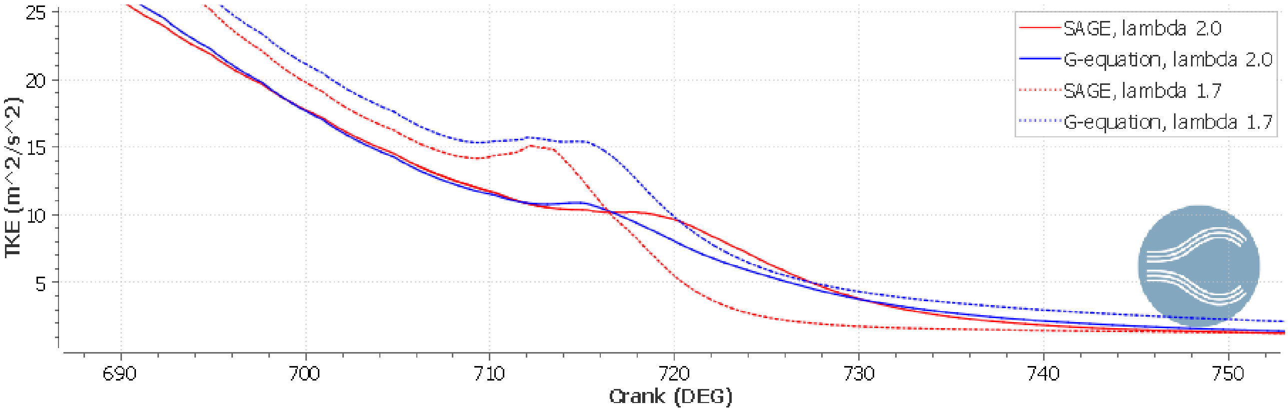

Figure 132. TKE comparison for the SAGE and G-equation models, different mixture conditions and ST = -20 CAD

The image shows the values for TKE both at the instant of the spark but also later during the whole combustion. The main difference in the simulations is visible for the spark moment, when the $\lambda = 1.7$ case has higher values with both models, and then predicts a peak increase earlier than the other simulations. Moreover, in the simulations with standard mixture, the prediction of values for the two models is shifted in time, with the SAGE that is retarded with respect to the other one. Instead, in the richer mixture simulation, the G-equation model for all the time has higher values, but with the same behaviour as the SAGE one, just shifted in values. This consideration is correlated with the one done in the previous section for the analysis of the S_t for the different ST. Here the correlation between the turbulence parameters and the performance one was found as not on how much the curves are close each other, but on how much the curves have the same behaviour and develops in parallel. In this case the curves for the $\lambda = 1.7$ cases are not perfectly parallel, but better that the other cases, that, despite having similar values, the pressure and temperature curves are highly different each other.
Next parameter that should be analysed is the laminar flame speed, reported in Figure 133 for the simulations considered.

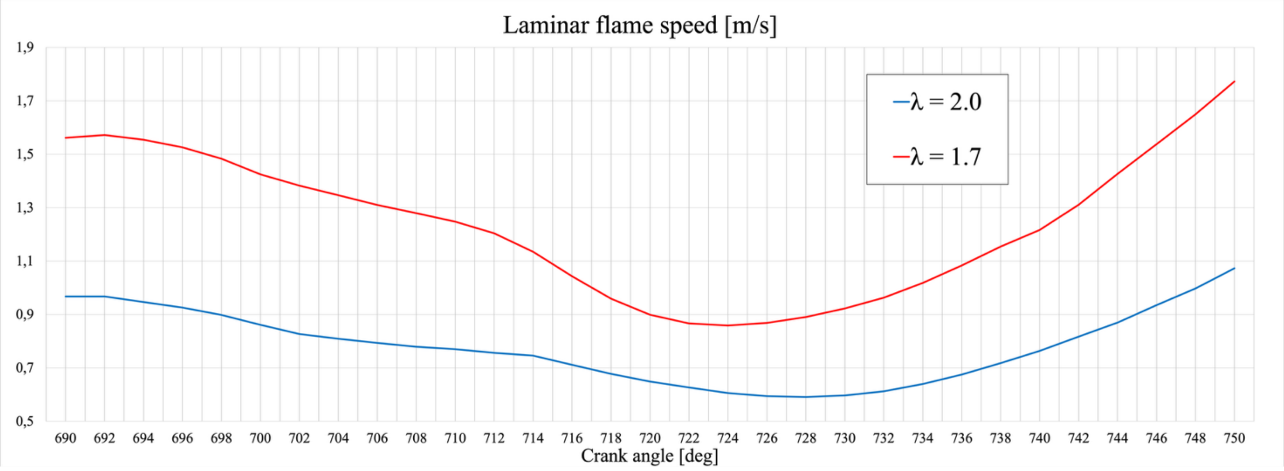

Figure 133. Laminar flame speed comparison for the SAGE and G-equation models, different mixture conditions and ST = -20 CAD

The relationship between the curves is what expected, considering that for the simulation with $\lambda = 1.7$ the higher amount of fuel leads to higher performance features and so also the flame speed will increase. Moreover, the curves show a good correlation each other with a similar behaviour.
Instead, the opposite is represented in the next figure, related to the laminar flame thickness, that, as already demonstrated in the previous sections has an inversely proportional correlation with S_l.

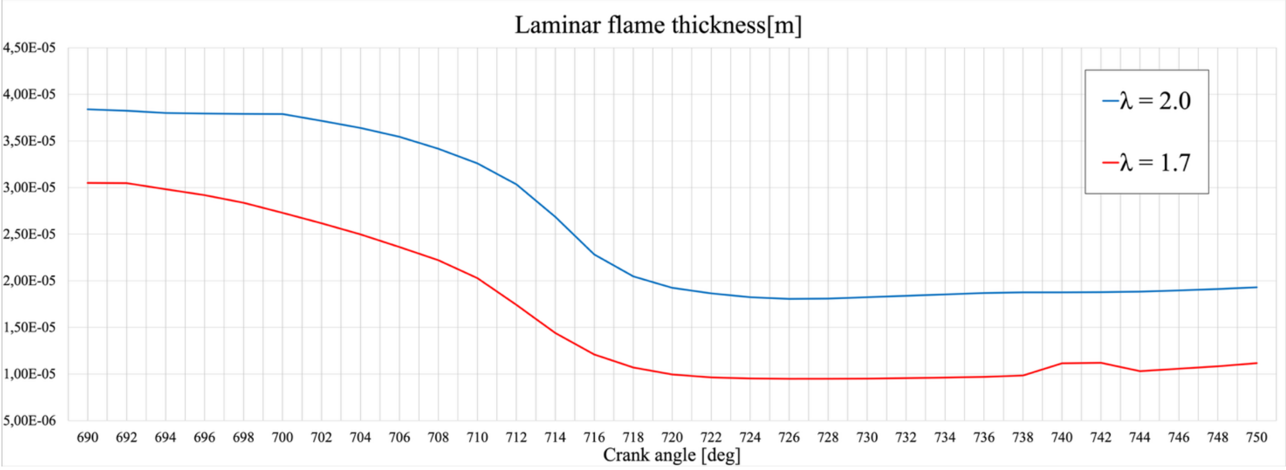

Figure 134. Laminar flame thickness for the SAGE and G-equation models, different mixture conditions and ST = -20 CAD

Moving to the study of the other parameters, necessary to the definition of the turbulent flame speed that is the main element of comparison, the first shown in the figure below is the length scale. Also, in this diagram the trend that could be seen is coherent with the already analysed ones, indeed the simulation with $\lambda = 1.7$ had a stronger difference in values, with the SAGE models that predict lower values, underling the difference in the model's definition. Instead, the $\lambda = 2.0$ simulation had closer values, with less difference in magnitude, but with an important delay in the curves. Moreover, at the instant of the spark, at 700 CAD, this last simulation case has the values for the two models that are almost overlapped each other, instead the richer mixture case shows higher differences at the ST.

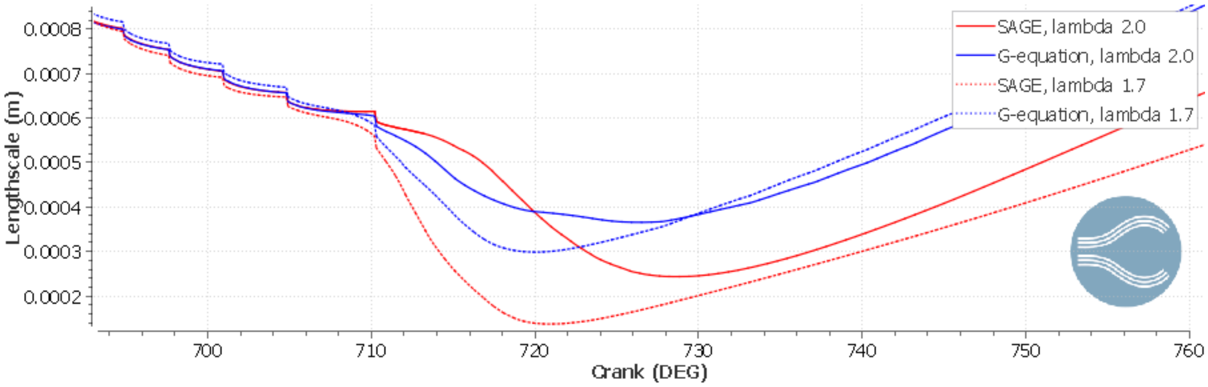

Figure 135. Length scale comparison for the SAGE and G-equation models, different mixture conditions and ST = -20 CAD

Similar consideration could be done for the turbulent velocity fluctuation, in Figure 136, where the values for the $\lambda = 2.0$ case are close each other for all the simulation times represented, but right after the spark there is a fast and short increase of values, at 715-720 CAD, that for the two models is defined at different times, with a delay. Instead, the same peak is present also in the $\lambda = 1.7$ case, but in that one it's earlier and the two models predict it at almost the same time.
This consideration about the peak value after the spark is coherent with what already been described for other diagram, that the $\lambda = 1.7$ simulation gives for both models earlier results, and it's visible also for the valley in the previous results related to the length scale.

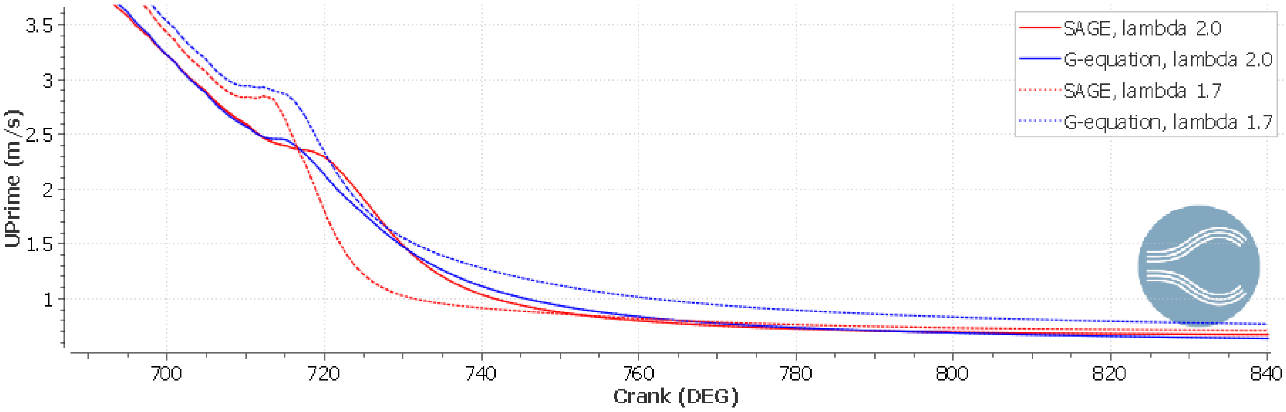

Figure 136. Turbulent velocity fluctuation for the SAGE and G-equation models, different mixture conditions and ST = -20 CAD

Lastly is possible to study the difference for the turbulent flame speed, reported in the figure below. The consideration that could be done in this image is almost the same already done for the other turbulence parameters.

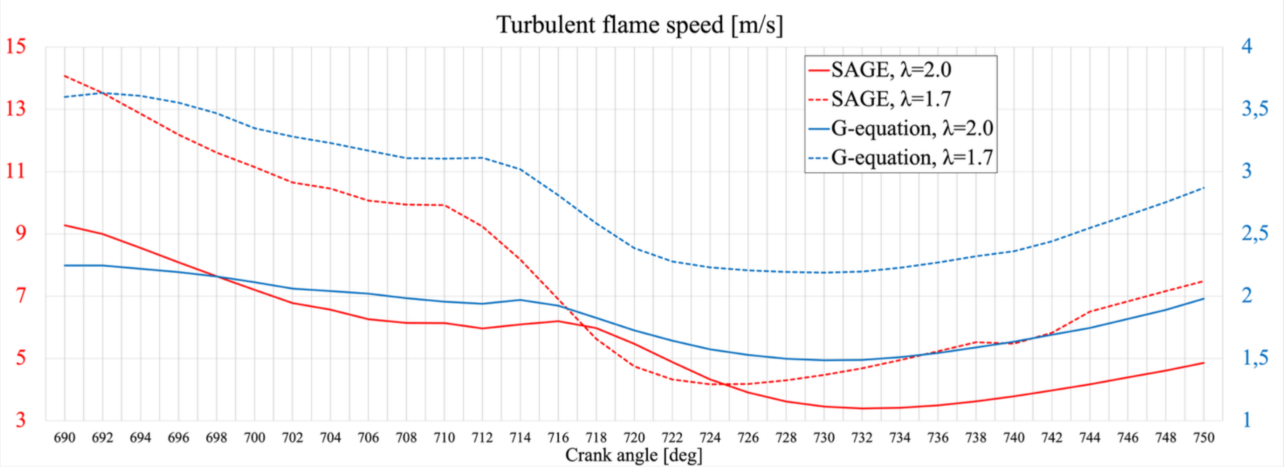

Figure 137. Turbulent flame speed comparison for the SAGE and G-equation models, different mixture conditions and ST = -20

However, the possible correlation between these turbulence parameters and the performance, P and T, could be analysed more specifically in this case looking at the actual degrees when the curves related to the same air/fuel ratio become parallel. Indeed, going back to the Figures 128 and 129 of pressure and temperature, the curves became overlapped around 730 CAD, when here, the S_t ones become parallel. Saing that, must also be taken into account that the two models have a different correlation between the turbulence parameters and the performance ones. Moreover, the difference in how the curves of the two models interact between them is significant. For the G-equation models the curves of different air/fuel ratio don't meet during the period and they had similar behaviour. Instead, for the SAGE model there are two points of interaction, the peak value after the ST is highly retarded, and the phase in which the values decreases is very strong for the $\lambda = 1.7$.

NO_x emissions

For the analysis of the NO_x emissions the elements of comparison are mostly the same already done for the other cases, however in this situation the differences between simulations are particularly clear for several reasons. Indeed, not only the in-cylinder temperature peak value is higher in the $\lambda = 1.7$ case, but also the instant in which it starts rising is earlier for the richer mixture case. Both these elements will influence the NO_x formation inside the chamber.

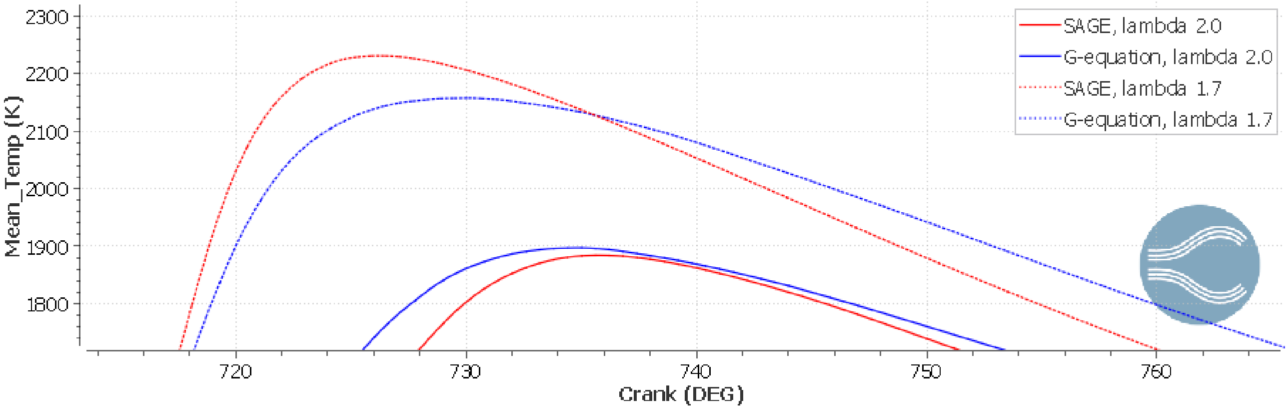

Figure 138. Zoom of peak temperature values for the SAGE and G-equation models, different mixture conditions and ST = -20 CAD

The differences in temperature are then transported in the NO_x emissions diagram, as expected, the higher the temperature reached in the chamber, the higher emissions. Moreover, the difference in temperature between the λ values are significant and translate in huge differences in the NO_x mass.

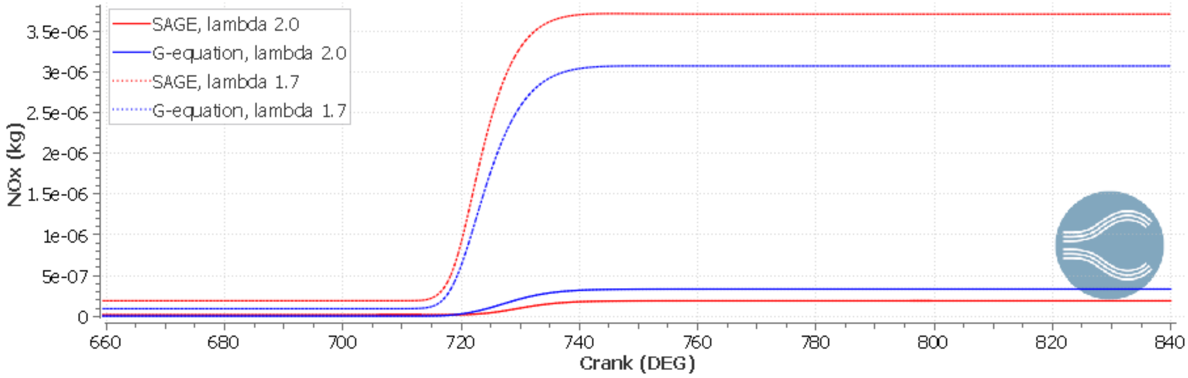

Figure 139. NO_x emissions comparison for the SAGE and G-equation models, different mixture conditions and ST = -20 CAD

Below the table with all the important data is reported.

MODEL	PEAK TEMPERATURE [K]	DELTA TEMPERATURE [K]	PEAK NO_X EMISSION [PPM]	DELTA EMISSION [PPM]
SAGE, λ = 2.0	1884.19	12.87	0.190	0.145
G-EQUATION, λ = 2.0	1897.06		0.335	
SAGE, λ = 1.7	2230.6	73.5	3.706	0.637
G-EQUATION, λ = 1.7	2157.1		3.069	

Table 27. Comparison of temperature and NO_x emissions peak values for the SAGE and G-equation models, different mixture conditions and ST = -20 CAD

The relevant data that comes from this table is more related not only on the differences in the two models, that predict values similar but obviously with some differences, but in the differences in results for the two values of air/fuel ratios. Indeed, in the richer mixture conditions the values of temperature are higher than the standard conditions (an increment of more than 200 K), this is then reflected to the emission values that are one order of magnitude higher.

However, also the differences in the models are relevant. The main consideration that could be done looking at the results is that increasing the λ value, and so the performance parameters, the differences in the two models create a higher difference in the results. The reason of this could be found, as said in the previous sections, in the way the models predict the chemical reaction.

ST = -25 CAD

Performance

Going on with the comparison of how the air/fuel ratio influence the result for the different models, Figure 140 show the pressure and temperature evolutions for the ST -25 case in the two λ configurations.

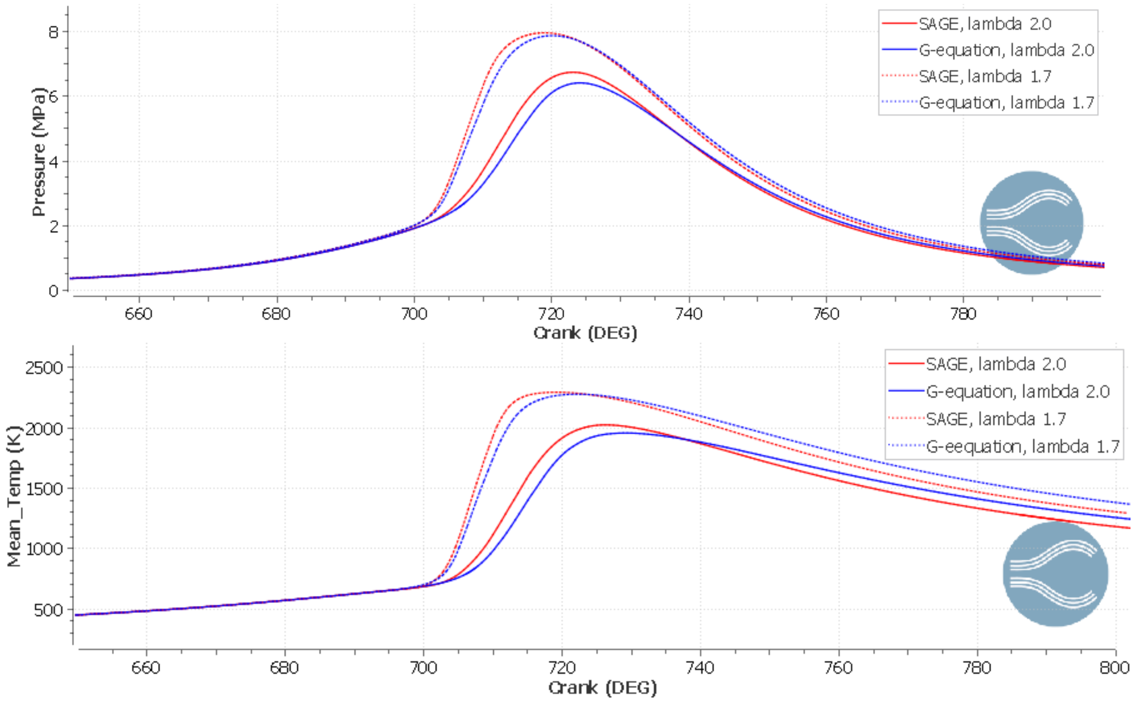

Figure 140. Comparison of pressure and temperature for the SAGE and G-equation models, different mixture conditions and ST = -25 CAD

The images above show that for the cases compared there's an increasing of results due to the higher amount of fuel for the λ = 1.7 case, but the differences in the trends produced by the two models are lower. However, for this specific case are close each other, but as for the previous cases, seams that with higher fuel the two models predict performance values with higher cohesion. This is also visible looking at how the models predict the instant in which both the pressure and the temperature rise, for the standard condition there's a delay between them that, instead, for the richer mixture case is almost cancelled.

In order to give an explanation to the results obtained, the spark in this case is neither too earlier, neither too later. This could lead to have a more stable condition between the models and so they do not predict too far results.

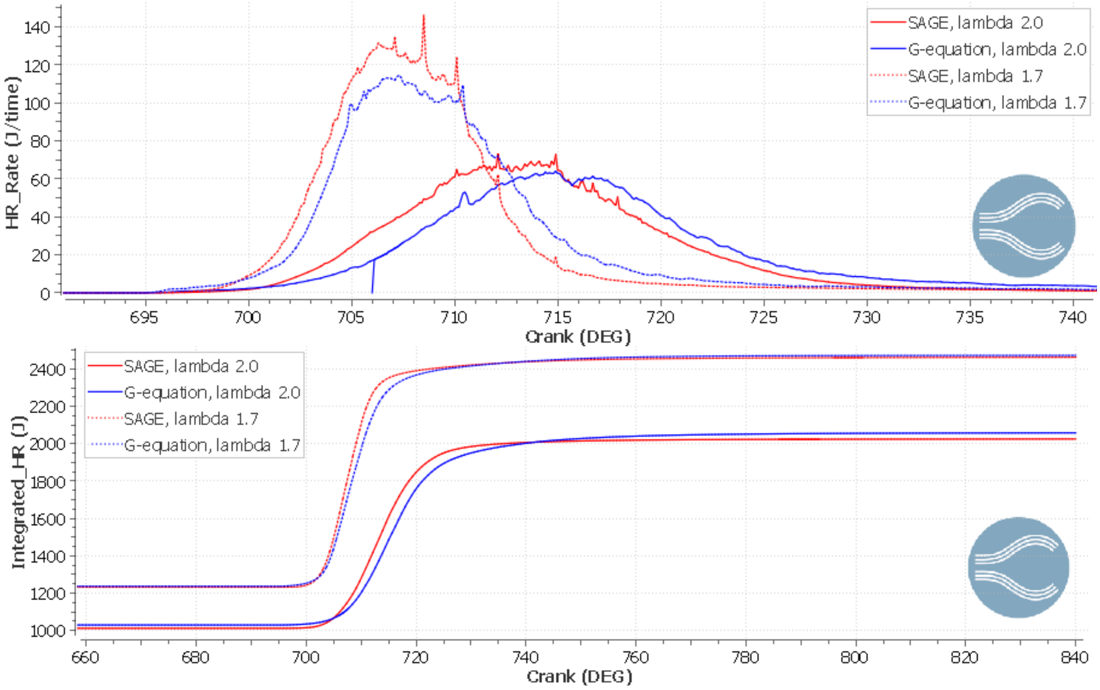

Figure 141. Comparison of HRR and IHR for the SAGE and G-equation models, different mixture conditions and ST = -25 CAD

Figure 141 above show both HRR and IHR, underlining the impact of the higher fuel quantity, indeed the HRR of the richer mixture simulation is more than the double of the standard case one. Moreover, it shows in a clear way the delay between the model's prediction, that is higher in the $\lambda = 2.0$ case. However, the consideration that could be done for those diagrams are pretty much the same previously described.

Moving to the turbulence parameter, that are the ones with more differences between the models, the TKE is represented below.

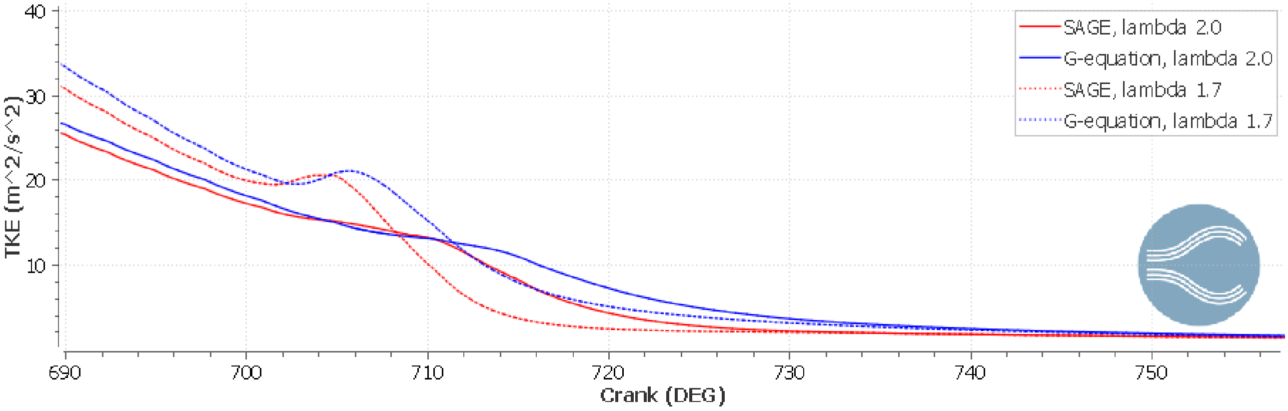

Figure 142. Comparison of TKE for the SAGE and G-equation models, different mixture conditions and ST = -25 CAD

For this comparison, the results between models are not so far from each other. Indeed, in both standard and richer mixture condition, after the spark the TKE has a peak of values, this is predicted always before by the SAGE model, with lower peak values. For the $\lambda = 2.0$ case this peak is very low and almost invisible, more important instead for the other simulation done with higher fuel.

The results obtained are also coherent with all the others previously analysed, indeed the G-equation models show higher values at the instant of the spark and later.

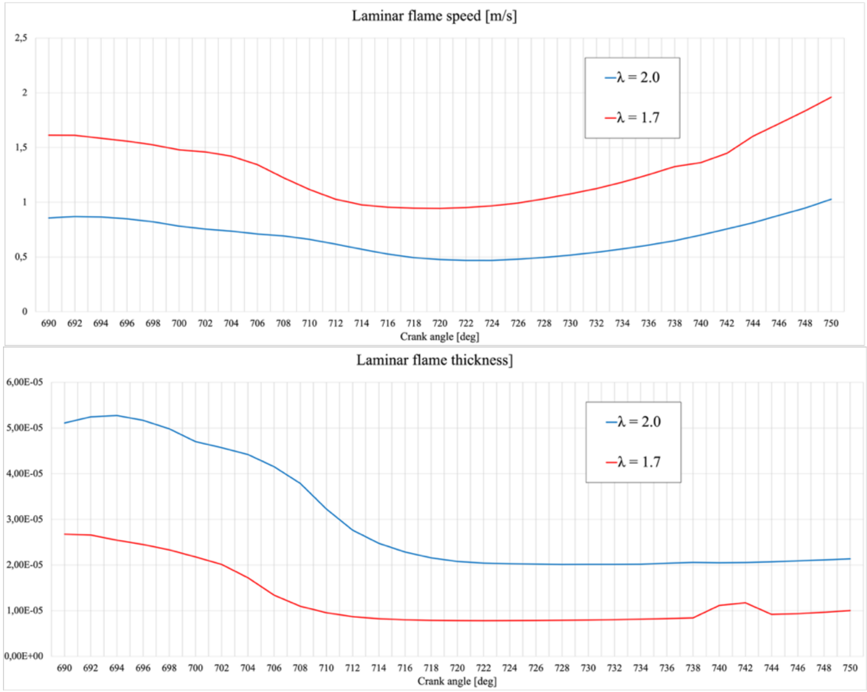

Figure 143. Laminar flame speed and flame thickness for the SAGE and G-equation models, different mixture conditions and ST = -25 CAD

The figure above shows both the laminar flame speed and laminar flame thickness. The results are coherent with the condition of the simulation, indeed more fuel leads to higher turbulence and flame speed, and for higher speed the flame thickness is lower.

The other parameters related to the calculation of the turbulent flame speed are reported below, in Figure 144.

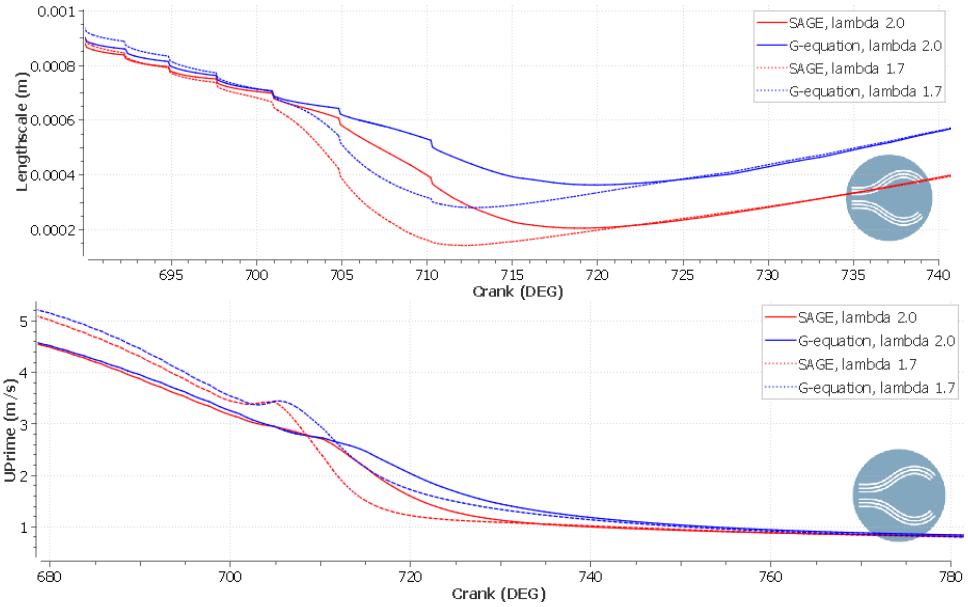

Figure 144. Comparison of length scale and turbulent velocity fluctuation for the SAGE and G-equation models, different mixture conditions and ST = -25 CAD

The results here do not report anything different from the previous, with the G-equation model that predict higher values and the $\lambda = 1.7$ case that has higher turbulence. However, what could be point out for all the results studied until now regarding those simulations for fixed ST is that both models predict for all the mixture condition the same trends, meaning that this combination of fuel mixture and ST leads to stable and optimal condition for both the models.
Lastly, the turbulent flame speed could be analysed.

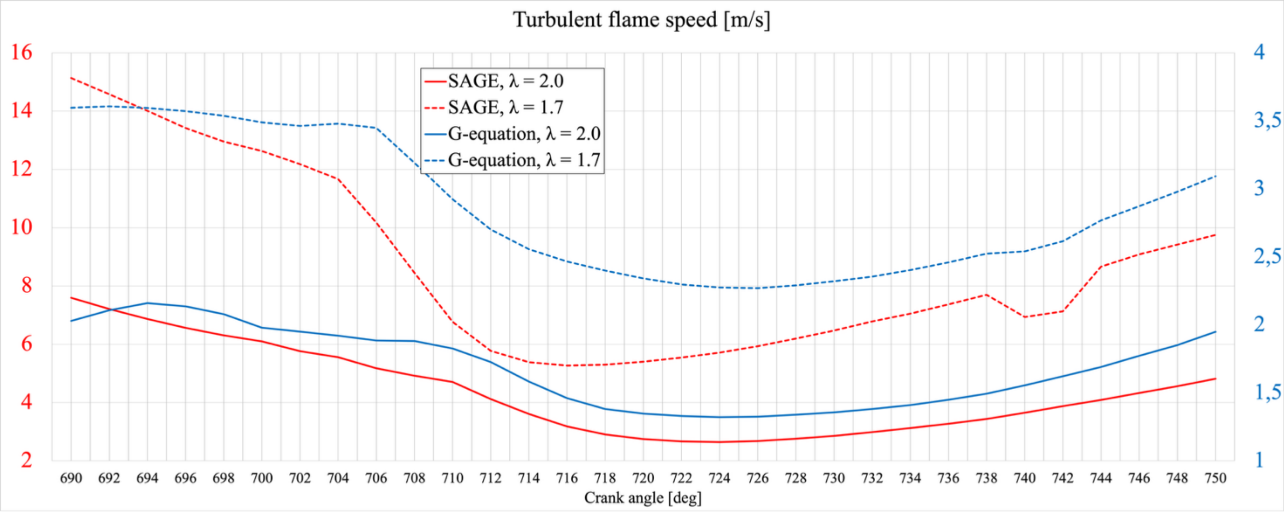

Figure 145. Turbulent flame speed for the SAGE and G-equation models, different mixture conditions and ST = -25 CAD

Some relevant consideration that could be done is that, at the ST, the S_t in the standard mixture condition are closer between the models, however the results saw before related to pressure, temperature, HRR ect. shows more close correlation between the data of the $\lambda = 1.7$ case.

NO$_x$ emissions

For the analysis of the NO$_x$ emissions the figure below shows the peak of in-cylinder temperature and the mass of NO$_x$.

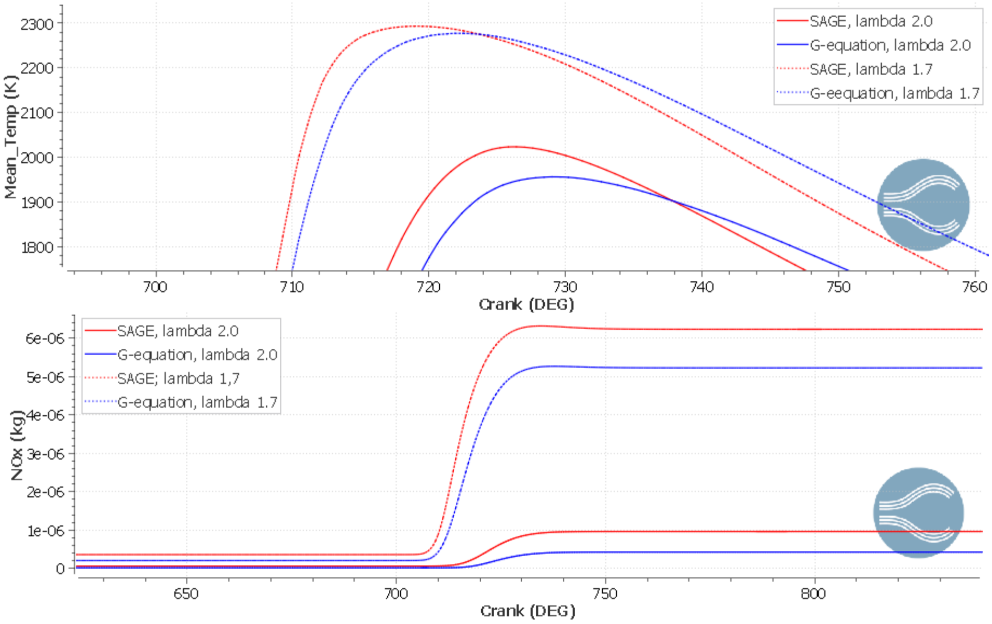

Figure 146. Zoom of peak temperature values and NO_x emissions for the SAGE and G-equation models, different mixture conditions and ST = -25 CAD

The results are coherent with the one already studied on the other ST case. In particular, here is possible to see more clearly that for the λ = 1.7 case the rising of the emission starts earlier than the other case, this could be done to a better mixing between the oxygen and the fuel, leading to more stable and rapid combustion, as saw also in the other figures.
Below is reported the table with the major data relative to those simulations.

MODEL	PEAK TEMPERATURE [K]	DELTA TEMPERATURE [K]	PEAK NO_X EMISSION [PPM]	DELTA EMISSION [PPM]
SAGE, λ = 2.0	2023.47	67.18	0.963	0.538
G-EQUATION, λ = 2.0	1956.29		0.425	
SAGE, λ = 1.7	2293.2	15.9	6.236	1.008
G-EQUATION, λ = 1.7	2277.3		5.228	

Table 28. Comparison of peak temperature and NO_x emission values for the SAGE and G-equation models, different mixture conditions and ST = -25 CAD

The relevant results that should be discussed about the table above is related to the fact that, despite higher difference in temperature peaks for the λ = 2.0 case, the highest difference in emission for the two models happened for the other mixing condition. This could be justify considering what have already been said about the rich mixture condition, indeed that case is more sensitive to chemical reaction and not only the temperature influence. In this condition the fuel present is higher but not too much, leading to the chemical reaction to complete and maybe, due to the fact that the SAGE model is based on it, this model predict higher values of emission without necessary have significant difference in temperatures. However, must be considered that the SAGE model for the λ = 1.7 case start at a higher point from the previous cycle.

ST = -30 CAD

Last comparison done is related to the earliest ST.

Performance

Like the previous cases, starting with the analysis of pressure and temperature distribution, shown in Figure 147.

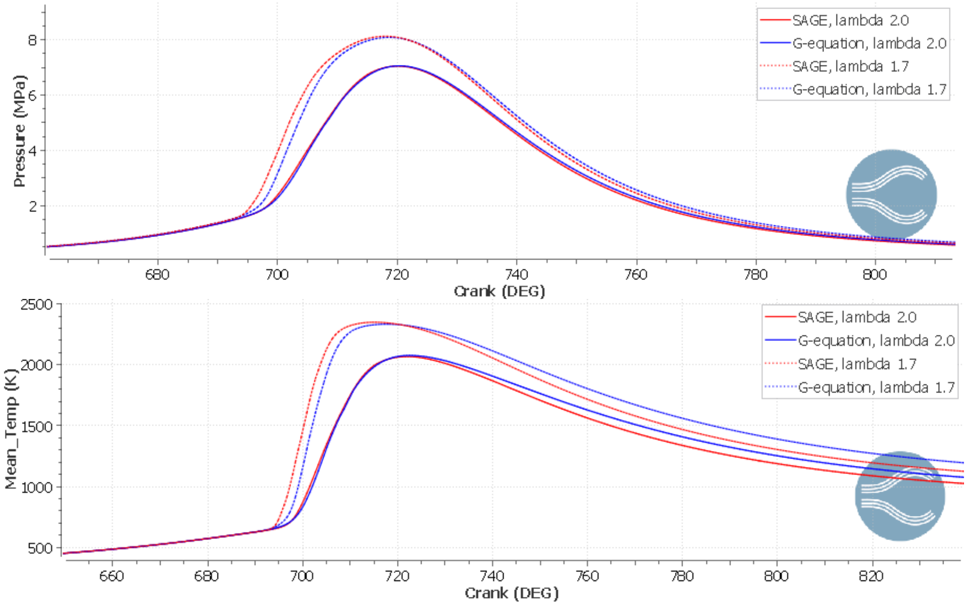

Figure 147. Comparison of pressure and temperature for the SAGE and G-equation models, different mixture conditions and ST=-30 CAD

This mixing condition gives different results than the previous, indeed in this case the simulations done with $\lambda = 1.7$ give results that are more far from each other for the two models. Is visible from the diagram that the SAGE model has an increasing phase earlier than the G-equation one, both for pressure and temperature.

The reason that could lead to these results could be several, the presence of more fuel lead to an increase of the model's differences. In particular, the combustion chemistry becomes more non-linear. Moreover, SAGE can model multi-point or spontaneous ignition ahead of the flame front, causing pressure and temperature to rise earlier.

What seems to be from the picture is that at ST = -30 CAD and $\lambda = 2.0$ a stable condition in which both models work similarly is reached, and moving from that condition leads to a reduction of the correspondence of the models results.

Same consideration could be done looking at the diagrams of the HRR and IHR.

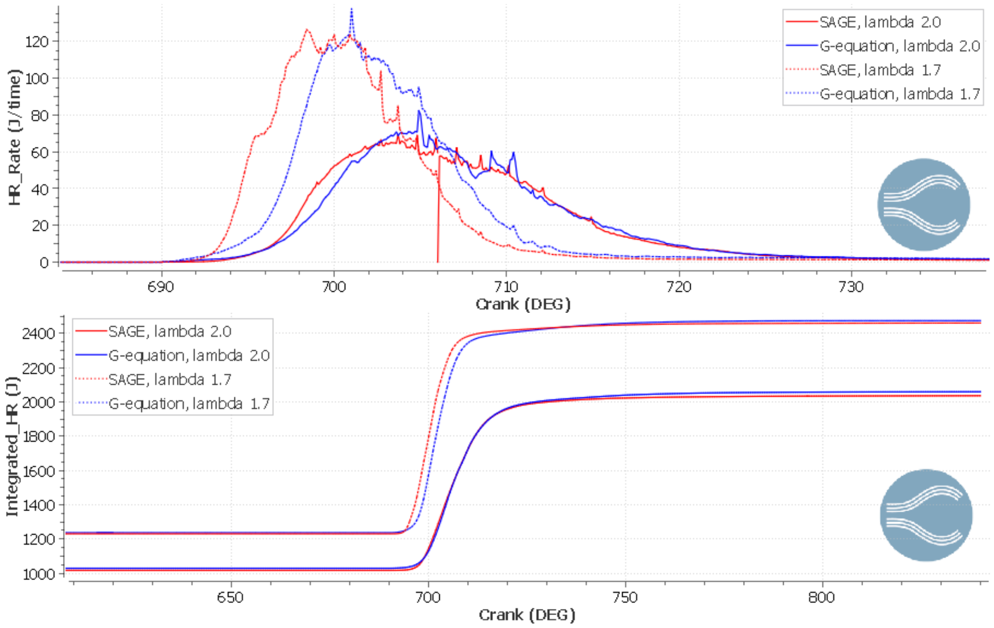

Figure 148. Comparison of HRR and IHR for the SAGE and G-equation models, different mixture conditions and ST = -30 CAD

The spark starts at the same instant, but the SAGE model for the $\lambda = 1.7$ case has an earlier peak of values, that then lead to an earlier decreasing phase after the peak.
However, the IHR image show that for both simulations the value of energy released after the combustion still higher for the G-equation model. This could be due to the fact that before the ST, the G-equation model has already higher energy coming from the previous cycle than the SAGE model. Another way to see this is related to the later energy release of the G-equation model, that due to this has higher heat at the ending phase of the combustion, when instead the SAGE model is already at zero.
About the turbulent parameters, the TKE is reported in the figure below.

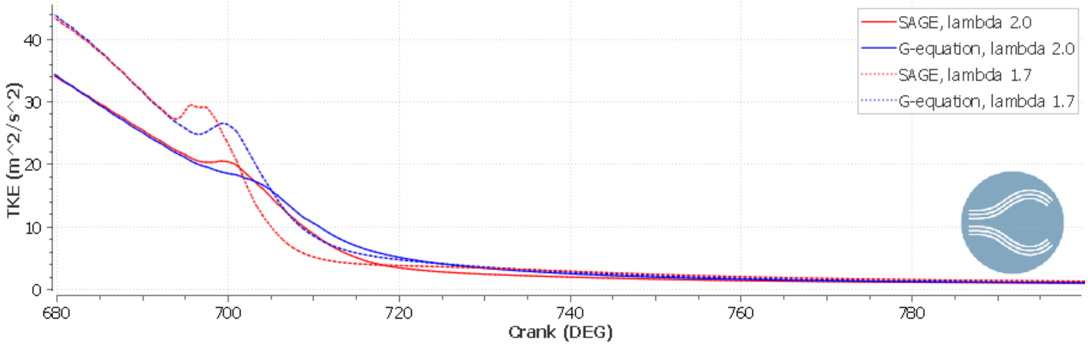

Figure 149. TKE values for the SAGE and G-equation models, different mixture conditions and ST = -30 CAD

The results shown in the figure above are similar to the same already studied for the other simulation cases. However, in this case, unlike previous comparison on the TKE, the G-equation model doesn't show higher results that the SAGE one, although at the spark time both have almost the same value. This led to the consideration that for this specific combination of ST and λ the G-equation model has a reduction in values. Moreover, the delay present for the two models here is clearly visible, despite the ST -25 or -20 case in which, especially for the $\lambda = 1.7$ case, the curves were close each other.
A possible explanation of this behaviour could be related to, again, the condition in which the simulation take place.

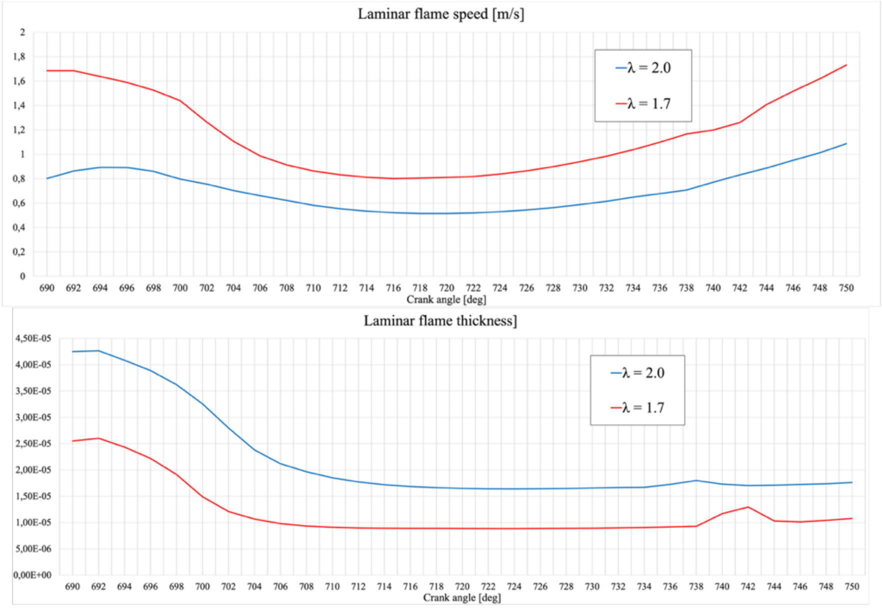

Figure 150. Comparison of laminar flame speed and laminar flame thickness for the SAGE and G-equation models, different mixture conditions and ST = -30 CAD

Moving to the plot of the laminar flame speed and flame thickness, the relationship between the different simulations don't show anything anomalous or different from what expected, the simulation done with higher fuel has more speed and less thickness that the case with higher air/fuel ratio.

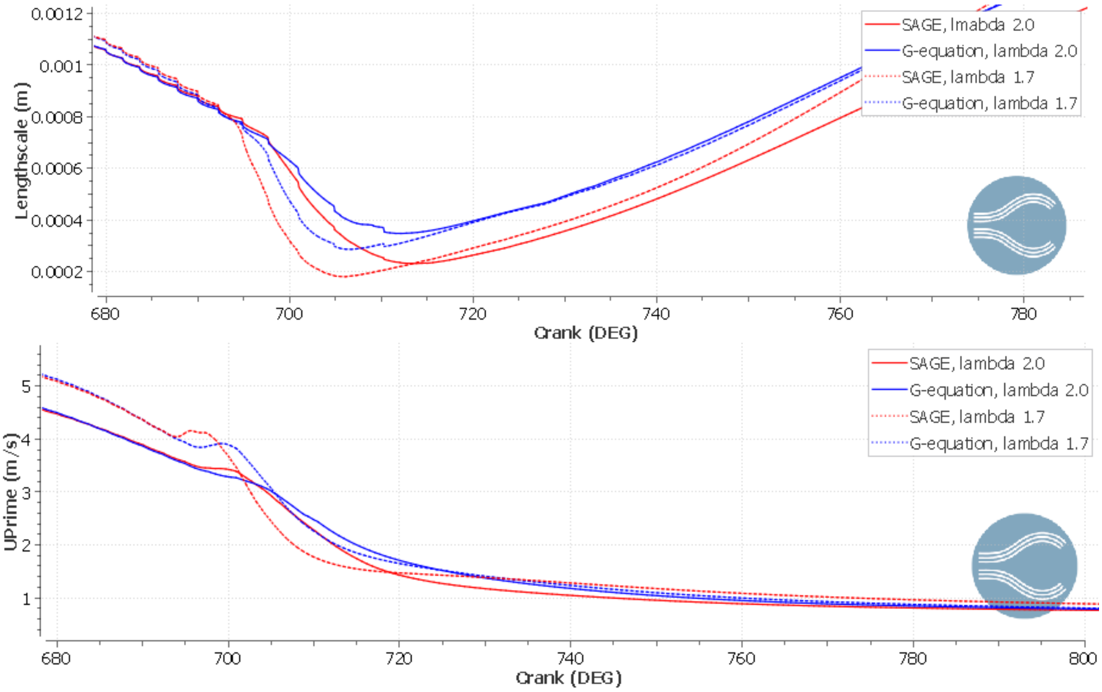

Figure 151. Length scale and turbulent velocity fluctuation for the SAGE and G-equation models, different mixture conditions and ST=-30 CAD

The next element to be analysed related to the turbulent field are the length scale and the turbulent velocity fluctuation, that, as shown in Figure 151, have a coherent behaviour with the TKE, with the λ = 1.7 case that has higher values for both models at the ST, then decrease lower values than the λ = 2.0 case. Comparing the models, the trends are also like the TKE ones, with the G-equation model that has lower and retarded values with respect to the SAGE model ones.

Lastly, from the previous parameters described, the S_t for the simulation described in this section could be study.

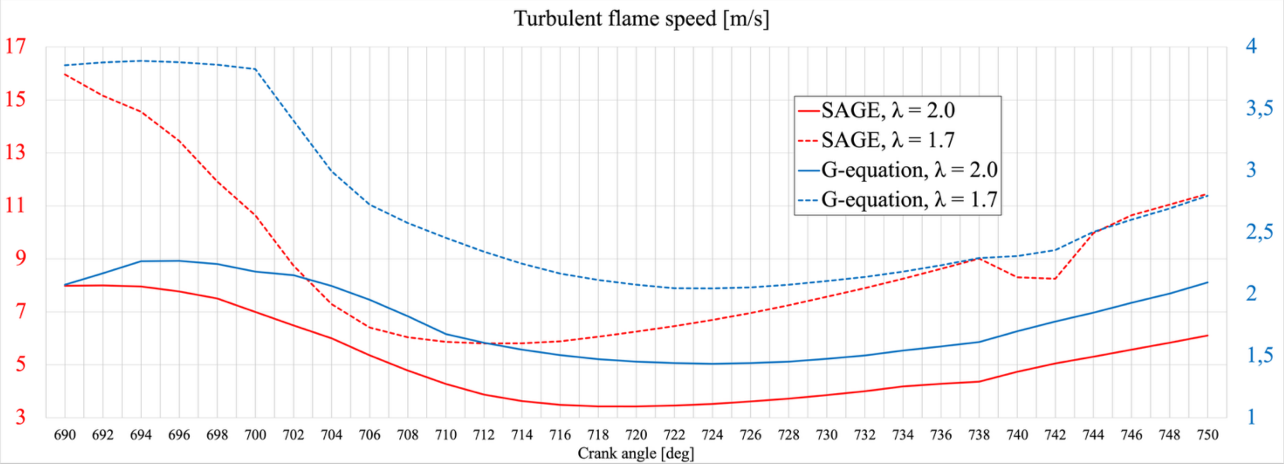

Figure 152. Turbulent flame speed comparison for the SAGE and G-equation models, different mixture conditions and ST = -30 CAD

Form the comparison of the turbulent flame speed above the main differences that could be seen are related to the $\lambda = 1.7$ case, where the trend of the two curves is highly different, this is coherent with what shown previously for pressure and temperature. Instead, the $\lambda = 2.0$ results show almost parallels behaviour. The main conclusion on this is that the hypothesis for which the way the curves develops and how much are parallel each other gives an idea of how the results of performance are close between the models. However, is important to point out that, like all the previously done comparison on the S_t, the way it's calculated for the different models is different and this influence also the results.

NO_x emissions

Last comparison done for this section is related to the NO_x emission for the ST -30 case with variable air/fuel ratio. the image below shows the peak of temperature reached during the combustion and as already said previously the $\lambda = 1.7$ case reach higher values but with more discrepancy between the models.

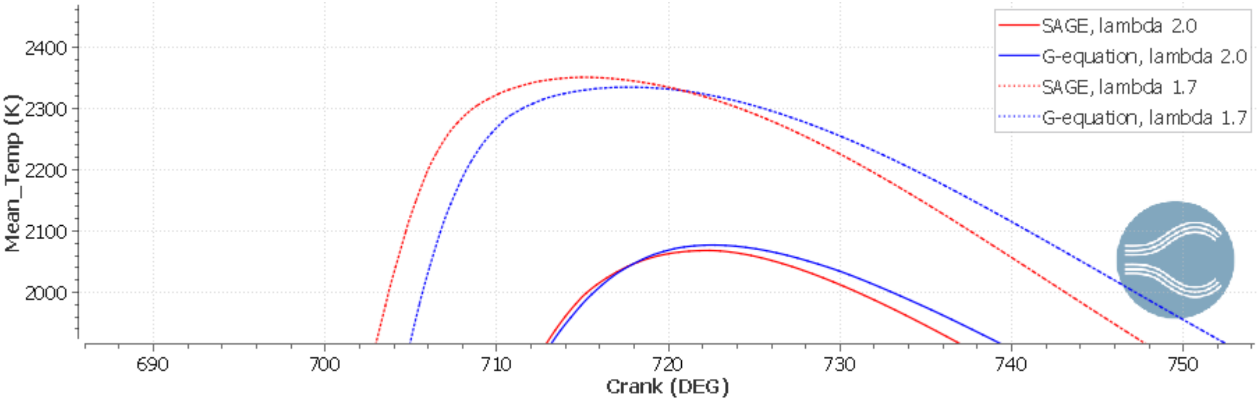

Figure 153. Zoom of peak temperature values for the SAGE and G-equation models, different mixture conditions and ST = -30 CAD

Form those results the NO_x emissions prediction is close to the one already described for the other comparison with the $\lambda = 1.7$ case that has higher emission and the SAGE models that overtake the G-equation one.

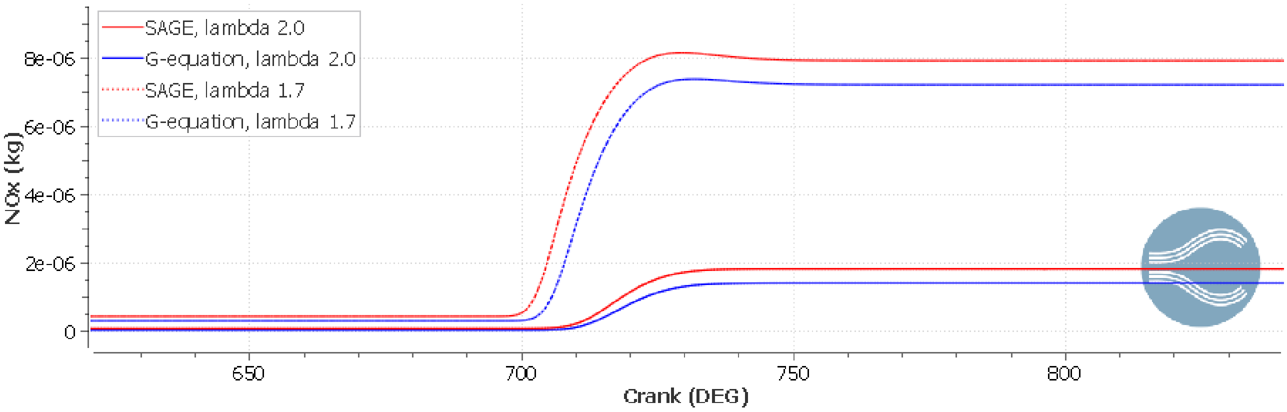

Figure 154. NO_x emissions comparison for the SAGE and G-equation models, different mixture conditions and ST = -30 CAD

From the pictures above the table with the more relevant results could be define.

MODEL	PEAK TEMPERATURE [K]	DELTA TEMPERATURE [K]	PEAK NO_X EMISSION [PPM]	DELTA EMISSION [PPM]
SAGE, $\lambda = 2.0$	2068.06	8.89	1.83	0.41
G-EQUATION, $\lambda = 2.0$	2076.95		1.42	
SAGE, $\lambda = 1.7$	2350.4	16.5	7.945	0.711
G-EQUATION, $\lambda = 1.7$	2333.9		7.234	

Table 30. Comparison of NO_x and temperature peak values for the SAGE and G-equation models, different mixture conditions and ST = -30 CAD

Considering all the previous cases studied and the relative results, this table shows the more expected results. Could be said that the ST -30 is a condition of mixing and other parameters in which the models could work in a more similar and predictable way.

Change of b_1 parameter in G-equation model

The last analysis conducted was related to the influence of the constants that define the turbulent flame speed in the G-equation model, that, as already explained, depend on three constants: a_4, b_1 and a_3. The G-equation model is highly influenced by the turbulence, and it starts from those parameters to predict all the other variables related both to the performance and the emissions for specific simulation conditions.

The way those constants influence the S_t is difficult to define, however, as the CONVERGE manual [38] expresses, the constant b_1 is the one that has the highest influence in the definition of the turbulent flame speed. Therefore, the next section will show how changing that constant will influence the results for the G-equation model, in order to determine if and how the results could be modified and manipulated in presence of experimental results.

Knowing this, the study that has been done is related to the change in that parameter for several values: 3 (standard condition used in all the previous simulation), 3.5, 4, 4.5 and 5. The values of λ and ST are the standard one, so λ= 2.0 and ST = -25 CAD.

Performance

The first parameter where the influence of the b_1 constant is shown is the pressure, reported over time.

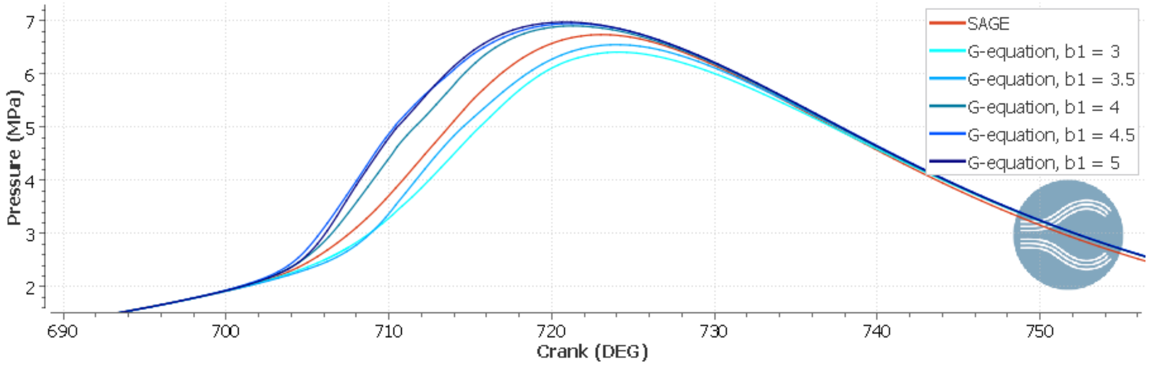

Figure 155. Pressure evolution for different b_1 values in standard conditions

From the image above it is possible to see that there is a high difference in results from the simulations done with b_1= 3.5, to the one using b_1= 4. Moreover, compared to the results obtained with the SAGE model, all the simulations done for values of b_1 higher that 3.5 exceed it.
To better see the differences in peak pressure values obtained and try to define a correlation, Figure 156 show a zoom of it and a diagram with reported the peak values for all the simulations done.

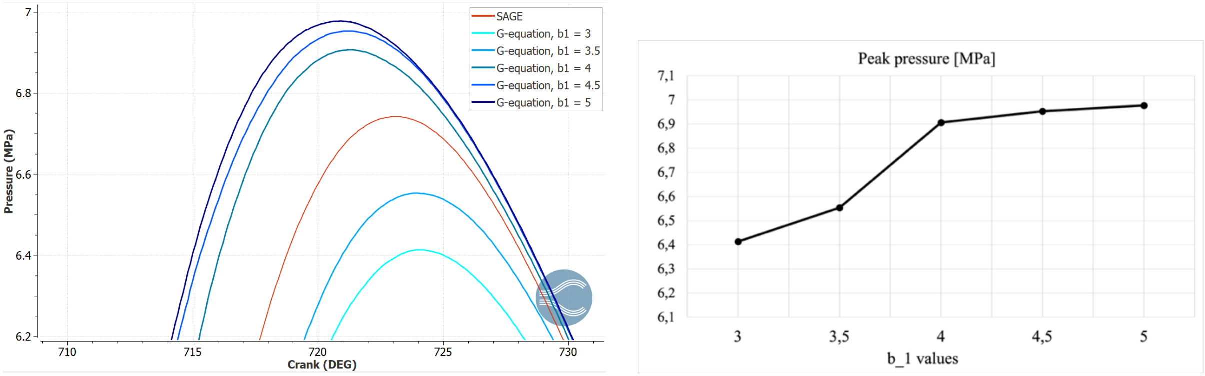

Figure 156. Zoom of pressure evolution and peak pressure values for different b_1 values in standard conditions

The trend that could be seen from the figure above is that with higher b_1 values the peak pressure is higher, with a limitation, indeed the difference between the b_1= 3.5 and the b_1= 4 case is visibly higher than the difference between b_1= 4, 4.5 5, bringing the results to a sort of saturation. This led to the conclusion that the parameter b_1 highly influences the results obtained, but the condition in which that simulation take place gives also a relevant impact.
Similar consideration could be done for the temperature evolution over time, shown in Figure 157.

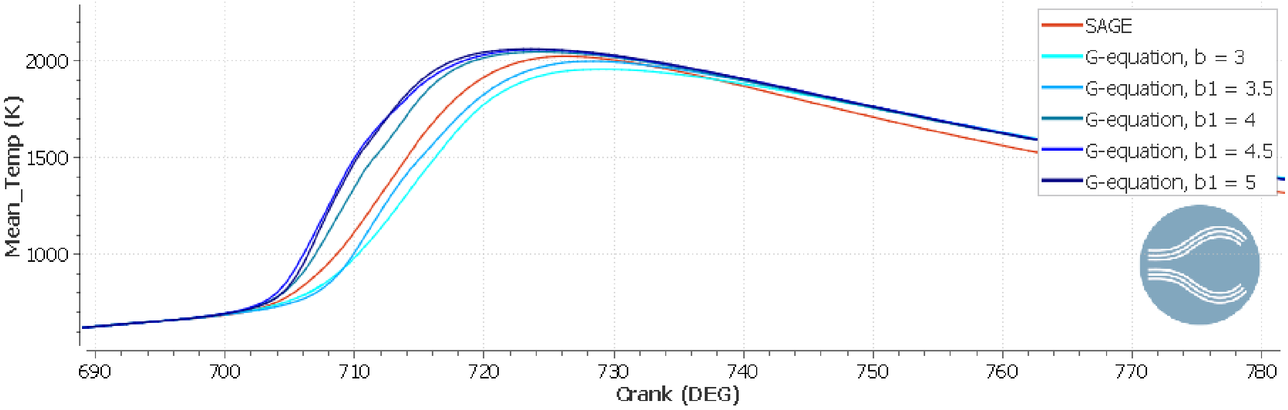

Figure 157. Temperature evolution for different b_1 values in standard conditions

Also, for this parameter it is visible that for higher values of b_1 the peaks increase, but not only. The other main difference is related to the way the curves rise, this is directly related to the turbulent flame speed, indeed with higher turbulence the flame propagates faster, and both pressure and temperature rise faster, leading to steeper curves.

As for the pressure evolution, the peaks are difficult to see, so Figure 158 represents the different peaks with the trend that correlates them.

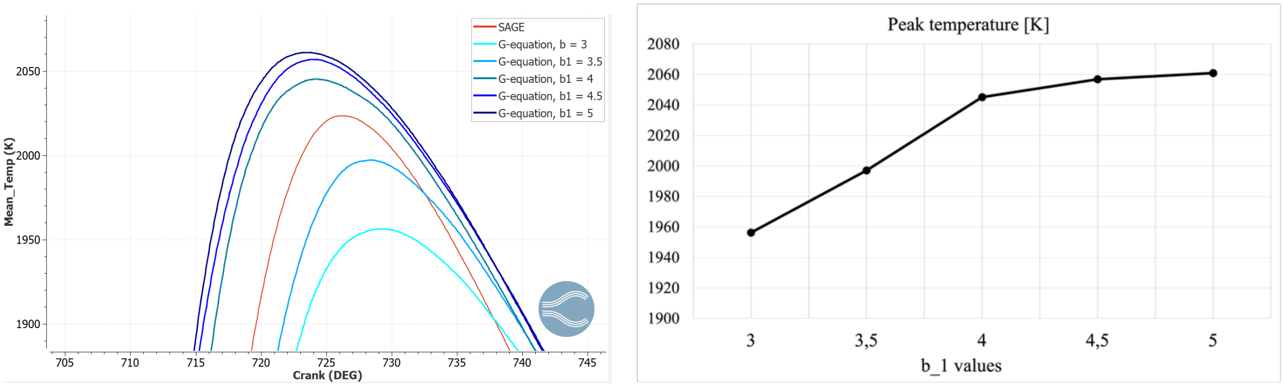

Figure 158. Zoom of temperature evolution and peak temperature values for different b_1 values in standard conditions

Also, for the temperature the trend of the peak values seems to be a saturation, as the pressure one previously shown.

This could be explained looking back at the equation that defines the S_t, where the b_1 factor is defined and where it has impact. Indeed, in the equation 37, the constant b_1 is always at the denominator, leading an increase of it to a reduction, until the cancel, of the factor where it appears. Below the equation without the factors where the constant is present is shown to see what could happened for a hypothetically infinite value of b_1.

$$s_t = s_l + u'\left\{[a_4 b_3^2 D_a]^{1/2}\right\} \tag{56}$$

Therefore, this demonstrate that increasing the value of b_1 the turbulent flame speed and, as consequence of it, the other parameters for the G-equation model, loses the dependence on the b_1 factor, leading to an actual saturation.

Next parameters to be compared are the IHR and the HRR. Figure 159 shows the evolution of the HR and as expected the higher the value of the b_1 parameter, the steeper is the curve related to it, confirming that the influence of the turbulent flame propagation on the energy released during the combustion phase. However, something interesting is that, before and after the combustion all the curves related to the G-equation model unite in only one value, meaning that the element that change is only the way the energy is released, through the flame propagation, but not the total amount of it.

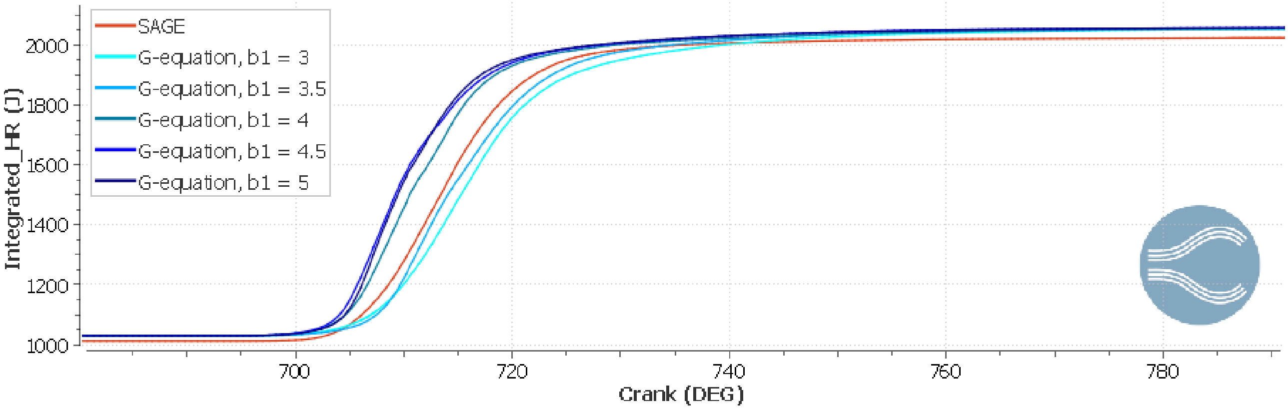

Figure 159. IHR evolution for different b_1 values in standard conditions

Moving to the study of the HRR diagram, what reported is coherent with what already said, for higher values of b_1 the higher flame propagation bring to higher energy released. Another interesting consideration is related to the difference in peak values, in particular the difference in the time when that peak values are reached. Indeed, the differences between the results for b_1=3.5 and b_1=4 are clearly visible and shows the influence on the turbulence for the G-equation model. Moreover, also for this diagram the influence of that parameter is more related to the impact of the flame at the ST, that leads the energy to be released more rapidly with respect to the other cases.

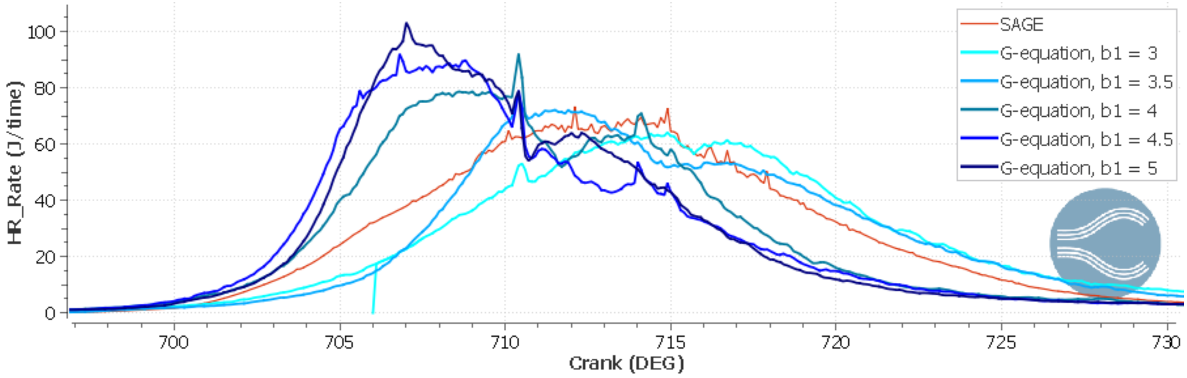

Figure 160. HRR evolution for different b_1 values in standard conditions

Following the comparison done in the previous section the other element that is interesting to see is the density. In this case, as shown in the figure below, the change in the b_1 constant doesn't influence the density values, or at least the influence is so small that could be considered negligible. The only simulation that shows differences is the one related to b_1= 4.5, where a small increase on the density value is reported.

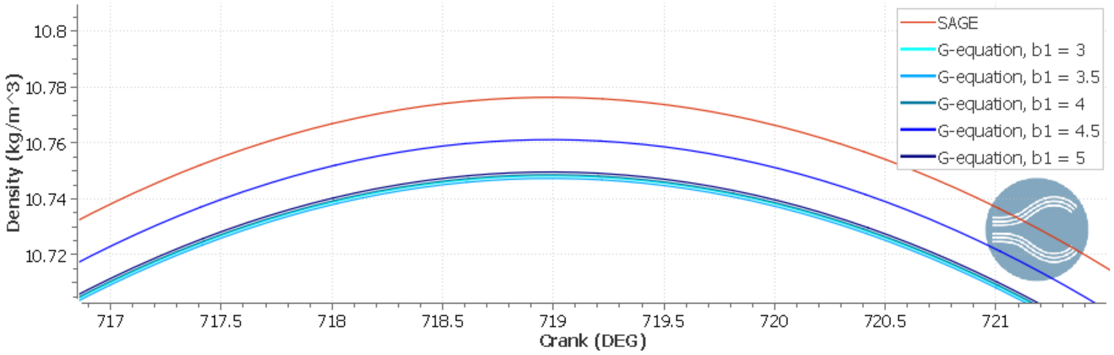

Figure 161. Density peak values for different b_1 values in standard conditions

Moving to the study of the turbulence parameters, the first important element is the TKE that, as reported in Figure 162, has a behaviour similar to the simulation done for rich mixture conditions compared for different ST, shown in Figure 119.

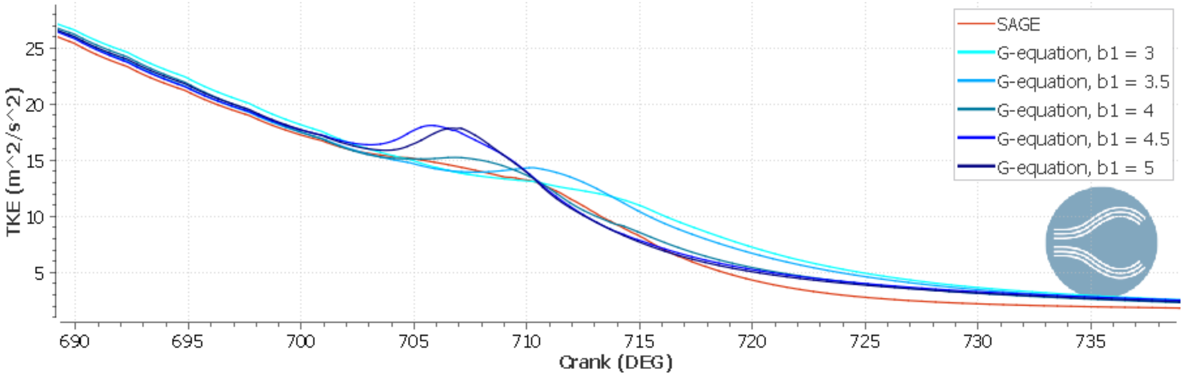

Figure 162. TKE evolution for different b_1 values in standard conditions

The visible effect of an increase of the b_1 constant in the TKE evolution is in general an increase in the flame propagation, that for this parameter translates in earlier and higher TKE peaks values after the ST (that in this case is at 695 CAD). Moreover, different from the other parameters reported, for

the TKE the saturation to a threshold value is less visible. Indeed, the simulation done with b_1= 4.5 and 5 show close results, but highly different from the one of the b_1= 4, 3.5 and 3.
To better understand the evolution at the beginning of the combustion phase, Figure 163 shows a zoom at the peak moment for all the simulations.

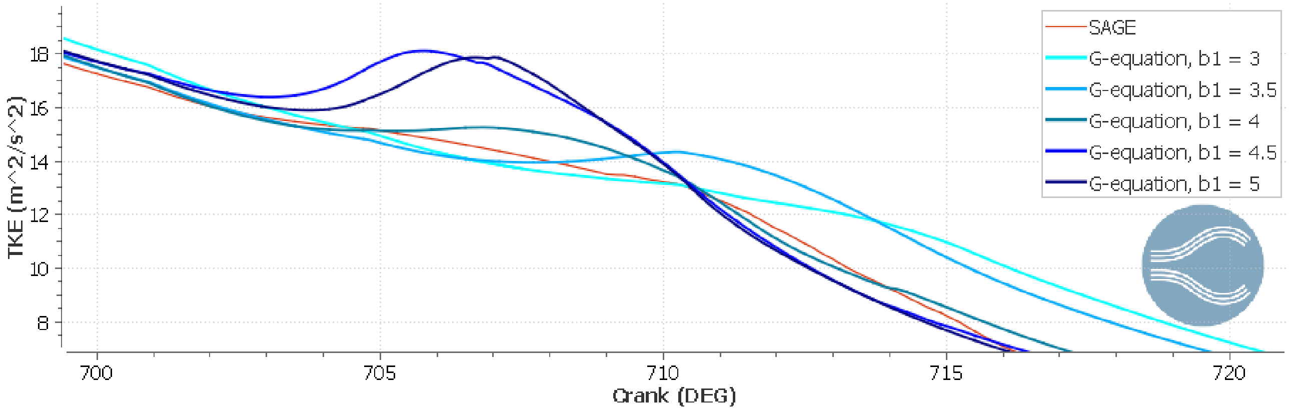

Figure 163. Zoom of TKE at the start of the combustion for different b_1 values in standard conditions

What could be stated from figure above is that the trend expressed before is almost what expected, but the case with b_1= 4.5 actually has earlier peak value than the b_1= 5 case. This is directly related to the different behaviour that this simulation has already shown for the density in Figure 161.
Moving to another important parameter that with the variation of the constant b_1 is highly influenced, the laminar flame speed.

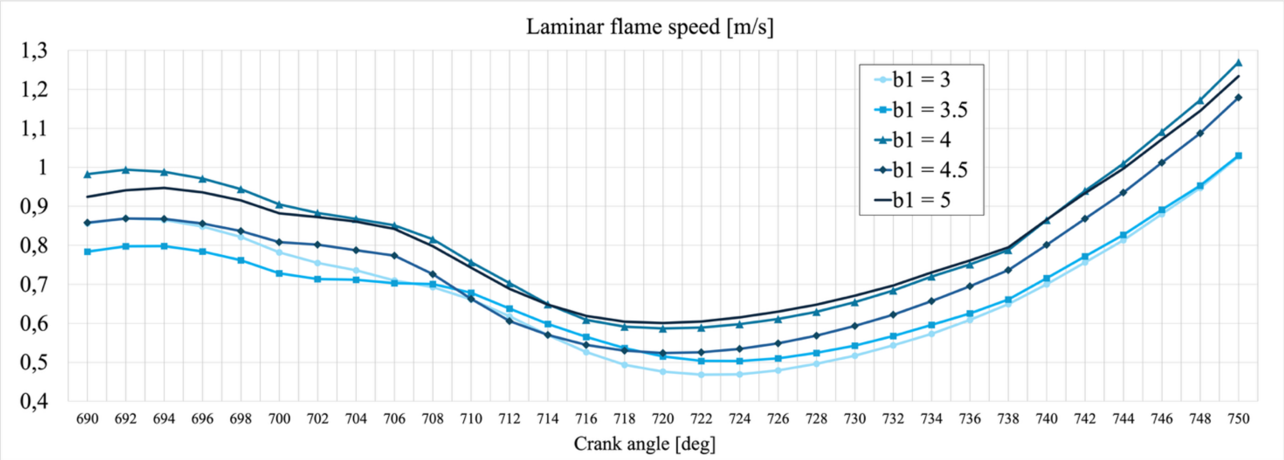

Figure 164. Laminar flame speed evolution for different b_1 values in standard conditions

The results above shows that the laminar flame speed almost doesn't follow the order of values of the b_1 constant, indeed the lowest value is related to b_1= 3, after that b_1= 3.5 and then there's b_1= 4.5. The reason behind this behaviour is related to the way the model calculates the S_l, indeed it depends not only on pressure and temperature, that increase as the b_1 constant increase, but also for the equivalence ratio. However, the differences between the curves are very small and the trend that they follow is almost the same.
Similar consideration could be done for the laminar flame thickness, shown in the figure below.

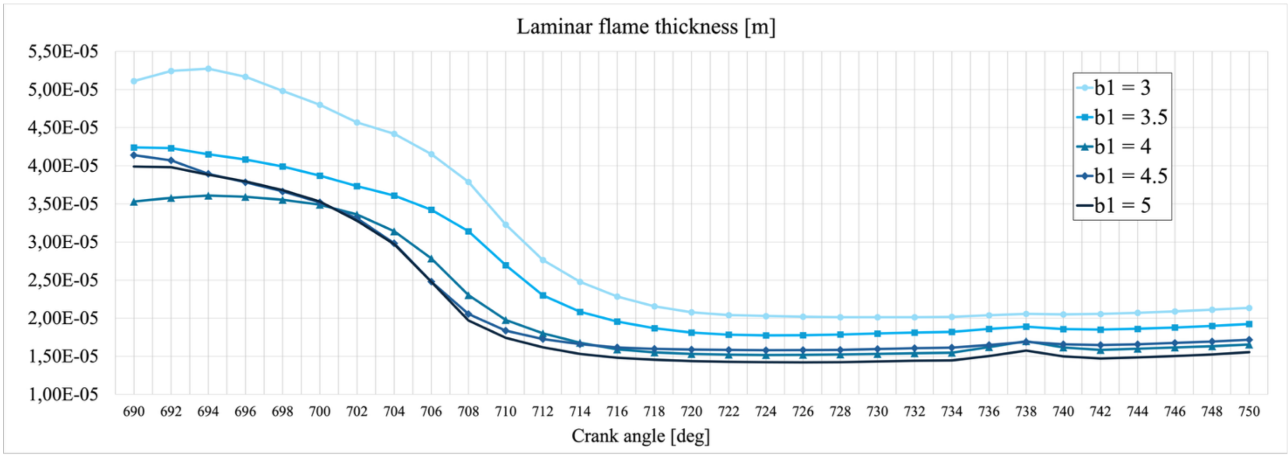

Figure 165. Laminar flame thickness evolution for different b_1 values in standard conditions

The curves for this parameter are very close each other, almost overlapped, the only difference that could be seen is related to the b_1= 3 case, that, shows the same trend as the other results but with higher values. This is coherent with the relationship between the laminar flame speed and the laminar flame thickness, where the b_1= 3 case, predicting the lowest S_l value among the others, become the highest in the δ_l evaluation.

Next turbulence parameters important to the definition of the S_t are the length scale and the turbulent velocity fluctuations, both shown in the figure below. The second has a behaviour very similar to the TKE one and the correlation between them has already been explained in equation 50.

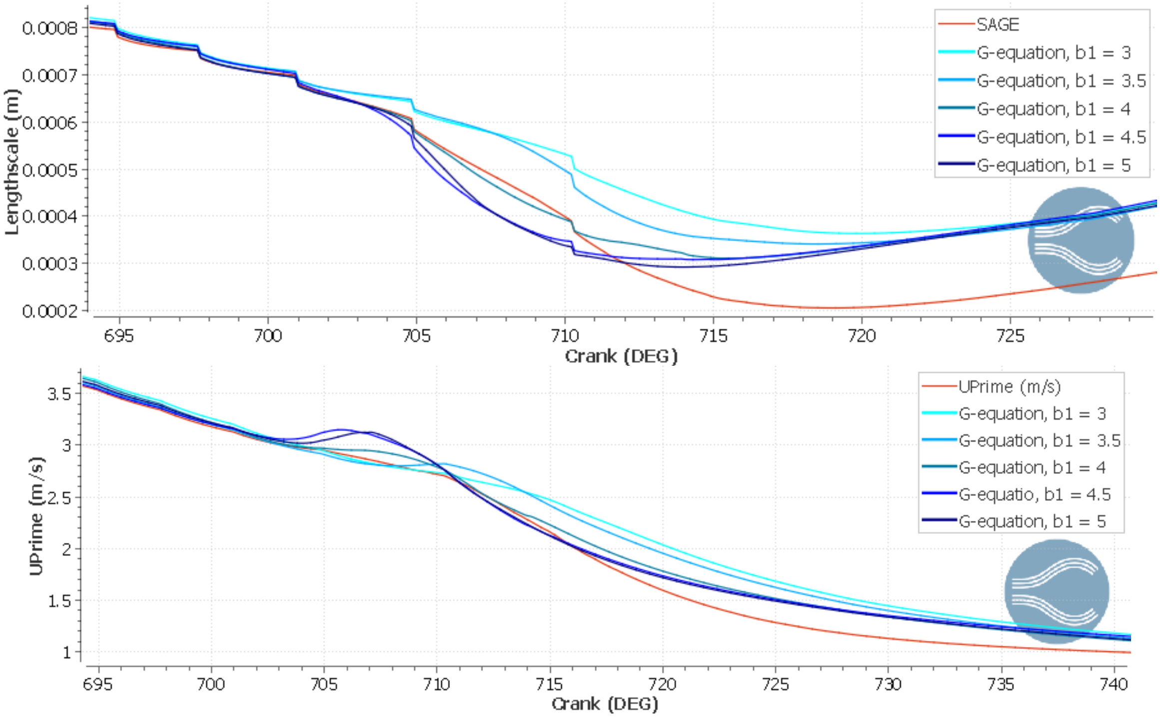

Figure 166. Length scale and turbulent velocity fluctuation for different b_1 values in standard conditions

However, the trend visible for the length scale is interesting due to the fact that no one of the simulation done for the G-equation model reached the values of the SAGE one during the decreasing phase. Moreover, similarly to the results shown for the IHR in Figure 159, after the combustion all the curves related to the G-equation model converge to the same result and almost overlap each other's.

Lastly, form all the elements previously shown it is possible to define the turbulent flame speed for the SAGE model and compare it with the different values obtained for all the simulation done with the G-equation model.

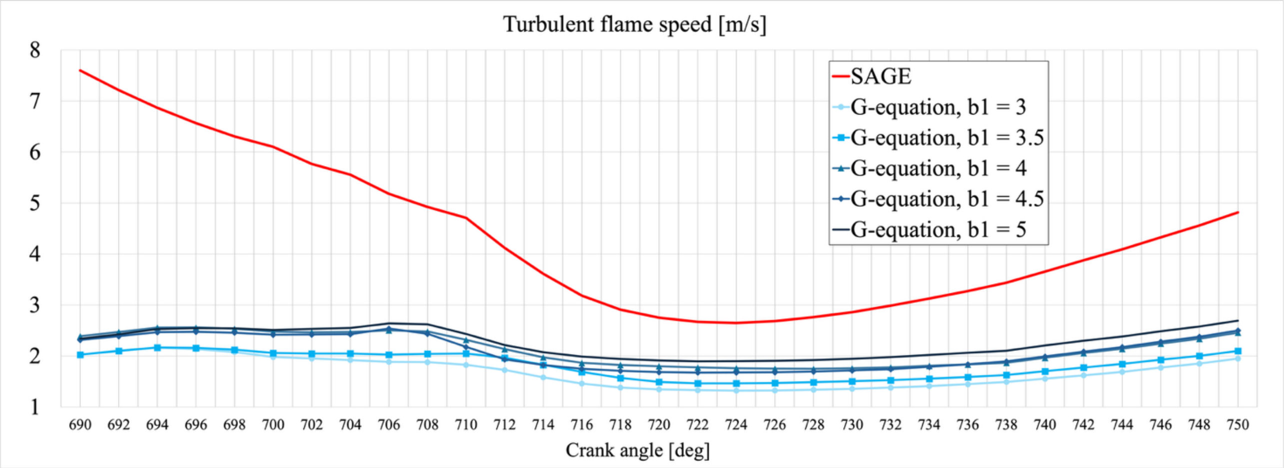

Figure 167. Turbulent flame speed comparison SAGE and G-equation models for different b_1 values in standard conditions

The figure above shows how much the turbulent flame speed calculated through the Peters formula (10) change with respect to the b_1 constant, compared to the S_t calculated trough the simplified formula for the SAGE model. The scales of values obtained remain different and the values could not be compared, however is clear that, increasing the b_1 constant, the value of turbulent flame speed changes.

The way in which the S_t changes is represented in a clearer way in Figure 168, where the first consideration that could be done is that all the simulations with the G-equation model reports a close behaviour with small differences in peak values and timing. This is due to the different effects of the flame propagation in the combustion.

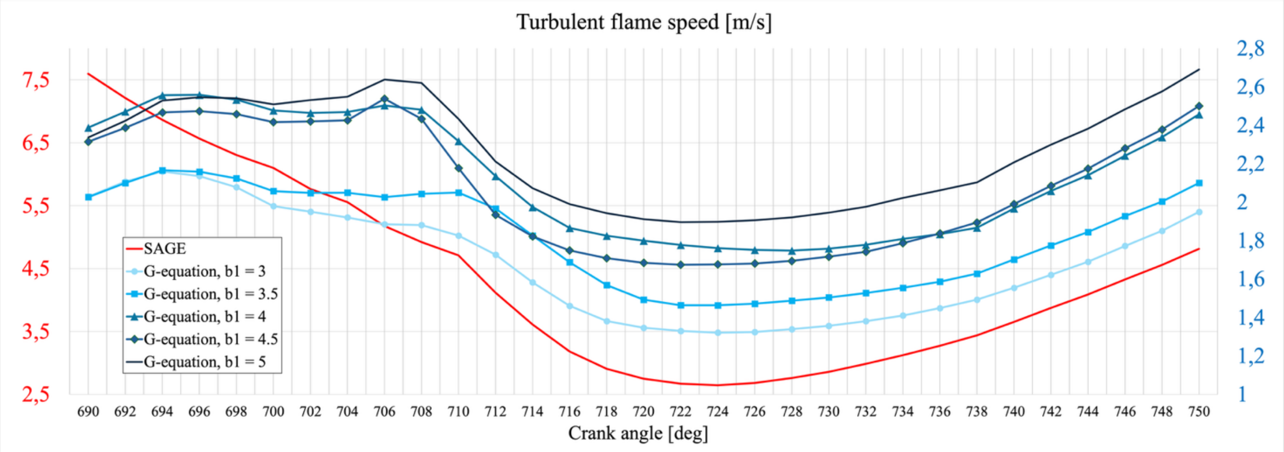

Figure 168. Comparison in different scales of the turbulent flame speed for SAGE and G-equation models with different b_1 values in standard conditions

Moreover, after the ST, the S_t for all the simulations has a peak that, for the G-equation model increases and occurs earlier if the value of the constant b_1 is higher. This behaviour is directly correlated to the results shown previously on pressure, temperature etc. and is related also in this case to the higher flame propagation that, thanks to the higher value of b_1, lead the model to be more reactive to spark and combustion.

However, Figure 168 shows that, like in the other figures, the effect of increase of that constant is not infinite, indeed the difference in results obtained for the simulations done with b_1=3 and 3.5 is higher than the one obtained with b_1=4.5 and 5. This has been explained before and the concept is the same also here for the S_t that is the variable in which the constant b_1 is defined.

NO_x emissions

Last analysis is related to the difference in emissions predicted by the different models to understand the influence that the constant b_1 gives in this field to the G-equation model. Figure 169 reports the peak temperature values for all the simulations done.

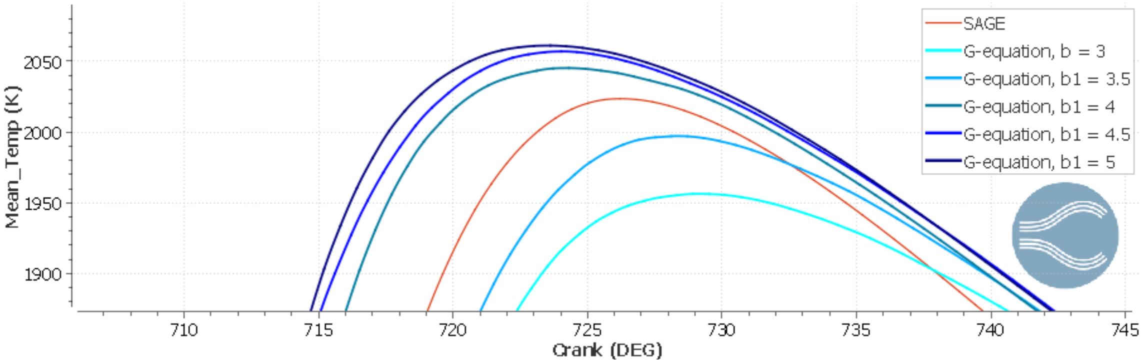

Figure 169. Zoom of peak temperature values for different b_1 values in standard conditions

The results show that with an increase in b_1 constant, the peak value of temperature rises, however, as already explained, this rise of the peak values is not infinite and seems to be saturated.

Figure 170 reports instead the NO_x emissions for the different simulations and what could be seen is that the order of the temperature peak is not strictly respected, this due to the high number of factors that influence the NO_x emissions, indeed the simulation done for b_1=4.5 shows the highest emissions among the others. A possible reason to this phenomenon is related to the max temperature achieved during the combustion in the different simulations, that gives a lot of influence in the NO_x emissions, instead Figure 169 shows the mean value in the cylinder chamber.

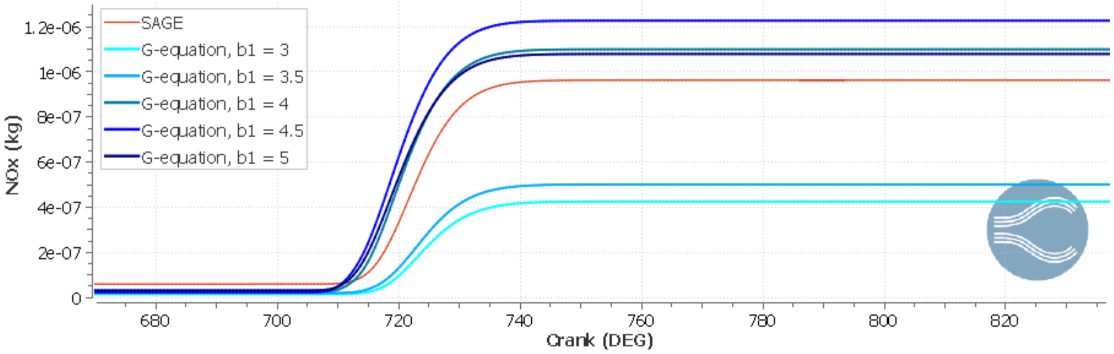

Figure 170. NO_x emissions for different b_1 values in standard conditions

Moreover, for the above plot the consideration done before are still valid, indeed the emissions for cases with b_1= 3 or 3.5 predict NO_x mass lower that the other simulations.

In the figure below the maximum temperatures reached in the cylinder during the combustion phase are shown at each crank angle.

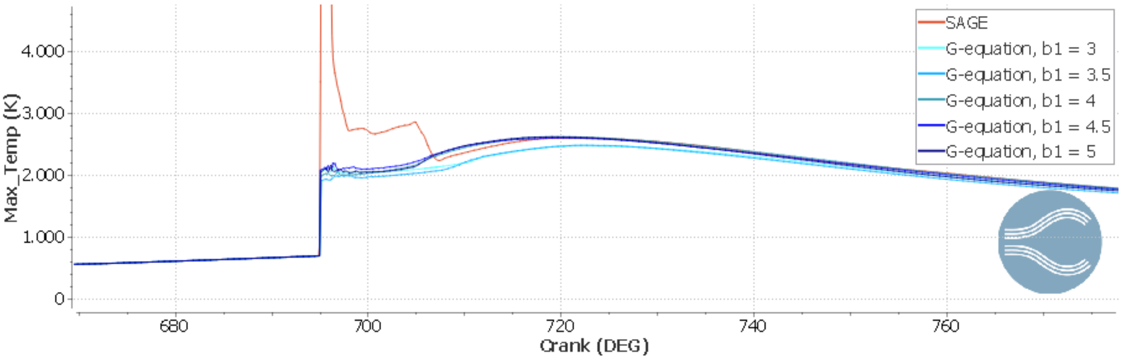

Figure 171. In-cylinder maximum temperature for different b_1 values in standard conditions

The main consideration that could be done is that the SAGE model predicts a huge value of temperature at the ST, highly different from the G-equation one. Moreover, all the G-equation model simulations are close each other. Figure 172 show a zoom of them to better see the differences.

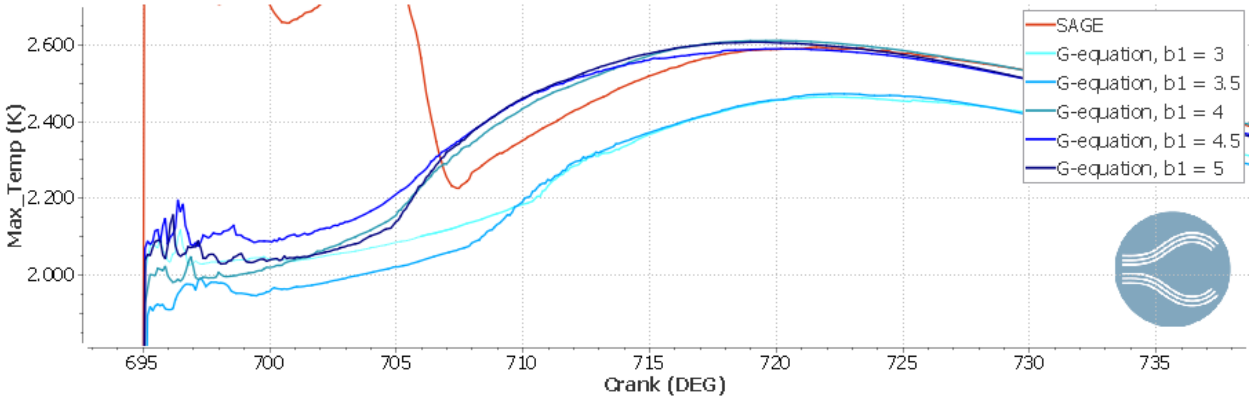

Figure 172. Zoom of the differences in max temperature between G-equation model for different b_1 values in standard conditions

The image shows that the simulation done with b_1= 4.5 predicts higher temperature values at the ST, then all the values with different constants stabilize during the peak of the combustion phase. This, as said, could be one of the reasons that leads in Figure 170 to have higher emissions for the b_1= 4.5 case instead on others.

Conclusions

After the analysis of previous studies in the introduction part, the following conclusions could be done regarding the application of hydrogen as fuel for ICE:

- The main application possible now, considering the available technologies and costs of them are related to heavy duty vehicles, busses or naval application. This is due to the necessity to have huge space for the storing system that, for safety requirement needs to have important dimensions.

- The main problem related to the application of the H2ICEs in the passenger's cars are related more to the production and storage of the fuel, rather than the powertrain itself. Moreover, the greener way to produce hydrogen is also the more costly one.

- Authors previously mentioned claim that, if in the future the costs related to the production of the hydrogen in a sustainable way will reduce, it would reach the same, if not lower, costs of maintenance not only to a FCEV or BEV, but also than a conventional gasoline or diesel car.

Moving to the conclusions related to the validation of the turbulence combustion models considered in this work, the scientific articles analysed bring to the following considerations:

- Considering the models, all of them have some difficulties in the prediction of the NO_x emissions, this probably related to the high number of parameters that collaborate to the definition of them.

- The simulation conditions that lead to better prediction by the different models are the higher fuel in the chamber (lower air/fuel ratio value) and higher spark advance with respect to the TDC, that instead give more time to the model to define the mixture and the combustion itself.

Lastly, from the analysis done using the CONVERGE software, and for all the simulation done with the models considered, the following conclusion could be done:

- The different nature of the SAGE, G-equation and ECFM models bring to different results, in particular if the hydrogen is the fuel, the ECFM model is the one that leads to higher differences in results compared to other two.

- Considering only SAGE and G-equation models, the variable that influences mostly the differences in results obtained is the air/fuel ratio, where an increase in the fuel mass leads to closer results for both the models and, for those conditions, the change in ST doesn't have high impact in the results. However, it is important to point out that a too high increase of the fuel mess could lead to autoignition or, in case of too low oxygen, no ignition.

- Changing the ST the models have better coherence in results for earlier ST, where there's more time for the fuel to mix and better describe the combustion phase.

- The SAGE model is more sensitive to the chemical variables defined during the combustion, therefore the values of the variables directly related to chemistry, at the ST, have a huge impact on the results predicted at the peak of the combustion itself.

- The G-equation model, being based on transport equation and turbulent flame speed calculation has a dependence also on some constants, that, with the proper modification could lead to more precise results in presence of experimental results.

- The SAGE model is the most used among the others for this type of analysis, it’s the one that most frequently is present in scientific articles and the model directly suggested to be used by the CONVERGE software manual [38]. However, the G-equation, has higher possibility of calibration that make it more flexible and adaptable to different simulation conditions and fuels.

- For the G-equation model, the constant b_1 gives high influence in the calculation of the turbulent flame speed and, as consequence, to all the other variable related to both the combustion and emissions. However, to manipulate the results for that specific model b_1 is not the only parameter. Indeed, as previously described, some elements don’t follow the increase in b_1, like density, TKE or the NO_x emissions, there is an important influence from the environmental variables and the simulation settings like ST and λ.

List of abbreviations

AHRR	Apparent HRR
AMR	Adaptive Mesh Refinement
ATS	After Treatment System
BDC	Bottom Dead Centre
BEV	Battery Electric Vehicles
BMEP	Brake Mean Effective Pressure
BOP	Balance Of Plant
bTDC	before Top Dead Center
BTE	Brake Thermal Efficiency
CAD	Crank Angle Degrees
CFD	Computational Fluid Dynamic
CH_4	Methane
CI	Compression Ignition Engines
CNG	Carbon Natural Gas
CO	Carbon Monoxide
CO_2	Carbon Dioxide
CR	Compression Ratio
DI	Direct Injection
DLR	German Aerospace Centre
ECFM	Extended Coherent Flame Model
EGR	Exhaust Gas Recirculation
FCEV	Fuel Cells Eclectic Vehicles
FSD	Flame Surface Density
GHG	Greenhouse gases
H_2	Hydrogen
H2ICE	Hydrogen Internal Combustion Engines
IHR	Integrated Heat Release
HRR	Hear Release Rate
IMEP	Indicated Mean Effective Pressure
ISSIM	Imposed Stretch Spark Ignition Model
ISNOx	Indicated Specific NO_x
IVC	Intake Valve Closing
JCB	Joseph Cyril Bamford Limited
LCA	Life Cycle Assessment
MFB	Mass Fuel Burned
MFR	Mass Flow Rate
MPRR	Maximum Pressure Rise Rate
NO	Nitric Oxide
NO_2	Nitrogen Dioxide
NH_3	Ammonia
ODE	Ordinary Differential Equations
PEM	Proton Exchange Membrane electrolysis
PEMFC	Polymer Electrolyte Membrane Fuel Cell
PFI	Port Fuel Injection
ppm	Part Per Million
PV	Photovoltaic
RCEM	Rapid Compression Expansion Machine
ROHR	Rate of Heat Release
S_l	Laminar Flame Speed
S_t	Turbulent Flame Speed
SA	Spark Advance
SI	Spark ignition engines
SOI	Start of injection
SR	Swirl Ratio
ST	Spark Timing
TCO	Total Cost of Ownership
TDC	Top Dead Centre
TKE	Turbulent Kinetic Energy
TTW	Tank To Well
TWC	Three Way Catalyst
UHC	Unburned Hydrocarbons
WTT	Wheel To Tank
WTW	Wheel To Well
λ	Air-fuel Ratio
φ	Equivalence Ratio
δ_l	Laminar Flame Thickness

Bibliography

[1] VOLVO, “Hydrogen trasport,” 2024. [Online]. Available: https://www.volvogroup.com/en/sustainable-transportation/sustainable-solutions/hydrogen-fuel-cells.html.

[2] aggbusiness, “hyunday,” [Online]. Available: https://www.aggbusiness.com/hyundai-doosan-infracore-mass-produce-hydrogen-internal-combustion-engines-2025/.

[3] A. Baldinelli, M. Francesconi and M. Antonelli, “Hydrogen, E-Fuels, Biofuels: What Is the Most Viable Alternative to Diesel for Heavy-Duty Internal Combustion Engine Vehicles?,” *Energies,* vol. 17, no. 4728, 2024.

[4] acciona, “Green hydrogen,” 2024. [Online]. Available: https://www.acciona.com/green-hydrogen#:~:text=Green%20hydrogen%20is%20achieved%20through,oxygen%20and%20hydrogen%20by%20electrodes.

[5] A. M. Abdalla, S. Hossain, O. B. Nisfindy, A. T. Azad, M. Dawood and A. K. Azad, “Hydrogen production, storage, transportation and key challenges with applications: A review,” *Energy conversion and management,* vol. 165, pp. 602-627, 2018.

[6] Y. Manoharan, S. E. Hosseini, B. Butler, H. Alzhahrani, B. T. F. Senior, T. Ashuri and J. Krohn, “Hydrogen Fuel Cell Vehicles; Current Status and Future Prospect,” *Applied scinces,* vol. 9, no. 2296, 2019.

[7] W. Jung, M. Choi, J. L. Jinyeong Jeong and D. Chang, “Design and analysis of liquid hydrogen-fuelled hybrid ship propulsion system with dynamic simulation,” *ScinceDirect,* vol. 50, pp. 951-967, 2024.

[8] H. Wu, J. Gao, Q. Tan, N. Huang, F. Gao, P. Puranen and Z. Rong, “Hydrogen fuel cell technology: A sustainable solution for revolutionizing aviation and achieving significant carbon reduction in the industry,” *International Journal of Hydrogen Energy,* vol. 111, pp. 711-722, 2025.

[9] L. M. Das, “HYDROGEN ENGINES: A VIEW OF THE PAST AND A LOOK INTO THE FUTURE,” *International journal hydrogen energy,* vol. 15, no. 6, pp. 425-443, 1990.

[10] C. White, R. Steeper and A. Lutz, “The hydrogen-fuelled internal combustion engine: a technical review,” *International Journal of Hydrogen Energy,* vol. 31, pp. 1292-1305, 2006.

[11] H. L. Yip, A. Srna, A. C. Y. Yuen, S. Kook, R. A. Taylor, G. H. Yeoh and P. R. M. a. Q. N. Chan, “A Review of Hydrogen Direct Injection for Internal Combustion Engines: Towards Carbon-Free Combustion,” *Applied scinces,* vol. 9, no. 4842, 2019.

[12] M. Fischer, S. Sterlepper, S. Pischinger, J. Seibel, U. Kramer and T. Lorenz, “Operation principles for hydrogen spark ignited direct injection engines for passenger car applications,” *International Journal of Hydrogen Energy,* vol. 47, pp. 5638-5649, 2022.

[13] K. M. Cabezas, G. Vorraro, X. Liu, R. Menaca, H. G. Im and a. J. W. Turner, “Numerical Analysis of Hydrogen Injection and Mixing in Wankel Rotary Engines,” *SAE international,* vol. 24, no. 69, 2024.

[14] H. Shen, P. C. d. Granado, R. S. Jorge and K. Löffler, “Environmental and climate impacts of a large-scale deployment of green hydrogen in Europe,” *Energy and climate change,* vol. 5, no. 100133, 2024.

[15] A. M. Kuyumcu, B. Bingül, F. Akar and A. Yıldız, “Well-to-wheel carbon footprint and cost analysis of gasoline, diesel, hydrogen ICE, hybrid and fully electric city buses,” *Energy,* vol. 301, no. 131685, 2024.

[16] cummis, “Benefits of hydrogen engines in trasportation,” [Online]. Available: https://www.cummins.com/news/2022/09/09/benefits-hydrogen-engines-transportation.

[17] R. L. Sari, A. F. Robles, J. M. Serrano and D. Cleary, “Techno-economic assessment of hydrogen as a fuel for internal combustion engines and proton exchange membrane fuel cells on long haul applications,” *Energy conversion and management,* vol. 311, no. 118522, 2024.

[18] A. Magnino, P. Marocco, A. Saarikoski, J. Ihonen, M. Rautanen and M. Gandiglio, “Total cost of ownership analysis for hydrogen and battery powertrains: A comparative study in Finnish heavy-duty transport,” *Journal of anargy storage,* vol. 99, no. 113215, 2024.

[19] H2X, “Hydrogen combustion vs hydrogen fuel cells vehicles,” 2024. [Online]. Available: https://h2xglobal.com/2024/05/23/hydrogen-combustion-vs-hydrogen-fuel-cell-vehicles-a-comparative-analysis-by-h2x-global/.

[20] Yamaha, “TAPPING THE POTENTIAL WITHIN 100% HYDROGEN-POWERED ENGINES,” 2022. [Online]. Available: https://www.yamaha-motor.eu/gb/en/news/tapping-the-potential-within-100--hydrogen-powered-engines/.

[21] FasTech, “The Promising Future of Hydrogen Combustion Engines,” 2024. [Online]. Available: https://www.fastechus.com/blog/hydrogen-internal-combustion-engines.

[22] EVcentral, “Why burning hydrogen in an awful idea?,” 2021. [Online]. Available: https://evcentral.com.au/why-burning-hydrogen-in-an-ice-is-an-awful-idea/.

[23] M. S. Kumar, M. Muniyappan and S. A. Selvan, “Experimental and CFD analysis on the impact of hydrogen as fuel on the behaviour of a passenger car gasoline direct injection engine,” *Journal of the energy institute,* vol. 113, no. 101487, 2024.

[24] M. U. S. Akhtar, F. Asfand, M. I. Khan, R. Mishra and A. D. Ball, “Performance and emissions characteristics of hydrogen-diesel dual-fuel combustion for heavy-duty engines,” *International Journal of Hydrogen Energy,* 2025.

[25] M. C. Cameretti, R. D. Robbio, M. Palomba and T. Z. d. Souza, “Strategies to improve ammonia combustion in a dual fuel marine engine by using CFD,” *Fuel,* vol. 381, no. 133440, 2025.

[26] F. Berni, V. Pessina, L. Teodosio, A. d’Adamo, M. Borghi and S. Fontanesi, “An integrated 0D/1D/3D numerical framework to predict performance, emissions, knock and heat transfer in ICEs fuelled with NH3-H2 mixtures: T,” *International Journal of Hydrogen Energy,* vol. 50, pp. 908-938, 2024.

[27] H. Aljabri, M. Silva, M. B. Houidi, X. Liu, M. Allehaibi, F. Almatrafi, A. S. AlRamadan, B. Mohan and E. C. a. H. G. Im, “Comparative Study of Spark-Ignited and Pre-Chamber Hydrogen-Fueled Engine: A Computational Approach,” *Energies,* vol. 15, no. 8951, 2022.

[28] N. Panthi, P. Sharma, A. S. AlRamadan, E. Cenker and G. Mignotti, “Hydrogen Combustion using Port-fuel Injections in a Heavy-Duty Optical Diesel Engine Converted to Spark Ignition Operation,” *SAE international,* vol. 32, no. 43, 2023.

[29] L. Zhao, A. Zhang, R. L. Sari, S. S. Popuri, N. Bowen and G. Matuszak, “Simulated-based combustion system development in a direct-injection spark-ignited hydrogen engine,” *Fuel,* vol. 388, no. 134434, 2025.

[30] S. Sfriso, F. Berni, S. Fontanesi, A. d’Adamo, S. Breda, L. Teodosio, S. Frigo and M. Antonelli, “Combination of G-Equation and Detailed Chemistry: An application to 3D-CFD hydrogen combustion simulations to predict NOx emissions in reciprocating internal combustion engines,” *International Journal of Hydrogen Energy,* vol. 89, pp. 161-176, 2024.

[31] S. Sfriso, F. Berni, S. Fontanesi and A. D'Adamo, “A 3D-CFD Numerical Approach for Combustion Simulations of Spark Ignition Engines Fuelled with Hydrogen: A Preliminary Analysis,” *SAE international,* vol. 1, no. 207, 2023.

[32] R. D. Robbio and E. Mancaruso, “Hydrogen combustion analysis via infrared and visible optical diagnostics combined with CFD in a dual fuel engine at low load,” *International Journal of Hydrogen Energy,* vol. 81, pp. 418-435, 2024.

[33] H. Aljabri, R. Menaca, N. Panthi, K. Moreno-Cabezas, F. Almatrafi, X. Liu, M. Silva, E. Cenker, A. AlRamadan, B. Mohan, M. Al-lehaibi, A. A. Amer, G. Magnotti and H. G. Im, “Assessment of combustion models in hydrogen engine simulations using optical measurements,” *Fuel,* vol. 392, no. 134871, 2025.

[34] W. Wei, X. He, H. Zhu, J. Duan and G. Qin, “Effect of Different Combustion Modes on the Performance of Hydrogen Internal Combustion Engines under Low Load,” *Sustainability,* vol. 14, no. 6095, 2022.

[35] V. Knop, A. Benkenida, S. Jay and O. Colin, “Modelling of combustion and nitrogen oxide formation in hydrogen-fuelled internal combustion engines within a 3D CFD code,” *International Journal of Hydrogen Energy,* vol. 33, pp. 5083-5097, 2008.

[36] G. Maio, A. Boberic, L. Giarracca, D. Aubagnac-Karkar, O. Colin, F. Duffour, K. Deppenkemper, L. Virnich and S. Pischinger, “Experimental and numerical investigation of a direct injection spark ignition hydrogen engine for heavy-duty applications,” *International Journal of Hydrogen Energy,* vol. 47, pp. 29069-29084, 2022.

[37] R. Sola, M. Baratta, D. Misul, F. Santonicito and H. Kanawabe, “Premixed hydrogen-methane combustion modelling with ECFM in a pre-chamber equipped RCEM,” *SAE intenrational,* vol. 24, no. 46, 2012.

[38] C. Science, “CONVERGE 3.0 Manual”.

[39] Wikipedia, “Set level method,” 2025. [Online]. Available: https://en.wikipedia.org/wiki/Level-set_method#:~:text=The%20Level%2Dset%20method%20(LSM,having%20to%20parameterize%20these%20objects..

[40] Wikipedia, “Paschen's law,” 2025. [Online]. Available: https://en.wikipedia.org/wiki/Paschen%27s_law.

[41] Wikipedia, “Zeldovich mechanism,” 2025. [Online]. Available: https://en.wikipedia.org/wiki/Zeldovich_mechanism.

[42] Wikipedia, “Arrhenius equation,” 2025. [Online]. Available: https://en.wikipedia.org/wiki/Arrhenius_equation.